frontiers | Research Topics

Novel reliable approaches for prediction and clinical decision-making in cancer

Edited by
Ines Zidi, Safa Bhar Layeb and Vera Rebmann

Published in
Frontiers in Immunology
Frontiers in Oncology

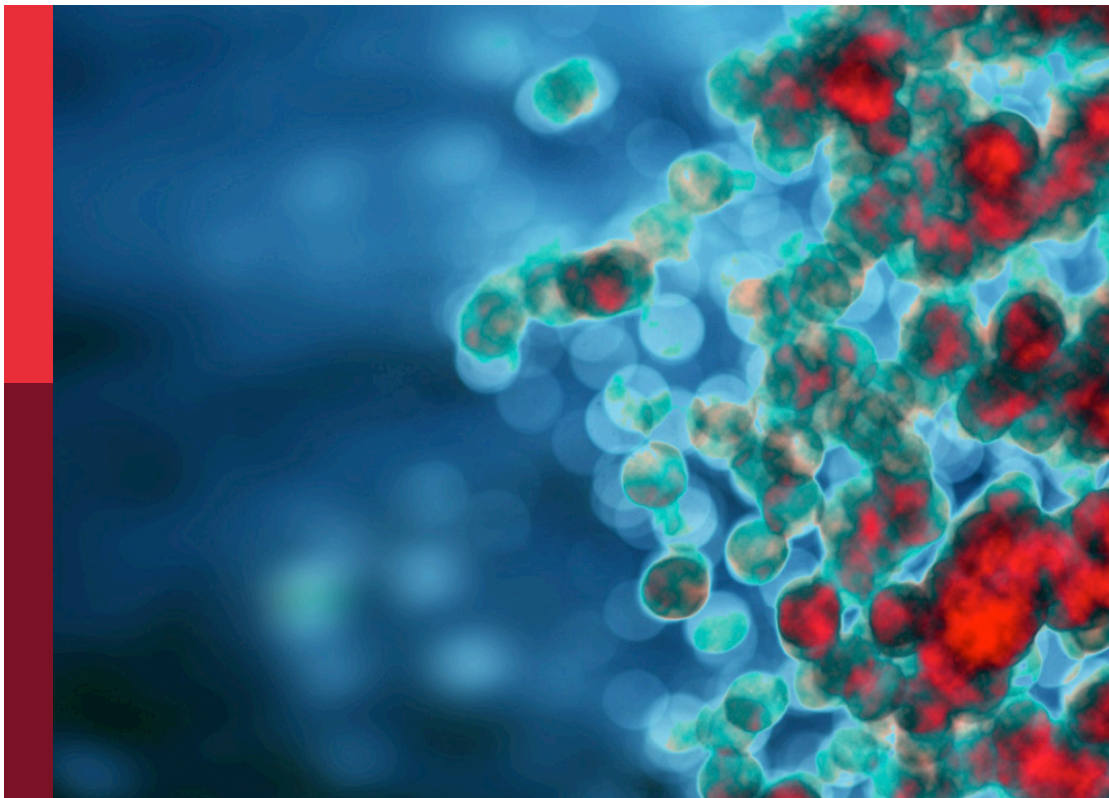

ISSN 1664-8714
ISBN 978-2-8325-5901-7
DOI 10.3389/978-2-8325-5901-7

About Frontiers

Frontiers is more than just an open access publisher of scholarly articles: it is a pioneering approach to the world of academia, radically improving the way scholarly research is managed. The grand vision of Frontiers is a world where all people have an equal opportunity to seek, share and generate knowledge. Frontiers provides immediate and permanent online open access to all its publications, but this alone is not enough to realize our grand goals.

Frontiers journal series

The Frontiers journal series is a multi-tier and interdisciplinary set of open-access, online journals, promising a paradigm shift from the current review, selection and dissemination processes in academic publishing. All Frontiers journals are driven by researchers for researchers; therefore, they constitute a service to the scholarly community. At the same time, the *Frontiers journal series* operates on a revolutionary invention, the tiered publishing system, initially addressing specific communities of scholars, and gradually climbing up to broader public understanding, thus serving the interests of the lay society, too.

Dedication to quality

Each Frontiers article is a landmark of the highest quality, thanks to genuinely collaborative interactions between authors and review editors, who include some of the world's best academicians. Research must be certified by peers before entering a stream of knowledge that may eventually reach the public - and shape society; therefore, Frontiers only applies the most rigorous and unbiased reviews. Frontiers revolutionizes research publishing by freely delivering the most outstanding research, evaluated with no bias from both the academic and social point of view. By applying the most advanced information technologies, Frontiers is catapulting scholarly publishing into a new generation.

What are Frontiers Research Topics?

Frontiers Research Topics are very popular trademarks of the *Frontiers journals series*: they are collections of at least ten articles, all centered on a particular subject. With their unique mix of varied contributions from Original Research to Review Articles, Frontiers Research Topics unify the most influential researchers, the latest key findings and historical advances in a hot research area.

Find out more on how to host your own Frontiers Research Topic or contribute to one as an author by contacting the Frontiers editorial office: frontiersin.org/about/contact

Novel reliable approaches for prediction and clinical decision-making in cancer

Topic editors

Ines Zidi — Tunis El Manar University, Tunisia

Safa Bhar Layeb — University of Tunis, Tunisia

Vera Rebmann — University of Duisburg-Essen, Germany

Citation

Zidi, I., Layeb, S. B., Rebmann, V., eds. (2025). *Novel reliable approaches for prediction and clinical decision-making in cancer*. Lausanne: Frontiers Media SA. doi: 10.3389/978-2-8325-5901-7

Table of contents

frontiers | Frontiers in Immunology

TYPE Editorial
PUBLISHED 03 January 2025
DOI 10.3389/fimmu.2024.1537956

OPEN ACCESS

EDITED AND REVIEWED BY
Peter Brossart,
University of Bonn, Germany

*CORRESPONDENCE
Ines Zidi
ines.zidi@istmt.utm.tn

RECEIVED 02 December 2024
ACCEPTED 17 December 2024
PUBLISHED 03 January 2025

CITATION
Zidi I, Layeb SB and Rebmann V (2025) Editorial: Novel reliable approaches for prediction and clinical decision-making in cancer.
Front. Immunol. 15:1537956.
doi: 10.3389/fimmu.2024.1537956

Editorial: Novel reliable approaches for prediction and clinical decision-making in cancer

Ines Zidi[1]*, Safa Bhar Layeb[2,3] and Vera Rebmann[4]

[1]Université de Tunis El Manar, Faculté des Science de Tunis, LR03ES03 Laboratoire des Microorganismes et Biomolécules Active, Tunis, Tunisia, [2]LR-OASIS, National Engineering School of Tunis, University of Tunis El Manar, Tunis, Tunisia, [3]Centre Génie Industriel, Université Toulouse, IMT Mines Albi, Albi, France, [4]Institute for Transfusion Medicine, University Hospital Essen, University of Duisburg-Essen, Essen, Germany

KEYWORDS

cancer, systemic analysis, data science, clinical data, prediction, decision-making

Editorial on the Research Topic
Novel reliable approaches for prediction and clinical decision-making in cancer

Although significant progress has been made in recent decades in understanding the development and progression of cancer, cancer remains one of the leading causes of death. Recent insights on immunobiological dysregulations involved in the development and progression of cancer demonstrate the complexity and heterogeneity of cancer, which play crucial role in the pharmacokinetic variability of cancer therapies. With regard to the prevalence of recurrence/metastases and prognosis, as well as the prediction of cancer treatment success, further investigations are urgently needed to establish cancer signatures or treatment modalities that enable improved risk stratification and improved patient management. This Research Topic focuses on studies that integrate new comprehensive systemic, combinatorial, or complexed data that could be useful to develop personalized treatment regimens, to improve immunotherapies and clinical decision-making.

It is worthy to note that the term 'complex data' is usually used to refer to high-dimensional and heterogeneous datasets resulting from several diversified fields involving genomics, transcriptomics, proteomics, and advanced medical imaging techniques such as tomography and contrast-enhanced ultrasound. These data bring important insights into the detailed processes of biological and systemic aspects and are therefore a source of invaluable knowledge for research and clinical applications.

Furthermore, the heterogeneity in data types introduces complexities with respect to data integration and analysis. The interpretation of findings in biologically or clinically relevant contexts then requires the application of sophisticated methods and the use of expert knowledge. This calls for the use of advancing techniques like Artificial intelligence (AI) and machine learning to include deep learning models, which identify patterns and make predictions. Advanced visualization tools go a step further in unraveling such complex relationships.

With the advent of AI, several algorithms are being used to integrate cancer-related data. The study of Wang et al. evaluated multiple machine learning models to build and validate a diagnostic model for patients with advanced adenoma (AA). The XGBoost model identified AA with high sensitivity (70.8%) and specificity (83.4%).

Numerous studies have addressed the pathogenesis of cancer and the phenomena that determine its persistence and progression. In this Research Topic, two studies by Bin Masood et al., and by Zhao and Ren focus on the programmed cell death ligand-1 (PD-L1) marker. Bin Masood et al. demonstrated the importance of plasma PD-L1 testing in the diagnosis of glioblastoma multiforme. Receiver operating characteristic curve analysis was used to calculate the area under the curve for specificity (100%) and sensitivity (57.81%) analysis. Kaplan-Meier survival analysis showed that patients with high PD-L1 levels before surgery had poor overall survival. Zhao and Ren showed that the tracer ^{18}F-AlFNOTA-fibroblast activation protein inhibitor (FAPI)-04 in positron emission tomography/computed tomography (PET/CT) SUVsd parameter could predict positive PD-L1 expression in patients with locally advanced esophageal squamous cell carcinoma. Both studies demonstrated the importance of the PD-L1 checkpoint molecule in the targeted therapy by identifying excellent candidates.

Data is also used to analyze the prognosis of cancer patients. The aim of different strategies is to precisely define which patients have a poor prognosis and to be able to easily guide them to other options using a cartesian scientific approach. Wang et al. for example, proposed a prognostic prediction model based on differential gene expression between muscle invasive bladder cancer (BLC) and non-muscle invasive BLC. They reported that the protein S100A9 was significantly elevated in recurrent patients. It may promote BLC cell proliferation, migration, and invasion, and may be a potential therapeutic target for BLC to further support clinical treatment decisions. Li et al. highlighted the importance of the lipid metabolism and immune-related genes in the prognosis of acute myeloid leukemia (AML). They constructed a prognostic signature with hub genes significantly associated with survival using a Gene Set Enrichment Analysis. The created risk signature was negatively correlated with immune cell infiltration. Low-risk patients were more likely to respond to immunotherapy, while high-risk patients responded better to specific targeted drugs. The risk-scoring model is expected to be a valuable tool for individualized treatment decision-making and provide valuable insights to improve patient prognosis and treatment outcomes in AML.

Furthermore, Wang et al. and Liang et al. investigated the value of disulfidptosis, a variant of cell death characterized by disulfide accumulation, in cancer. In fact, Wang et al. computed an optimal predictive model disulfidptosis score (DS) in patients with lung adenocarcinoma. They showed that patients with low DS had a better prognosis, characterized by higher OS, reduced mutation status, improved immune status, and increased sensitivity to immunotherapy. Meanwhile, Liang et al. investigated the predictive value of disulfidptosis-related genes in breast cancer (BC) and their relationship with TME. They constructed a disulfidptosis prognostic model that efficiently predicted BC prognosis.

Four contribution address clinical decision support: The mini-review by Li et al. focuses on hyperprogressive disease (HPD), which occurs in response to immunotherapy with PD-1/PD-L1 immune checkpoint inhibitors (ICIs) in a small proportion of patients with non-small cell lung cancer. It summarizes all aspects of HPD, which is characterized by accelerated tumor growth and early death, including its definition, current biomarkers, potential mechanisms and treatment options. This review provides a detailed insight into the advantages and disadvantages of immunotherapy.

Although immunotherapy, especially PD-1/PD-L1 ICIs, has contributed to a crucial breakthrough in effective cancer treatment, there is still a shortage of surrogate markers or models that guide clinical treatment or predict immunotherapeutic outcomes. For BLC, Xu et al. developed a multidimensional expression regulation model based on immunotherapeutic anti-PD-L1 genes, consisting of the following four genes IGF2BP3, P4HB, RAC3 and CLK2, which predict the efficacy of therapy and identify BLC patients, who will benefit from PD-L1 ICIs therapy. This introduces a new tool for managing BLC.

For advanced hepatocellular carcinoma, Sun et al. established a nomogram in their study that integrates quantitative parameters of tumor characteristics based on pre-treatment contrast-enhanced ultrasound and clinical and laboratory data that predict therapy efficacy of anti-PD-1 in combination with anti-VEGF treatment.

Concerning decision-marking tools for oncologists the study by Xie et al. investigated whether adjuvant therapy (AT) provides an additional benefit for recurrence-free survival (RFS) in patients with squamous cell carcinoma of the esophagus after neoadjuvant chemoimmunotherapy (nICT) and surgery in a multi-center propensity score match study including 155 nICT patients. The results of this study evidenced that postoperative AT is not necessary for an improved RFS in esophageal cancer patients undergoing nICT.

Author contributions

IZ: Conceptualization, Methodology, Validation, Writing – original draft, Writing – review & editing, Project administration, Supervision. SBL: Validation, Writing – original draft, Writing – review & editing. VR: Validation, Writing – original draft, Writing – review & editing.

Acknowledgments

The Guest editors would like to express their gratitude to all the authors who contributed their valuable work to the Research Topic,

Abbreviations: AA, advanced adenoma; AI, artificial intelligence; AML, acute myeloid leukemia; AT, adjuvant therapy; BC, breast cancer; BLC, bladder cancer; CT, computed tomography; DS, disulfidptosis score; FAPI, fibroblast activation protein inhibitor; HPD, hyperprogressive disease; ICI, immune checkpoint inhibitors; nICT, neoadjuvant chemoimmunotherapy; PD-1, programmed cell death protein-1; PD-L1, programmed cell death ligand-1; PET, positron emission tomography; TME, tumor microenvironment.

and to all the reviewers who expertly evaluated the submitted manuscripts. The efforts and dedication of everyone mentioned here have made this Research Topic a great success. The Guest editors would like to thank Frontiers for their trust and for producing a second volume on their Research Topic.

Conflict of interest

The authors declare that the research was conducted in the absence of any commercial or financial relationships that could be construed as a potential conflict of interest.

The author(s) declared that they were an editorial board member of Frontiers, at the time of submission. This had no impact on the peer review process and the final decision.

Publisher's note

frontiers | Frontiers in Immunology

TYPE Mini Review
PUBLISHED 22 May 2023
DOI 10.3389/fimmu.2023.1200875

OPEN ACCESS

EDITED BY
Vera Rebmann,
University of Duisburg-Essen, Germany

REVIEWED BY
Jianjun Zhang,
University of Texas MD Anderson Cancer Center, United States

*CORRESPONDENCE
Yanping Li
39242728@163.com
Li Zhang
Dreammaker-li@outlook.com

†These authors have contributed equally to this work and share first authorship

RECEIVED 05 April 2023
ACCEPTED 24 April 2023
PUBLISHED 22 May 2023

CITATION
Li Y, Chen T, Nie TY, Han J, He Y, Tang X and Zhang L (2023) Hyperprogressive disease in non-small cell lung cancer after PD-1/PD-L1 inhibitors immunotherapy: underlying killer. *Front. Immunol.* 14:1200875. doi: 10.3389/fimmu.2023.1200875

Hyperprogressive disease in non-small cell lung cancer after PD-1/PD-L1 inhibitors immunotherapy: underlying killer

Yanping Li[1*†], Tianhong Chen[2†], Tian Yi Nie[1], Juyuan Han[1], Yunyan He[3], Xingxing Tang[2] and Li Zhang[4*]

[1]Department of Respiratory Medicine, The Third People's Hospital of Honghe Prefecture, Gejiu, China, [2]Department of Thoracic Surgery , The Third People's Hospital of Honghe Prefecture, Gejiu, China, [3]Department of Thoracic Surgery, Yunnan Cancer Center, The Third Affiliated Hospital of Kunming Medical University, Kunming, China, [4]Department of Oncology, Gejiu City People's Hospital, Diannan Central Hospital of Honghe Prefecture, The Fifth Affiliated Hospital of Kunming Medical University, Gejiu, China

Immune checkpoint inhibitors (ICIs) target the negative regulatory pathway of T cells and effectively reactive the anti-tumor immune function of T cells by blocking the key pathway of the immune escape mechanism of the tumor—PD-1/PD-L1, and fundamentally changing the prospect of immunotherapy for non-small cell lung cancer patients. However, such promising immunotherapy is overshadowed by Hyperprogressive Disease, a response pattern associated with unwanted accelerated tumor growth and characterized by poor prognosis in a fraction of treated patients. This review comprehensively provides an overview of Hyperprogressive Disease in immune checkpoint inhibitor-based immunotherapy for non-small cell lung cancer including its definition, biomarkers, mechanisms, and treatment. A better understanding of the black side of immune checkpoint inhibitors therapy will provide a more profound insight into the pros and cons of immunotherapy.

KEYWORDS

non-small cell lung cancer, PD-1/PD-L1, response pattern, hyperprogressive disease, immunotherapy

Introduction

Lung cancer is a serious life-threatening disease, and non-small cell lung cancer (NSCLC) is one of its most prevalent subtypes (1, 2). Immune checkpoint inhibitors (ICIs), as PD-1/PD-L1 inhibitors based immunotherapy has made revolutionized effects and become a milestone in the treatment history of NSCLC (3). However, PD-1/PD-L1 blockade can lead to an unsatisfactory response pattern characterized by accelerated tumor growth and associated with poor prognosis——Hyperprogressive Disease (HPD) (4). Detrimental patterns such as

HPD and early death (ED) have been respectively observed in a proportion of NSCLC patients treated with ICIs (5). Overall survival (OS) is significantly reduced in NSCLC patients who develop HPD after PD-1/PD-L1 inhibitors blockade (4). For instance, although the PD-1 antibody Nivolumab is quite effective in clinical practice, HPD is not rare in patients with advanced NSCLC treated with Nivolumab and paralleled with a poor prognosis (6, 7). There are also several case reports about HPD events after treatment with another PD-1 inhibitor Pembrolizumab and the PD-L1 inhibitor - Durvalumab (8, 9). However, the definition and predictive biomarkers of HPD in NSCLC remain controversial, and the associated clinicopathological features or biological mechanisms are not yet determined. This significantly restricts the utilization of ICIs in patients with NSCLC (Figure 1).

Definition of HPD in NSCLC immunotherapy

The accelerate growth in tumor size and volume measured by computed tomography(CT) during ICIs blockade are the most objective characteristics of HPD by using the Response Evaluation Criteria in Solid Tumors (RECIST) 1.1 criteria (10). However, the main limitation of conventional response assessment criteria RECIST 1.1 remains due to the inadequate ability to capture the response to immunotherapies and the inapplicability to patients without pre-baseline imaging or progression on unmeasurable lesions (11, 12). Therefore, novel criteria like iRECIST is clinically used as a response evaluation tool in patients undergoing immunotherapy (13). Despite the improvement, the definition of HPD has not been standardized and the prevalence of it varies based on different criteria (14) (Table 1). The assessment criteria should address the relevance of the clinical presentation, poor prognosis, and biological behavior of the NSCLC (21). The standard definition of HPD should be continuously optimized to guide better PD-1/PD-L1 inhibitors immunotherapy.

Differentiating HPD from pseudoprogression

However, definitions based on radiological assessment alone have substantial technical limitations. The possibility of pseudoprogression (PsPD) exists when progressive deterioration of pulmonary infiltrative shadows is observed within 4 weeks among advanced NSCLC patients after the initial administration of anti-PD-1 antibody (22). Current clinical and radiological assessment strategies are inadequate to distinguish PsPD with HPD. PsPD has a similar response pattern of tumor increase or appearance of new lesions monitored by imaging at the beginning of treatment with ICIs, but shrinks later, whereas HPD is a rapid and poor prognosis progression pattern (23, 24). Consequently, repeat biopsies should be considered even if radiographic tumor progression is detected during immunotherapy (25–27). Besides, immune system-related response criteria such as NLR and ctDNA also have the potential to differentiate HPD from PsPD (28).

Clinical characteristics and biomarkers for HPD

Conventional imaging methods are restricted to determine HPD. Image-based radiomic markers extracted from baseline CT of advanced NSCLC treated with PD-1/PD-L1 inhibitors including the features of peritumoral texture and nodule vessel-related tortuosity may have prospective value for identifying the HPD. Meanwhile, using radiomics features at the lesion-level analysis has the same effect. The novel radiomic models have translational implications to distinguish vulnerable NSCLC patients at risk of HPD (29–31).

In addition to imaging indices, sensitive predictive markers of positive and negative responses to immunotherapy and clinical factors that identify high-risk NSCLC populations that potentially progress to HPD after treatment with ICIs should be continuously

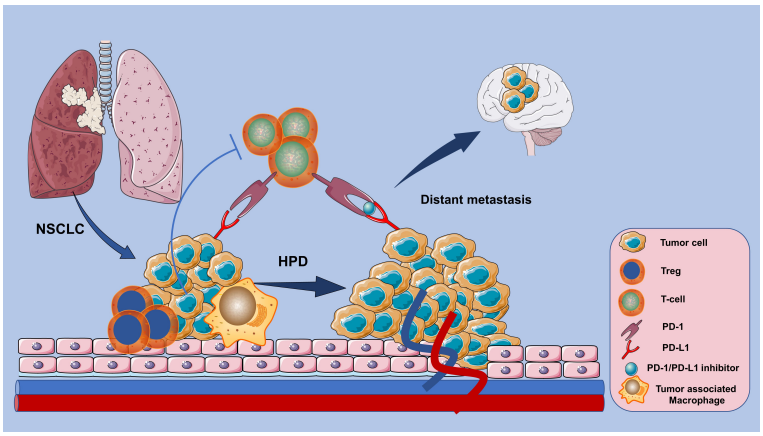

FIGURE 1
HPD response patterns associated with poor prognosis in NSCLC patients whose tumors instead accelerated in growth after PD-1/PD-L1 inhibitor-based immunotherapy.

TABLE 1 The prevalence of HPD is varied based on different criteria in NSCLC.

Study	Incidence	Criteria	Conclusion	Ref
Ignacio Matos et al	12.5% (4/32)	HPD = 1.4 x baseline sum Target lesions Or HPD = 1.2 x baseline sum Target lesions + new lesions in at least two different organs	Capturing HPD by using RECIST criteria is intuitive and easy to implement.	(15)
	16.2% (1/27)	HPD = TGR experimental period/TGR reference period ≥ 2		
Youjin Kim et al	14.3% (48/135)	volumetry	volumetric measurement is more precise than the basis of one-dimensional analysis.	(16)
	13.1%(44/135)	RECIST 1.1		
Deirdre M.H.J. ten Berge et al	7%(4/58)	TGK	TGK has predictive value for OS	(17)
Roberto Ferrara et al	13.8%	ΔTGR exceeding 50%.	HPD is associated with high metastatic burden and poor prognosis	(4)
Baptiste Kas et al	18.5%(22/406)	the TGR ratio	ΔTGR>100 is close to the characteristics of HPD (increase of the tumor kinetics and poor survival).	(18)
	5.4%(75/406)	a progression pace >2-fold and TTF<2 months		
C G Kim et al	20.9%(55/263)	TGK	HPD meeting both TGK and TGR criteria is associated with worse PFS and OS	(19)
	20.5%(54/263)	TGR		
	37.3%(98/263)	TTF		
B Abbar et al	11.3%	TGRratio	TTF is the only indicator of significantly worsened OS.	(20)
	5.7%	ΔTGR		
	17.0%	TGK		
	9.6%	RECIST		
	31.7%	TTF		

PFS, progression-free survival; TGK, tumor growth kinetics; OS, overall survival; ΔTGR, The difference between TGR before and during therapy; TTF, time to treatment failure.

developed (32, 33). There are lots of clinicopathological features associated with HPD in NSCLC patients treated with ICIs, as HPD was found associated with higher age (>65 years old) rather than higher tumor burden or specific tumor type (34) (Table 2). Subsequently, the related risk-predicting model based on clinical features is under exploring. Lung immune prognostic index (LIPI) based on dNLR > 3 and LDH > ULN is a promising tool for selecting patients who may not benefit from ICIs therapy (42).

TABLE 2 Clinicopathological features associated with HPD in NSCLC patients.

Study	Incidence	Risk factors	Ref
Yan Chen et al	8.02 to 30.43% (1389)	ECOG> 1, RMH score≥ 2, serum LDH level > ULN, the number of metastasis sites > 2, and liver metastasis	(35)
Yong Jun Choi et al	19.2% (15/78)	age, size of tumor and number of various metastatic lesions	(36)
Lee X Li et al	119/3129	elevated NLR	(37)
Youjin Kim et al	/	dNLR > 4 and LDH level > ULN	(16)
Jehun Kim et al	15.9%(35/219)	PD-L1 expression < 50%, metastatic sites≥ 3 NLR ≥ 3.3, and hemoglobin level < 10	(38)
Seo Ree Kim et al	11.3% (26/231)	heavy smoker, very low PD-L1 expression, multiple metastasis, and CAR index,	(39)
M P Petrova et al	4.8%(8/167)	a high pre-immunotherapy NLR2 and the presence of sarcopenia	(40)
Kristin L Ayers et al	/	African American patient group had lower incidence (14.7%) of HPD than the White patient group (24.5%).	(41)

ECOG, Eastern Cooperative Oncology Group; RMH score, Royal Marsden Hospital score; NLR, neutrophil-to-lymphocyte ratio; dNLR, derived neutrophil-to-lymphocyte ratio; ULN, upper limit of normal; LDH, lactate dehydrogenase; STK11, serine/threonine kinase 11 gene; ctDNA, circulating tumor DNA.

Genomic profiles is another key component of risk prediction models for HPD after immunotherapy. A case report illustrates that patients carrying EGFR exon 20 insertion and MYC amplification have the risk of developing to HPD after Nivolumab blockade (43). Besides, the coexistence of STK11 gene mutations and KRAS mutations can be used as potential biomarkers for HPD (16). Simultaneously, MDM2 family amplification or EGFR aberrations are closely linked with increasing TGR after PD-1/PD-L1 inhibitors monotherapy (44). Furthermore, long non-coding RNA (lncRNA) plays a critical role in the immune regulation of LUAD and the immune-related lncRNAs (IRLs) manifest a promising prediction value of ICIs efficacy in LUAD. Patients with low risk might gain benefits from ICIs whereas some have a risk of HPD (45). Additionally, Liquid biopsy could be assisted to identify patients at high risk of HPD, and ctDNA may be a novel prognostic biomarker of PD-1 blockade (46, 47).

There are more and more studies evaluating the predictive and prognostic value of the various immune cells in pretreatment tissue samples and identifying determinants associated with response in patients with NSCLC treated with ICIs. Levels of tumor-infiltrating lymphocytes (TILs) were strongly and independently associated with response to ICIs therapy (48). These studies illustrate that the different predictive and prognostic values for infiltrating immune cells in tumor tissue may help in selecting patients for ICIs. More importantly, the patient's TILs assessment is relatively easy to incorporate into the pathology laboratory workflow, easy to perform and inexpensive. Besides, the analyzing of immune cell of PBMC gradually draws more and more attention (Table 3).

Mechanism of HPD in NSCLC

Exploring the mechanisms of HPD in NSCLC is critical for understanding immunotherapy represented by ICIs. The tumour microenvironment (TME) is involved in influencing the response to immunotherapy as it plays a predominant role in the multiple interactions between tumor cells and the immune system (52). The biological basis and mechanisms of HPD are being elucidated and some studies have proposed immune checkpoint antibody-Fc/FcR interactions on macrophages as a mechanism of HPD after PD-1/PD-L1 blockade. Reprogramming of tumor associated macrophage (TAM) with the involvement of the Fc receptor of ICIs contribut to the induction of HPD (51). While, a study revealed that HPD was significantly linked with intratumoral B-cell density but not T-cell or macrophage (53). An animal model of a regulatory T cell (Treg)-dominated TME formed by selective depletion of CD8+ T cells by targeting CD8β antigen with near-infrared photoimmunotherapy (NIR-PIT) has shown that HPD after PD-1 blockade can be partly responsible for an imbalance between effector T cells and Tregs in the TME (54). Intrestingly, the interaction between the redox and immune system may lead to the local immunosuppression in the TME which accelerate tumor growth. Such as the administration of IgG4 and glutathione could promote tumor growth in the mouse lung cancer model (55).

Notably, analysis of the pathological features of patients who developed HPD during Pembrolizumab treatment for NSCLC suggests that the pathological type conversion of adenocarcinoma to small cell carcinoma may be the cause of HPD during ICIs treatment (56). Furthermore, changes in PD-L1 expression in tumor tissues may also be associated with HPD (8). It has been demonstrated that HPD can be prevented in preclinical models by targeting the IFNγ-PKM2-β-catenin axis. Tandem through the immunogenic, metabolic, and oncogenic pathway of the IFNγ-PKM2-β-catenin cascade is the primary mechanism of ICIs-associated HPD (57). There is an urgent need for further expansion of the scope of research and invasive research tools, and in-depth exploration of the underlying molecular mechanisms is of paramount importance.

The management of HPD in NSCLC

A comprehensive and thorough study of the mechanisms involved not only provides a plausible explanation for HPD, but also offers new opportunities to manipulate this mechanism to improve cancer immunotherapy. PD-1 blockade may promote the proliferation of highly suppressive PD-1+ eTreg cells, leading to suppression of antitumor immunity and HPD. Therefore targeting depletion of eTreg cells in tumor tissue would be an effective strategy for the treatment and prevention of HPD (58). More importantly, salvage treatment after the onset of HPD in NSCLC is also under active investigation in clinical practice. Alternative therapies, like high-dose corticosteroids, antibiotics and drainage, can be effective in treating the symptoms of HPD caused by Nivolumab (59). Besides, termination of immunotherapy should be discussed after the onset of HPD is monitored and an early switch to cytotoxic therapy is

TABLE 3 Potential predictive immune biomarkers of HPD.

Study	Immune cell	Characteristics of TILs	Ref
C G Kim	CD8+ T lymphocytes	a lower frequency of effector/memory subsets (CCR7-CD45RA- T cells among the total CD8+ T cells) a higher frequency of severely exhausted populations (TIGIT+ T cells among PD-1+CD8+ T cells)	(19)
Kyung Hwan Kim		high pre-treatment frequency of $CD39^{+}CD8^{+}$ T cells	(49)
Hugo Arasanz	CD4+ T lymphocytes	A strong expansion of highly differentiated $CD28^{-}$ CD4 T lymphocytes (CD4 THD) $CD28^{-}$ CD4 T lymphocytes ≥ 1.3 (CD4 THD burst) was significantly associated with HPD	(50)
Giuseppe Lo Russo	Macrophages	infiltration by M2-like $CD163^{+}CD33^{+}PD\text{-}L1^{+}$ clustered epithelioid macrophages.	(51)
Seo Ree Kim		fewer CD8+/PD-1+ TIL and more M2 macrophages in the tumor microenvironment	(39)

NLR, neutrophil-to-lymphocyte ratio; NLR1, neutrophil lymphocyte ratio; PLR1, platelet: lymphocyte ratio; PBMC, peripheral blood mononuclear cells; TAM, tumor-associated macrophages.

essential to avoid further disease progression (60). For instance, a comparative study retrospectively screened patients with pathologically confirmed advanced or recurrent NSCLC demontrated that the HPD rate was significantly lower in the combination therapy (cytotoxic chemotherapy plus PD-1/PD-L1 inhibitor) group than in the PD-1/PD-L1 inhibitor monotherapy group (61). Chemotherapy has the value to increase a tumor's response to immunotherapy and overcome the associated resistance (62). The combination therapy warrant further study to reduce the incidence of HPD. Moreover, informing patients of the risk of HPD is an indispensable component before the administration of ICIs. Health auhorities and trial sponsors are under obligation to monitor tumor progression in trials to help oncologists properly inform patients of the expected incidence of HPD.

Discussion

Immunotherapy based on immune checkpoint inhibitors has brought revolutionary clinical benefits to patients with NSCLC, however, immunotherapy is also a double-edged sword that may bring about serious response patterns such as HPD, which deviates from the original intent of immunotherapy's excellent clinical efficacy and high safety profile. The lack of consensus on the definitional criteria and biological basis of HPD necessitates larger studies and multicenter collaborations to standardize the criteria. How to maximize the efficacy and minimize the HPD caused by ICIS while consolidating existing therapeutic gains to benefit more NSCLC patients remains an open question. The importance of positive predictive markers for screening NSCLC patients who may benefit from immunotherapy with ICIs and the role of developing negative response predictive markers to screen out subgroups of NSCLC that do not benefit or may even develop HPD cannot be underestimated, therefor identifying potential molecular mechanisms and developing predictive biomarkers for HPD is an important direction.

Author contributions

Conception and design: LZ, YL. Administrative support: TC, TN, JH. Provision of study materials: TC, XT. Collection and assembly of data: LZ, YH. Data analysis and interpretation: YL. Manuscript writing: All authors. Final approval of manuscript: All authors. All authors contributed to the article and approved the submitted version.

Conflict of interest

The authors declare that the research was conducted in the absence of any commercial or financial relationships that could be construed as a potential conflict of interest.

Publisher's note

References

1. Sung H, Ferlay J, Siegel RL, Laversanne M, Soerjomataram I, Jemal A, et al. Global cancer statistics 2020: GLOBOCAN estimates of incidence and mortality worldwide for 36 cancers in 185 countries. *CA Cancer J Clin* (2021) 71(3):209–49. doi: 10.3322/caac.21660

2. Li Z, Feiyue Z, Gaofeng L. Traditional Chinese medicine and lung cancer–from theory to practice. *BioMed Pharmacother* (2021) 137. doi: 10.1016/j.biopha.2021.111381

3. Li Z, Feiyue Z, Gaofeng L, Haifeng L. Lung cancer and oncolytic virotherapy–enemy's enemy. *Transl Oncol* (2023) 27. doi: 10.1016/j.tranon.2022.101563

4. Ferrara R, Mezquita L, Texier M, et al. Hyperprogressive disease in patients with advanced non-small cell lung cancer treated with PD-1/PD-L1 inhibitors or with single-agent chemotherapy. *JAMA Oncol* (2018) 4(11):1543–52. doi: 10.1001/jamaoncol.2018.3676

5. Ferrara R, Mezquita L, Texier M, Lahmar J, Audigier-Valette C, Tessonnier L, et al. Comparison of fast-progression, hyperprogressive disease, and early deaths in advanced non-Small-Cell lung cancer treated with PD-1/PD-L1 inhibitors or chemotherapy. *JCO Precis Oncol* (2020) 4:829–40. doi: 10.1200/PO.20.00021

6. Costantini A, Fallet V, Corny J, Friard S, Chouaid C, Duchemann B, et al. Nivolumab-refractory patients with advanced non-small-cell lung cancer. *Lung Cancer (Amsterdam Netherlands)* (2019) 130:128–34. doi: 10.1016/j.lungcan.2019.01.015

7. Kim SH, Choi CM, Lee DH, Kim SW, Yoon S, Kim WS, et al. Clinical outcomes of nivolumab in patients with advanced non-small cell lung cancer in real-world practice, with an emphasis on hyper-progressive disease. *J Cancer Res Clin Oncol* (2020) 146(11):3025–36. doi: 10.1007/s00432-020-03293-9

8. Tanaka Y, Matsubara O, Asada K, Muramatsu A, Suzuki M, Shirai T, et al. Hyperprogressive disease after treatment with pembrolizumab in lung adenocarcinoma: an autopsy case study. *Respir Med Case Rep* (2019) 28:100885. doi: 10.1016/j.rmcr.2019.100885

9. Khreis TJ, Azar IH, Patel R, Mehdi SA. Durvalumab-induced hyperprogressive disease in nonmetastatic lung cancer. *J Oncol Pract* (2019) 15(4):217–9. doi: 10.1200/JOP.18.00739

10. Lo Russo G, Facchinetti F, Tiseo M, Garassino MC, Ferrara R. Hyperprogressive disease upon immune checkpoint blockade: focus on non-small cell lung cancer. *Curr Oncol Rep* (2020) 22(5):41. doi: 10.1007/s11912-020-00908-9

11. Léger MA, Routy B, Juneau D. FDG PET/CT for evaluation of immunotherapy response in lung cancer patients. *Semin Nucl Med* (2022) 52(6):707–19. doi: 10.1053/j.semnuclmed.2022.04.010

12. Champiat S, Ferrara R, Massard C, Besse B, Marabelle A, Soria JC, et al. Hyperprogressive disease: recognizing a novel pattern to improve patient management. *Nat Rev Clin Oncol* (2018) 15(12):748–62. doi: 10.1038/s41571-018-0111-2

13. Seymour L, Bogaerts J, Perrone A, Ford R, Schwartz LH, Mandrekar S, et al. iRECIST: guidelines for response criteria for use in trials testing immunotherapeutics. *Lancet Oncol* (2017) 18(3):e143–e52. doi: 10.1016/S1470-2045(17)30074-8

14. Park HJ, Kim KW, Won SE, Yoon S, Chae YK, Tirumani SH, et al. Definition, incidence, and challenges for assessment of hyperprogressive disease during cancer treatment with immune checkpoint inhibitors: a systematic review and meta-analysis. *JAMA Netw Open* (2021) 4(3):e211136. doi: 10.1001/jamanetworkopen.2021.1136

15. Matos I, Martin-Liberal J, García-Ruiz A, Hierro C, Ochoa de Olza M, Viaplana C, et al. Capturing hyperprogressive disease with immune-checkpoint inhibitors using RECIST 1.1 criteria. *Clin Cancer Res* (2020) 26(8):1846–55. doi: 10.1158/1078-0432.CCR-19-2226

16. Kim Y, Kim CH, Lee HY, Lee SH, Kim HS, Lee S, et al. Comprehensive clinical and genetic characterization of hyperprogression based on volumetry in advanced non-small cell lung cancer treated with immune checkpoint inhibitor. *J Thorac Oncol* (2019) 14(9):1608–18. doi: 10.1016/j.jtho.2019.05.033

17. Ten Berge D, Hurkmans DP, den Besten I, Kloover JS, Mathijssen RHJ, Debets R, et al. Tumour growth rate as a tool for response evaluation during PD-1 treatment for non-small cell lung cancer: a retrospective analysis. *ERJ Open Res* (2019) 5 (4):00179–2019. doi: 10.1183/23120541.00179-2019

18. Kas B, Talbot H, Ferrara R, Richard C, Lamarque JP, Pitre-Champagnat S, et al. Clarification of definitions of hyperprogressive disease during immunotherapy for non-small cell lung cancer. *JAMA Oncol* (2020) 6(7):1039–46. doi: 10.1001/jamaoncol.2020.1634

19. Kim CG, Kim KH, Pyo KH, Xin CF, Hong MH, Ahn BC, et al. Hyperprogressive disease during PD-1/PD-L1 blockade in patients with non-small-cell lung cancer. *Ann Oncol* (2019) 30(7):1104–13. doi: 10.1093/annonc/mdz123

20. Abbar B, De Castelbajac V, Gougis P, Assoun S, Pluvy J, Tesmoingt C, et al. Definitions, outcomes, and management of hyperprogression in patients with non-small-cell lung cancer treated with immune checkpoint inhibitors. *Lung Cancer* (2021) 152:109–18. doi: 10.1016/j.lungcan.2020.12.026

21. Wang M, Huang H, Xu Z, Li Z, Shen L, Yu Y, et al. Proposal for multiple new lesions as complement of hyperprogressive disease in NSCLC patients treated with PD-1/PD-L1 immunotherapy. *Lung Cancer* (2022) 173:28–34. doi: 10.1016/j.lungcan.2022.09.001

22. Hashimoto K, Kaira K, Kawasaki T, Yamaguchi O, Kagamu H. Psuedoprogression mimicking hyperprogressive disease after pembrolizumab treatment in a patient with lung cancer. *Lung Cancer* (2020) 139:221–3. doi: 10.1016/j.lungcan.2019.11.019

23. Rashid AS, Venigalla S, Dzeda M, Masters GA. A case report of the clinico-radiologic challenges of assessing treatment response after stereotactic radiation of oligometastases preceded by immunotherapy: pseudoprogression, mixed response patterns, and opportunities for precision radiation. *Cureus* (2019) 11(3):e4264. doi: 10.7759/cureus.4264

24. Guaitoli G, Baldessari C, Bertolini F, Tomasello C, Cascinu S, Barbieri F. Are we ready to describe response or progression to immunotherapy in lung cancer? *Crit Rev Oncol Hematol* (2019) 138:112–9. doi: 10.1016/j.critrevonc.2019.04.002

25. Shionoya Y, Hirohashi Y, Takahashi H, Hashimoto M, Nishiyama K, Takakuwa Y, et al. Possible pseudo-progression of non-small cell lung carcinoma in a patient with clinical hyper-progression associated with trousseau syndrome who was treated with pembrolizumab: a case report. *Anticancer Res* (2021) 41(7):3699–706. doi: 10.21873/anticanres.15161

26. Ando C, Ichihara E, Kano H, Iwamoto Y, Hirabae A, Nakasuka T, et al. Granulation tissue-induced pseudo-relapse during nivolumab treatment in advanced non-small cell lung cancer. *In Vivo* (2019) 33(6):2113–5. doi: 10.21873/invivo.11711

27. Kurman JS, Murgu SD. Hyperprogressive disease in patients with non-small cell lung cancer on immunotherapy. *J Thorac Dis* (2018) 10(2):1124–8. doi: 10.21037/jtd.2018.01.79

28. Zhou L, Zhang M, Li R, Xue J, Lu Y. Pseudoprogression and hyperprogression in lung cancer: a comprehensive review of literature. *J Cancer Res Clin Oncol* (2020) 146 (12):3269–79. doi: 10.1007/s00432-020-03360-1

29. Vaidya P, Bera K, Patil PD, Gupta A, Jain P, Alilou M, et al. Novel, non-invasive imaging approach to identify patients with advanced non-small cell lung cancer at risk of hyperprogressive disease with immune checkpoint blockade. *J Immunother Cancer* (2020) 8(2):e001343. doi: 10.1136/jitc-2020-001343

30. Song C, Park H, Lee HY, Lee S, Ahn JH, Lee SH. Evaluation of response to immune checkpoint inhibitors using a radiomics, lesion-level approach. *Cancers (Basel)* (2021) 13(23):6050. doi: 10.3390/cancers13236050

31. Tunali I, Gray JE, Qi J, Abdalah M, Jeong DK, Guvenis A, et al. Novel clinical and radiomic predictors of rapid disease progression phenotypes among lung cancer patients treated with immunotherapy: an early report. *Lung Cancer* (2019) 129:75–9. doi: 10.1016/j.lungcan.2019.01.010

32. Castello A, Rossi S, Mazziotti E, Toschi L, Lopci E. Hyperprogressive disease in patients with non-small cell lung cancer treated with checkpoint inhibitors: the role of (18)F-FDG PET/CT. *J Nucl Med* (2020) 61(6):821–6. doi: 10.2967/jnumed.119.237768

33. Wang X, Wang F, Zhong M, Yarden Y, Fu L. The biomarkers of hyperprogressive disease in PD-1/PD-L1 blockage therapy. *Mol Cancer* (2020) 19 (1):81. doi: 10.1186/s12943-020-01200-x

34. Champiat S, Dercle L, Ammari S, Massard C, Hollebecque A, Postel-Vinay S, et al. Hyperprogressive disease is a new pattern of progression in cancer patients treated by anti-PD-1/PD-L1. *Clin Cancer Res* (2017) 23(8):1920–8. doi: 10.1158/1078-0432.CCR-16-1741

35. Chen Y, Hu J, Bu F, Zhang H, Fei K, Zhang P. Clinical characteristics of hyperprogressive disease in NSCLC after treatment with immune checkpoint inhibitor: a systematic review and meta-analysis. *BMC Cancer* (2020) 20(1):707. doi: 10.1186/s12885-020-07206-4

36. Choi YJ, Kim T, Kim EY, Lee SH, Kwon DS, Chang YS. Prediction model for hyperprogressive disease in non-small cell lung cancer treated with immune checkpoint inhibitors. *Thorac Cancer* (2020) 11(10):2793–803. doi: 10.1111/1759-7714.13594

37. Li LX, Cappuzzo F, Matos I, Socinski MA, Hopkins AM, Sorich MJ. Low risk of hyperprogression with first-line chemoimmunotherapy for advanced non-small cell lung cancer: pooled analysis of 7 clinical trials. *Oncologist* (2023) 28(4):e205–e211. doi: 10.1093/oncolo/oyad043

38. Kim J, Kim T, Jang TW, Kang H, Kim MH, Yoon SH, et al. Clinical outcomes of hyperprogression based on volumetry in non-small cell lung cancer after immune checkpoint inhibitor treatment. *Thorac Cancer* (2022) 13(15):2170–9. doi: 10.1111/1759-7714.14539

39. Kim SR, Chun SH, Kim JR, Kim SY, Seo JY, Jung CK, et al. The implications of clinical risk factors, CAR index, and compositional changes of immune cells on hyperprogressive disease in non-small cell lung cancer patients receiving immunotherapy. *BMC Cancer* (2021) 21(1):19. doi: 10.1186/s12885-020-07727-y

40. Petrova MP, Donev IS, Radanova MA, Eneva MI, Dimitrova EG, Valchev GN, et al. Sarcopenia and high NLR are associated with the development of hyperprogressive disease after second-line pembrolizumab in patients with non-small-cell lung cancer. *Clin Exp Immunol* (2020) 202(3):353–62. doi: 10.1111/cei.13505

41. Ayers KL, Mullaney T, Zhou X, Liu JJ, Lee K, Ma M, et al. Analysis of real-world data to investigate the impact of race and ethnicity on response to programmed cell death-1 and programmed cell death-ligand 1 inhibitors in advanced non-small cell lung cancers. *Oncologist* (2021) 26(7):e1226–e39. doi: 10.1002/onco.13780

42. Mezquita L, Auclin E, Ferrara R, Charrier M, Remon J, Planchard D, et al. Association of the lung immune prognostic index with immune checkpoint inhibitor outcomes in patients with advanced non-small cell lung cancer. *JAMA Oncol* (2018) 4 (3):351–7. doi: 10.1001/jamaoncol.2017.4771

43. Huang X, Xia L, Lan F, Shao YW, Li W, Xia Y. Treatment of nivolumab results in hyperprogressive disease in a patient harboring EGFR exon 20 insertion and MYC amplification. *J Thorac Oncol* (2019) 14(9):e189–e91. doi: 10.1016/j.jtho.2019.04.009

44. Kato S, Goodman A, Walavalkar V, Barkauskas DA, Sharabi A, Kurzrock R. Hyperprogressors after immunotherapy: analysis of genomic alterations associated with accelerated growth rate. *Clin Cancer Res* (2017) 23(15):4242–50. doi: 10.1158/1078-0432.CCR-16-3133

45. Zeng Z, Liang Y, Shi J, Xiao L, Tang L, Guo Y, et al. Identification and application of a novel immune-related lncRNA signature on the prognosis and immunotherapy for lung adenocarcinoma. *Diagnostics (Basel)* (2022) 12(11):2891. doi: 10.3390/diagnostics12112891

46. Zulato E, Del Bianco P, Nardo G, Attili I, Pavan A, Boscolo Bragadin A, et al. Longitudinal liquid biopsy anticipates hyperprogression and early death in advanced non-small cell lung cancer patients treated with immune checkpoint inhibitors. *Br J Cancer* (2022) 127(11):2034–42. doi: 10.1038/s41416-022-01978-1

47. Chen Y, Li X, Liu G, Chen S, Xu M, Song L, et al. ctDNA concentration, MIKI67 mutations and hyper-progressive disease related gene mutations are prognostic markers for camrelizumab and apatinib combined multiline treatment in advanced NSCLC. *Front Oncol* (2020) 10:1706. doi: 10.3389/fonc.2020.01706

48. Rakaee M, Adib E, Ricciuti B, Sholl LM, Shi W, Alessi JV, et al. Association of machine learning-based assessment of tumor-infiltrating lymphocytes on standard histologic images with outcomes of immunotherapy in patients with NSCLC. *JAMA Oncol* (2023) 9(1):51–60. doi: 10.1001/jamaoncol.2022.4933

49. Kim KH, Hur JY, Koh J, Cho J, Ku BM, Koh JY, et al. Immunological characteristics of hyperprogressive disease in patients with non-small cell lung cancer treated with anti-PD-1/PD-L1 abs. *Immune Netw* (2020) 20(6):e48. doi: 10.4110/in.2020.20.e4

50. Arasanz H, Zuazo M, Bocanegra A, Gato M, Martínez-Aguillo M, Morilla I, et al. Early detection of hyperprogressive disease in non-small cell lung cancer by monitoring of systemic T cell dynamics. *Cancers (Basel)* (2020) 12(2):344. doi: 10.3390/cancers12020344

51. Lo Russo G, Moro M, Sommariva M, Cancila V, Boeri M, Centonze G, et al. Antibody-Fc/FcR interaction on macrophages as a mechanism for hyperprogressive disease in non-small cell lung cancer subsequent to PD-1/PD-L1 blockade. *Clin Cancer Res* (2019) 25(3):989–99. doi: 10.1158/1078-0432.CCR-18-1390

52. Genova C, Dellepiane C, Carrega P, Sommariva S, Ferlazzo G, Pronzato P, et al. Therapeutic implications of tumor microenvironment in lung cancer: focus on immune checkpoint blockade. *Front Immunol* (2021) 12:799455. doi: 10.3389/fimmu.2021.799455

53. Ku BM, Kim Y, Lee KY, Kim SY, Sun JM, Lee SH, et al. Tumor infiltrated immune cell types support distinct immune checkpoint inhibitor outcomes in patients with advanced non-small cell lung cancer. *Eur J Immunol* (2021) 51(4):956–64. doi: 10.1002/eji.202048966

54. Wakiyama H, Kato T, Furusawa A, Okada R, Inagaki F, Furumoto H, et al. Treg-dominant tumor microenvironment is responsible for hyperprogressive disease after PD-1 blockade therapy. *Cancer Immunol Res* (2022) 10(11):1386–97. doi: 10.1158/2326-6066.CIR-22-0041

55. Zhang W, Quan Y, Ma X, Zeng L, Li J, Chen S, et al. Synergistic effect of glutathione and IgG4 in immune evasion and the implication for cancer immunotherapy. *Redox Biol* (2023) 60:102608. doi: 10.1016/j.redox.2023.102608

56. Okeya K, Kawagishi Y, Muranaka E, Izumida T, Tsuji H, Takeda S. Hyperprogressive disease in lung cancer with transformation of adenocarcinoma to small-cell carcinoma during pembrolizumab therapy. *Intern Med* (2019) 58(22):3295–8. doi: 10.2169/internalmedicine.2892-19

57. Li G, Choi JE, Kryczek I, Sun Y, Liao P, Li S, et al. Intersection of immune and oncometabolic pathways drives cancer hyperprogression during immunotherapy [J]. *Cancer Cell* (2023) 41(2):304–22.e7. doi: 10.1016/j.ccell.2022.12.008

58. Kamada T, Togashi Y, Tay C, Ha D, Sasaki A, Nakamura Y, et al. PD-1(+) regulatory T cells amplified by PD-1 blockade promote hyperprogression of cancer. *Proc Natl Acad Sci USA* (2019) 116(20):9999–10008. doi: 10.1073/pnas.1822001116

59. Kanazu M, Edahiro R, Krebe H, Nishida K, Ishijima M, Uenami T, et al. Hyperprogressive disease in patients with non-small cell lung cancer treated with nivolumab: a case series. *Thorac Cancer* (2018) 9(12):1782–7. doi: 10.1111/1759-7714.12894

60. Grecea M, Marabelle A, Ammari S, Massard C, Champiat S. Managing hyperprogressive disease in the era of programmed cell death protein 1/Programmed death-ligand 1 blockade: a case discussion and review of the literature. *Oncologist* (2020) 25(5):369–74. doi: 10.1634/theoncologist.2019-0671

61. Matsuo N, Azuma K, Kojima T, Ishii H, Tokito T, Yamada K, et al. Comparative incidence of immune-related adverse events and hyperprogressive disease in patients with non-small cell lung cancer receiving immune checkpoint inhibitors with and without chemotherapy. *Invest New Drugs* (2021) 39(4):1150–8. doi: 10.1007/s10637-021-01069-7

62. Zouein J, Haddad FG, Eid R, Kourie HR. The combination of immune checkpoint inhibitors and chemotherapy in advanced non-small-cell lung cancer: the rational choice. *Immunotherapy* (2022) 14(2):155–67. doi: 10.2217/imt-2021-0014

frontiers | Frontiers in Immunology

TYPE Original Research
PUBLISHED 17 July 2023
DOI 10.3389/fimmu.2023.1202098

OPEN ACCESS

EDITED BY
Ines Zidi,
Tunis El Manar University, Tunisia

REVIEWED BY
Michael C. Burger,
Goethe University Frankfurt, Germany
Luoyang Wang,
Qingdao University, China

*CORRESPONDENCE
Sajida Batool
sajida.batool@comsats.edu.pk
Kamil Kuca
kamil.kuca@uhk.cz

RECEIVED 07 April 2023
ACCEPTED 27 June 2023
PUBLISHED 17 July 2023

CITATION
Masood AB, Batool S, Bhatti SN, Ali A, Valko M, Jomova K and Kuca K (2023) Plasma PD-L1 as a biomarker in the clinical management of glioblastoma multiforme—a retrospective cohort study. *Front. Immunol.* 14:1202098. doi: 10.3389/fimmu.2023.1202098

Plasma PD-L1 as a biomarker in the clinical management of glioblastoma multiforme—a retrospective cohort study

Aetsam Bin Masood[1], Sajida Batool[1]*, Sajid Nazir Bhatti[2], Asad Ali[3], Marian Valko[4], Klaudia Jomova[5] and Kamil Kuca[6,7]*

[1]Department of Biosciences, COMSATS University Islamabad, Islamabad, Pakistan, [2]Neurosurgery Department, Pakistan Institute of Medical Sciences (PIMS), Islamabad, Pakistan, [3]Department of Medical Lab Technology, Muslim Youth University, Islamabad, Pakistan, [4]Faculty of Chemical and Food Technology, Slovak University of Technology in Bratislava, Bratislava, Slovakia, [5]Department of Chemistry, Faculty of Natural Sciences and Informatics, Constantine The Philosopher University in Nitra, Nitra, Slovakia, [6]Faculty of Science, Department of Chemistry, University of Hradec Kralove, Hradec Kralove, Slovakia, [7]Biomedical Research Center, University Hospital Hradec Kralove, Hradec Kralove, Czechia

Background and objectives: Glioblastoma multiforme (GBM) is the most aggressive, malignant, and therapy-resistant tumor of the brain. Blockade therapy targeting the programmed cell death protein 1 (PD-1)/programmed death ligand (PD-L1) axis is currently under investigation for the clinical management of the GBM. This study has quantified the plasma levels of PD-L1 as a biomarker for the clinical management of GBM.

Methods: A cohort (n = 128) of Pakistani adult glioblastoma patients together with age- and sex-matched healthy controls was used for quantification of pre-surgery levels of plasma PD-L1. PD-L1 protein and mRNA were measured by PD-L1 platinum enzyme-linked immunosorbent assay and quantitative real-time PCR, respectively. Receiver operating characteristic (ROC) curve analysis was used to compute area under the curve (AUC) for specificity and sensitivity analyses. The Kaplan–Meier survival analysis was employed to compute overall survival.

Results: PD-L1 protein and mRNA were significantly higher in GBM compared to the healthy controls ($p < 0.0001$). Mean PD-L1 concentration for the GBM was found to be 48.98 $\pm$ 2.290 pg/ml compared to 27.63 $\pm$ 1.281 pg/ml for controls. Gene expression analysis showed statistically significant upregulation ($p < 0.0001$) of PD-L1 in blood of GBM compared to healthy controls. Plasma PD-L1 showed an AUC of 0.840 ($p < 0.0001$; 95% CI = 0.7716 to 0.9090) where a cutoff value higher than 46 pg/ml demonstrated 100% specificity and 57.81% sensitivity. Higher pre-surgery levels of PD-L1 were found to be associated with overall poor survival [$p < 0.0001$; HR (log-rank) = 0.08; 95% CI = 0.04 to 0.15]. Age, gender, and ethnic background were not found to be associated with plasma PD-L1 levels.

Conclusion: The study concludes that blood-based measurements of PD-L1 in GBM can be a promising prognostic marker and therapeutic target besides a rapid and relatively non-invasive screening tool for routine clinical management.

Future work extending the analysis to larger cohorts through multi-center collaborations involving pre-treatment and post-treatment groups is required to fully explore the usefulness of circulating PD-L1 for effective clinical applications.

KEYWORDS

GBM, PD-L1, blockade therapy, immune checkpoint inhibitors, liquid biopsy, PD-L1

1 Introduction

Glioblastoma multiforme (GBM) is a highly aggressive, malignant, and therapy-resistant primary brain tumor with poor prognosis. GBM is also the most abundant of malignant brain tumors accounting for nearly 50% of reported gliomas in USA alone (1). Though much has been learned over the past decades about the progression of GBM, the prognosis, however, remains poor. Studies have reported the median survival time of less than 24 months with a majority of afflicted succumbing to death within 12 months of the diagnosis (2). Magnetic resonance imaging (MRI) remains the gold standard for the diagnosis of GBM, yet the disease is already at an advanced stage by the time imaging reveals a tumor lesion in the brain (3). Surgical resurrection of the tumor mass is the standard first step towards therapeutic control followed by adjuvant therapy, making combined use of radiation and chemotherapy. Despite the multimodal treatment regimen, recurrence and relapse are almost always inevitable; hence, treatment of GBM remains a challenge for clinicians and biologists despite their best efforts (4).

Immune checkpoint inhibitors have been reported to confer anti-tumor resistance by augmenting the ability of immune system to eliminate the cancerous cells (5). Lately, the PD-1/PD-L1 pathway has become of interest for the clinical management of multiple cancers (6). Immune checkpoints are the inhibitory pathways regulating the cellular and systemic immune cascades through ligand–receptor interactions. These checkpoint mechanisms ensure the tight balance between protective and damaging impacts of the immune pathways and can therefore be exploited using specific antibodies for anti-tumor immunity (7). Programmed cell death protein 1, also known as PD-1, is one such transmembrane surface protein encoded by the CD274 gene located on chromosome 9. The main ligand for PD-1 protein is programmed death ligand (PD-L1), also known as B7 Homolog 1 (B7H1), which induces a co-inhibitory signal for the activated T cells expressing PD-L1. This B7H1/PD-L1 pathway inhibits the activity of cytotoxic T cells promoting their apoptosis and functional exhaustion and, hence, facilitating immune evasion of the tumor cells (8). Thus, immunotherapy by blocking these immune checkpoint inhibitors has been attempted and found promising for the treatment of many solid tumors (9). Monoclonal antibodies against the PD1/PD-L1 axis are now among the prescribed cancer treatment regimen (7).

PD-L1 has been shown to be upregulated in GBM and is particularly associated with poor prognosis, malignancy, and aggressiveness (10). Extracellular vesicles that promote the progression of GBM are also shown to express PD-L1 on their surface and therefore are considered to participate in immunosuppression (11). These findings have prompted the evaluation of immune checkpoint inhibitors for the management of hitherto unmanaged GBM (12). Many phase II and phase III clinical trials are now underway to develop antibodies against PD-L1/PD-1 nexus and to investigate new immune checkpoint inhibitors in an effort to therapeutically manage the devastating GBM (13). Besides being used as a therapeutic target for anti-tumor therapy, the levels of PD-L1 in the tumor microenvironment have also been shown as promising prognostic markers (10, 14). However, invasive procedures such as surgical excision and biopsy are required to extract enough tumor tissue material for the measurements of the levels of PD-L1, somewhat constraining the usefulness of this assay in clinical settings (15).

A soluble form of plasma PD-L1 thought to originate from PD-L1-expressing cells in the tumor microenvironment has attracted notable attention as a surrogate marker (16). Many research studies have reported the use of plasma PD-L1 as a reliable prognostic marker in multiple cancers and particularly for the evaluation of the efficacy of the checkpoint blockade therapies (17). Blood-based biomarkers have always been of clinical interest owing to their relatively non-invasive, painless, and cost-effective nature. The present study endeavored to measure the levels of plasma PD-L1 in the blood of pre-operative GBM patients in an effort to document their role in cancer prognosis and clinical management. To our knowledge, this is the first report documenting the levels of plasma PD-L1 from a local cohort of Pakistani origin. The findings of this work are expected to contribute to a broader understanding of the sensitivity, specificity, and reliability of plasma PD-L1 as a biomarker in the GBM tumor management.

2 Methods

2.1 Collection of blood samples

Adult patients with clinically confirmed diagnosis of glioblastoma (GBM) were recruited to participate in the study from the Neurosurgery ward of the Pakistan Institute of Medical Sciences (PIMS), Islamabad after granting ethical approval from both the ethical review board (ERB) of COMSATS University Islamabad (CUI) and PIMS hospital. A written informed consent

was obtained from all the study participants wherein each was informed about the research prior to collecting the blood. Healthy controls were selected with no prior history of malignant disease, diabetes, cardiovascular disease, and/or any other major illness. Controls were matched for age and gender with the malignant cohort. All the study subjects in the GBM cohort were followed up for 6 months after initial surgical excision of the tumor.

To determine the efficacy and usefulness of plasma PD-L1 as a biomarker in the therapeutic management of GBM, blood samples were collected from 64 confirmed GBM patients prior to their initial surgery. Venous blood (3 ml) was drawn by the trained hospital phlebotomist in a pre-labeled ethylene diamine tetra-acetic acid (EDTA) tube to prevent clotting following standard clinical practices. A questionnaire about the disease-related information was also completed by each participant of the study for demographic analysis. The tubes were then safely transferred to the laboratory at the Department of Bioscience, CUI, in an ice box and plasma was separated. First, the blood samples were centrifuged at low speed to separate the aqueous phase and then at high speed to remove residual cells, and finally, the separated plasma was stored at −20°C until further use.

2.2 Extraction of RNA and DNase treatment

RNA from the pelleted cells obtained after centrifugation, described in the previous step, was extracted using TRIzol reagent (Thermo Scientific) following their protocol. RNA was dissolved in RNase-free water and was quantified using NanoDrop spectrophotometer and thereafter subjected to DNase (Thermo Scientific) treatment to remove contaminating genomic DNA. First, the DNase enzyme was added to the RNA solution and incubated for an hour at 37°C as described in the manufacturer's assay. After incubation, samples were re-extracted using phenol-chloroform-isoamyl alcohol (PCI, Invitrogen), and finally, the RNase-free water was added to dissolve the RNA and stored at −20°C.

2.3 cDNA synthesis and quantitative real-time PCR

RNA was reverse transcribed using the first-strand cDNA synthesis kit (Thermo Scientific) as per their protocol. Reaction mix consisted of RNase inhibitor, reaction buffer, and dNTPs together with reverse transcriptase (RT) enzyme. After the completion of the reaction, cDNA was stored at −20°C until further analysis. qRT-PCR (Applied Biosystems) was performed using maxima SYBR® green master mix (Thermo Scientific) with β-actin gene as internal control and gene-specific PD-L1 primers.

2.4 ELISA for measurement of plasma PD-L1

PD-L1 in the plasma was measured using a commercially available assay (Human PD-L1 Platinum ELISA Kit BMS2212, Thermo Fisher Scientific) according to the protocol. Briefly, wash buffer and assay buffers were prepared and human PD-L1 standard was reconstituted and dilutions were prepared. Samples and controls were added to the micro-well plate and kit-supplied biotin conjugate was then added to each of the well. This was followed by the addition of Streptavidin-horseradish peroxidase and tetramethylbenzidine (TMB) substrate solution. The reaction was terminated by the addition of the stop solution and optical density (OD) values were measured using the automated microplate reader (AMP) Platos R II at a primary wavelength of 450 nm with 620 nm as the reference wavelength. All the measurements were made in triplicate.

2.5 Statistical analysis

The differences between two groups were analyzed by Student's *t*-test or Mann–Whitney *U*-test based on the normality of the data. The chi-square test was used to compare categorical variables between different study groups. One-way analysis of variance (ANOVA) was used to compare more than two groups. Pearson's or Spearman's correlation was used to assess associations among different parameters as appropriate. Kaplan–Meier's survival analysis was carried out to compute overall survival subsequent to initial surgery. The specificity and sensitivity of PD-L1 measurement as biomarker were determined by the area under the curve (AUC) in receiver operator characteristic (ROC) curves. Microsoft Excel (Microsoft Corporation) and GraphPad Prism V9.0 (GraphPad Software, San Diego, CA) were used for all the statistical analyses.

2.6 Role of the funding bodies

The funding bodies did not play any role in the study design, data collection, data analysis and interpretation of the data, and writing of this manuscript. The corresponding authors were responsible for undertaking the study and ensuring the accuracy and integrity of the work. All authors have read and approved the final version.

3 Results

3.1 Demographic characteristics of the study cohort

The study cohort consisted of 128 individuals, of whom 64 were confirmed GBM patients and 64 were age- and sex-matched healthy controls. Table 1 summarizes the demographic profile of the study participants. Majority of the GBM patients were in the age group of 20–39 years and showed varied ethnic backgrounds. All the subjects belonging to the GBM cohort were asked about the family history of brain tumors, and it was observed that 7.81% of them were affirmative while 92.18% did not have familial past.

10.3389/fimmu.2023.1202098

TABLE 1 Summary of the demographic features of the study cohort.

Demographic parameters	Controls (n = 64)	GBM (n = 64)	p-value*
Gender			>0.99
Male	34 (53.12%)	34 (53.12%)	
Female	30 (46.87%)	30 (46.87%)	
Age (years)			0.89
Mean age	37.70	37.94	
10–19	2 (3.12%)	2 (3.12%)	
20–29	24 (37.50%)	23 (35.93%)	
30–39	25 (39.06%)	23 (35.93%)	
40–49	6 (9.37%)	7 (10.93%)	
50–59	5 (7.81%)	6 (9.37%)	
>60	2 (3.12%)	3 (4.68%)	
Ethnicity			0.12
Punjabi	41 (64.06%)	37 (57.81%)	
Seraiki	0	1 (1.56%)	
Kashmiri	2 (3.12%)	5 (7.81%)	
Pushtun	15 (23.43%)	20 (31.25%)	
Gilgiti	6 (9.37%)	1 (1.56%)	
Family History			
Yes	–	5 (7.81%)	
No	–	59 (92.18%)	

*Chi-square test was used to compare categorical variables and t-test was used for quantitative variables.

3.2 Plasma PD-L1 levels are higher in GBM

PD-L1 concentration was found to be statistically significantly different between controls and GBM ($p < 0.0001$) as shown in Figure 1A. Mean plasma concentration of PD-L1 was 27.63 ± 1.281 pg/ml for controls and 48.98 ± 2.290 pg/ml for GBM. These concentrations were calculated using a standard curve ($R^2 = 0.9971$) where the concentrations of known standards ranged from 9.4 pg/ml to 300 pg/ml. Pearson correlation found no statistically significant association between plasma PD-L1 levels and age ($p = 0.6445$, $r = 0.058$, 95% CI = −0.1898 to 0.3003) as can be seen in Figure 1B. Male patients were found to have mean plasma PD-L1 concentrations of 51.56 ± 3.272 pg/ml and female patients had 46.05 ± 3.152 pg/ml (Figure 1C) with no statistically significant difference ($p = 0.2330$). One-way ANOVA found no significant differences in plasma PD-L1 among different ethnic groups (Figure 1D) ($p = 0.123$; $f = 1.86$; $R^2 = 0.113$).

3.3 PD-L1 gene expression was upregulated in the GBM cohort

PD-L1 was significantly upregulated in peripheral blood of GBM compared to the healthy controls ($p < 0.0001$) as shown in Figure 2A. Correlation analysis showed no statistically significant association (Figure 2B) of gene expression with age ($p = 0.6463$; $r = 0.058$; 95% CI = −0.1901 to 0.3000). The gene expression was not found to be significantly different (Figure 2C) between male and female patients ($p = 0.2121$). Ethnicity of the study participants was also not found to be associated with PD-L1 gene expression ($p = 0.051$; $f = 2.511$; $R^2 = 0.1455$) as can be seen in Figure 2D.

3.4 PD-L1 sensitivity and specificity as biomarker

ROC curve analysis was undertaken to determine the specificity and sensitivity of the plasma levels of PD-L1 gene and protein. AUC of ROC of PD-L1 gene expression in blood (Figure 3A) was found to be 0.8245 ($p < 0.0001$; 95% CI = 0.7529 to 0.8960). AUC of ROC calculated from the measured values of circulating PD-L1 (Figure 3B) was observed to be 0.840 ($p < 0.0001$; 95% CI = 0.7716 to 0.9090). Based on Youden index, a cutoff value of less than 46 pg/ml showed a specificity of 98.44% and a sensitivity of 59.38%. A value higher than 46 pg/ml demonstrated 100% specificity and 57.81% sensitivity. Table 2 summarizes the demographics of GBM cohort based on the low (<46pg/ml) and high (>46pg/ml) plasma PD-L1.

3.5 Kaplan–Meier survival analysis found an overall poor survival

The GBM cohort was followed for 6 months after initial surgery and survival was found to be 34.37%, as shown by the Kaplan–Meier curve in Figure 4A. The GBM cohort was classified into two groups based on the Youden index cutoff value of 46 pg/ml, and a statistically significant difference [$p < 0.0001$; HR (log-rank) = 0.08; 95% CI = 0.04 to 0.15] between these two groups was observed (Figure 4B).

4 Discussion

GBM is categorized as grade IV glioma with an overall poor survival and is still a challenge to be managed by conventional therapies, i.e., surgical removal, chemotherapy, and radiation (12). The tumor microenvironment created by GBM is conducive for immune evasion and suppression of the normal immune curbing of the cancer spread. Immune checkpoint inhibitors therefore offer a promising avenue for the control of such difficult-to-manage and therapy-resistant tumors (18). The PD-1/PD-L1 pathway is one such immune regulatory nexus that has been shown to have a promising anti-tumor role in the non-small cell lung cancer, head and neck squamous cell carcinoma, cervical cancer, renal cancer, gastric cancer, chronic Hodgkin's lymphoma, hepatocellular carcinoma, urothelial cancer, and melanoma (12). Though the efficacy of the PD-1/PD-L1 blockade therapy is yet somewhat controversial in the clinical management of GBM, it still has shown an overall reduction in the tumor burden combined with the activation of local and systemic immune responses suppressed by the tumor microenvironment (19, 20). The amount of PD-L1 protein is critical in predicting the therapeutic efficacy of PD-1/PD-

10.3389/fimmu.2023.1202098

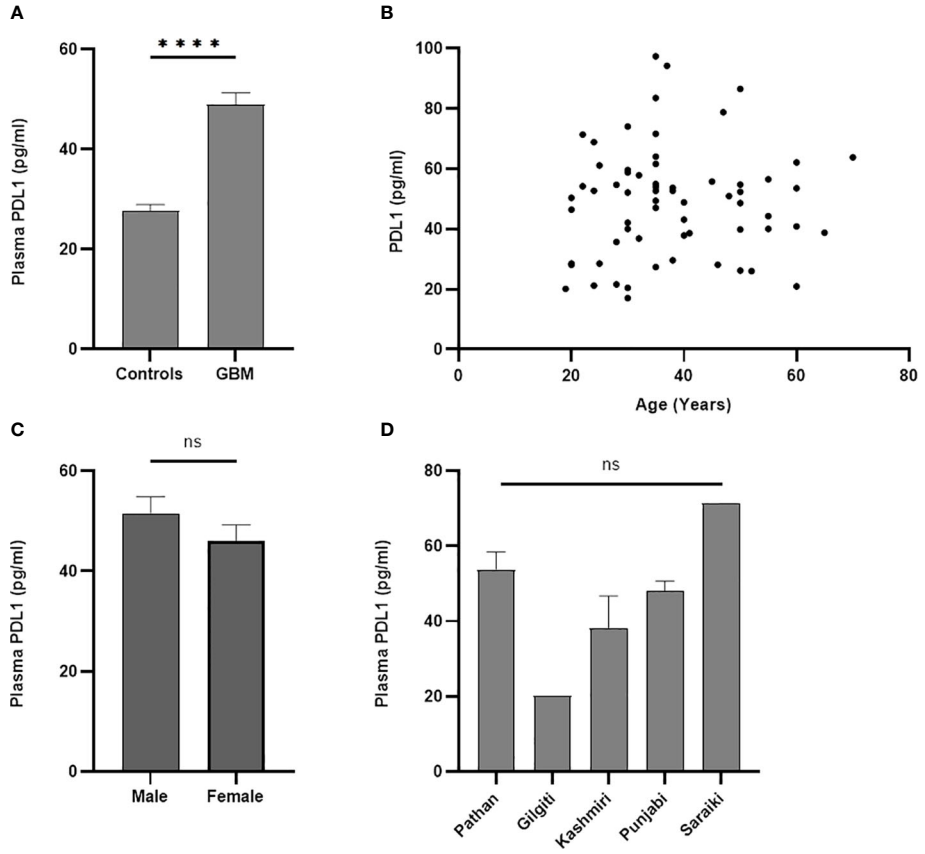

FIGURE 1
Comparative analysis of concentration of plasma PD-L1 between controls and GBM. A statistically significant difference ($p < 0.0001$) in the concentration of plasma PD-L1 was found between controls and GBM **(A)**. Plasma PD-L1 levels were found to have no association with age ($p = 0.64$) **(B)**, gender ($p = 0.23$) **(C)**, and ethnicity ($p = 0.12$) **(D)**. The '*' sign is used to represent the statistical significance. The 'ns' refers to 'not significant'.

L1 blockade therapy in different types of cancers (21). It is therefore important to investigate the expression of PD-L1 in GBM to comprehensively understand its role in cancer prognosis, diagnosis, and effective therapeutic management.

The present study quantified the levels of RNA and protein of plasma PD-L1 in the blood of the confirmed cases of GBM recruited from local cohort together with age- and sex-matched healthy controls. A large number of study participants were observed to be middle-aged with a mean age of 37.94 ± 1.58 years, a much younger age of onset compared to the other parts of the globe. The median age for most of the primary brain tumors in the developed countries has been reported as 59 years, while for GBM, it was 64 years (22). The incidence of GBM in comparatively young individuals is difficult to explain given the lack of epidemiological studies in our population, though partly this disparity in age could be explained by the fact that Pakistan hosts a larger young population where 64% are under the age of 30 years and overall life expectancy is 65.6 years (23, 24) compared to developed countries where people lived to advanced years. Study participants were asked about their family history of cancer, and it was observed that only approximately 7% were familial cases consistent with the fact that GBM is a sporadic brain tumor (25).

Pakistan is home to many different ethnic sub-groups, and since the study subjects were recruited from one of the largest government-run hospital in the capital city where treatment of GBM is available, all were asked about ethnicities to establish its putative association with PD-L1 expression. It was observed that no correlation existed with the ethnic origin and expression of the PD-L1 RNA and protein. The patients were selected randomly so that bias in sampling can be disregarded for overrepresentation of one ethnic group over the other. One possible reason for Punjabis to be present in larger number among cancer subjects may be that the capital city hosts a large population of Punjabi ethnic group followed by Pushto-speaking Pakhtuns/Pathans. Demographic differences in incidence of GBM have been observed for developed countries, and it was found that GBM was more prevalent in male than in female patients (22, 26).

GBM is currently diagnosed using imaging technologies, particularly magnetic resonance imaging (MRI) with/without contrast, and definitive pathology is confirmed by tissue biopsies. Imaging, though non-invasive, is limited by failing to distinguish actual tumor lesions from treatment-induced lesions and can often lead to diagnostic errors. Tumor biopsy, on the other hand, is highly invasive and can only offer a static glimpse into the tumor microenvironment, which, for GBM, is highly heterogeneous and

10.3389/fimmu.2023.1202098

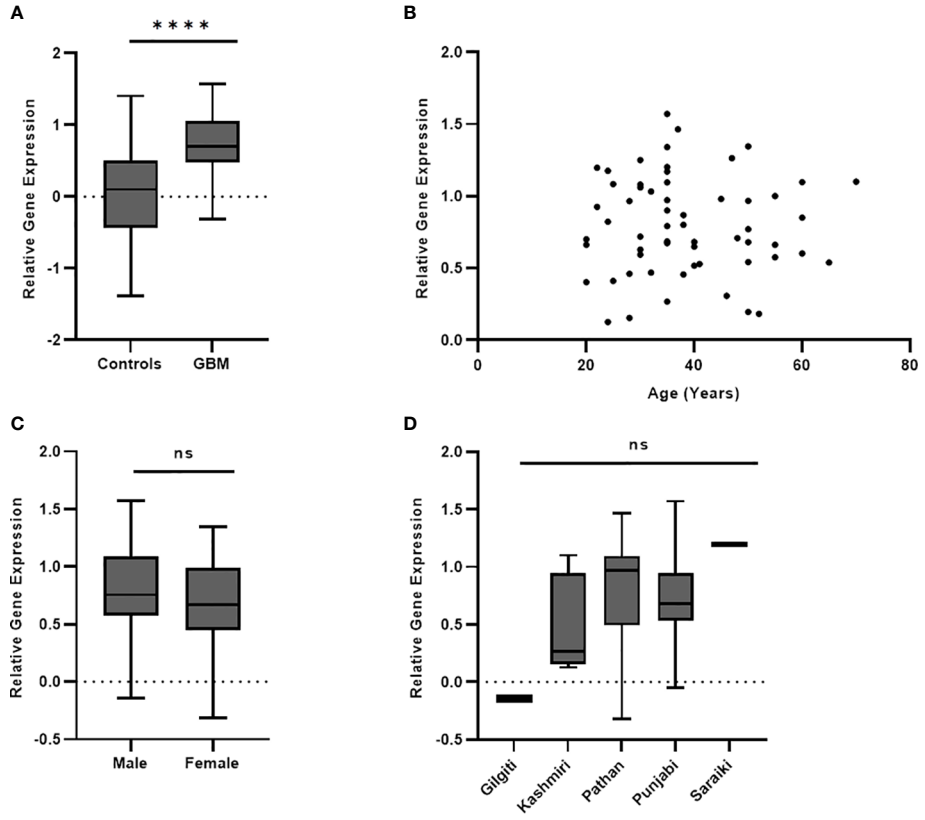

FIGURE 2
PD-L1 gene expression in blood was significantly different ($p < 0.0001$) between controls and GBM **(A)**. PD-L1 gene expression was not found to have association with age ($p = 0.64$) **(B)**, gender ($p = 0.21$) **(C)**, and ethnicity ($p = 0.05$) **(D)** of study participants. The '*' sign is used to represent the statistical significance. The 'ns' refers to 'not significant'.

ever changing with additional risk of hemorrhage and neural dysfunction (27, 28). Liquid biopsies utilizing body fluids particularly blood are minimally invasive and safe alternates for the diagnosis, pre- and post-treatment monitoring, and prognostic predictions in clinical settings. Cerebrospinal fluid (CSF) and peripheral blood are now under intensive investigation for the estimation of biomarkers that can help in the early diagnosis of GBM together with post-treatment management of the disease where tissue biopsy is not possible and/or feasible (29, 30). These minimally invasive liquid biopsies offer an additional advantage for resource-limited settings such as developing countries and underdeveloped societies where healthcare facilities are either

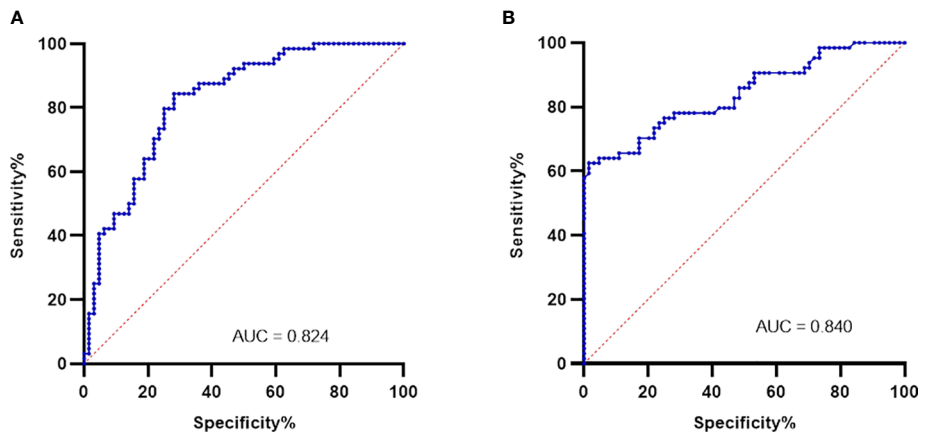

FIGURE 3
Plasma PD-L1 levels as biomarkers were evaluated using ROC analysis. PD-L1 gene expression in blood gave an AUC of 0.824 ($p < 0.0001$) as shown in **(A)**. Plasma levels of PD-L1 protein was found to have an AUC of 0.840 ($p < 0.0001$) and is shown in **(B)**.

10.3389/fimmu.2023.1202098

TABLE 2 Distribution of the GBM cohort based on the low (≤46 pg/ml) and high (≥46 pg/ml) plasma PD-L1.

Demographic parameters	Plasma PD-L1 (≤46 pg/ml)	Plasma PD-L1 (≥46 pg/ml)	*p*-value*
No. of patients	26 (40.62%)	38 (59.37%)	
Mean PD-L1 (pg/ml)	31.63	60.85	<0.0001
Gender			0.35
Male	12 (46.15%)	22 (57.89%)	
Female	14 (53.84%)	16 (42.10%)	
Mean age (years)	41.69	35.37	0.04
Mean survival time (months)	6	5	<0.0001

*Chi-square test was used to compare categorical variables, t-test was used for quantitative variables, and survival was compared by Kaplan–Meier analysis.

non-existent or burdened enough to support the routine imaging and invasive biopsies, which are obvious diagnostic choices but costly.

PD-L1 expression as a putative biomarker in GBM has been investigated with contradictory roles in prognosis mainly within tumors. Plasma PD-L1 has been shown by few other studies as a marker for primary and recurrent brain malignancies with poor prognosis and overall poor survival (17, 31–33). PD-L1 levels have been reported to be higher for other types of aggressive malignancies and are therefore attributed as an independent marker to predict overall survival and treatment efficacy (34, 35). These studies have described the differences in the levels of plasma PD-L1 following radiotherapy in gliomas and anti-PD-1 immune therapy in recurrent glioblastomas as a promising biomarker. However, the measured levels of the plasma PD-L1 were different in all these studies, necessitating further explorative studies involving large and diverse cohorts to determine its clinical usefulness. For effective cancer immunotherapeutic management using blockade therapy, PD-L1 expression in tumor tissues has been approved as companion diagnostics for pembrolizumab-based treatment (36).

Many studies have reported the elevated levels of plasma PD-L1 in several types of malignancies with a potential to be used as a prognostic biomarker but still a baseline has not been established. It therefore is of paramount importance to characterize the expression of plasma PD-L1 in larger cohorts of different ethnicities, races, tumor types, and stages of malignancy for establishing robust and reproducible cutoff values to characterize the progress of the disease and outcome of the therapy. Also, given the role of PD-L1/PD-1 in blockade therapies, the expression has to be characterized to compensate for heterogeneity in the tumor microenvironment and measurement techniques/technologies for the effective applications of immune checkpoint inhibitors. The present study compared the differences in the expression levels of plasma PD-L1 between GBM and healthy controls recruited from local population. Blood was collected from adults with a confirmed diagnosis of GBM prior to their initial surgery, and overall survival was computed following 6 months post-surgery. To our knowledge, this is the first study describing the plasma levels of PD-L1 in a GBM cohort of Pakistani origin. The present study is limited by two important considerations: first, the study has only investigated the pre-surgery levels of plasma PD-L1 and has not contrasted it with post-surgery levels. Second, the number of patients for survival analysis was small because the study recruited participants from the largest tertiary-care hospital in the capital city where treatment to multiple brain malignancies is offered. Hence, the patient pool is highly heterogeneous with clinical presentation of different types of gliomas. This study only focused on GBM, and other gliomas were not the focus of investigation; hence, it reduced the number

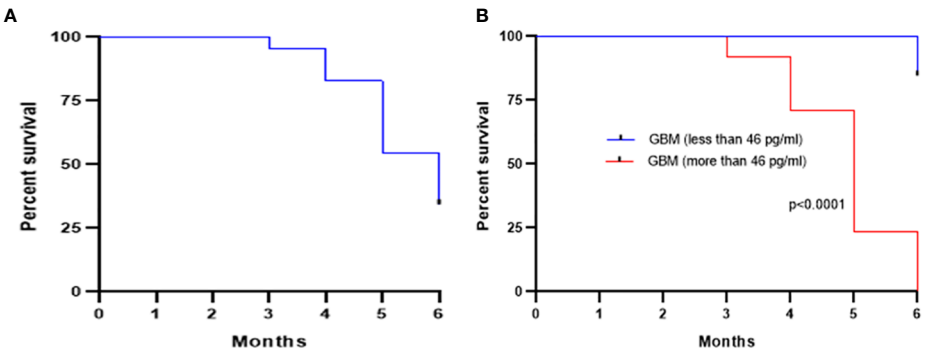

FIGURE 4
Kaplan–Meier survival curve showing an overall survival of 34.37% after 6 months of initial surgery based on the levels of plasma PD-L1 **(A)**. Further stratification of the GBM cohort based on a cutoff of 46 pg/ml (calculated from ROC curve) showed a statistically significant ($p < 0.0001$) improved survival for low pre-surgery levels of plasma PD-L1 **(B)**.

of eligible participants. For a comprehensive understanding of the role of plasma PD-L1 in overall survival and prognosis of GBM, future studies should compare the pre-surgery and post-surgery groups with a large sample size so that patient groups can be stratified and an optimized therapy regimen be devised.

Data availability statement

The original contributions presented in the study are included in the article, further inquiries can be directed to the corresponding authors.

Ethics statement

The studies involving human participants were reviewed and approved by Ethical Committee of PIMS Islamabas, Ethics Review Board of Department of Biosciences, COMSATS University Islamabad. The patients/participants provided their written informed consent to participate in this study.

Author contributions

Conceptualization: SB and KK. Methodology: AM and AA. Software, AM and SB. Validation: SB, SNB, and KK. Formal analysis: SB, MV, and KJ. Investigation: AM and SB. Resources: SB, MV, KJ, and KK. Data curation: AM, AA, and SB. Writing—original draft preparation: AM. Writing—review and editing: SB, SNB, MV, KJ, and KK. Visualization: SB and AA. Supervision: SB and KK. Project administration: SB and KK. Funding acquisition: MV, KJ, and KK. All authors have read and agreed to the published version of the manuscript.

Funding

This research was supported by the project MH CZ-DRO (UHHK, 00179906) and Excellence project PrF UHK 2217/2022-2023 Czech Republic and Research program of University of Granada awarded to KK.

Acknowledgments

The authors are greatly thankful to all the participants of the study.

Conflict of interest

The authors declare that the research was conducted in the absence of any commercial or financial relationships that could be construed as a potential conflict of interest.

Publisher's note

References

1. Low JT, Ostrom QT, Cioffi G, Neff C, Waite KA, Kruchko C, et al. Primary brain and other central nervous system tumors in the united states (2014-2018): a summary of the CBTRUS statistical report for clinicians. *Neurooncol Pract* (2022) 9(3):165–82. doi: 10.1093/nop/npac015

2. Tan AC, Ashley DM, López GY, Malinzak M, Friedman HS, Khasraw M. Management of glioblastoma: state of the art and future directions. *CA Cancer J Clin* (2020) 70(4):299–312. doi: 10.3322/caac.21613

3. Alexander BM, Cloughesy TF. Adult glioblastoma. *J Clin Oncol* (2017) 35 (21):2402–9. doi: 10.1200/JCO.2017.73.0119

4. Upadhaya PG, Pulakkat S, Patravale VB. Nose-to-brain delivery: exploring newer domains for glioblastoma multiforme management. *Drug Deliv Transl Res* (2020) 10 (4):1044–56. doi: 10.1007/s13346-020-00747-y

5. Patsoukis N, Wang Q, Strauss L, Boussiotis VA. Revisiting the PD-1 pathway. *Sci Adv* (2020) 6(38):eabd2712. doi: 10.1126/sciadv.abd2712

6. Ledford H, Else H, Warren M. Cancer immunologists scoop medicine Nobel prize. *Nature* (2018) 562(7725):20–1. doi: 10.1038/d41586-018-06751-0

7. Robert C. A decade of immune-checkpoint inhibitors in cancer therapy. *Nat Commun* (2020) 11(1):3801. doi: 10.1038/s41467-020-17670-y

8. Khan M, Zhao Z, Arooj S, Fu Y, Liao G. Soluble PD-1: predictive, prognostic, and therapeutic value for cancer immunotherapy. *Front Immunol* (2020) 11:587460. doi: 10.3389/fimmu.2020.587460

9. Gou Q, Dong C, Xu H, Khan B, Jin J, Liu Q, et al. PD-L1 degradation pathway and immunotherapy for cancer. *Cell Death Dis* (2020) 11(11):955. doi: 10.1038/s41419-020-03140-2

10. Chen RQ, Liu F, Qiu XY, Chen XQ. The prognostic and therapeutic value of PD-L1 in glioma. *Front Pharmacol* (2019) 9:1503. doi: 10.3389/fphar.2018.01503

11. Ricklefs FL, Alayo Q, Krenzlin H, Mahmoud AB, Speranza MC, Nakashima H, et al. Immune evasion mediated by PD-L1 on glioblastoma-derived extracellular vesicles. *Sci Adv* (2018) 4(3):eaar2766. doi: 10.1126/sciadv.aar2766

12. Wang X, Lu J, Guo G, Yu J. Immunotherapy for recurrent glioblastoma: practical insights and challenging prospects. *Cell Death Dis* (2021) 12(4):299. doi: 10.1038/s41419-021-03568-0

13. Yang T, Kong Z, Ma W. PD-1/PD-L1 immune checkpoint inhibitors in glioblastoma: clinical studies, challenges and potential. *Hum Vaccin Immunother* (2021) 17(2):546–53. doi: 10.1080/21645515.2020.1782692

14. Xue S, Song G, Yu J. The prognostic significance of PD-L1 expression in patients with glioma: a meta-analysis. *Sci Rep* (2017) 7(1):4231. doi: 10.1038/s41598-017-04023-x

15. Antonios JP, Soto H, Everson RG, Moughon DL, Wang AC, Orpilla J, et al. Detection of immune responses after immunotherapy in glioblastoma using PET and MRI. *Proc Natl Acad Sci USA* (2017) 114(38):10220–5. doi: 10.1073/pnas.1706689114

16. Shen H, Ji Y, Zhou D, Zhang Y, Wang W, Sun J, et al. Soluble programmed death-ligand 1 are highly expressed in peripheral T-cell lymphoma: a biomarker for prognosis. *Hematology* (2019) 24(1):392–8. doi: 10.1080/16078454.2019.1590965

17. Liu S, Zhu Y, Zhang C, Meng X, Sun B, Zhang G, et al. The clinical significance of soluble programmed cell death-ligand 1 (sPD-L1) in patients with gliomas. *Front Oncol* (2020) 10:9. doi: 10.3389/fonc.2020.00009

18. Scheffel TB, Grave N, Vargas P, Diz FM, Rockenbach L, Morrone FB. Immunosuppression in gliomas via PD-1/PD-L1 axis and adenosine pathway. *Front Oncol* (2021) 10:617385. doi: 10.3389/fonc.2020.617385

19. Tritz ZP, Ayasoufi K, Johnson AJ. Anti-PD-1 checkpoint blockade monotherapy in the orthotopic GL261 glioma model: the devil is in the detail. *Neurooncol Adv* (2021) 3(1):vdab066. doi: 10.1093/noajnl/vdab066

20. Cloughesy TF, Mochizuki AY, Orpilla JR, Hugo W, Lee AH, Davidson TB, et al. Neoadjuvant anti-PD-1 immunotherapy promotes a survival benefit with intratumoral and systemic immune responses in recurrent glioblastoma. *Nat Med* (2019) 25(3):477–86. doi: 10.1038/s41591-018-0337-7

21. Herbst RS, Soria JC, Kowanetz M, Fine GD, Hamid O, Gordon MS, et al. Predictive correlates of response to the anti-PD-L1 antibody MPDL3280A in cancer patients. *Nature* (2014) 515(7528):563–7. doi: 10.1038/nature14011

22. Ostrom QT, Cioffi G, Gittleman H, Patil N, Waite K, Kruchko C, et al. CBTRUS statistical report: primary brain and other central nervous system tumors diagnosed in the united states in 2012-2016. *Neuro Oncol* (2019) 21(Suppl 5):v1–v100. doi: 10.1093/neuonc/noz150

23. UNDP (United Nations Development Program). *National human development report (2017)* (2017). Pakistan. New York. Available at: https://hdr.undp.org/content/national-human-development-report-2017-pakistan (Accessed 15 December 2022).

24. *The world bank data* . Pakistan. Available at: https://data.worldbank.org/country/Pakistan (Accessed 15 December 2022).

25. Grochans S, Cybulska AM, Simińska D, Korbecki J, Kojder K, Chlubek D, et al. Epidemiology of glioblastoma multiforme-literature review. *Cancers (Basel)* (2022) 14 (10):2412. doi: 10.3390/cancers14102412

26. Carrano A, Juarez JJ, Incontri D, Ibarra A, Guerrero Cazares H. Sex-specific differences in glioblastoma. *Cells* (2021) 10(7):1783. doi: 10.3390/cells10071783

27. Müller Bark J, Kulasinghe A, Chua B, Day BW, Punyadeera C. Circulating biomarkers in patients with glioblastoma. *Br J Cancer* (2020) 122(3):295–305. doi: 10.1038/s41416-019-0603-6

28. Gatto L, Franceschi E, Di Nunno V, Tosoni A, Lodi R, Brandes AA. Liquid biopsy in glioblastoma management: from current research to future perspectives. *Oncologist* (2021) 26(10):865–78. doi: 10.1002/onco.13858

29. An Y, Fan F, Jiang X, Sun K. Recent advances in liquid biopsy of brain cancers. *Front Genet* (2021) 12:720270. doi: 10.3389/fgene.2021.720270

30. Bonosi L, Ferini G, Giammalva GR, Benigno UE, Porzio M, Giovannini EA, et al. Liquid biopsy in diagnosis and prognosis of high-grade gliomas; state-of-the-Art and literature review. *Life (Basel)* (2022) 12(3):407. doi: 10.3390/life12030407

31. Mair MJ, Pajenda S, Ilhan-Mutlu A, Steindl A, Kiesel B, Widhalm G, et al. Soluble PD-L1 is associated with local and systemic inflammation markers in primary and secondary brain tumours. *ESMO Open* (2020) 5(6):e000863. doi: 10.1136/esmoopen-2020-000863

32. Mair MJ, Ilhan-Mutlu A, Pajenda S, Kiesel B, Wöhrer A, Widhalm G, et al. Circulating PD-L1 levels change during bevacizumab-based treatment in recurrent glioma. *Cancer Immunol Immunother* (2021) 70(12):3643–50. doi: 10.1007/s00262-021-02951-2

33. Cabezas-Camarero S, García-Barberán V, Pérez-Alfayate R, Gandia ML, Diaz-Millan I, Perez-Segura P. Plasma PD-L1 levels according to histologic grade and IDH status in patients with gliomas. *J Clin Oncol* (2020) 5(suppl):69–9. doi: 10.1200/JCO.2020.38.5_suppl.69

34. Oh SY, Kim S, Keam B, Kim TM, Kim DW, Heo DS. Soluble PD-L1 is a predictive and prognostic biomarker in advanced cancer patients who receive immune checkpoint blockade treatment. *Sci Rep* (2021) 11(1):19712. doi: 10.1038/s41598-021-99311-y

35. Han Y, Liu D, Li L. PD-1/PD-L1 pathway: current researches in cancer. *Am J Cancer Res* (2020) 10(3):727–42.

36. Twomey JD, Zhang B. Cancer immunotherapy update: FDA-approved checkpoint inhibitors and companion diagnostics. *AAPS J* (2021) 23(2):39. doi: 10.1208/s12248-021-00574-0

frontiers | Frontiers in Immunology

TYPE Original Research
PUBLISHED 27 July 2023
DOI 10.3389/fimmu.2023.1229560

OPEN ACCESS

EDITED BY
Safa Bhar Layeb,
University of Tunis, Tunisia

REVIEWED BY
Li Li,
Peking University, China
Sajida Batool,
COMSATS University, Pakistan

*CORRESPONDENCE
Lijuan Niu
niulijuan8197@126.com
Yu Chen
xxchenyu@sina.com

RECEIVED 26 May 2023
ACCEPTED 11 July 2023
PUBLISHED 27 July 2023

CITATION
Sun C, Wang Q, Hou L, Zhang R, Chen Y and Niu L (2023) A contrast-enhanced ultrasound-based nomogram for the prediction of therapeutic efficiency of anti-PD-1 plus anti-VEGF agents in advanced hepatocellular carcinoma patients. *Front. Immunol.* 14:1229560. doi: 10.3389/fimmu.2023.1229560

A contrast-enhanced ultrasound-based nomogram for the prediction of therapeutic efficiency of anti-PD-1 plus anti-VEGF agents in advanced hepatocellular carcinoma patients

Chao Sun[1], Qian Wang[1], Lu Hou[2], Rui Zhang[1], Yu Chen[1]* and Lijuan Niu[1]*

[1]Department of Ultrasound, National Cancer Center/National Clinical Research Center for Cancer/Cancer Hospital, Chinese Academy of Medical Sciences and Peking Union Medical College, Beijing, China, [2]Department of Radiotherapy, National Cancer Center/National Clinical Research Center for Cancer/Cancer Hospital, Chinese Academy of Medical Sciences and Peking Union Medical College, Beijing, China

Background: There is no study focusing on noninvasive predictors for the efficacy of sintilimab (anti-PD-1) plus IBI305 (a bevacizumab biosimilar) treatment in advanced hepatocellular carcinoma (HCC).

Method: A total of 33 patients with advanced HCC were prospectively enrolled and received sintilimab plus IBI305 treatment from November 2018 to October 2019. Baseline characteristics including clinical data, laboratory data, and tumor features based on pretreatment CT/MR were collected. Meanwhile, pretreatment contrast-enhanced ultrasound (CEUS) for target tumor was performed and quantitative parameters were derived from time–intensity curves (TICs). A nomogram was developed based on the variables identified by the univariable and multivariable logistic regression analysis. The discrimination, calibration, and clinical utility of the nomogram were evaluated.

Results: Tumor embolus and grad ratio were significant variables related to the efficacy of sintilimab plus IBI305 strategy. The nomogram based on these two variables achieved an excellent predictive performance with an area under curve (AUC) of 0.909 (95% CI, 0.813–1). A bootstrapping for 500 repetitions was performed to validate this model and the AUC of the bootstrap model was 0.91 (95% CI, 0.8–0.98). The calibration curve and decision curve analysis (DCA) showed that the nomogram had a good consistency and clinical utility.

Conclusions: This study has established and validated a nomogram by incorporating the quantitative parameters of pretreatment CEUS and baseline clinical characteristics to predict the anti-PD-1 plus anti-VEGF treatment efficacy in advanced HCC patients.

KEYWORDS

hepatocellular carcinoma, programmed death receptor-1, contrast-enhanced ultrasound, nomogram, anti-VEGF (vascular endothelial growth factor)

Introduction

Hepatocellular carcinoma (HCC), with a 5-year survival rate of 5%–30%, ranks as the fourth most common malignant tumor and the second leading cause of cancer-related death (1, 2). The insidious onset and slow progression of symptoms usually result in delayed diagnosis of HCC. Considering the severity of HCC, only 10%–15% of HCC patients are eligible for surgical resection (3). In general, systemic treatment is the main option for advanced HCC patients (4). Anti-vascular endothelial growth factor (anti-VEGF) drugs were applied as standard systemic treatment agent, but the median overall survival (OS) ranges from 10.7 to 13.6 months (5–9).

Immune checkpoint inhibitors (ICIs), particularly antibodies targeting programmed cell death-1 (PD-1) or programmed cell death ligand-1 (PD-L1), have exhibited promising potential at improving tumor response and survival of HCC patients. The United States Food and Drug Administration (FDA) has approved anti-PD-1/PD-L1 for the treatment of advanced HCC (10). However, the efficacy of mono-immunotherapy remains limited. As first-line treatment, nivolumab monotherapy did not prolong the median OS compared with sorafenib monotherapy (11). The combination of ICIs and VEGF inhibitors is a promising strategy to fight tumors in a synergistic way. The VEGF inhibitor helps to induce the normalization of tumor vascularization, alleviate immunosuppression of tumor microenvironment, and increase the infiltration and activation of immune cells. Meanwhile, PD-1/PD-L1 inhibitors can enhance the stimulation of immune cells by targeting immune checkpoints (12–14). Recently, a series of clinical trials had demonstrated that ICIs plus anti-VEGF can result in more improvements in objective response rate (ORR), disease control rate (DCR), and progression-free survival (PFS) (15, 16). In 2020, FDA had approved the combined strategy as first-line treatment for advanced HCC.

In the background of precision medicine, it is urgent to identify the population who are likely to benefit from combined treatment. Imaging plays an important role in the management of HCC and has potential to provide noninvasive information for the prediction of treatment efficacy. Current studies mainly focused on applying imaging features to predict treatment response to mono-immunotherapy. Based on radiomics features extracted from pretreatment contrast-enhanced CT images, Yuan developed a nomogram to predict the anti-PD-1 treatment efficacy in patients with advanced HCC (17). Huang reported that the presence of the hyper-enhanced rim on the Kupffer phase images obtained from Sonazoid-contrast-enhanced ultrasound (Sonazoid-CEUS) is a promising biomarker to predict unfavorable response with anti-PD-1/PD-L1 therapy in HCC patients (18). At present, no noninvasive predictors for the efficacy of ICI plus anti-VEGF inhibitor treatment have been reported.

CEUS is a first-line modality in the management of HCC with high temporal resolution and high sensitivity to detect hypervascularization (19, 20). Different from contrast-enhanced CT/MR agents that deposit into extravascular space, ultrasound contrast agents are true intravascular contrast agents that are capable of quantification analysis of tumor perfusion information. Quantification parameters of CEUS had been widely used for the early evaluation or prediction of the response to antiangiogenic therapy in tumors with various types (21–24).

In order to screen population that might potentially benefit from combined treatments, our study develops a nomogram based on quantification parameters of pretreatment CEUS to predict the efficacy of ICI plus anti-VEGF inhibitor treatment.

Materials and methods

This was a single-center prospective study approved by the ethics committee of the cancer hospital of the Chinese Academy of Medical Sciences (No.18-126/1704). All enrolled patients had given their informed consent.

Patient selection and sample size estimation

From November 2018 to October 2019, 33 HCC patients treated with sintilimab (anti-PD-1) plus a bevacizumab biosimilar (anti-VEGF) were included in this study. The inclusion criteria were listed as follows: (1) patients who were aged ≥ 18 and diagnosed with HCC by histology or cytology; (2) with the presence of measurable lesions (≥1) proven by CEUS and contrast-enhanced CT/MR examination performed within 1 week before the start of combined treatment; (3) with a regular CT/MR follow-up duration ≥ 12 weeks; (4) patients in stage B or C according to the Barcelona

Clinic Liver Cancer (BCLC) staging system; (5) with Eastern Cooperative Oncology Group (ECOG) performance status of 0 or 1; and (6) with Child–Pugh liver function scores ≤7. The exclusion criteria were as follows: (1) without baseline CEUS and CT/MR examination; (2) accepted locoregional therapy during follow-up; (3) currently has or had a history of malignant tumors besides HCC; (4) allergic to ultrasound/CT/MR contrast agents or other contraindication for ultrasound contrast agent application; and (5) incomplete follow-up.

The sample size estimation was based on the reported DCR in advanced HCC patients treated with anti-PD-1/PD-L1 plus anti-VEGF agents and on the principle of 10 outcome events per variable (25). According to a systematic review and meta-analysis, The DCR was 0.75 in PD-L1/PD-1 plus anti-VEGF agents. Using an estimated DCR of 0.75 in the study population and for two predictors (15), we aimed to enroll 27 HCC patients but actually enrolled 33.

Dosage of anti-PD-1 plus anti-VEGF agents

Sintilimab was given intravenously at a fixed dose of 200 mg every 3 weeks and the bevacizumab biosimilar (IBI305) was given intravenously at a fixed dose of 7.5 mg/kg or 15 mg/kg. The incidence and severity of AEs were graded and recorded according to the Common Terminology Criteria for AEs version 5.0 (CTCAE 5.0).

Clinical data and assessments of response to therapy

Baseline clinical characteristics including basic data, laboratory data, and abdominal CT/MR data of enrolled patients were collected and documented. Basic data included age, gender, BCLC stage, ECOG performance, and Child–Pugh score. Laboratory data included alpha-fetoprotein (AFP), total bilirubin (TBIL), alanine aminotransferase (ALT), aspartate aminotransferase (AST), and prothrombin time (PT). Target tumor size, tumor number, vascular invasion, and extra-hepatic metastasis status were documented according to baseline abdominal CT and/or MRI performed within 2 weeks before the initial treatment. Then, the follow-up abdominal CT was performed every 4 weeks after the initial treatment for treatment evaluation. Meanwhile, the baseline CEUS was performed within 1 week before the start of combined treatment and the details will be illustrated in *Examination procedure of CEUS*. Both CEUS and CT/MR chose the same HCC lesion as target lesion of each patient for evaluation. Based on anatomical location, a radiologist with over 20 years' specialization in CEUS diagnosis was assigned to ensure that the target lesion observed by CEUS is consistent with the target lesion evaluated by CT/MR. If multiple HCC lesions exist in a patient, the biggest lesion that can be clearly revealed by CEUS was chosen as the target lesion.

Modified response evaluation criteria in solid tumor (mRECIST) was used to evaluate tumor response to treatment, and the classifications were listed as follows: (1) complete response (CR), disappearance of any arterial enhancement in target lesion; (2) partial response (PR), the total reduction of the diameters of the target lesions (arterial phase) by ≥30%; and (3) stable disease (SD), any cases that do not qualify for either PR or progressive disease (PD); PD, the diameter of the target lesion increased by at least 20% compared with the baseline value or the appearance of new lesions with enhancement in the arterial phase. Based on the response evaluation by two experienced radiologists (with 10 years' experience in abdominal CT/MR diagnosis), the patients with CR, PR, or SD ≥ 12 weeks were classified as the non-PD group while the patients with PD during follow-up were categorized as the PD group.

Examination procedure of CEUS

The conventional ultrasound and CEUS were performed using LOGIQ E9 (GE Healthcare, WI, USA) by an experienced radiologist (with 3 years' experience in CEUS) within 1 week before the initial treatment. The frequency range of the probe was 3 to 5 MHz. The lyophilized powder of contrast agent Sono Vue (Bracco SpA, Milan, Italy) was reconstituted by adding 5 ml of 0.9% saline and shaking to form a homogeneous microbubble suspension. Before activating CEUS mode, conventional ultrasound was performed to screen the whole liver and choose target HCC lesions and best sonographic sections for observation. If multiple HCC lesions exist in a patient, the biggest lesion that can be clearly and completely presented by conventional ultrasound was selected as target lesion. The final sonographic sections for revealing target lesions were acquired by slightly adjusting on the basis of one of the standard sections introduced by the color atlas of ultrasound anatomy (26). The location (Couninaud liver segment), surrounding anatomic markers, and observing section of each target lesion were documented in order to facilitate the further identification in CT/MR images by a radiologist with over 20 years' experience in HCC diagnosis. Then, a bolus of 2.4-ml suspension of the contrast agent was administered *via* antecubital vein. The CEUS mode and the chronograph were activated simultaneously. Continuous imaging was acquired immediately after injection of the contrast agent and lasted for 3 min. The imaging was presented as a dynamic video with a DICOM format. The dynamic videos were stored in LOGIQ E9 and backed up in a portable hard drive for further analysis.

Quantification analysis of CEUS

The dynamic videos acquired from CEUS was analyzed using the built-in software of LOGIQ E9. Two radiologists (both with 3 years' experience in CEUS) reviewed the dynamic video of each target lesion and selected the proper frame to draw the region of interest (ROI) including the tumor region (TR) and peritumoral region (PTR). The contour of each target lesion was manually drawn and the time–intensity curve (TIC) was automatically generated by the built-in software. Quantitative parameters generated from TIC included (1) time to peak (TtoPk), the time from zero intensity (right before the contrast arrives in the ROI) to

maximum intensity; (2) peak intensity* (PI*), showing the difference between the peak intensity (PI) and baseline intensity (BI); (3) grad, the gradient from arrival intensity to PI, reflecting the average perfusion velocity; (4) area under curve (AUC), the area under TIC with the arrival intensity as baseline. The TIC obtained from TR (TIC-TR) and PTR (TIC-PTR) respectively generated corresponding quantitative parameters for each patient. The final variables used for binary logistic regression analysis was obtained by calculating the ratio of the parameters generated by TIC-TR to those generated by TIC-PTR.

Development and internal validation of nomogram

Multivariable logistic regression was used to explore the relationship between variables and non-PD. Variables with p-value < 0.05 in univariate logistic regression were included in multivariable logistic regression. Redundant variable was excluded if collinearity existed. The variables with the variance inflation factors (VIFs) >5 indicated suspicious multicollinearities. Classification variables were set with a dummy variable. A nomogram model for predicting non-PD was developed using the independent risk factors identified by multivariable logistic regression analysis. The discriminatory ability of the model was evaluated using receiver operating characteristic (ROC) curve analysis. The predictive accuracy of the model was evaluated by a calibration curve. An internal bootstrap validation was performed using computer resampling for 500 repetitions of simple random sampling with replacement. Decision curve analysis (DCA) was performed to determine the clinical usefulness.

Statistical analysis

R software (ver.1.4.1717, R Development Core Team) and SPSS 22.0 software (IBM Corporation, NY, USA) were used for statistical analysis. The χ (2) test or Fisher's exact test were used for the comparison of classification variables, whereas the independent-sample t test was used for the comparison of continuous variables. A p-value < 0.05 was considered statistically significant. SPSS was used for binary logistic regression analysis and R software was used to develop the predictive model and test the diagnostic performance of the model with the corresponding package.

Results

Baseline characteristics of patients in the PD group and non-PD group

A total of 33 patients were enrolled in this study from November 2018 to October 2019. Each enrolled patient received at least one cycle of sintilimab plus IBI 305 treatment. According to tumor response evaluation, the enrolled patients were divided into a PD group and a non-PD (PR+CR+SD) group as illustrated in the *Clinical data and assessments of response to therapy*. The baseline characteristics summarized from clinical data, laboratory data, and imaging data of baseline abdominal CT/MR are listed in Table 1. BCLC staging, ECOG performance status, and Child–Pugh liver function scores were not assigned as variables in baseline characteristics since these clinical data were taken as inclusion criteria. In addition, considering the IBI305 was given at two different doses of 7.5 mg/kg or 15 mg/kg, the dose of IBI305 was also listed as a variable in Table 1. Except for the variable of embolus, there were no significant differences in baseline characteristics including IBI305 dose between the PD group and non-PD group, indicating a good consistency between two groups.

Quantitative parameters generated based on baseline CEUS

Based on the TR (tumor region) and PTR (peritumor region), corresponding TICs were generated by built-in software. The TIC of TR was defined as TIC-TR while that of PTR was defined as TIC-PTR. Corresponding quantitative parameters of TIC-TR and TIC-PR are listed in Table 2. These quantitative parameters included TtoPK, PI*, grad, and AUC. The ratios of quantitative parameters of TIC-TR to those of TIC-PTR were calculated and are listed in Table 2. The representative images of CEUS and corresponding TICs are presented in Figures 1, 2.

Target tumor response to treatment

The response to treatment of target tumor was evaluated by the follow-up CT/MR. The follow-up duration of every enrolled patient was ≥12 weeks after initial treatment. While no CR was observed in enrolled patients, 11 patients experienced PR, 11 patients experienced SD, and 11 patients experienced PD. A DCR of 66.67% was obtained in our study (Table 3).

Nomogram for predicting non-PD

Univariable and multivariable logistic regression analysis were performed to identify the independent variables related to non-PD (Tables 4, 5). Finally, embolus and grad ratio were considered to be significant variables related to non-PD. The absence of embolus in portal vein and the lower value of grad ratio were predictive factors for non-PD. With these two variables, a nomogram was established and the probability of non-PD can be estimated (Figure 3). The discriminative ability was evaluated by ROC curve analysis. The area under the ROC curve (AUC) (AUC, 0.909 [95% confidence interval (CI), 0.813–1]) of the nomogram was higher than that for applying embolus alone (AUC: 0.773 [95% CI, 0.612–0.934]) (Figure 4).

TABLE 1 Baseline characteristics of patients in the PD group and non-PD group.

Characteristic	PD group (n = 11)	Non-PD group (n = 22)	p-value
Age at diagnosis (years)	59.09 ± 11.03	55.86 ± 11.97	0.46
Gender			
Male	9 (81.8%)	18 (81.8%)	0.671
Female	2 (18.2%)	4 (18.2%)	
AFP (ng/ml)			
<20	1 (9.1%)	5 (22.7%)	0.409
20–400	5 (45.5%)	7 (31.8%)	
>400	5 (45.5%)	10 (45.5%)	
Alb (g/L)	41.23 ± 7.69	44.21 ± 4.09	0.153
PLT (10^9/L)	12.86 ± 0.98	12.30 ± 0.66	0.06
Tbil (μmol/L)	17.54 ± 9.79	13.94 ± 4.62	0.158
Tumor size (cm)	8.02 ± 5.86	8.40 ± 4.19	0.837
Tumor number			
<3	1 (9.1%)	8 (36.4%)	0.104
≥3	10 (90.9%)	14 (63.6%)	
Embolus			
Present	8 (72.7%)	4 (18.2%)	0.004
Absent	3 (27.3%)	18 (81.8%)	
Extra-hepatic metastasis			
Yes	10 (90.9%)	19 (86.4%)	0.593
No	1 (9.1%)	3 (13.6%)	
IBI305 dose			
7.5 mg/kg	7 (63.6%)	12 (54.5%)	0.453
15 mg/kg	4 (36.4%)	10 (45.5%)	

PD, progressive disease; IBI305, a bevacizumab biosimilar for anti-VEGF.

Model validation

The developed nomogram was validated with internal bootstrap validation. The ROC curve was evaluated by bootstrapping for 500 repetitions and the AUC of the bootstrap nomogram was 0.909 (95% CI, 0.793–0.979) (Figure 5). Also based on the internal bootstrap validation, the AUC of the ROC curve for applying the embolus status alone to predict the therapeutic efficiency was only 0.773 (95% CI, 0.612–0.934) (Figure 6). Based on internal bootstrap validation, the calibration curve of the nomogram showed a good fitting with the idea curve. When the probability was less than 0.5, the nomogram may slightly

TABLE 2 Quantitative parameters based on TR/PTR in the PD group and non-PD group.

Parameters	PD group (n = 11)			non-PD group (n = 22)		
	TIC-TR	TIC-PTR	Related ratios	TIC-TR	TIC-PTR	Related ratios
TtoPK (s)	14.18 ± 3.21	29.32 ± 8.09	0.51 ± 0.15	17.32 ± 6.93	32.417 ± 10.05	0.54 ± 0.15
PI* (dB)	26.84 ± 5.22	23.98 ± 4.91	1.13 ± 0.22	23.94 ± 5.60	25.05 ± 5.30	0.97 ± 0.18
Grad	1.99 ± 0.69	0.87 ± 0.24	2.3 ± 0.62	1.46 ± 0.41	0.81 ± 0.31	1.8 ± 0.42
AUC	3,234.36 ± 732.45	3,117.00 ± 876.33	1.11 ± 0.50	2,887.81 ± 880.25	3,255.74 ± 846.78	0.90 ± 0.22

TIC, time–intensity curve; TR, tumor region; PTR, peritumor region; TtoPK, time to peak; PI, peak intensity; BI, baseline intensity; PI*, the difference between PI and BI; AUC, area under the operating characteristic curve. TIC-TR represents the TIC generated from TR; TIC-PTR represents the TIC generated from PTR; ratio represents the ratio of quantitative parameters of TIC-TR to those of TIC-PTR.

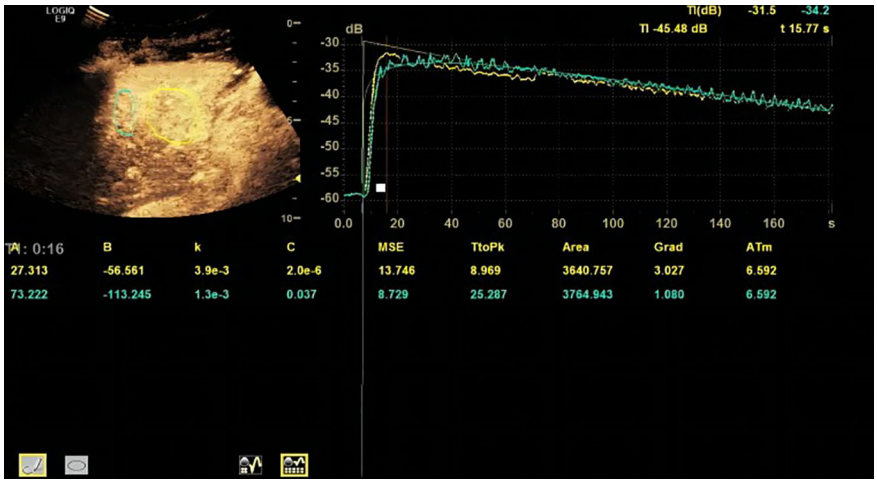

FIGURE 1
Representative image of contrast-enhanced ultrasound (CEUS) and time–intensity curve (TIC) of patients in the progressive disease (PD) group.

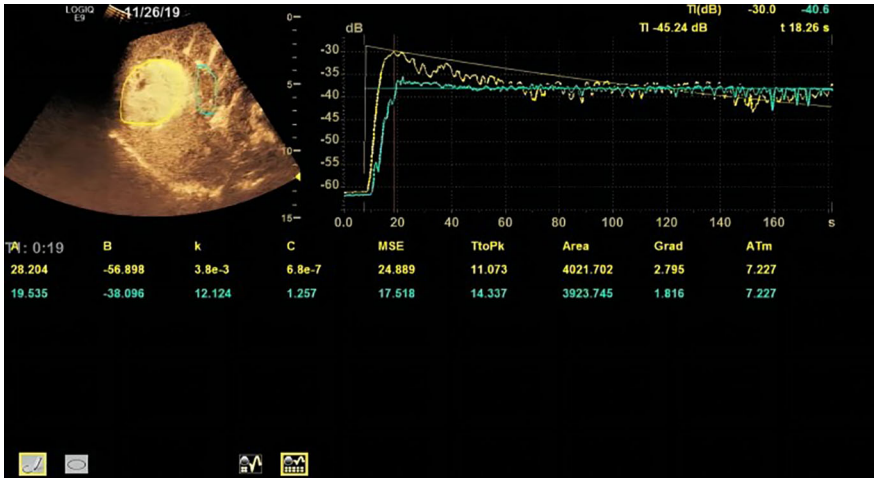

FIGURE 2
Representative images of CEUS and TIC of patients in the non-PD group.

underestimate the probability. When the probability was higher than 0.5, the nomogram may slightly overestimate the probability (Figure 7). The DCA showed a positive net benefit for the nomogram and embolus when a threshold probability was greater than 0.2. When compared with the net benefit achieved by applying embolus status alone to predict therapeutic efficiency, a better clinical utility was achieved after incorporating grad and embolus to establish the nomogram (Figure 8).

TABLE 3 Tumor response for enrolled patients after anti-PD-1 plus anti-VEGF treatment.

Tumor response	All patients (n = 33)
Complete response (CR)	0
Partial response (PR)	11 (33.33%)
Stable disease (SD)	11 (33.33%)
Progressive disease (PD)	11 (33.33%)
DCR (CR+PR+SD)	22 (66.67%)

Discussion

In this study, a CEUS quantitative parameter-based nomogram was developed and validated by bootstrap method to predict the anti-tumor efficacy in advanced HCC patients treated with sintilimab plus IBI305. By incorporating the variables of embolus and grad ratio, the nomogram achieved a good performance in predicting the probability of non-PD after anti-PD-1 plus anti-VEGF treatment.

Compared with anti-PD-1/PD-L1 monotherapy, the combined strategy of PD-1/PD-L1 inhibitors plus anti-VEGF agents achieved more clinical improvements for advanced HCC patients in ORR

TABLE 4 Univariable logistic regression analysis to identify risk factors for non-PD.

Variables	Odds ratio	95% confidence interval	*p*-value
Age	1.042	0.975–1.042	0.223
Gender (male)	1.00	0.153–6.531	1.00
Tumor size (cm)	1.227	0.995–1.513	0.055
Tumor number (≥3)	5.714	0.613–53.229	0.126
Embolus (present)	0.083	0.015–0.462	0.04
Extra-hepatic metastasis (yes)	0.708	0.145–17.218	0.708
IBI305 dose (15 mg/kg)	0.686	0.155–3.036	0.619
TtoPK ratio	5.431	0.03–978.72	0.523
PI* ratio	0.007	0.000–1.280	0.062
Grad ratio	0.136	0.023–0.789	0.026
AUC ratio	0.098	0.003–3.352	0.198

TtoPK ratio is defined as the ratio of the TtoPK obtained from TIC-PR to that obtained from TIC-PTR
PI* ratio is defined as the ratio of the PI*(PI-BI) obtained from TIC-PR to that obtained from TIC-PTR.
Grad ratio is defined as the ratio of the grad obtained from TIC-PR to that obtained from TIC-PTR.
AUC ratio is defined as the AUC obtained from TIC-PR to that obtained from TIC-PTR.

TABLE 5 Multivariate logistic regression analysis to identify risk factors for non-PD.

Variables	Odds ratio	95% confidence interval	*p*-value
Embolus (present)	0.015	0.001–0.338	0.008
Grad ratio	0.025	0.001–0.596	0.023

(0.26 vs. 0.21), DCR (0.75 vs. 0.59), and PFS (6.2 months vs. 4.19 months) according to the results of the meat analysis based on recent clinical trials (15). However, patients with unfavorable response to this combined strategy still existed. Studies focusing on exploring the biomarkers that aid in predicting the response to anti-PD-1 plus anti-VEGF agents are urgently needed. Generally, tumor neovascularization significantly differs from normal vasculature due to the presence of dilation, distortion, and

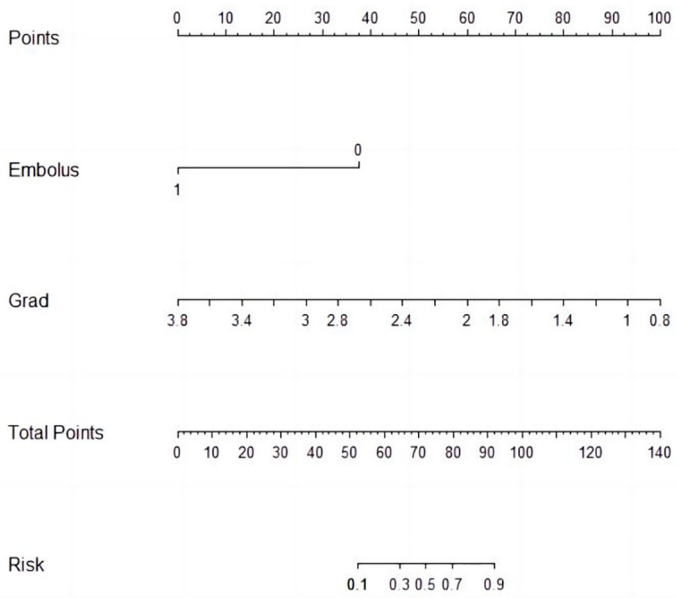

FIGURE 3
Nomogram prediction of non-PD.

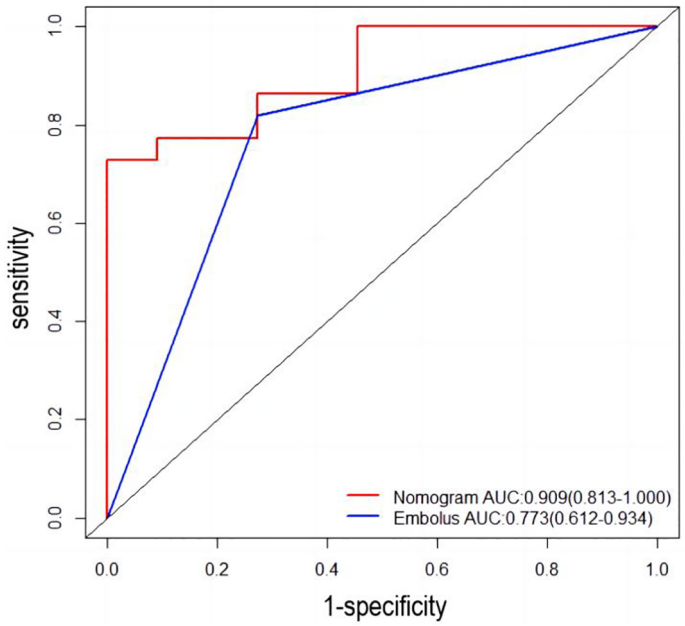

FIGURE 4
Receiver operating characteristic (ROC) curve. AUC: area under the receiver operating characteristic curve for the nomogram and for applying the embolus alone to predict non-PD.

formation of abnormal division branch, leading to corresponding blood perfusion patterns (27). The anti-VEGF agent can induce the normalization of tumor vascularization and thereby result in the changes of blood perfusion patterns (28, 29). Tumor-associated macrophages (TAMs) were considered to play an important role in immunotherapy resistance (30). As we know, TAMs can be divided into M1-like and M2-like subtypes. The high ratio of M1-like TAM to M2-like TAM can lead to a better long-term prognosis of cancer patients (31). The immune resistance can also be partially attributed to the predominant presence of M2-like TAM in the tumor environment (TME) (32). In patients with advanced HCC, high infiltration of M2 macrophage was considered to be associated with

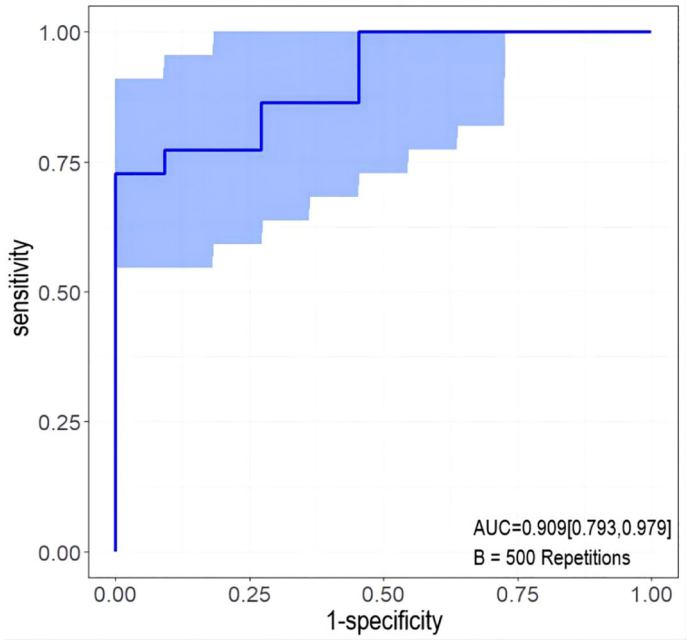

FIGURE 5
The ROC curve measured by bootstrapping for 500 repetitions and the AUC of the bootstrap stepwise nomogram. The snow blue area shows the 95% confidence interval of the ROC curve.

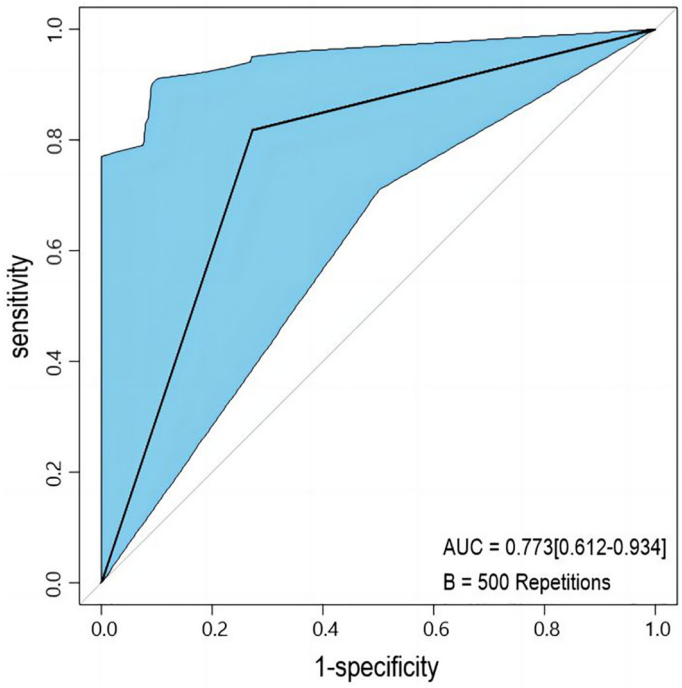

FIGURE 6
The ROC curve measured by bootstrapping for 500 repetitions and the AUC for applying embolus alone to predict non-PD. The lake blue area shows the 95% confidence interval of the ROC curve.

resistance to anti-PD-1 monotherapy (33). A research team from our institution recently reported that the tumor infiltration of M1 macrophages may serve as a potential predictive biomarker for anti-PD-1 plus anti-VEGF therapy in patients with advanced HCC (16). It is worth emphasizing that the M2-like TAMs is also associated with the microvessel density in tumor (31). This view was further supported by the finding that close association was observed between TAMs and tumor angiogenesis during cervical cancer

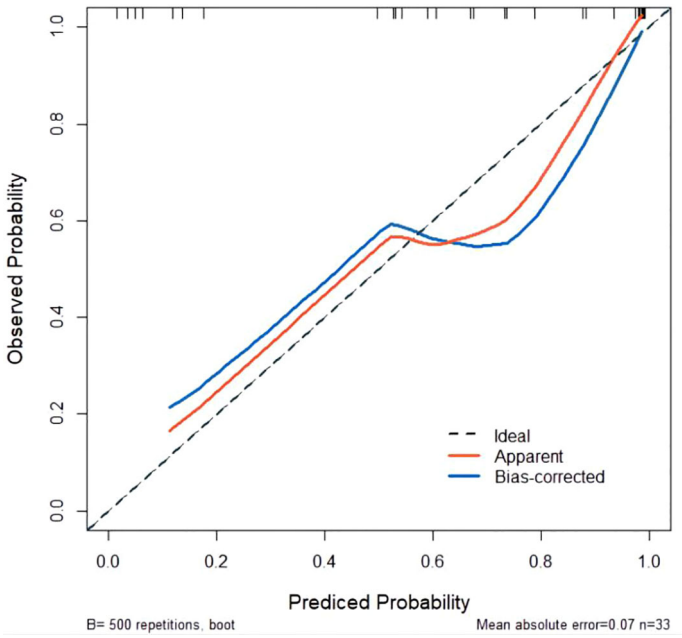

FIGURE 7
Calibration curve for predicted probability. The *X*-axis represents the probability of non-PD predicted by the nomogram. The *Y*-axis represents the actual probability of non-PD. The diagonal dashed line represents the ideal calibration line.

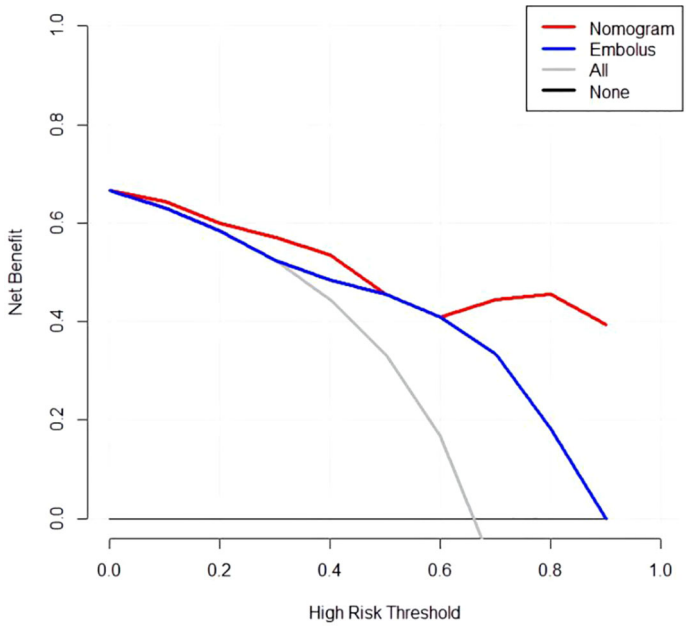

FIGURE 8
Decision curve analysis for the nomogram. Thin slash line: assume all patients are non-PD. Solid horizontal line: assume no patients are non-PD. The graph shows the expected net benefit per patient relative to the nomogram and embolus for the prediction of non-PD.

progression (34). In well-differentiated HCC, tumor vascularity was also proved to be correlated with M2-like TAM count (35). Thus, the microvessel intensity in tumor is potentially useful to predict the immune resistance in TME by indicating the proportion of M2 TAMs. For now, no non-invasive predictors were mentioned for predicting the efficacy of the treatment using ICIs plus anti-VEGF agents in advanced HCC patients.

CEUS is a non-invasive imaging modality using a contrast agent consisting of gas bubbles that are small enough to transverse through pulmonary vasculature and finally reach the target organ vasculature. Different from CT/MR contrast agents, the ultrasound contrast agent is a true intravascular contrast agent without deposition into the extravascular space and has the potential to reflect the vascular distribution and intensity without the concerns of ionizing radiation. Zheng reported that a good correlation (r = 0.624, $p < 0.001$) was obtained between the quantitative CEUS variable (maximum intensity, namely, PI) and the intratumoral microvessel density (MVD) estimated based on surgical tissue sections stained with CD34 (36). By revealing the changes of microvessel perfusion, quantitative CEUS had been widely used in the early evaluation or prediction for the treatment efficacy of anti-VEGF monotherapy (24, 37, 38). Several studies had emphasized that the anti-PD-1 treatment was also capable of promoting vascular normalization, indicating a potential application of CEUS in treatment evaluation among patients treated with anti-PD-1 monotherapy (22, 39). A series of quantitative parameters including TtoPK, PI, grad, and AUC can be acquired from TIC analysis based on CEUS imaging data. These parameters can comprehensively reflect the characteristics of microvessel by depicting the perfusion information and thereby indicate the infiltration status of M2-like macrophages in tumor.

In total, tumor embolus and grad ratio were included as variables in developing our nomogram model. Tumor embolus, presented as enhanced solid areas within the portal vein and its branches in the arterial phase of contrast-enhanced CT/MR images, is a widely used poor prognostic factor for HCC (40–42). In our model, the absence of portal vein embolus was an indicator for non-PD response, which is consistent with a previous study (17). Grad represents the gradient from arrival intensity to PI, reflecting the mean perfusion velocity in concerned regions. Grad depicts the blood flow per unit time and indirectly reflects the microvessel intensity of tumor. Considering that the value of quantitative parameters can be affected by the liver background or the image depth, we introduced the concept of ratio to provide more objective comparison among enrolled patients. The final variable for developing a nomogram was defined as the ratio of the grad derived from TR to that derived from PTR. There was a study addressing that the peritumoral hyper-enhanced ring on the Kupffer phase images obtained *via* Sonazoid-CEUS is a promising marker for predicting the response of anti-PD-1/PD-L1 monotherapy. However, the Sone Vue used in our study was capable of remaining inside the vasculature and avoiding the possibility of being taken by Kupffer cells. The parameters obtained from PTR merely represent the perfusion information of microvessels. According to the odds ratio calculated by logistic regression analysis, patients with lower grad ratios were more likely to benefit from the combined treatment. Considering the positive correlation between microvessel intensity and M2-like TAM infiltration, a lower grad ratio may indirectly reflect the low microvessel intensity in the tumor area, leading to a lower M2-like TAM infiltration and a better treatment efficacy. A nomogram is a practical tool to quantify variables and incorporate multiple variables to establish a prediction model. In our study, ROC curve analysis,

calibration curve analysis, and DCA were performed to evaluate the performance of the nomogram and achieved a satisfactory result.

Although a dose gradient of IBI305 (7.5 mg/kg vs. 15mg/kg) was present in our study, there is no significant difference in terms of the IBI305 dose between the PD group and the non-PD group in baseline analysis, excluding the possibility that the difference in IBI305 dose may affect the treatment efficacy. In addition, all enrolled patients received the same therapeutic combination of sintilimab and IBI305 in our study, ensuring the consistency of treatment strategy in each patient. According to RECIST, a patient may be misclassified as non-responder because the tumor size may remain unchanged or slightly increase due to hemorrhage, necrosis, or edema. In order to better evaluate the viable tumor portions, mRECIST was applied to evaluate the response on CT images.

There are several limitations to our study. First, the sample size was relatively small and the survival data like OS and PFS were not included in this study. Second, only internal validation was performed due to the restriction of sample size. Third, patient body habitus, bowel gas, and lesion size and location within the liver may limit imaging access and affect the target lesion selection in some patients. Fourth, operator dependence in the acquisition of sonographic images may limit the generalized application of this prediction model. Therefore, a quantitative CEUS-based prospective study with a larger sample size and detailed survival data was needed to screen the advanced HCC population who may benefit from a combined strategy.

Conclusions

This study has established and validated a nomogram by incorporating pretreatment CEUS quantitative parameters and baseline clinical characteristics to predict the anti-PD-1 plus anti-VEGF treatment efficacy in advanced HCC patients, which may help in clinical decision-making for patients with advanced HCC.

Data availability statement

The raw data supporting the conclusions of this article will be made available by the authors, without undue reservation.

Ethics statement

The studies involving human participants were reviewed and approved by Ethics committee of the cancer hospital of the Chinese Academy of Medical Sciences. The patients/participants provided their written informed consent to participate in this study.

Author contributions

LN, CS were responsible for the study design and instruction. CS was in charge of the data acquisition, data processing, statistical analysis and manuscript writing. QW was in charge of data preservation and data collection. LH was in charge of data processing and mapping. YC was in charge of paper polishing and revision. All authors contributed to the article and approved the submitted version.

Funding

This study was supported by the CAMS Initiative for Innovative Medicine (No. 2018-12M-3-001) and the National Natural Science Foundation of China (No. 82171965).

Conflict of interest

The authors declare that the research was conducted in the absence of any commercial or financial relationships that could be construed as a potential conflict of interest.

Publisher's note

All claims expressed in this article are solely those of the authors and do not necessarily represent those of their affiliated organizations, or those of the publisher, the editors and the reviewers. Any product that may be evaluated in this article, or claim that may be made by its manufacturer, is not guaranteed or endorsed by the publisher.

References

1. Cao W, Chen HD, Yu YW, Li N, Chen WQ. Changing profiles of cancer burden worldwide and in China: a secondary analysis of the global cancer statistics 2020. *Chin Med J (Engl)* (2021) 134(7):783–91. doi: 10.1097/CM9.0000000000001474

2. Allemani C, Matsuda T, Di Carlo V, Harewood R, Matz M, Niksic M, et al. Global surveillance of trends in cancer survival 2000–14 (CONCORD-3): analysis of individual records for 37 513 025 patients diagnosed with one of 18 cancers from 322 population-based registries in 71 countries. *Lancet* (2018) 391(10125):1023–75. doi: 10.1016/S0140-6736(17)33326-3

3. Liu W, Li X, Zheng W, Yao R, Zheng J. Preoperative evaluation of the degree of liver fbrosis based on matter-element analysis using serological indicators in patients with hepatocellular carcinoma. *Biosci Trends* (2019) 13(1):70–6. doi: 10.5582/bst.2018.01311

4. Vogel A, Cervantes A, Chau I, Daniele B, Llovet JM, Meyer T, et al. Hepatocellular carcinoma: ESMO Clinical Practice Guidelines for diagnosis, treatment and follow-up. *Ann Oncol* (2019) 30(5):871–3. doi: 10.1093/annonc/mdy308

5. Kudo M, Finn RS, Qin S, Han KH, Ikeda K, Piscaglia F, et al. Lenvatinib versus sorafenib in fifirst-line treatment of patients with unresectable hepatocellular carcinoma: a randomised phase 3 non-inferiority trial. *Lancet* (2018) 391 (10126):1163–73. doi: 10.1016/S0140-6736(18)30207-1

6. Llovet JM, Ricci S, Mazzaferro V, Hilgard P, Gane E, Blanc JF, et al. Sorafenib in advanced hepatocellular carcinoma. *N Engl J Med* (2008) 359(4):378–90. doi: 10.1056/NEJMoa0708857

7. Bruix J, Qin S, Merle P, Granito A, Huang YH, Bodoky G, et al. Regorafenib for patients with hepatocellular carcinoma who progressed on sorafenib treatment (RESORCE): a randomised, double-blind, placebo-controlled, phase 3 trial. *Lancet* (2017) 389(10064):56–66. doi: 10.1016/S0140-6736(16)32453-9

8. Abou-Alfa GK, Meyer T, Cheng AL, El-Khoueiry AB, Rimassa L, Ryoo BY, et al. Cabozantinib in patients with advanced and progressing hepatocellular carcinoma. *N Engl J Med* (2018) 379:54–63. doi: 10.1056/NEJMoa1717002

9. Zhu AX, Kang Y-K, Yen C-J, Finn RS, Galle PR, Llovet JM, et al. Ramucirumab after sorafenib in patients with advanced hepatocellular carcinoma and increased a-fetoprotein concentrations (REACH-2): a randomised, double-blind, placebo-controlled, phase 3 trial. *Lancet Oncol* (2019) 20(2):282–96. doi: 10.1016/S1470-2045(18)30937-9

10. Zhu AX, Finn RS, Edeline J, Cattan S, Ogasawara S, Palmer D, et al. Pembrolizumab in patients with advanced hepatocellular carcinoma previously treated with sorafenib (KEYNOTE-224): a non-randomised, open-label phase 2 trial. *Lancet Oncol* (2018) 19(7):940–52. doi: 10.1016/S1470-2045(18)30351-6

11. Yau T, Park JW, Finn RS, Cheng AL, Mathurin P, Edeline J, et al. Nivolumab versus sorafenib in advanced hepatocellular carcinoma (CheckMate 459): a randomised, multicentre, open-label, phase 3 trial. *Lancet Oncol* (2022) 23(1):77–90. doi: 10.1016/S1470-2045(21)00604-5

12. Lapeyre-Prost A, Terme M, Pernot S, Pointet AL, Voron T, Tartour E, et al. Immunomodulatory activity of VEGF in cancer. *Int Rev Cell Mol Biol* (2017) 330:295–342. doi: 10.1016/bs.ircmb.2016.09.007

13. Kudo M. A new era in systemic therapy for hepatocellular carcinoma: atezolizumab plus bevacizumab combination therapy. *Liver Cancer* (2020) 9(2):119–37. doi: 10.1159/000505189

14. Song Y, Fu Y, Xie Q, Zhu B, Wang J, Zhang B. Anti-angiogenic agents in combination with immune checkpoint inhibitors: a promising strategy for cancer treatment. *Front Immunol* (2020) 11:1956. doi: 10.3389/fimmu.2020.01956

15. Wen W, Zhang Y, Zhang H, Chen Y. Clinical outcomes of PD-1/PD-L1 inhibitors in patients with advanced hepatocellular carcinoma: a systematic review and meta-analysis. *J Cancer Res Clin Oncol* (2023) 149(3):969–78. doi: 10.1007/s00432-022-04057-3

16. Zhang W, Gong C, Peng X, Bi X, Sun Y, Zhou J, et al. Serum concentration of CD137 and tumor infiltration by M1 macrophages predict the response to sintilimab plus bevacizumab biosimilar in advanced hepatocellular carcinoma patients. *Clin Cancer Res* (2022) 28(16):3499–508. doi: 10.1158/1078-0432.CCR-21-3972

17. Yuan G, Song Y, Li Q, Hu X, Zang M, Dai W, et al. Development and validation of a contrast-enhanced CT-based radiomics nomogram for prediction of therapeutic efficacy of anti-PD-1 antibodies in advanced HCC patients. *Front Immunol* (2021) 11:613946. doi: 10.3389/fimmu.2020.613946

18. Huang Z, Zhu RH, Xin JY, Li KY. HCC treated with immune checkpoint inhibitors: a hyper-enhanced rim on Sonazoid-CEUS Kupffer phase images is a predictor of tumor response. *Eur Radiol* (2023) 33(6):4389–400. doi: 10.1007/s00330-022-09339-5

19. Jang HJ, Kim TK, Burns PN, Wilson SR. CEUS: An essential component in a multimodality approach to small nodules in patients at high-risk for hepatocellular carcinoma. *Eur J Radiol* (2015) 84(9):1623–35. doi: 10.1016/j.ejrad.2015.05.020

20. Terzi E, Iavarone M, Pompili M, Veronese L, Cabibbo G, Fraquelli M, et al. Contrast ultrasound LI-RADS LR-5 identifies hepatocellular carcinoma in cirrhosis in a multicenter restropective study of 1,006 nodules. *J Hepatol* (2018) 68(3):485–92. doi: 10.1016/j.jhep.2017.11.007

21. Lassau N, Coiffier B, Kind M, Vilgrain V, Lacroix J, Cuinet M, et al. Selection of an early biomarker for vascular normalization using dynamic contrast-enhanced ultrasonography to predict outcomes of metastatic patients treated with bevacizumab. *Ann Oncol* (2016) 27(10):1922–8. doi: 10.1093/annonc/mdw280

22. Lassau N, Bonastre J, Kind M, Vilgrain V, Lacroix J, Cuinet M, et al. Validation of dynamic contrast-enhanced ultrasound in predicting outcomes of antiangiogenic therapy for solid tumors: the French multicenter support for innovative and expensive techniques study. *Invest Radiol* (2014) 49(12):794–800. doi: 10.1097/RLI.0000000000000085

23. Sugimoto K, Moriyasu F, Saito K, Rognin N, Kamiyama N, Furuichi Y, et al. Hepatocellular carcinoma treated with sorafenib: early detection of treatment response and major adverse events by contrast-enhanced US. *Liver Int* (2013) 33(4):605–15. doi: 10.1111/liv.12098

24. Frampas E, Lassau N, Zappa M, Vullierme MP, Koscielny S, Vilgrain V. Advanced Hepatocellular Carcinoma: early evaluation of response to targeted therapy and prognostic value of Perfusion CT and Dynamic Contrast Enhanced-Ultrasound. *Preliminary results Eur J Radiol* (2013) 82(5):e205–11. doi: 10.1016/j.ejrad.2012.12.004

25. Harrell FEJr. *Regression modelling strategies with application to linear models, logistic regression, and survival analysis. 1ed*. New York: Springer-Verlag New York (2001). doi: 10.1007/978-1-4757-3462-1

26. Vincenzo P. *Color Atlas of Ultrasound Anatomy, 2nd edn*. Block B, editor . German Stuttgart: Georg Thieme Verlag. (2012). doi: 10.1007/s00259-012-2105-0.

27. Russo G, Mischi M, Scheepens W, de la Rosette JJ, Wijkstra H. Angiogenesis in prostate cancer: onset, progression and imaging. *BJU Int* (2012) 110(11 Pt C):E794–808. doi: 10.1111/j.1464-410X.2012.11444

28. Ferrara N, Kerbel RS. Angiogenesis as a therapeutic target. *Nature* (2005) 438 (7070):967–74. doi: 10.1038/nature04483

29. Kazerounian S, Lawler J. Integration of pro- and anti-angiogenic signals by endothelial cells. *J Cell Commun Signal* (2018) 12(1):171–9. doi: 10.1007/s12079-017-0433-3

30. Ding T, Xu J, Wang F, Shii M, Zhang Y, Li S-P, et al. High tumor-infiltrating macrophage density predicts poor prognosis in patients with primary hepatocellular carcinoma after resection. *Hum Pathol* (2009) 40(3):381–9. doi: 10.1016/j.humpath.2008.08.011

31. Herwig MC, Bergstrom C, Wells JR, Höller T, Grossniklaus HE. M2/M1 ratio of tumor associated macrophages and PPAR-gamma expression in uveal melanomas with class 1 and class 2 molecular profiles. *Exp Eye Res* (2013) 107:52–8. doi: 10.1016/j.exer.2012.11.012

32. Mills CD, Lenz LL, Harris RA. A breakthrough: macrophage-directed cancer immunotherapy. *Cancer Res* (2016) 76(3):513–6. doi: 10.1158/0008-5472.CAN-15-1737

33. Zhu Y, Yang J, Xu D, Gao XM, Zhang Z, Hsu JL, et al. Disruption of tumour-associated macrophage trafficking by the osteopontin-induced colony-stimulating factor-1 signalling sensitises hepatocellular carcinoma to anti-PD-L1 blockade. *Gut* (2019) 68(9):1653–66. doi: 10.1136/gutjnl-2019-318419

34. Jiang S, Yang Y, Fang M, Li X, Yuan X, Yuan J. Co-evolution of tumor-associated macrophages and tumor neo-vessels during cervical cancer invasion. *Oncol Lett* (2016) 12(4):2625–31. doi: 10.3892/ol.2016.5014

35. Fujita N, Nishie A, Aishima S, Kubo Y, Asayama Y, Ishigami K, et al. Role of tumor-associated macrophages in the angiogenesis of well-differentiated hepatocellular carcinoma: pathological-radiological correlation. *Oncol Rep* (2014) 31(6):2499–505. doi: 10.3892/or.2014.3138

36. Zheng W, Xiong YH, Han J, Guo ZX, Li YH, Li AH, et al. Contrast-enhanced ultrasonography of cervical carcinoma: perfusion pattern and relationship with tumour angiogenesis. *Br J Radiol* (2016) 89(1065):20150887. doi: 10.1259/bjr.20150887

37. Lassau N, Koscielny S, Chami L, Chebil M, Benatsou B, Roche A, et al. Advanced hepatocellular carcinoma: early evaluation of response to bevacizumab therapy at dynamic contrast-enhanced US with quantification–preliminary results. *Radiology* (2011) 258(1):291–300. doi: 10.1148/radiol.10091870

38. Lo GM, Al Zahrani H, Jang HJ, Menezes R, Hudson J, Burns P, et al. Detection of early tumor response to axitinib in advanced hepatocellular carcinoma by dynamic contrast enhanced ultrasound. *Ultrasound Med Biol* (2016) 42(6):1303–11. doi: 10.1016/j.ultrasmedbio.2016.01.025

39. Tian L, Goldstein A, Wang H, Ching Lo H, Sun Kim I, Welte T, et al. Mutual regulation of tumour vessel normalization and immunostimulatory reprogramming. *Nature* (2017) 544(7649):250–4. doi: 10.1038/nature21724

40. Zheng X, Fang Z, Liu X, Deng S, Zhou P, Wang X, et al. Increased vessel perfusion predicts the efficacy of immune checkpoint blockade. *J Clin Invest* (2018) 128 (5):2104–15. doi: 10.1172/JCI96582

41. Zhang XP, Gao YZ, Chen ZH, Chen MS, Li LQ, Wen TF, et al. An eastern hepatobiliary surgery hospital/portal vein tumor thrombus scoring system as an aid to decision making on hepatectomy for hepatocellular carcinoma patients with portal vein tumor thrombus: A multicenter study. *Hepatology* (2019) 69(5):2076–90. doi: 10.1002/hep.30490

42. Zhang XP, Chen ZH, Zhou TF, Li LQ, Chen MS, Wen TF, et al. A nomogram to predict early postoperative recurrence of hepatocellular carcinoma with portal vein tumour thrombus after R0 liver resection: A large-scale, multicenter study. *Eur J Surg Oncol* (2019) 45(9):1644–51. doi: 10.1016/j.ejso.2019.03.043

frontiers | Frontiers in Immunology

TYPE Original Research
PUBLISHED 24 August 2023
DOI 10.3389/fimmu.2023.1187286

OPEN ACCESS

EDITED BY
Vera Rebmann,
University of Duisburg-Essen, Germany

REVIEWED BY
Eswar Shankar,
The Ohio State University, United States
Hana Rohn,
University of Duisburg-Essen, Germany

*CORRESPONDENCE
Ke Zhang
weizhuo9527@foxmail.com

†These authors have contributed equally to this work

RECEIVED 15 March 2023
ACCEPTED 26 July 2023
PUBLISHED 24 August 2023

CITATION
Wang W, Zhang X, Jiang S, Xu P, Chen K, Li K, Wang F, Le X and Zhang K (2023) A novel signature constructed by differential genes of muscle-invasive and non-muscle-invasive bladder cancer for the prediction of prognosis in bladder cancer.
Front. Immunol. 14:1187286.
doi: 10.3389/fimmu.2023.1187286

A novel signature constructed by differential genes of muscle-invasive and non-muscle-invasive bladder cancer for the prediction of prognosis in bladder cancer

Weizhuo Wang[1†], Xi Zhang[2†], Silin Jiang[3†], Peng Xu[2†], Kang Chen[4], Kai Li[1], Fei Wang[1], Xiang Le[1] and Ke Zhang[1*]

[1]Department of Urology, The Affiliated Suzhou Hospital of Nanjing Medical University, Suzhou Municipal Hospital, Gusu School, Nanjing Medical University, Suzhou, China, [2]Department of Urology, Department of Urology, The First Affiliated Hospital of Nanjing Medical University, Nanjing, China, [3]Department of Urology, Department of Urology, The Second Affiliated Hospital of Nanjing Medical University, Nanjing, China, [4]Department of Urology, North China University of Science and Technology, Tangshan, China

Background: Bladder cancer (BCa) is a malignant tumor that usually forms cancer cells in the inner lining of the bladder. Hundreds of thousands of people worldwide have BCa diagnosed each year. The purpose of this study was to construct a prognostic model by differential expression of genes between muscular and non-muscular invasive BCa, and to investigate the prognosis of BCa patients.

Methods: The data of BCa patients was sourced from the GEO and TCGA database. Single-cell sequencing data was obtained from three patients in the GSE135337 database, and microarray data for verification was obtained from GSE32894. Univariate, Lasso and multivariate cox regression analyses were performed to construct the prognostic model. The prognostic features, immune features and drug sensitivity of the model were further evaluated. Single-cell data and microarray data were used to validate the differential expression of model genes between muscle-invasive and non-muscle-invasive BCa. The invasion and migration of BCa cells were evaluated using the transwell assay and wound-healing assay. The cell proliferation capacity was simultaneously evaluated using Colony formation experiments. The protein expression of the specific gene was detected by western blot analysis.

Results: We identified 183 differentially expressed muscle-invasive-related differential genes (MIRDGs), among which four were selected to establish a prognostic model. Based on our signature, patients in different groups displayed varying levels of immune infiltration and immunotherapy profiles. Single-cell sequencing data and microarray data confirmed that four invasion-related genes were expressed at higher levels in muscle-invasive BCa. Given the critical role of S100A9 in the progression of BCa, we performed further analysis. The results

showed that protein expression of S100A9 was high in muscle-invasive BCa, and S100A9 knockdown could inhibit the proliferation, migration and invasion of BCa.

Conclusion: These findings demonstrated that the prognostic model for BCa patients was reasonably accurate and valid, and it may prove to be of considerable value for the treatment and prognosis of BCa patients in the future. S100A9 may become a better prognostic marker and potential therapeutic target to further guide clinical treatment decisions.

KEYWORDS

bladder cancer, muscle-invasive, prognostic signature, immune microenvironment, biomarker

1 Introduction

Bladder cancer (BCa) is a type of malignant tumor that typically forms cancer cells in the inner layer of the bladder. Hundreds of thousands of people are diagnosed with BCa worldwide every year, and its incidence is increasing year by year (1). BCa is common in older people, while in developing countries, it is often related to work environments and environmental pollution. According to statistics, men are more likely than women to develop cancer, and factors such as smoking, long-term exposure to chemicals, and chronic cystitis are also related to cancer (2).

Regarding the treatment of BCa, existing researches show that whether infiltration of the muscle layer is present is a key factor in determining a patient's treatment plan. Based on this, BCa patients can be divided into non-muscle-invasive and muscle-invasive types. Among them, 60%-70% of non-muscle-invasive types are confined to the bladder mucosa (Ta stage), 20%-30% show subepithelial connective tissue infiltration (T1 stage), and about 10% show *in situ* carcinoma. The main treatment for non-muscle-invasive BCa is transurethral resection of bladder tumor (TURBT), followed by immediate injection of bacillus Calmette-Guerin (BCG) vaccine or intravesical chemotherapy. The decision to administer BCG and/or chemotherapy is based on the risk of cancer progression or recurrence. Muscle-invasive BCa invades the muscle layer, including invasion of the muscle layer (T2 stage), invasion of surrounding tissue (T3 stage), and invasion of any surrounding organ such as the prostate, seminal vesicles, uterus, vagina, pelvic wall, abdominal wall (T4 stage), etc. Given the invasiveness of muscle-invasive BCa, timely diagnosis and treatment are crucial (3). Existing treatments strongly recommend radical cystectomy with bilateral pelvic lymph node dissection and platinum-based neoadjuvant chemotherapy for all resectable non-metastatic muscle-invasive BCa patients (4).

The prognosis and treatment of muscle-invasive and non-muscle-invasive BCa are significantly different, and the likelihood of recurrence and poor prognosis is higher in muscle-invasive BCa (5). Most non-invasive BCa only require bladder resection and instillation therapy, while muscle-invasive BCa requires bladder removal and surrounding cleaning, and even bladder reconstruction, but this method has no evidence of improving long-term outcomes and has a significant impact on the patient's life (6). Non-muscle-invasive progresses to muscle-invasive BCa in approximately 10% to 20% of cases, requiring continuous follow-up and subsequent treatment (7).Additionally, the treatment of BCa often involves a significant amount of follow-up and subsequent treatment, which can place a heavy financial burden on patients (8). For example, the recommended Bacillus Calmette-Guérin (BCG) attention treatment for non-invasive BCa patients in current guidelines costs approximately $100,000 in the first year alone (9). For non-invasive BCa patients, an effective target that can identify their prognosis is needed to roughly determine their possible progression and adjust the treatment plan accordingly. In clinical practice, sometimes patients experience repeated recurrence despite transurethral resection and BCG treatment (10). In such cases, more aggressive treatment methods, such as partial bladder resection or bladder removal surgery, should be considered to prevent disease progression. Pathological grading, recurrence frequency, and growth range of the tumor are used as means of judging the situation. With the rapid development of genomic technologies, the cost of sequencing is also decreasing. The cost of single-sample sequencing is now under $100,especially for clinical exome sequencing (CES), and if a unified platform is used for sequencing, the cost is likely to decrease further (11). This is a small fraction of the long-term follow-up and treatment costs for BCa patients. In addition, standardized sequencing at scale will standardize the various gene expression values that affect patient prognosis.

In the process of BCa, various genes such as TFPI-2 and GATA3 have been revealed to cause a change in the invasive ability of BCa (12, 13). For the specific staging diagnosis of BCa, clinical identification often relies on samples obtained through transurethral resection of bladder tumor (TURBT) (3).Convenient sample acquisition provides good convenience for gene sequencing that can be performed. Although recent studies have shown that detecting urinary methylation levels contributes to the diagnosis and prognostic prediction of BCa, the current gold standard diagnostic method remains TURBT. In existing research, certain biomarkers have been identified for their value in the progression

and prognosis of BCa. For example, BUB1 has been found to predict the prognosis of non-muscle-invasive BCa (14), while STAG2 has demonstrated independent prognostic value in low-grade non-muscle-invasive BCa (15). Regarding the prediction of BCa recurrence, BCL-2 Family, p63 have been considered to have some clinical value (16). In existing research, several genes have been identified to have an impact on the prognosis of bladder cancer, such as SERPINE2, SNCAIP, S100A9, and others (17–19). Particularly, S100A9 has been shown to be highly expressed in bladder cancer tissues in large-scale clinical studies (20), and its expression levels are also elevated in the urine of patients (21). However, there is limited research on its role in muscle-invasive and non-muscle-invasive bladder cancer. Existing studies often rely on databases, and there is a lack of comparative analysis regarding its influence on bladder cancer recurrence and progression. Therefore, further exploration and standardized guidelines are still needed before these genes can be clinically applied.

2 Method

2.1 Data source

The consolidated transcriptome expression matrix and clinical data of BCa were obtained from the Cancer Genome Atlas (TCGA) and Gene Expression Omnibus (GEO) databases. GSE13507 dataset was used as the training cohort for building the model, while the TCGA-BLCA dataset was used as the testing cohort. The single-cell sequencing data used to validate the differential gene expression of the model came from the GSM4006647, GSM400644, and GSM4006645 in the GSE135337 dataset. The microarray data used to validate the differential gene expression came from the GSE32894 dataset.

2.2 Differential genes in the muscle-invasive and non-muscle-invasive bladder cancer

After downloading the gene expression data from GSE13507, the data was organized and analyzed for differential expression using the limma package in R language (22). MIRDGs were selected based on criteria such as |Log2FC|>1 and adj.P.Val <0.05, and visualized in a volcano plot using the ggplot2 package. Enrichment analysis was performed on the resulting MIRDGs (23), and a heatmap was generated to display the results. Additionally, a protein-protein interaction network was constructed for the MIRDGs (24).

2.3 Construction of bladder cancer related prognostic model

We employed statistical analyses to investigate the impact of genes on patient prognosis. Specifically, we first used univariate cox regression analysis on training cohort GSE13507 to identify prognostic genes, and presented the results using a heatmap. Subsequently, we employed the least absolute shrinkage and selection operator (LASSO) Cox regression and multivariate Cox regression analysis to construct the bladder cancer related prognostic model. The patients were then divided into either the low risk group or the high risk group based on the median riskscore. TCGA-BLCA was used as the testing cohort to verify the accuracy of the prognostic model. The prognostic accuracy of the riskscore was evaluated using kaplan-meier (KM) analysis, the area under the curve (AUC) of the receiver operating characteristic (ROC) curve, as well as univariate and multivariate independent prognostic analysis.Then we construct a nomogram based on the training cohort (GSE13507).

2.4 Single-cell data and microarray data validation data exist for differential expression of the genes identified by the model

We integrated the pTa (GSM4006644), pT2 (GSM4006647), and pT1 (GSM4006645) samples in order to compare the expression patterns of model genes in the single-cell data. Microarray data from the GSE32894 dataset were further used to validate the expression differences.

2.5 Immune infiltration and immunotherapy analysis

Single-sample gene set enrichment analysis (ssGSEA) was performed using the "GSVA" package to calculate enrichment scores for different immune cell types and immunologic functions using immune-related gene sets (25). The immunosuppressive checkpoints were sourced from relevant literature and the website (https://www.immport.org/home, Supplementary Table 9) (26). Tumor microenvironment (TME) may affect the occurrence and development of cancer, so we employed the ESTIMATE algorithm to evaluate the TME score (ImmuneSocre, StromalScore, and tumor purity) of BCa samples. The Gene expression profiling data and clinical results of 348 BCa immunotherapy patients were obtained from in IMvigor210 cohort. The results of anti PD-L1 immunotherapy responses were divided into complete response (CR), partial response (PR), stable disease (SD), and disease progression (PD).

2.6 Western blot assay

The tested proteins are derived from 12 postoperative pathological tissue samples obtained from 8 patients. Among these samples, there are four from patients with muscle-invasive BCa and four from patients with non-muscle-invasive BCa. Additionally, four samples of normal tissue were obtained from adjacent tissue to the cancerous area. WB assay was performed after the detection of protein concentration. 20 μg of samples were separated on a 10% SDS-PAGE gel, then transferred to a PVDF membrane and blocked for 1 hour at room temperature. The

membranes were incubated with primary antibodies (S100A9 concentration, 0.5 μg/mL; β-actin dilution rate, 1:500; Abmart) at 4° C overnight. The next day, the membranes were incubated with the secondary antibody (Abmart; dilution rate, 1:2000) at 24°C for 1 h. Signals of targeted proteins were detected using an enhanced chemiluminescence detection system.

2.7 Wound-healing assay

Cell migration was assessed by performing a wound healing assay. Briefly, T24 and UMUC3 cells were transfected with S100A9. Approximately 2x10^6 cells were seeded into 6-well plates and cultured for 24 h. Then, a yellow plastic pipette tip was used to create a wound by scraping the cells. Cell migration was monitored under a Nicon Eclipse microscope and photographed at 100×.

2.8 Cell proliferation assay and transwell assay

Following the standard procedure, the proliferation ability of the cells was assessed with colony formation assays. T24 and UMUC3 cells (with an incubation density of 2x10^5) were incubated in the upper chambers (Labselect). For the invasion assay, the upper chambers were pre-coated with Matrigel (BD Biosciences). Culture medium without and with 10% FBS was added into the upper and lower chambers, respectively. After 12h, non-migrated cells were wiped out while migrated or invaded CRC cells were fixed, stained and counted using an inverted microscope.

3 Results

3.1 Identification of the differentially expressed genes

First, we downloaded the expression matrix and clinical data (Supplementary Tables 1, 2) files of GSE13507 from GEO, including 103 samples of primary non-muscle-invasive BCa and 61 samples of primary muscle-invasive cancer. We then performed differential analysis using the limma package in R language, setting the differential value as |logFC|> 1 and adj.P.Val.< 0.05. A total of 183 DEGs were selected (Supplementary Table 3) and we presented them using the volcano plot and heatmap (Figures 1A, C).

3.2 Enrichment analysis of differentially expressed genes and construction of protein interaction networks

After identifying the DEGs, we performed enrichment analysis on these genes using the org.Hs.eg.db package in R. Our analysis criteria were set at adj.P.Val < 0.1 and q.value < 0.2 (Supplementary Table 4). Enrichment analysis of the gene ontology biological process (GO : BP) showed significant enrichment in extracellular matrix organization,

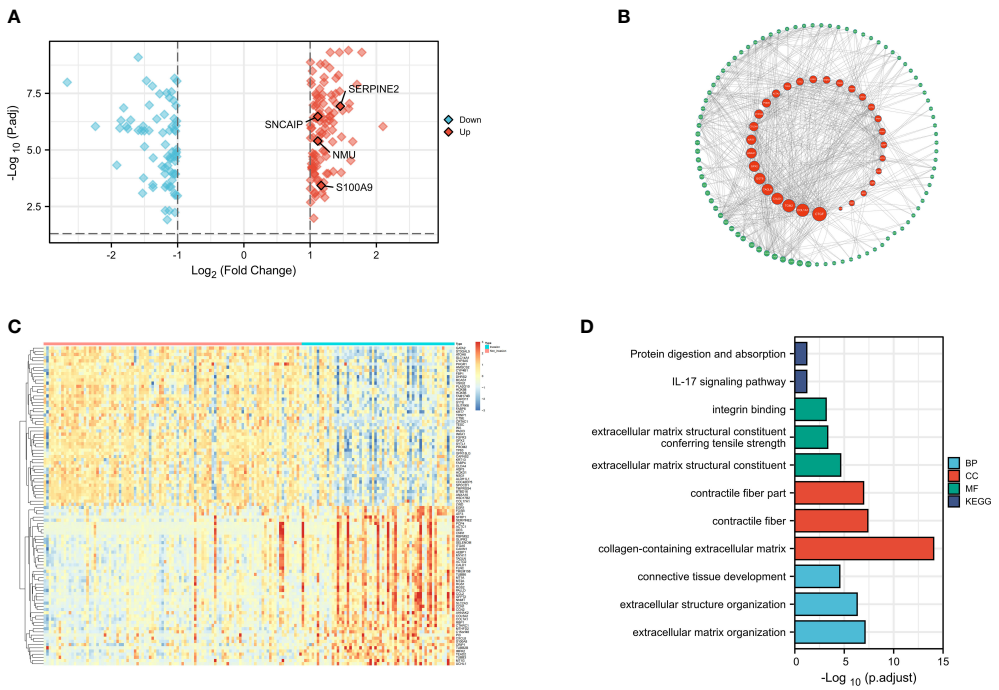

FIGURE 1
Differential Analysis, Protein Network Construction, GO Analysis, and KEGG Analysis(revised). **(A)** Volcano plot of differential gene muscle-invasive and non-muscle-invasive bladder cancer; **(B)** PPI protein network; **(C)** Heatmap of differential gene muscle-invasive and non-muscle-invasive bladder cancer; **(D)** GO analysis and KEGG analysis.

extracellular structure organization, connective tissue development, while the cellular component (GO : CC) analysis showed significant enrichment in collagen-containing extracellular matrix, contractile fiber, contractile fiber part. Molecular function (GO : MF) analysis revealed significant enrichment in extracellular matrix structural constituent, extracellular matrix structural constituent conferring tensile strength, integrin binding. Furthermore, KEGG analysis revealed that these DEGs were mainly involved in IL-17 signaling pathway, protein digestion and absorption (Figure 1B). These results were consistent with previous studies and suggested that changes in cell adhesion and interaction in the tumor tissue may lead to the invasive changes observed in the tumor as a whole. In addition, a protein-protein interaction (PPI) network analysis was performed using the STRING database (Supplementary Table 5), and the PPI network diagram showed that FABP6, ACTC1, and S100A9 had the strongest interactions with other MIRDGs (Figure 1D).

3.3 Identification of the prognostic features of bladder cancer related prognostic model

To construct BCa related prognostic model, the univariate cox regression analysis was adopted to screen out prognostic genes. According to the P-value <= 0.01 standard, twenty-one prognostic related genes were screened (Figure 2A). Eight prognostic genes were further analyzed using Lasso regression (Figures 2B, D). Because Lasso regression only helped us compress the variables to 8 genes, but in the end, we used multivariate Cox regression to build a prognostic model that includes 4 genes: SERPINE2, SNCAIP, NMU, and S100A9. (Supplementary Table 6) (Figure 2C). Then we evaluated whether our model was an independent factor affecting patient prognosis. Because whether there was muscular infiltration was based on TNM staging, we did not include TNM staging in the evaluation, and since the model was based on whether there was muscular invasion, we compared whether there was muscular invasion and model genes to observe whether they were independent prognostic factors. Therefore, we performed univariate and multivariate independent prognostic analyses on age, sex, pathological grade, and whether there was muscular invasion, and finally found that our model was an independent factor affecting patient prognosis (P<0.01) (Figures 2E, F). Then, the risk score was calculated by formula (Specific values were included in Supplementary Table 2). The distribution of risk score, survival status, gene expression and the KM survival curve in the training set (Figures 3A-D) and testing set (Figures 3E-H) demonstrated a positive association between risk score and mortality. In addition, the AUC of the ROC curve was 0.842 in training cohort (GSE13507) (Figure 4A). Compared with other factors, the AUC of the model was the highest, indicating that our model had the best predictive ability for patient survival. The ROC curves for riskscore at 1, 2, and 3 years in the training dataset were 0.842, 0.758, and 0.744, respectively (Figure 4B). TCGA-BLCA dataset was adopted as an external validation dataset to validate the accuracy of model (Supplementary Table 7). We found that the diagnostic ability of the model was significantly higher than that of other factors (Figure 4C). The AUC of the 1, 2, and 3-year OS of riskscore in the TCGA-BLCA dataset was 0.753, 0.747, and 0.723, respectively (Figure 4D). At the same time, multiple-index ROC analysis showed that age, sex, tumor grade, whether there was muscular infiltration, and risk score may all have an impact on patient prognosis, so we also constructed a nomogram based on age, sex, whether there was muscular invasion, tumor pathology grade, and risk score to predict the patient's 1-year, 3-year, and 5-year survival rates (Figure 4E).

3.4 Single-cell sequencing data and microarray data validate the differential gene expression of the model

To validate the expression of genes in our model in muscle-invasive and non-muscle-invasive bladder cancer, we utilized single-cell sequencing data. Firstly, we downloaded the expression matrix of the single-cell data, including pTa (GSM4006644), pT2 (GSM4006647), and pT1 (GSM4006645), where pT1 and pTa represent non-muscle-invasive BCa, and pT2 represents muscle-invasive BCa. Subsequently, we performed data analysis using the Seurat package in R programming language. We defined the number of highly variable genes as 3000. Finally, we conducted visualization-based dimensionality reduction using the obtained highly variable genes and principal components (PCs). For this purpose, we employed the UMAP method as our dimensionality reduction technique (Figure 5A). We integrated the data using the FindIntegrationAnchors function and identified two cell types: epithelial cells and monocytes. Since BCa primarily originates from epithelial cells, we extracted the epithelial cells separately and displayed their distribution in each BCa type (Figure 5B). We examined the expression of model-associated genes in pTa, pT2, and pT1 to investigate the expression differences of model genes between muscle-invasive and non-muscle-invasive BCa. We observed significant expression differences in S100A9, with higher levels observed in patients with muscle-invasive BCa (Figures 5C, E). However, due to the limited sequencing depth in the single-cell data, the detection rates of SERPINE2, SNCAIP, and NMU were relatively low (Figure 5D). As the expression data for non-muscle-invasive BCa in TCGA was limited, we further validated our results using a microarray dataset (GSE32894, Supplementary Table 8). First, we downloaded the gene expression matrix and grouped patients based on T-stage (Supplementary Table 4). The data had already been log2-transformed and standardized, resulting in gene expression values with negative values. By extracting and comparing the expression of model-related genes, we found significant differences in gene expression between muscle-invasive and non-muscle-invasive BCa patients in the model (Figure 5F). Moreover, the expression of model genes was significantly higher in patients with muscle-invasive BCa, consistent with our previous differential analysis and single-cell sequencing analysis. In the model, the risk coefficients of the relevant genes were all positive, consistent with the increased expression trend

10.3389/fimmu.2023.1187286

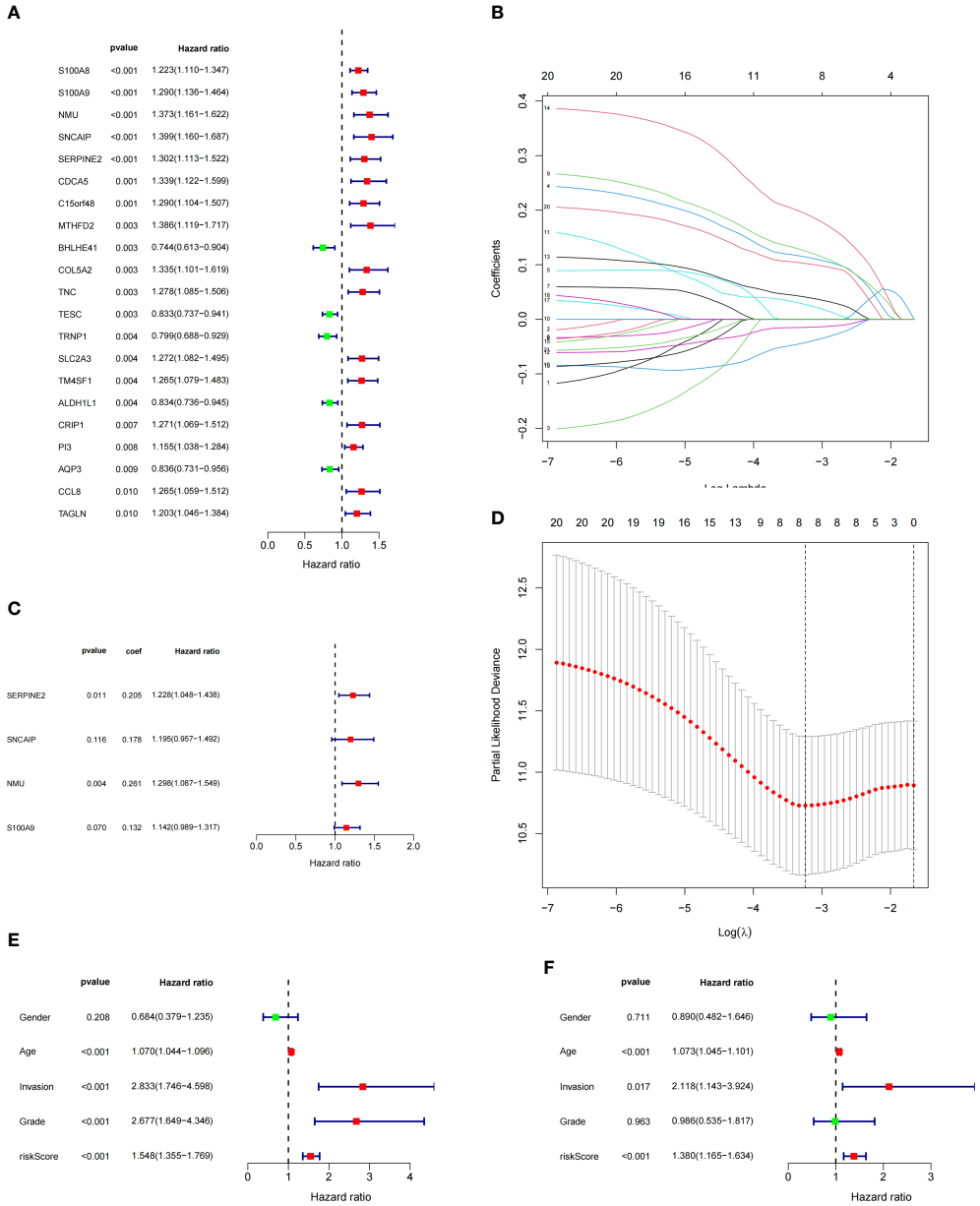

FIGURE 2
Model Construction and Independent Evaluation(revised). **(A)** Genes identified by univariate cox regression, **(B, D)** lasso regression, **(C)** Model genes identified by multivariate cox regression, **(E)** Univariate independent prognosis analysis, **(F)** Multivariate independent prognosis analysis.

of model genes in muscle-invasive BCa in the validation dataset. These findings indicate the reliability of our model construction. Combined with previous clinical data analysis, we have reason to believe that the identified model genes play an important role in predicting the risk of muscle invasion and prognosis in BCa patients.

3.5 Identification of immunoinfiltration features of the prognostic model

As BCa is known to be an immunoresponsive tumor with high heterogeneity and metastatic potential, we further investigated the prognostic model of the immune microenvironment characteristics. The heatmap showed the distribution of the TME scores and immune cells between high and low risk groups (Figure 6A). The association between the immune infiltration cells and riskscore was illustrated in Figure 6B, revealing a strong relationship between riskscore and immune cells. Furthermore, the expression levels of immunosuppressive cells, including Myeloid-derived suppressor cells (MDSCs), Regulatory T cells, and macrophages, were found to be significantly higher in the high risk group (Figure 6C). Moreover, the scores of immune-related molecules such as Checkpoint, CCR, and Inflammation-promoting molecules were significantly elevated in the high risk group compared to the low risk group (Figure 6D). Additionally, we analyzed the potential relationship between riskscore and tumor microenvironment

10.3389/fimmu.2023.1187286

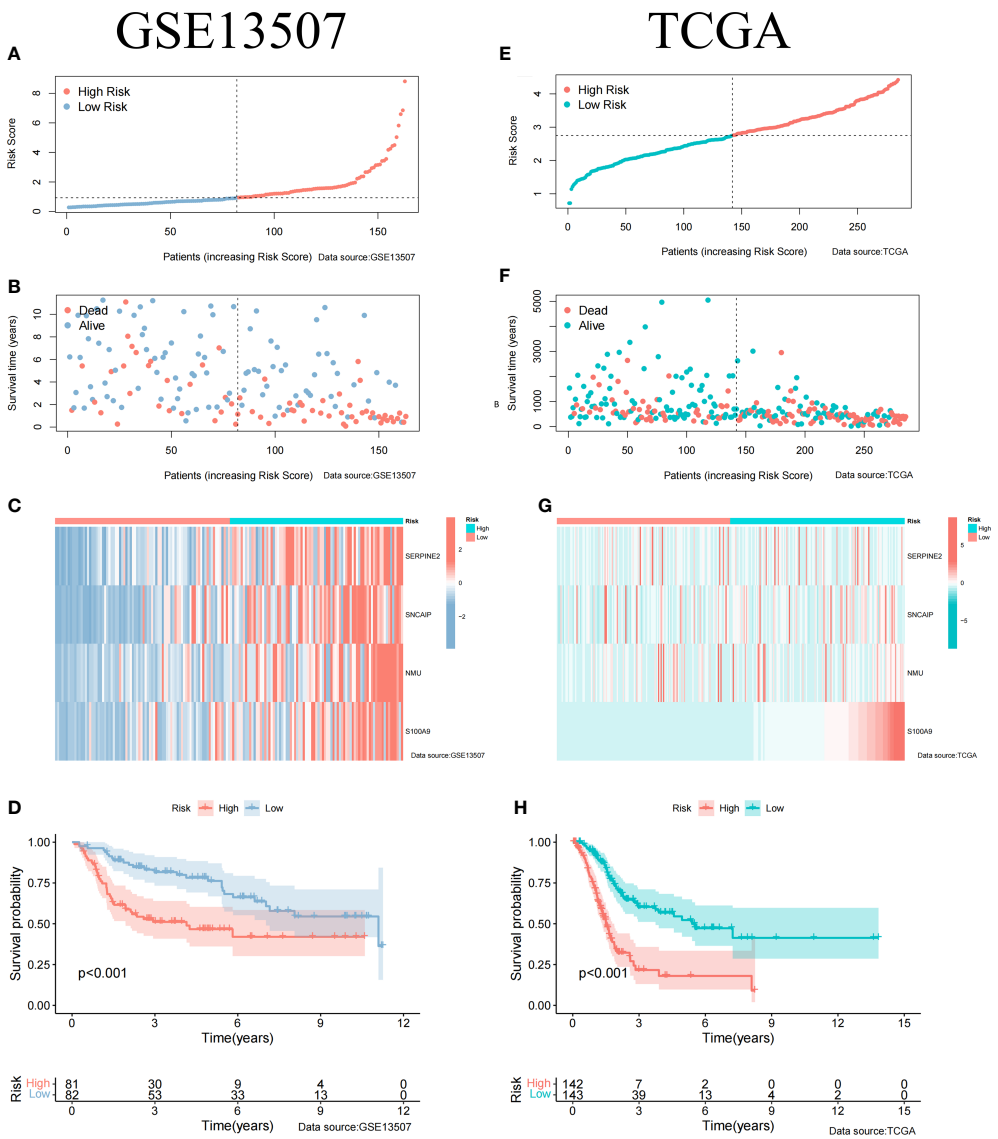

FIGURE 3
Clinical Relevance of the Model in GSE13507 and TCGA cohort. **(A)** Riskscore information for patients in GSE13507. **(B)** Survival status of patients in GSE13507 with increasing riskscore. **(C)** Gene expression profile of patients in GSE13507 model with increasing riskscore. **(D)** Survival curves of high and low risk groups in GSE13507 patients. **(E)** Riskscore information for patients in TCGA. **(F)** Survival status of patients in TCGA with increasing riskscore. **(G)** Gene expression profile of patients in TCGA model with increasing riskscore. **(H)** Survival curves of high and low risk groups in TCGA patients.

scores. The ESTIMATE Score, Stromal Score, and Immune Score were significantly higher in the high risk group (Figure 6E). We used the reshape2 package in R to analyze and compare the immunosuppressive checkpoints of high- and low-risk groups. Most of the differentially expressed immunosuppressive checkpoints have higher expression levels in the high-risk group than in the low-risk group (Figure 6F).

3.6 Immunotherapy and drug sensitivity analysis of the prognostic model

In order to evaluate the model's response to immunotherapy, we validated the association of risk scores with immunotherapy in the BCa immunotherapy dataset (IMvigor210 cohort). As a result, we found poor prognosis in the high-risk group in the immunotherapy dataset (IMvigor 210) (Figure 6G). The AUC of the 1, 2, and 3-year OS of riskscore in the IMvigor 210 dataset was 0.625, 0.604, and 0.57, respectively (Figure 6H). Figure 6I indicated that the proportion of SD and PD in the high risk group was higher. Meanwhile, riskscore was significantly over-expressed in the SD/PD group (Figure 6J). To further guide the development of clinical treatment strategies, we screened 9 major chemotherapeutic agents from the pRRophetic package to determine whether riskscore was associated with BCa resistance. The IC50 of Gefitinib, Bosutinib, Axitinib and Nilotinib was higher in high risk group, suggesting that these 4 drugs may be more suitable for patients with lower riskscore (Figures 7A-D). The IC50 of Sunitinib, Paclitaxel, Docetaxel, Bortezomib and Cisplatin

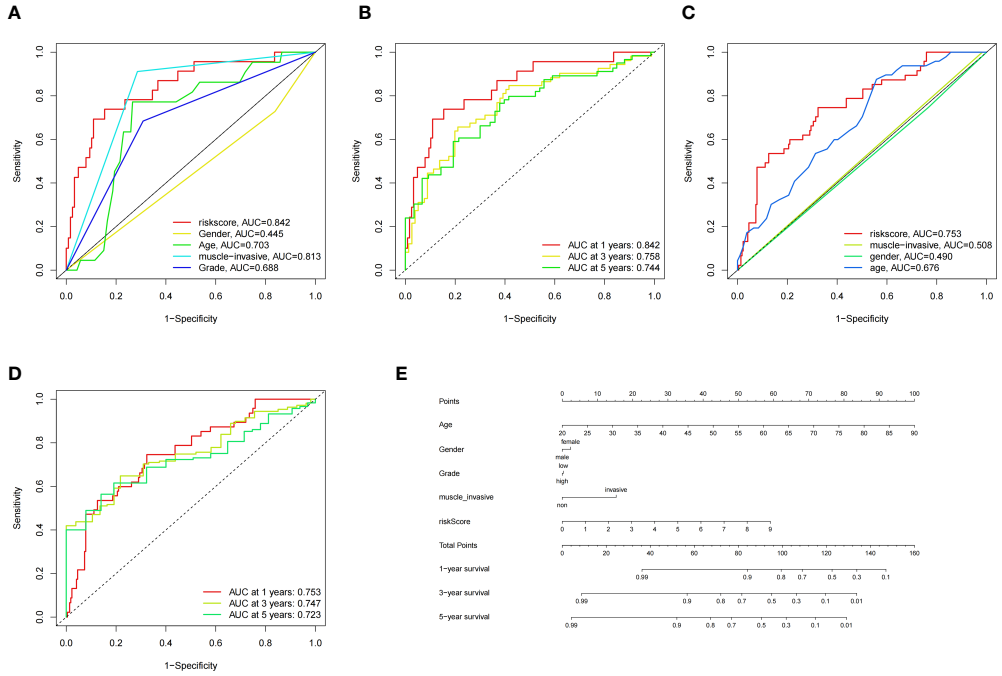

FIGURE 4
ROC Curves of the Model in GSE13507 and TCGA Datasets, and Nomogram. **(A)** Multiple-index ROC curves for GSE13507 patients, **(B)** Time-dependent ROC curve ROC curves for GSE13507 patients, **(C)** Multiple-index ROC curves for TCGA patients, **(D)** Time-dependent ROC curve ROC curves for TCGA patients, **(E)** Nomogram build based on training cohort.

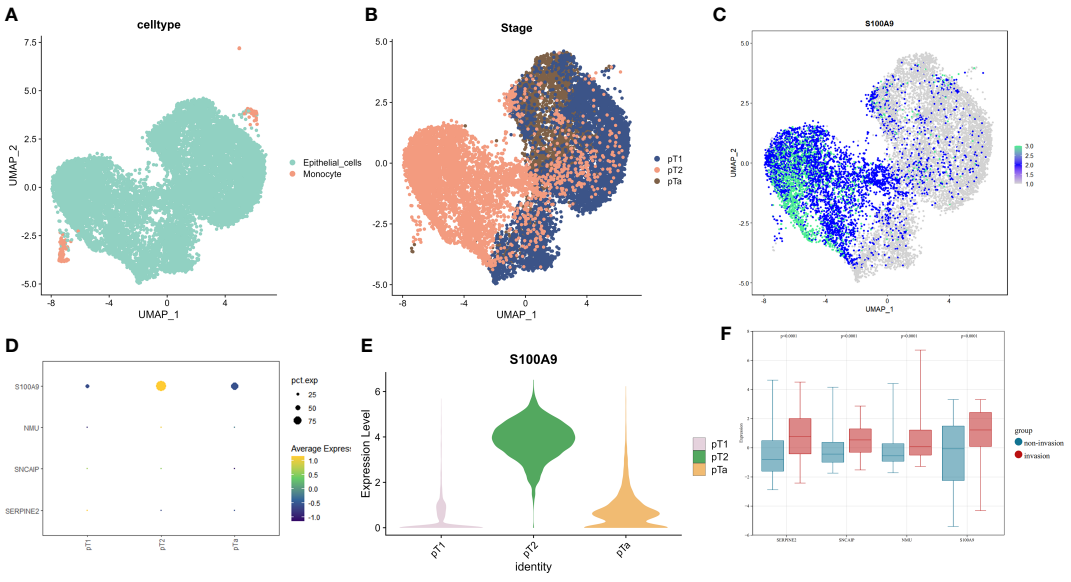

FIGURE 5
The expression profiles of model genes in single-cell data and GSE32894 dataset(revised). **(A)** UMAP dimensionality reduction displayed by cell type, **(B)** UMAP dimensionality reduction displayed by sample stage in epithelial cells. **(C)** Expression of S100A9 on UMAP dimensionality reduction in epithelial cells. **(D)** Expression levels of model genes in single-cell data based on sample T stage. **(E)** Violin plots showing the expression of S100A9 on UMAP in samples of pT1, pT2, and pTa stages. **(F)** Expression of model genes involved in muscle-invasive and non-muscle invasive bladder cancer in GSE32894.

10.3389/fimmu.2023.1187286

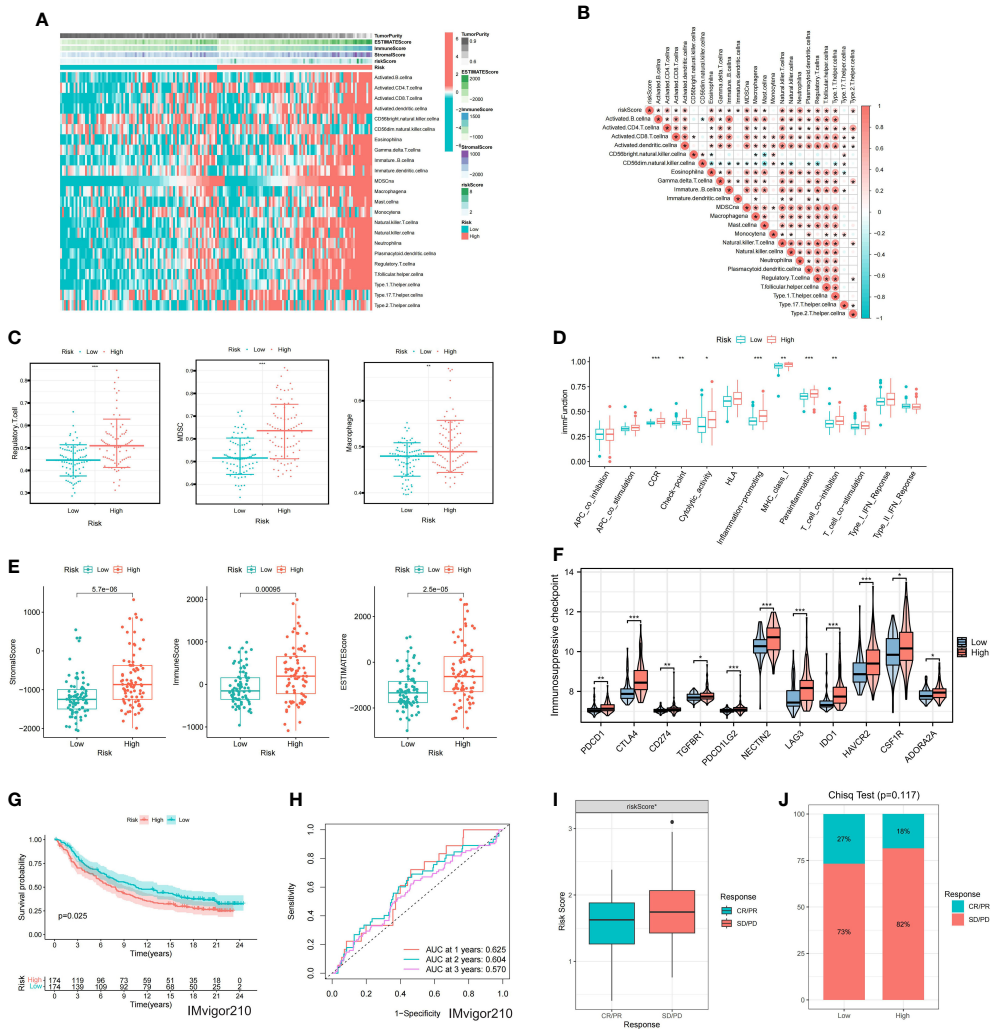

FIGURE 6
Immune characteristics of the model **(A)** Heatmap showing ssGSEA results for high and low-risk groups. **(B)** Correlation analysis between risk score and immune cells. **(C)** Differential expression of immunosuppressive cells between high and low-risk groups. **(D)** Differential expression of immune function scores within the model. **(E)** Differences in TME scores between high and low-risk groups. **(F)** Differential expression of immunosuppressive checkpoints between high and low-risk groups. **(G)** KM survival analysis for the model in the IMvigor210. **(H)** ROC curves for the model at 1, 2, and 3 years. **(I)** Differential expression of riskscore between CR/PR and SD/PD groups. **(J)** Differences in the proportion of CR/PR and SD/PD between high and low-risk groups. * represents p< 0.05; ** represents p< 0.01; *** represents p< 0.001.

was higher in low risk group (Figures 7E-I). These findings not only provide valuable insights for the selection of appropriate chemotherapy drugs according to the risk score of BCa patients, but also help to make clinical treatment decisions.

3.7 Overexpression of S100A9 in muscle-invasive and non-muscle-invasive BCa tissues

In the cohort used to construct the model (GSE13507), clinical data on the subsequent progression of BCa patients were available. We found that the expression of S100A9 was significantly elevated in recurrent patients (Figure 8A). Furthermore, in patients who progressed to muscle-invasive BCa compared to those who did not, the expression of S100A9 was also significantly increased (Figure 8B). Additionally, single-cell sequencing data demonstrated higher expression of S100A9 in epithelial cells of muscle-invasive BCa compared to non-muscle-invasive BCa. Therefore, we selected S100A9 from the model as the target for further experimental validation. To validate the biological function of S100A9 in BCa, we first evaluated the protein expression of S100A9 among normal, muscle-invasive and non-invasive BCa tissues. WB showed that the protein expression of S100A9 was higher in muscle-invasive and non-invasive BCa than in normal tissues, and the expression was the highest in muscle-invasive BCa (Figure 8C).

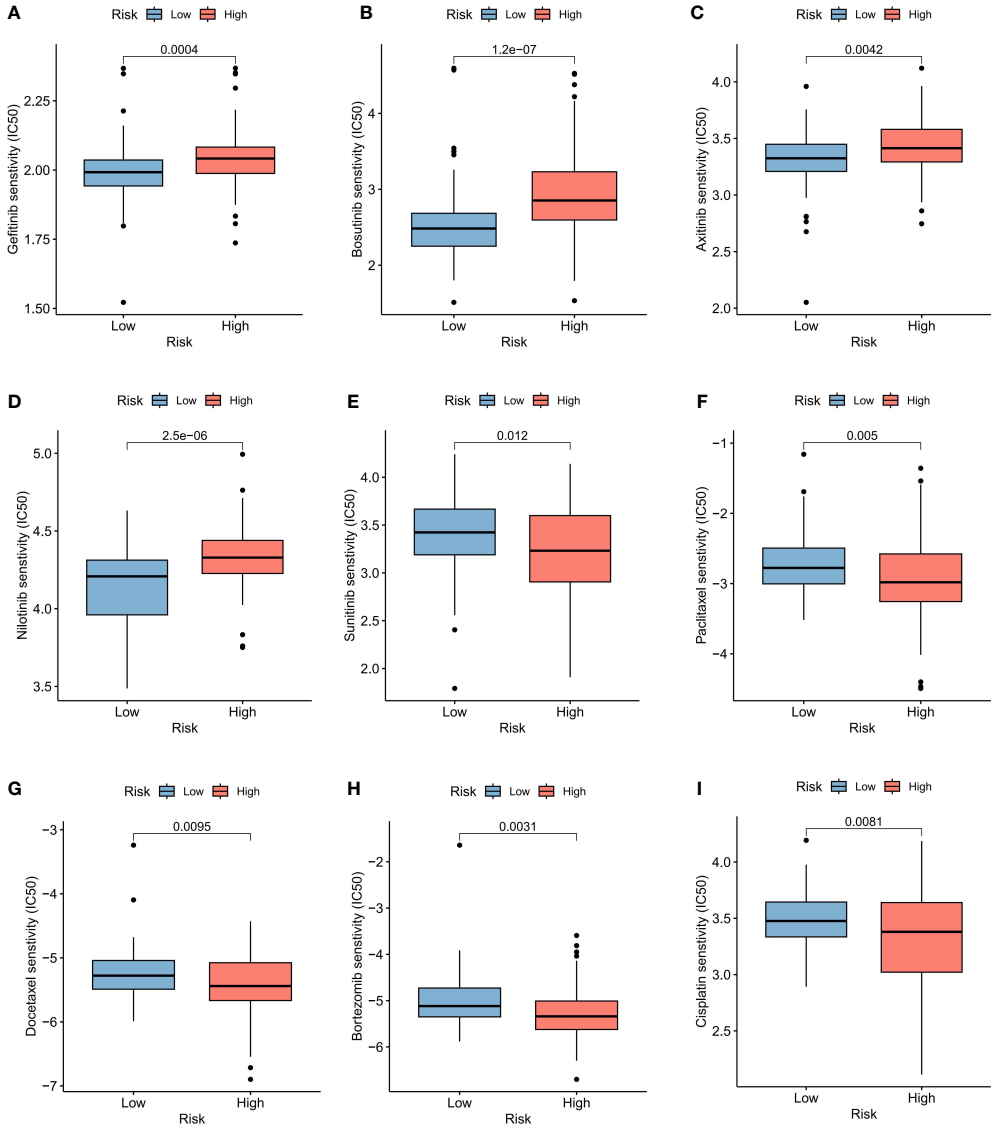

FIGURE 7
Drug sensitivity of BCa prognostic model. Sensitivity analysis for Gefitinib **(A)**, Bosutinib **(B)**, Axitinib **(C)**, Nilotinib **(D)**, Sunitinib **(E)**, Paclitaxel **(F)**, Docetaxel **(G)**, Bortezomib **(H)** and Cisplatin **(I)** between low and high risk groups.

3.8 S100A9 promotes BCa cell proliferation, migration and invasion *in vitro*

First, S100A9-siRNA was transfected into T24 and UMUC3 cells to knock down S100A9. The results indicated that the si-S100A9 used in the experiment effectively suppressed the expression of S100A9 (Figure 9A). Colony formation experiments confirmed that si-S100A9 significantly impaired the proliferative capacity of T24 and UMUC3 cells (Figure 9B). The transwell assay demonstrated that si-S100A9-treated T24 and UMUC3 cells exhibited reduced migration and invasion capacities compared to the control group (Figures 9C, D). This was consistent with the results of our previous analysis, indicating that S100A9 played a role in promoting proliferation, migration and invasion in BCa cells.

4 Discussion

With the rapid development of genomic technologies, the cost of sequencing is also decreasing. The cost of single-sample sequencing is now under $100,especially for clinical exome sequencing (CES), and if a unified platform is used for sequencing, the cost is likely to decrease further (11). This is a small fraction of the long-term follow-up and treatment costs for BCa patients. In addition, standardized sequencing at scale will standardize the various gene expression values that affect patient prognosis. In previous studies, although there have been differential analysis and gene identification of muscle-invasive and non-muscle-invasive bladder cancer based on databases, all of their research was solely database-driven. While seven genes, including S100A9, were investigated and validated in databases, no

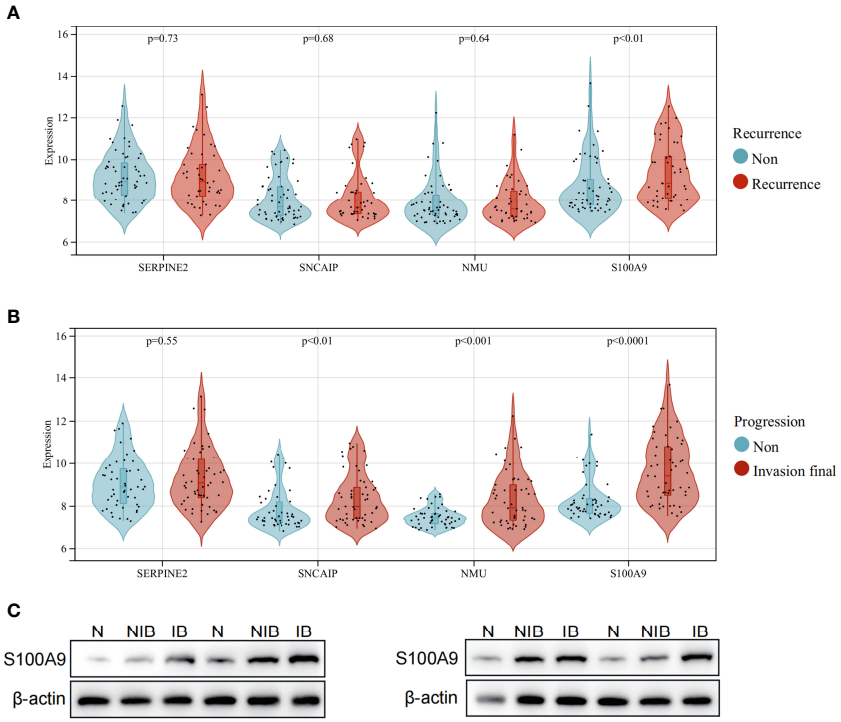

FIGURE 8
Expression of model genes in recurrent and progressive patients, and verification of protein expression levels of S100A9 in BCa. **(A)** Expression comparison of model genes between patients with no recurrence and recurrent patients. **(B)** Expression comparison of model genes between patients who did not progress to muscle-invasive BCa and patients who progressed to muscle-invasive BCa. **(C)** Western blot analysis showing the difference of S100A9 protein expression among normal, non-muscle-invasive and muscle-invasive BCa tissues.

experimental verification was conducted. The identified genes were not further validated in the normal, non- muscle-invasive bladder cancer, and muscle-invasive bladder cancer groups. Our research addressed these shortcomings by conducting experimental validation and utilizing single-cell sequencing data for further verification. Additionally, we explored the impact of the S100A9 gene on bladder cancer cells in cell lines, thereby advancing research in this field. In our study, because the sequencing platforms and expression data processing methods are different, there may be differences in the numerical expressions. Therefore, when studying the impact of risk scoring on patients' overall survival rates, we used median values to group high- and low-risk patients from both GSE13507 and TCGA patients. And we build nomogram only based on training cohort (GSE13507). Additionally, as the use of cystoscopy is essential for the diagnosis and treatment of BCa, obtaining sequencing samples is also extremely simple. Assuming that the standardized sequencing platform is successfully established, reference values for the standardized expression of various genes are available, which provides more options for the treatment and follow-up of BCa patients. For example, early-stage BCa patients can take aggressive treatment based on the high expression of certain invasive genes, thereby avoiding the risk of muscle infiltration. This approach can reduce patients' treatment costs and improve treatment efficacy. For patients with invasive BCa, based on the existing bioinformatics algorithms, their immune checkpoint status and tumor microenvironment can be estimated according to their gene expression information, the degree of infiltration can be observed, and personalized immunotherapy can be carried out accordingly. In recent years, there have been significant advances in research on immune therapy and targeted therapy for BCa (27). More accurate sequencing methods such as single cell sequencing and spatial transcriptome have also been added to the search for BCa markers (28). Precise sequencing can target specific cancer cell molecules or immune cells for targeted therapy, thereby improving treatment efficacy and prognosis.

In this study, we focused on using differential genes between muscle-invasive and non-muscle-invasive BCa to develop and validate prognostic features of BCa. First, 183 MIRDGs were identified between muscle-invasive and non-muscle-invasive BCa. Secondly, based on multivariate cox regression analysis, four genes (SERPINE2, SNCAIP, NMU, S100A9) were determined as prognostic features. At the same time, the KM survival curve in the model also showed that the survival time of the low-risk group of patients was significantly better than that of the high-risk group. The survival results were independently validated using the TCGA dataset. and the AUC of the ROC curve was also good, and the survival curve results were consistent. Furthermore, single-cell sequencing data further confirmed that the S100A9 in the model had differential expression between the two types of cancer, and S100A9 in invasive BCa was significantly higher than that in non-invasive BCa. Because the depth of single-cell sequencing was insufficient, we used microarray data (GSE32894) for further validation. The results showed that the expression of the model genes was higher in the muscle-invasive BCa group than in the non-

10.3389/fimmu.2023.1187286

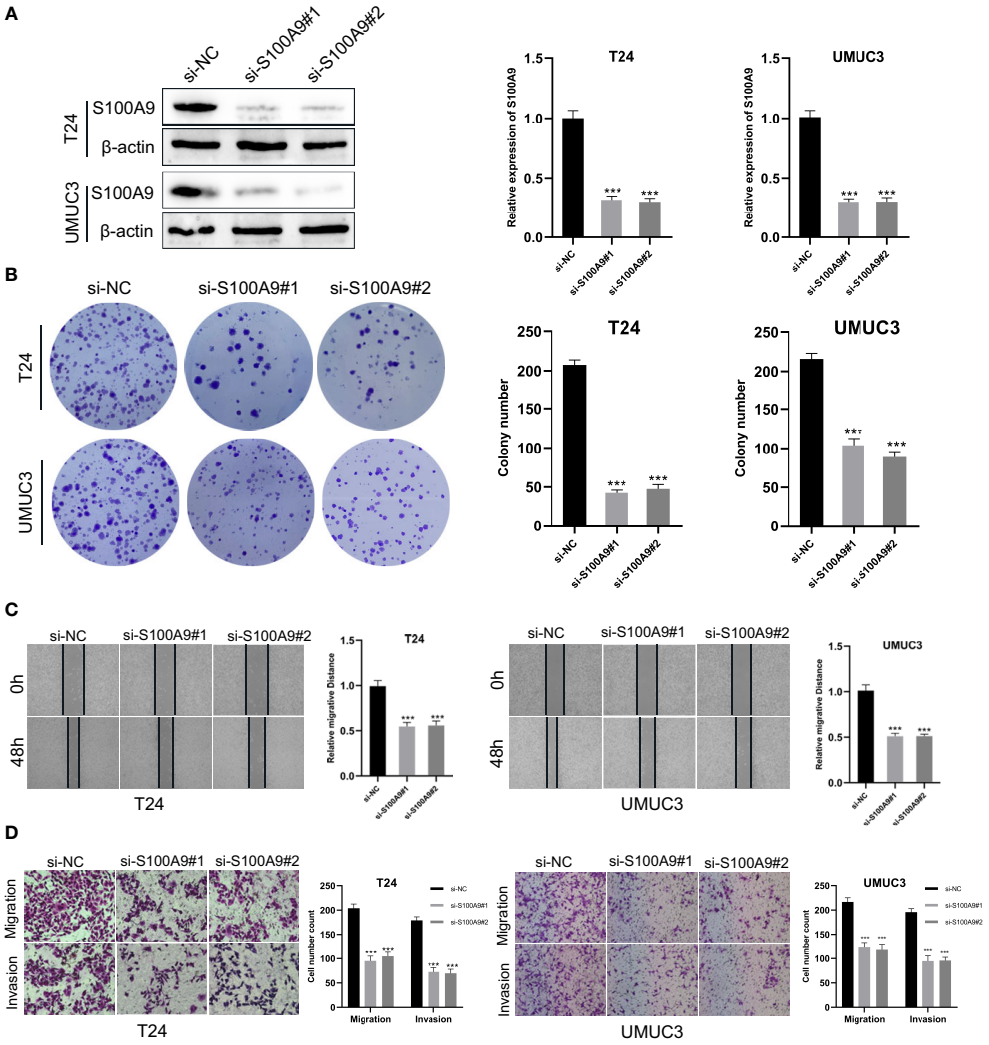

FIGURE 9
Downregulation of S100A9 suppressed the progression of BCa *in vitro*. **(A)** The protein expression of S100A9 was downregulated in T24 and UMUC3 cells, as determined by Western blot; **(B)** Colony formation assay in si-S100A9 and control cells; **(C)** Wound healing assay was used to detect the effect of S100A9-knockdown on BCa cell migration. Cell migration ability was represented by the wound gap distance in microscopic field at the time points of 0 and 48 h; **(D)** S100A9-knockdown suppressed BCa cell metastasis in T24 and UMUC3. *** represents p<0.001.

muscle-invasive bladder group, indicating that our model genes were consistent with the differential analysis we previously performed using GSE13507. Moreover, this is consistent with the calculation we obtained when building the model, where HR>1, indicating that high expression may lead to poor prognosis of BCa. In addition, immunosuppressive checkpoints and immunosuppressive cells were significantly overexpressed in the high-risk group. At the same time, there were significant differences in StromalScore, ImmuneScore, ESTIMATEScore, TumorPurity between the high- and low-risk groups. These results suggested that four model genes may be involved in constructing immunosuppressive microenvironments that promote tumor invasion and metastasis. The upregulation of immune checkpoints in the high-risk group suggests a stronger ability to evade immune surveillance, which may contribute to the poor prognosis in this group. Notably, we observed that the expression of PD-1-related immune checkpoints (CD274, PDCD1) showed significant differences but overall low expression levels. This finding is consistent with previous studies that have reported BCa's insensitivity to PD-1 therapy, further confirming the accuracy of our analysis. Furthermore, the higher immune scores in the high-risk group compared to the low-risk group indicate significant differences in the tumor microenvironment between these groups. This disparity may be an important factor contributing to the unfavorable prognosis observed in the high-risk group.

Our prognostic signature include four genes, SERPINE2, SNCAIP, NMU, and S100A9, each playing a critical role in tumor progression, invasion, and metastasis. SERPINE2 is a member of the serine protease inhibitor family and is mainly expressed in the placenta, brain, and urothelial epithelium. Upregulation of SERPINE2 has been reported to increase the radioresistance of lung cancer cells and is also involved in the invasion and metastasis of endometrial cancer (29). High expression of SERPINE2 indicates

poor prognosis of urothelial carcinoma, which is consistent with the results of our study (30), and it also promotes tumorigenesis in various cancers (31, 32). SNCAIP encodes synaptic nuclear protein α-interacting protein and has been found to be highly expressed in metastatic clear cell carcinoma (33). The NMU encodes a member of the neuropeptide neuromedin family. The encoded protein is a precursor that is processed by proteolytic cleavage to produce biologically active neuropeptides that play a role in pain, stress, and immune-mediated inflammatory diseases (34). Increased expression of this gene has been observed in kidney cancer (35), pancreatic cancer (36), and lung cancer (37). S100A9 has been found to be a protein that bridges inflammation and cancer. Increased expression of S100A9 is considered a sign of increased tumor proliferation and invasive ability and is believed to be a new therapeutic target for cancer treatment (38).

The occurrence of recurrence and progression in BCa treatment is a major concern for clinicians. Recurrence not only necessitates additional surgical interventions but also requires close monitoring and follow-up, which can impose a significant burden on patients in terms of time and financial resources. Progression to muscle-invasive disease leads to a worse prognosis, requiring more aggressive and invasive treatments such as bladder removal surgery, which rapidly diminishes the patient's quality of life. In our analysis of the GSE13507 cohort, we observed elevated expression of S100A9 in both recurrent and progressive BCa cases. Furthermore, single-cell data revealed increased expression of S100A9 in invasive BCa within the extracted epithelial cells. We conducted further experimental validation, including western blot, which confirmed high protein expression of S100A9 in invasive BCa patients. Cell-based assays demonstrated that silencing S100A9 reduced the invasiveness of BCa cells. These findings suggest that S100A9 may serve as a prognostic marker for early-stage BCa patients.

In non-invasive BCa patients with high expression of S100A9, more aggressive and timely treatments such as partial bladder resection or frequent follow-up should be considered. However, this decision requires validation through large-scale clinical trials. In other studies, increased expression of S100A9 has been observed in urine samples from both invasive and non-invasive BCa patients, accompanied by cell-based experiments. Our study, based on clinical information from patients, not only identified S100A9 but also provided an explanation for its elevated expression in invasive BCa and its association with recurrence and progression. This suggests that the diagnostic use of S100A9 during the initial assessment of bladder lesions would greatly assist clinicians in predicting patient prognosis. This is the innovative aspect of our research. However, our current study has certain limitations. Firstly, the data collected were from public databases, and the sample size was limited. Future research should overcome these limitations by employing larger sample sizes. Additionally, while we validated the performance of S100A9 in cell experiments and clinical samples, the specific mechanisms and the roles of the other three genes in our model remain unknown. Future studies will follow the following plans: designing more comprehensive clinical trials with well-defined clinical endpoints, such as the number and timing of recurrences in non-muscle-invasive BCa and the conversion to muscle-invasive disease, and their respective time points. Moreover, a standardized sequencing workflow will be designed to collate sequencing data for unified comparative analysis, which can be matched with newly added clinical events to more accurately identify genes influencing patient prognosis and provide treatment targets. Finally, the identified genes possess complex functionalities and molecular mechanisms, which will require further validation in cellular and animal models.

5 Conclusion

In this study, we further elucidated the role of differential genes in prognosis between muscle-invasive and non-muscle-invasive BCa. Moreover, we have constructed the prognostic model in BCa patients, which may be employed as a reliable predictor of prognosis and immune response.

Meanwhile, S100A9 may promote the proliferation, migration and invasion of BCa cells, which may be a potential therapeutic target of BCa.

Data availability statement

The datasets presented in this study can be found in online repositories. The names of the repository/repositories and accession number(s) can be found within the article/Supplementary Material.

Ethics statement

All the patients provided written informed consent, and the protocol was approved by ethical committee of Suzhou Municipal Hospital. The studies were conducted in accordance with the local legislation and institutional requirements. The participants provided their written informed consent to participate in this study.

Author contributions

KZ and WW designed this work. XZ and SJ wrote the manuscript. WW performed the bioinformatics analysis. PX performed the data review. KC, KL, FW, and XL provided administrative and financial support. All authors contributed to the article and approved the submitted version.

Funding

This research was supported by Suzhou Clinical Medical Center for Urological Diseases (No. Szlcyxzx202106).

Conflict of interest

The authors declare that the research was conducted in the absence of any commercial or financial relationships that could be construed as a potential conflict of interest.

Publisher's note

All claims expressed in this article are solely those of the authors and do not necessarily represent those of their affiliated organizations, or those of the publisher, the editors and the reviewers. Any product that may be evaluated in this article, or claim that may be made by its manufacturer, is not guaranteed or endorsed by the publisher.

Supplementary material

The Supplementary Material for this article can be found online at: https://www.frontiersin.org/articles/10.3389/fimmu.2023.1187286/full#supplementary-material

References

1. Babjuk M, Burger M, Capoun O, Cohen D., Compérat E. M., Dominguez Escrig J. L., et al. European association of urology guidelines on non-muscle-invasive bladder cancer (Ta, T1, and carcinoma in situ). *Eur Urol* (2022) 81(1):75–94. doi: 10.1016/j.eururo.2021.08.010

2. Zhao X, Wang Y, Liang C. Cigarette smoking and risk of bladder cancer: a dose-response meta-analysis. *Int Urol Nephrol* (2022) 54(6):1169–85. doi: 10.1007/s11255-022-03173-w

3. Flaig TW, Spiess PE, Abern M, Agarwal N., Bangs R., Boorjian S. A., et al. NCCN guidelines® Insights: bladder cancer, version 2.2022. *J Natl Compr Cancer Netw JNCCN* (2022) 20(8):866–78. doi: 10.6004/jnccn.2022.0041

4. Tran L, Xiao JF, Agarwal N, Duex JE, Theodorescu D. Advances in bladder cancer biology and therapy. *Nat Rev Cancer* (2021) 21(2):104–21. doi: 10.1038/s41568-020-00313-1

5. Liedberg F, Kjellström S, Lind AK, Sherif A, Söderkvist K, Falkman K, et al. Swedish National Guidelines on Urothelial Carcinoma: 2021 update on non-muscle invasive bladder cancer and upper tract urothelial carcinoma. *Scand J Urol* (2022) 56 (2):137–46. doi: 10.1080/21681805.2022.2041086

6. Büchler J, Gschwend JE, Retz M, Schmid SC. [Muscle-invasive bladder cancer]. *Urol Ausg A* (2021) 60(6):769–75. doi: 10.1007/s00120-021-01536-2

7. Shore ND, Palou Redorta J, Robert G, Hutson TE., Cesari R., Hariharan S., et al. Non-muscle-invasive bladder cancer: An overview of potential new treatment options. *Urol Oncol* (2021) 39(10):642–63. doi: 10.1016/j.urolonc.2021.05.015

8. Witjes JA. Follow-up in non-muscle invasive bladder cancer: facts and future. *World J Urol* (2021) 39(11):4047–53. doi: 10.1007/s00345-020-03569-2

9. Sharma V, Wymer KM, Borah BJ, Saigal CS., Litwin MS., Packiam VT., et al. Cost-effectiveness of maintenance bacillus calmette-guérin for intermediate and high risk nonmuscle invasive bladder cancer. *J Urol* (2020) 204(3):442–9. doi: 10.1097/JU.0000000000001023

10. Álvarez-Maestro M, Guerrero-Ramos F, Rodríguez-Faba O, Domínguez-Escrig JL, Fernández-Gómez JM. Current treatments for BCG failure in non-muscle invasive bladder cancer (NMIBC). *Actas Urol Esp* (2021) 45(2):93–102. doi: 10.1016/j.acuro.2020.08.003

11. Katragadda S, Hall TO, Bettadapura R, Dalton JC., Ganapathy A., Ghana P., et al. Determining cost-optimal next-generation sequencing panels for rare disease and pharmacogenomics testing. *Clin Chem* (2021) 67(8):1122–32. doi: 10.1093/clinchem/hvab059

12. Koll FJ, Schwarz A, Köllermann J, Banek S., Kluth L., Wittler C., et al. CK5/6 and GATA3 defined phenotypes of muscle-invasive bladder cancer: impact in adjuvant chemotherapy and molecular subtyping of negative cases. *Front Med* (2022) 9:875142. doi: 10.3389/fmed.2022.875142

13. Liu J, Xie J, Huang Y, Xie J, Yan X. TFPI-2 inhibits the invasion and metastasis of bladder cancer cells. *Progres En Urol J Assoc Francaise Urol Soc Francaise Urol* (2021) 31(2):71–7. doi: 10.1016/j.purol.2020.07.243

14. Piao XM, You C, Byun YJ, Kang HW., Noh J., Lee J., et al. Prognostic value of BUB1 for predicting non-muscle-invasive bladder cancer progression. *Int J Mol Sci* (2021) 22(23):12756. doi: 10.3390/ijms222312756

15. Taber A, Park Y, Lelo A, Prip F., Xiao J., Berry DL., et al. STAG2 as a prognostic biomarker in low-grade non-muscle invasive bladder cancer. *Urol Oncol* (2021) 39 (7):438.e1–9. doi: 10.1016/j.urolonc.2021.02.007

16. Miyata Y, Sakai H. Predictive markers for the recurrence of nonmuscle invasive bladder cancer treated with intravesical therapy. *Dis Markers* (2015) 2015:857416. doi: 10.1155/2015/857416

17. Su J, Zhang Q, Qi H, Wu L., Li Y., Yu D., et al. The G-protein-coupled bile acid receptor Gpbar1 (TGR5) protects against renal inflammation and renal cancer cell proliferation and migration through antagonizing NF-κB and STAT3 signaling pathways. *Oncotarget* (2017) 8(33):54378–87. doi: 10.18632/oncotarget.17533

18. Goodspeed A, Jean A, Theodorescu D, Costello JC. A gene expression signature predicts bladder cancer cell line sensitivity to EGFR inhibition. *Bladder Cancer* (2018) 4 (3):269–82. doi: 10.3233/BLC-170161

19. Yin H, Zhang C, Gou X, He W, Gan D. Identification of a 13−mRNA signature for predicting disease progression and prognosis in patients with bladder cancer. *Oncol Rep* (2020) 43(2):379–94. doi: 10.3892/or.2019.7429

20. Minami S, Sato Y, Matsumoto T, Kageyama T., Kawashima Y., Yoshio K., et al. Proteomic study of sera from patients with bladder cancer: usefulness of S100A8 and S100A9 proteins. *Cancer Genomics Proteomics* (2010) 7(4):181–9.

21. Yasar O, Akcay T, Obek C, Turegun FA. Significance of S100A8, S100A9 and calprotectin levels in bladder cancer. *Scand J Clin Lab Invest* (2017) 77(6):437–41. doi: 10.1080/00365513.2017.1336567

22. Ritchie ME, Phipson B, Wu D, Hu Y., Law CW., Shi W., et al. limma powers differential expression analyses for RNA-sequencing and microarray studies. *Nucleic Acids Res* (2015) 43(7):e47. doi: 10.1093/nar/gkv007

23. Yu G, Wang LG, Han Y, He QY. clusterProfiler: an R package for comparing biological themes among gene clusters. *Omics J Integr Biol* (2012) 16(5):284–7. doi: 10.1089/omi.2011.0118

24. von Mering C, Huynen M, Jaeggi D, Schmidt S, Bork P, Snel B. STRING: a database of predicted functional associations between proteins. *Nucleic Acids Res* (2003) 31(1):258–61. doi: 10.1093/nar/gkg034

25. Yoshihara K, Shahmoradgoli M, Martínez E, Vegesna R, Kim H, Torres-Garcia W, et al. Inferring tumour purity and stromal and immune cell admixture from expression data. *Nat Commun* (2013) 4:2612. doi: 10.1038/ncomms3612

26. Li B, Chan HL, Chen P. Immune checkpoint inhibitors: basics and challenges. *Curr Med Chem* (2019) 26(17):3009–25. doi: 10.2174/0929867324666170804143706

27. Salomé B, Sfakianos JP, Ranti D, Daza J., Bieber C., Charap A., et al. NKG2A and HLA-E define an alternative immune checkpoint axis in bladder cancer. *Cancer Cell* (2022) 40(9):1027–1043.e9. doi: 10.1016/j.ccell.2022.08.005

28. Wei W, Rong Y, Sanhe L, Chunxiu Y., Thokerunga E., Cui D., et al. Single-cell sequencing and its applications in bladder cancer. *Expert Rev Mol Med* (2022) 24:e6. doi: 10.1017/erm.2021.23

29. Zhang J, Wu Q, Zhu L, Xie S., Tu L., Yang Y., et al. SERPINE2/PN-1 regulates the DNA damage response and radioresistance by activating ATM in lung cancer. *Cancer Lett* (2022) 524:268–83. doi: 10.1016/j.canlet.2021.10.001

30. Chuang HW, Hsia KT, Liao JB, Yeh CC, Kuo WT, Yang YF. SERPINE2 overexpression is associated with poor prognosis of urothelial carcinoma. *Diagn Basel Switz* (2021) 11(10):1928. doi: 10.3390/diagnostics11101928

31. Zou G, Lv Y, Kong M, Xiang B, Chen J. Upregulation of SERPINE2 results in poor prognosis of hepatoblastoma *via* promoting invasion abilities. *Dis Markers* (2022) 2022:2283541. doi: 10.1155/2022/2283541

32. Chu H, Hu B, Su X. SERPINE2 feedback regulates EGF/EGFR signaling in human papillary thyroid carcinoma cells. *Mol Med Rep* (2021) 23(5):342. doi: 10.3892/mmr.2021.11981

33. Meng H, Jiang X, Cui J, Yin G., Shi B., Liu Q., et al. Genomic analysis reveals novel specific metastatic mutations in Chinese clear cell renal cell carcinoma. *BioMed Res Int* (2020) 2020:2495157. doi: 10.1155/2020/2495157

34. Budhiraja S, Chugh A. Neuromedin U: physiology, pharmacology and therapeutic potential. *Fundam Clin Pharmacol* (2009) 23(2):149–57. doi: 10.1111/j.1472-8206.2009.00667.x

35. Harten SK, Esteban MA, Shukla D, Ashcroft M, Maxwell PH. Inactivation of the von Hippel-Lindau tumour suppressor gene induces Neuromedin U expression in renal cancer cells. *Mol Cancer* (2011) 10:89. doi: 10.1186/1476-4598-10-89

36. Yoo W, Lee J, Jun E, Noh KH., Lee S., Jung D., et al. The YAP1-NMU axis is associated with pancreatic cancer progression and poor outcome: identification of a novel diagnostic biomarker and therapeutic target. *Cancers* (2019) 11(10):1477. doi: 10.3390/cancers11101477

37. Wallrapp A, Riesenfeld SJ, Burkett PR, Abdulnour R-EE., Nyman J., Dionne D., et al. The neuropeptide NMU amplifies ILC2-driven allergic lung inflammation. *Nature* (2017) 549(7672):351–6. doi: 10.1038/nature24029

38. Shabani F, Farasat A, Mahdavi M, Gheibi N. Calprotectin (S100A8/S100A9): a key protein between inflammation and cancer. *Inflammation Res Off J Eur Histamine Res Soc Al* (2018) 67(10):801–12. doi: 10.1007/s00011-018-1173-4

frontiers | Frontiers in Immunology

TYPE Original Research
PUBLISHED 20 September 2023
DOI 10.3389/fimmu.2023.1233260

OPEN ACCESS

EDITED BY
Ines Zidi,
Tunis El Manar University, Tunisia

REVIEWED BY
Fereshteh Yazdanpanah,
University of Pennsylvania, United States
Qiangzhe Zhang,
Nankai University, China
Marwa Hasni,
Higher National Engineering School of Tunis, Tunisia

*CORRESPONDENCE
Yi Zhang
472189926@qq.com
Chengliang Yuan
13568235628@163.com

†These authors have contributed equally to this work and share first authorship

RECEIVED 01 June 2023
ACCEPTED 04 September 2023
PUBLISHED 20 September 2023

CITATION
Wang Y, Xu Y, Liu C, Yuan C and Zhang Y (2023) Identification of disulfidptosis-related subgroups and prognostic signatures in lung adenocarcinoma using machine learning and experimental validation.
Front. Immunol. 14:1233260.
doi: 10.3389/fimmu.2023.1233260

Identification of disulfidptosis-related subgroups and prognostic signatures in lung adenocarcinoma using machine learning and experimental validation

Yuzhi Wang[1†], Yunfei Xu[2†], Chunyang Liu[3], Chengliang Yuan[1*] and Yi Zhang[4*]

[1]Department of Laboratory Medicine, Deyang People's Hospital, Deyang, Sichuan, China, [2]Department of Laboratory Medicine, Chengdu Women's and Children's Central Hospital, Chengdu, Sichuan, China, [3]Department of Ultrasound, The First People's Hospital of Yibin, Yibin, Sichuan, China, [4]Department of Blood Transfusion, Deyang People's Hospital, Deyang, Sichuan, China

Background: Disulfidptosis is a newly identified variant of cell death characterized by disulfide accumulation, which is independent of ATP depletion. Accordingly, the latent influence of disulfidptosis on the prognosis of lung adenocarcinoma (LUAD) patients and the progression of tumors remains poorly understood.

Methods: We conducted a multifaceted analysis of the transcriptional and genetic modifications in disulfidptosis regulators (DRs) specific to LUAD, followed by an evaluation of their expression configurations to define DR clusters. Harnessing the differentially expressed genes (DEGs) identified from these clusters, we formulated an optimal predictive model by amalgamating 10 distinct machine learning algorithms across 101 unique combinations to compute the disulfidptosis score (DS). Patients were subsequently stratified into high and low DS cohorts based on median DS values. We then performed an exhaustive comparison between these cohorts, focusing on somatic mutations, clinical attributes, tumor microenvironment, and treatment responsiveness. Finally, we empirically validated the biological implications of a critical gene, KYNU, through assays in LUAD cell lines.

Results: We identified two DR clusters and there were great differences in overall survival (OS) and tumor microenvironment. We selected the "Least Absolute Shrinkage and Selection Operator (LASSO) + Random Survival Forest (RFS)" algorithm to develop a DS based on the average C-index across different cohorts. Our model effectively stratified LUAD patients into high- and low-DS subgroups, with this latter demonstrating superior OS, a reduced mutational landscape, enhanced immune status, and increased sensitivity to immunotherapy. Notably, the predictive accuracy of DS outperformed the published LUAD signature and clinical features. Finally, we validated the DS

expression using clinical samples and found that inhibiting KYNU suppressed LUAD cells proliferation, invasiveness, and migration in vitro.

Conclusions: The DR-based scoring system that we developed enabled accurate prognostic stratification of LUAD patients and provides important insights into the molecular mechanisms and treatment strategies for LUAD.

KEYWORDS

disulfidptosis, lung adenocarcinoma, prognosis, tumor microenvironment, immunotherapy

Introduction

Lung cancer is a global health concern and one of the foremost sources of cancer patient morbidity and mortality, posing a grave threat to public health (1). In 2020, an estimated 2,206,771 new cases were diagnosed, and 1,796,144 fatalities occurred (2). Non-small cell lung cancer (NSCLC) stands as the prevalent pathological category among lung cancers, comprising about 85% of all cases, whereas lung adenocarcinoma (LUAD) is the most frequently occurring subtype of NSCLC (3). LUAD is plagued by a high incidence of invasive behavior and metastatic spread. However, significant advances in the treatment of LUAD have been achieved in the past few decades. Accordingly, targeted therapies and immunotherapies have been demonstrated to enhance the treatment efficacy and outcomes for patients with LUAD (4). However, the majority of patients develop drug resistance and relapse following initial treatment, resulting in no significant improvement in 5-year survival rates (5). Thus, to benefit more LUAD patients, there is an urgent need to identify new therapeutic targets and prognostic indicators for predicting survival and guiding clinical treatment in LUAD patients.

Programmed cell death (PCD) is a cellular death process governed by a molecular program that is controlled by particular genes. This process is essential for the normal development of organisms and the preservation of homeostasis (6). Exploration and characterization of these cell death mechanisms not only deepens our fundamental comprehension of cellular equilibrium, but also offers valuable perspectives for the therapeutic approach to a variety of diseases, including cancer. For instance, recent studies have progressively highlighted the tumor-inhibiting effects of ferroptosis, which is achieved through the deprivation of cysteine and the generation of reactive oxygen species (ROS) by p53 (7, 8). Moreover, the enhancement of lipid peroxidation by activated CD8 + T cells can induce ferroptosis, which contributes to the antitumor efficacy of immunotherapy (9). The role of autophagy in cancer can vary, depending on the specific tumor model and tumor stage. During the initial stages of cancer, autophagy functions as a protective mechanism, shielding normal cells from tumorigenesis by preventing DNA damage and mutations (10). However, in the context of fully-formed solid tumors, autophagy shifts its role and promotes tumor progression by promoting tumor growth, enhancing cell survival, enhancing resistance to platinum-based chemotherapy, and facilitating the formation of metastases (11). Autophagy inhibitors, therefore, comprise one of the treatment options for patients with advanced tumors. Recent research (Liu et al., 2023) demonstrates that excessive accumulation of disulfide induces a unique form of controlled cell death known as “disulfidptosis” that is distinct from apoptosis, necrosis, autophagy, and ferroptosis (12). SLC7A11 is an essential transport protein whose primary function is to facilitate the cellular uptake of cysteine (13). Cysteine is a necessary building block for the synthesis of glutathione and a crucial component for inhibiting oxidative stress in cells and regulating iron death pathways (14). However, it has also been shown to possess certain cytotoxic properties (15). Gan Bo et al., discovered that under conditions of glucose deprivation, high expression of SLC7A11 leads to a significant consumption of NADPH within cells, abnormal aggregation of disulfides like cysteine, inducing disulfide stress and rapid cell death (16). This form of cell death induced by glucose deprivation and high SLC7A11 expression in cancer cells cannot be prevented by inhibitors of cell death that act on other cells, nor is it caused by depletion of intracellular ATP. However, thiol-oxidizing agents, such as Diamide, can enhance this effect. Moreover, under glucose-deficient conditions, the number of disulfide bonds in the actin cytoskeleton increases significantly. Therefore, this study suggests that the induction of disulfide-dependent cell death by GLUT inhibitors may be an effective cancer treatment strategy. Consequently, focusing on disulfidptosis regulators (DRs) as potential targets provides new perspectives for understanding the complexities of the occurrence and development mechanism in LUAD. This approach is, therefore, of significant importance in enhancing the efficacy of treatment in patients with LUAD patients. However, the full scope of the impact of DRs on outcomes and treatments for LUAD patients has yet to be comprehensively explored.

In the current study, we divided 1569 LUAD samples into two disulfidptosis-associated subtypes according to 18 DRs and compared survival and immune infiltration between the subtypes. We also developed a disulfidptosis score (DS) to predict overall survival (OS) and to delineate the immunological landscape of LUAD. As indicated by the findings, a higher DS was associated with unfavorable prognostic outcomes and worse immunotherapy responses in LUAD, suggesting the potential clinical utility of DS as a tool for assessing prognosis and immunotherapy efficacy. Thus, the current study introduces an innovative approach for assessing

the efficacy of immunotherapy and predicting the prognosis of LUAD patients based on DS.

Materials and methods

Data collection

The LUAD data were obtained from The Cancer Genome Atlas (TCGA)-LUAD (https://portal.gdc.cancer.gov/), GSE31210, GSE68465, and GSE72094 in Gene Expression Omnibus (GEO) (https://www.ncbi.nlm.nih.gov/geo/), which included RNA sequencing data, somatic mutation data, copy number variation (CNV) data, and corresponding clinical information. The TCGA-LUAD cohort, which consisted of 539 LUAD tissues and 59 cancer-adjacent tissue samples, served as a training cohort. Meanwhile, GSE31210, GSE68465, and GSE72094 were utilized for the validation cohort, which consisted of 1,150 LUAD patients. Additionally, the "sva" package was used to correct the batch effect between the different datasets by adopting the "combat" algorithm (17). Moreover, patients who lacked OS time were filtered out. Finally, 1569 eligible patients were encompassed in the study. The detailed clinical characteristics of all LUAD patients is listed in Supplementary Table 1. Additionally, 18 DRs were collected from the previous study (Supplementary Table 2) (12).

Consensus cluster analysis of DRs

A consensus clustering algorithm was employed to discern optimal subtypes founded on the expression of 18 DRs using the R package "ConsensusClusterPlus". The number of clusters (K) and their stability (with 1,000 repeats for mast k = 9) were determined by the consensus clustering algorithm (18). The clustering was based on dividing centromeres with "Euclidean" distances (the most common and familiar distance measurement methods and correlation of K-Means clustering). Additionally, a T-distributed Stochastic Neighbor Embedding (tSNE) analysis was conducted to decrease the dimensions and differentiate the subtypes of information (tSNE can preserve local similarities between data points and is one of the most used unsupervised clustering visualization methods).

Differentially expressed genes and functional annotation

DEGs among DRs subtypes were determined using the "limma" R package with the filtering criteria of log (fold change) >1 and False-discovery rate (FDR) <0.05 (19). To further investigate the potential functions and enriched pathways of DEGs, functional enrichment analyses were conducted on DEGs employing the "clusterprofiler" R package (20).

Generation of DS

The DS was calculated to quantify the disulfidptosis patterns of the LUAD. Accordingly, a univariate cox regression analysis was conducted to identify the DEGs are related to prognosis. Subsequently, the patients were segregated into distinct gene cluster groups according to the expression of prognostic DEGs using the unsupervised clustering method. Based on prognostic DEGs, the 10 machine learning algorithms, including 'Least Absolute Shrinkage and Selection Operator (LASSO, "glmnet" package)', 'Ridge ("glmnet" package)', 'Elastic network ("glmnet" package)', 'StepCox ("survival" package)', 'Survival support vector machine (survival-SVM, "survivalsvm" package)', 'CoxBoost ("CoxBoost" package)' (21), 'Supervised principal components, "superpc" package' (22), 'partial least squares regression for COX, "plsRcox" package', 'random survival forest (RSF, "randomForestSRC" package)', 'generalized boosted regression modeling, "gbm" package' were used to constructed the models. Briefly, 101 combinations of 10 machine learning algorithms were used to build the models based on a leave-one-out cross-validation (LOOCV) framework. Models with <3 genes were excluded. Simultaneously, each patient's linear score and concordance index (C-index) are calculated based on various models, and the optimal model is selected based on the average highest C-index in the training and testing cohorts. Utilizing the optimal model, the DS for each patient was determined. See the supplementary methods table for details. The patients were then separated into high- and low-DS groups using the median DS value. Subsequently, Kaplan–Meier survival analysis was utilized to compare the OS rates of patients in various DS groups.

Somatic mutation and CNV analysis

The "maftools" package was utilized to evaluate and visualize the mutation type and frequency of the genes (23). Correspondingly, the tumor mutation burden (TMB) of each LUAD sample was calculated based on the total count of somatic mutations per megabase (MB) in the exon coding region of the human genome. Different mutation types were classified as either synonymous or nonsynonymous mutations. The nonsynonymous variants included Frame_Shift_Del, Frame_Shift_Ins, In_Frame_Del, In_Frame_Ins, Missense, Nonsense, Nonstop, Splice_Site, and Translation_Start_Site. The maftools analysis focused on identifying significantly mutated genes (P <0.05) between the two groups and assessing the interaction effect of gene mutations. Only genes with mutations occurring 30 times or more in at least one group were considered for both analyses. GISTIC 2.0 was used to identify significant regions within CNV data (24). To quantify and compare CNVs, we calculated the fraction of altered genome (FGA), fraction of genome gained (FGG), and fraction of genome lost (FGL) for each sample. FGA reveals the proportion of genomic segments that

have been altered. FGG/FGL considers specifically the genomic segments that have undergone gain or loss, respectively.

Tumor microenvironment landscape and hallmark pathway analyses

TME at LUAD were evaluated under four aspects. First, the immune score, stromal score, ESTIMATE score, and tumor purity were calculated using the ESTIMATE algorithm (25). Secondly, three algorithms, Single Sample Gene Set Enrichment Analysis (ssGSEA), Tumor Immune Estimation Resource (TIMER, https://cistrome.shinyapps.io/timer/), and "MCPcounter" were used to quantify the relative infiltration of immune cells in the entire cohort (26–28). Thirdly, the seven steps of cancer immunity cycle were analyzed using the Tracking Tumor Immunophenotype (TIP) website (http://biocc.hrbmu.edu.cn/TIP/) (29). In the fourth step, 35 inhibitory immune checkpoints were extracted from a prior study. Subsequently, Gene Set Enrichment Analysis (GSEA) was utilized to identify underlying mechanisms in hallmark gene sets with the recommended criteria (FDR <0.25 and NES >1), in order to determine the underlying hallmark pathways associated with DS (30). Meanwhile, "Gene Set Variation Analysis" (GSVA) package was applied to the two DS groups with an adjusted p value <0.01 (31). The "h.all.v7.4.symbols.gmt" hallmark gene sets from the MSigDB database were employed for GSVA implementation.

Assessment of immunotherapy and chemotherapy

To explore the predictive value of DS in LUAD patients after immunotherapy, we compared the immune dysfunction and exclusion (TIDE, http://tide.dfci.harvard.edu/) score; additionally, the submap algorithm was applied to compare the efficacy of immunotherapy among various DS subtypes (32, 33). In addition, four immunotherapy-treated cohorts, IMvigor210, GSE35640, GSE79671, and GSE173839, were collected to investigate the immunotherapy response ability of DS. The sensitivity of tumor cell lines to potential drugs was obtained from the Cancer Therapeutics Response Portal (CTRP, https://portals.broadinstitute.org/ctrp) and Profiling Relative Inhibition Simultaneously in Mixtures (PRISM, https://depmap.org/portal/prism/). The more sensitive a cell line is to a potential drug, the lower its area under the curve (AUC).

Single-cell RNA-sequencing analysis

ScRNA-seq data was downloaded from GSE131907. Subsequently, the "Seurat" R package was utilized to measure the gene expression levels by processing the raw data from each sample (34). Cells with fewer than 200 detected genes were removed. Accordingly, the top 2000 highly variable genes were selected for subsequent clustering analysis. Following this, single cells were classified into distinct subgroups via the application of the FindNeighbors and FindClusters functions (dim = 15 and resolution =0.2). In addition, the tSNE was constructed utilizing the top 15 primary components. Subsequently, immune cells and tumor cells were identified using the "single R" and "copyKAT" packages (35, 36). Pseudotime trajectory analysis is a method used to study the temporal order of cells during development, differentiation, or other biological processes. Its goal is to reduce the dimensionality of single-cell data from high-dimensional to one-dimensional, thus representing the temporal changes of cells in a pseudotime manner. This aids in understanding the timeline of processes like differentiation, development, and transformation in tumor cells. Hence, the cell trajectory cancer cell populations were ordered in pseudotime using the "Monocle" package (37).

Cell culture and transfection

Two human LUAD cells (PC-9 and H838) as well as a normal bronchial epithelial cell (BEAS-2B) were obtained from the American Type Culture Collection (Manassas, VA, USA). The PC-9 and H838 cells were grown in RPMI 1640 supplemented with 10% FBS and 1% penicillin-streptomycin, while BEAS-2B cells were grown in DMEM supplemented with 10% FBS and 1% penicillin-streptomycin in humidified air at 37°C and 5% CO_2 (This condition simulates the physiological environment in the human body, aiding in maintaining normal cellular growth, metabolism, and function). To construct KYNU knockdown and negative control (NC) cell lines, H838 and PC-9 cells were seeded in 6-well plates at a density of 5×10^4 cells/well and transfected with 50 nM siRNAs-KYNU and siRNA negative control (siRNA-NC) using lipofectamine 3000 (This reagent possesses high efficiency, broad spectrum, and low toxicity) following the manufacturer's guidelines (Hanheng, Shanghai, China). After 48 h of transfection, subsequent experiments were conducted (Typically, after 48 hours of transfecting siRNA, the target gene's expression is effectively disrupted in the vast majority of cases, while cells continue to maintain a relatively healthy and appropriate growth state). The siRNA sequences are provided in Supplementary Table 3.

Tissue microarray and immunohistochemistry

For this study, a total of 15 TM tissue samples (HLugA030PG04-1) were utilized, including 15 LUAD and 15 adjacent non-tumor tissues. All the tissues were procured from Shanghai Outdo Biotech Co., Ltd. (Shanghai, China). TM was stained using IHC with KYNU. In brief, the antibodies were diluted to the suitable concentration and incubated overnight with the sections at 4°C. The avidin–biotin and streptavidin complex were then incubated with the biotinylated goat anti-rabbit IgG secondary antibody for 0.5 h. The cell nuclei were counterstained blue with Hematoxylin. Each specimen was graded based on the intensity (0: absent, 1: mild, 2: moderate, and 3: pronounced) and the proportion of positively stained cells (0: 0%, 1: 1%–25%, 2: 26%–50%, 3: 51%–75%, and 4: 76%–100%). The final

IHC scores were then calculated as the product of the intensity score and the percentage score (38).

RNA-isolation and real-time reverse transcription polymerase chain reaction

RNA extraction was performed employing RNA extraction kit (AG, Changsha, China) in accordance with the manufacturer's instructions. The complementary DNA (cDNA) was synthesized from total RNA for each sample by using a reverse transcription kit (Promega, Madison, Wisconsin). Subsequently, the mRNA expression was quantitatively analyzed via RT-PCR (Roche Light Cycler® 480II System). The relative gene expression was normalized to β-actin, acting as the control gene. The primer sequences for the genes are outlined in Supplementary Table 4. The fold change of the target gene was computed utilizing the $2^{-\Delta\Delta Ct}$ method.

Proliferation assay

Cells in logarithmic phase were seeded into 96-well plates at density of 2,000 cells per 100 µl. They were then cultured for 0, 24, 48, 72, and 96 h. At the end of the incubation cycle, CCK-8 reagent (Saiku, Shanghai, China) was added to each well for 2 h at 37°C. Subsequently, the absorbance values of each well were measured at 450 nm. For colony formation assay, 500 cells were seeded into each well of a 12-well plate and incubated. After 10 days, the cells were stained with crystal violet solution, and fixed with 4% paraformaldehyde for 0.5 h. Finally, colonies consisting of more than 50 cells were counted.

Migration and invasion assay

The transwell experiment was executed using a transwell chamber (Transwell, Corning Costar, USA). For migration assays, a total of 4×10^4 cells were resuspended in 200 µl serum-free medium and placed to the upper chamber. The lower chamber was filled with 700 µl of medium containing 10% FBS. After 18 h, cells that migrated through the membrane were fixed and stained with hematoxylin. Following a 24 h-incubation period, cells that traversed the membrane were fixed with 4% paraformaldehyde for 30 minutes and stained with a crystal violet solution for 15 min. Subsequently, they were observed with a microscope, and five random fields of view were selected to count the cells. The protocol for the invasion assay was similar to the migration assay, with the exception that the upper chambers were coated with 70 µl of diluted Matrigel. In addition, the wound healing assay was utilized to examine cell migration. Serum-starved LUAD cells (2×10^5) were seeded in 6 well plates and then transfected with siRNA-NC or siRNA-KYNU. Upon reaching >95% cell confluence, a sterile 20 µl pipette tip was used to create a scratch in the monolayer of cells. After a PBS wash, the cells were incubated for 0 and 24 h in the corresponding basic culture medium. The monolayer cells were examined microscopically, and the gap distance was measured quantitatively to ascertain LUAD cell migration.

Statistical analysis

All statistical analyses and representations were conducted using R (version 4.2.1) and GraphPad Prism (version 9.00). The Chi-squared test was used to compare the proportion of individuals within two groups. Additionally, continuous variables in two or

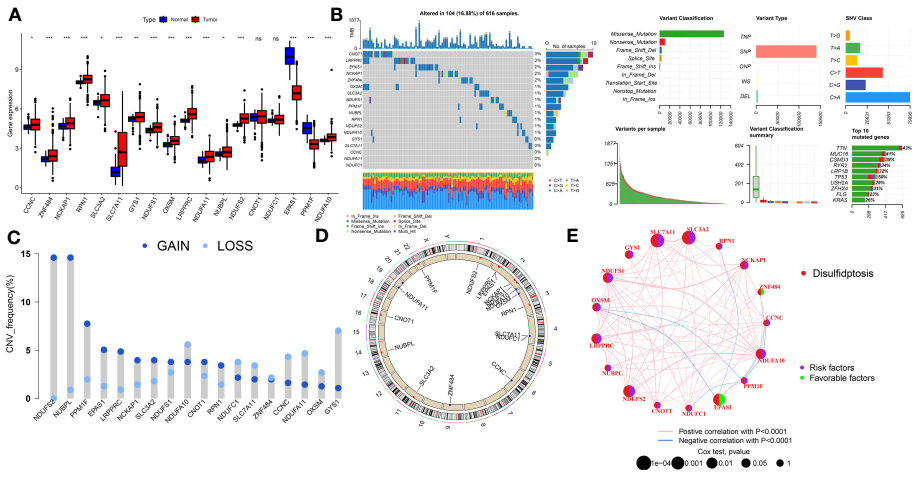

FIGURE 1
The genomic features and expression of DRs in LUAD. **(A)** The differential expression of DRs between tumor and normal samples. **(B)** Mutation landscape of DRs in TCGA-LUAD. **(C)** The CNV mutation frequency of DRs. **(D)** Chromosome position and alteration of DRs. **(E)** Molecular interaction network map of DRs Negative correlations are illustrated in green, while positive correlations are denoted in pink. ns, not significant, *P < 0.05, **P < 0.01, ***P < 0.001.

more groups were compared using Wilcoxon rank-sum test or Kruskal–Walli's test. For correlation analysis, the Pearson correlation test was employed. A p-value less than 0.05 was deemed statistically significant.

Results

Genetic and transcriptional alterations of DRs in LUAD

Gene expression analysis using bulk RNA-seq demonstrated that the majority of DRs displayed relative higher expression levels in LUAD tissues compared to para-carcinoma tissues (Figure 1A). As depicted in Figure 1B, 104 of 616 (16.88%) LUAD samples possessed genetic mutations. A total of 13 of 18 DRs were found to be mutated, with CNOT1 exhibiting the highest rate of mutation. Among them, missense mutations were found to be the most frequent (Figure 1B). In order to unmask the genetic modifications in DRs, we presented an overview of the frequency of somatic and copy number mutations with malignancies. Moreover, analysis of these 18 DRs revealed that CNV alterations were common. NDUFS2, NUBPL, PPM1F, EPAS1, and LRPPRC displayed widespread CNV amplification, whereas CCNC, NDUFA11, OXSM, and GYS1 showed widespread CNV deletions (Figure 1C). Figure 1D depicts the locations of CNV alterations in LUAD DRs. The correlation network composed of 18 DRs is illustrated in Figure 1E (correlation coefficient >0.4; the positive correlation is represented by the red line, negative correlation is represented by the blue line).

Identification of DRs subtypes in the LUAD cohort

In order to delve further into understanding the DRs' expression pattern in the oncogenesis of LUAD, 1569 patients from 4 independent LUAD cohorts were included. Accordingly, we performed unsupervised clustering and classification on the combined LUAD cohort based on DRs. Our results showed that k = 2 was the optimal choice (Figures S1). In addition, the tSNE results revealed significant differences between the two clusters in terms of DRs expression (Figure 2A). Moreover, the Kaplan–Meier survival analysis demonstrated that the DRcluster A had a greater survival advantage than DRcluster B (Figure 2B). In addition, the clinicopathological characteristics of the various DR clusters also revealed significant differences (Figure 2C). To further explore the biological behavioral difference between these two clusters, we also conducted a GSVA enrichment analysis (Figure 2D). The results demonstrated that DRcluster A was primarily enriched for carcinogenic pathways like focal adhesion, EMC receptor interaction, and others. Moreover, Figure 2E data also revealed significant differences in the relative expression of immune infiltration cells across two DRclusters.

Identification of genes subtypes and establishment of DS

A total of 51 DEGs were identified from two DRclusters using the "limma" package. These DRs subtypes-related genes were significantly enriched in cellular metabolism (Figures 3A, B).

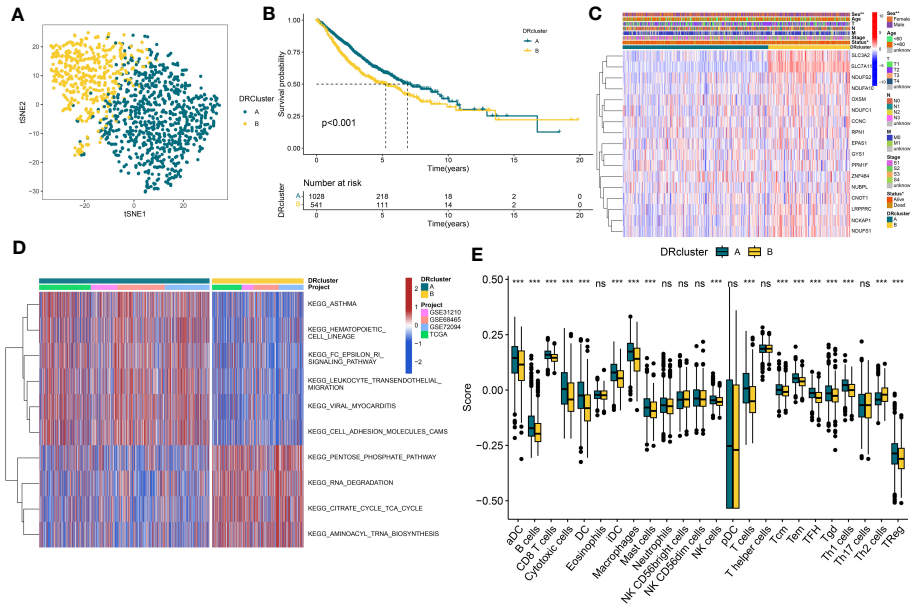

FIGURE 2
The construction of DRclusters. **(A)** tSNE plot of two DRclusters. **(B)** Kaplan-Meier survival analysis between two DRclusters. **(C)** Heatmaps of the distribution of DRs in the two DRclusters. **(D)** GSEA analysis indicating significant enrichment of pathways in the two DRclusters. **(E)** The proportion of 24 kinds of immune cells in two DRclusters. ns, not significant, *P < 0.05, **P < 0.01, ***P < 0.001.

10.3389/fimmu.2023.1233260

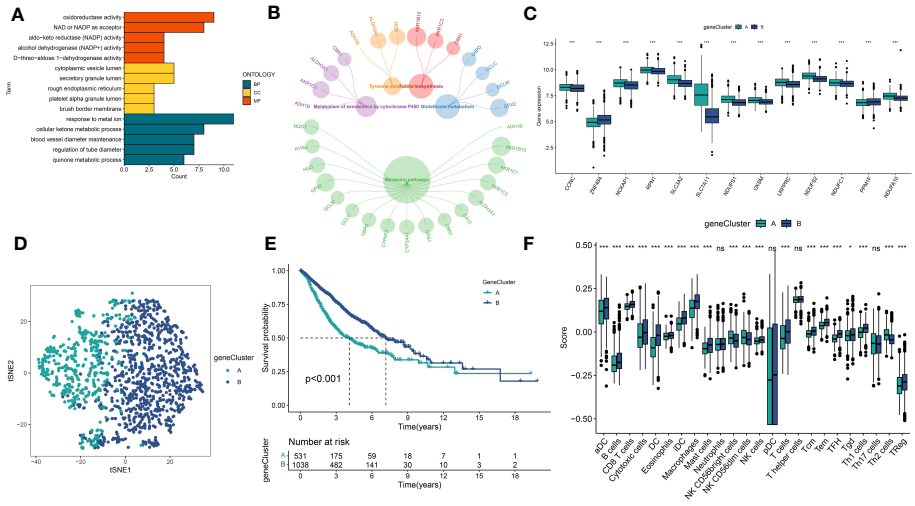

FIGURE 3
Identification of DRs gene clusters based on DEGs in DRclusters. **(A, B)** GO and KEGG enrichment analyses of DEGs among two DRclusters **(C)** Differences in the expression of DRs among the two genecluster **(D)** tSNE plot of two geneclusters. **(E)** Kaplan-Meier survival analysis between two geneclusters. **(F)** The proportion of 24 kinds of immune cells in two geneclusters. *p < 0.05; ***p < 0.001; ns, not significant.

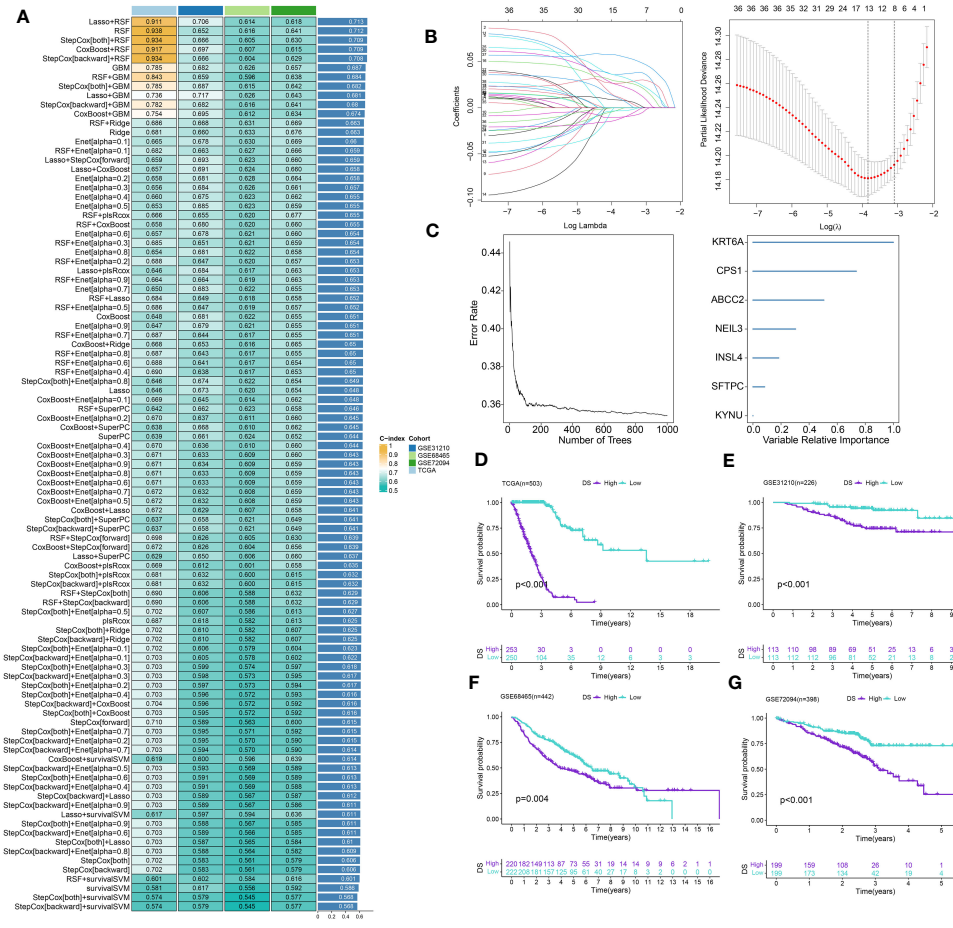

FIGURE 4
Construction of prognostic signature based on DEGs. **(A)** A total of 101 kinds of prediction models via a leave-one-out cross-validation framework and further calculated the C-index of each model. **(B)** Cvfit and lambda curves of LASSO regression applied with minimum criteria. **(C)** The number of trees determined by minimum error and importance of the four most valuable genes based on the RSF algorithm. **(D-G)** Kaplan-Meier survival curves of OS for high- and low-DS groups of patients in the TCGA, GSE31210, GSE68465, GSE72094 cohorts, respectively.

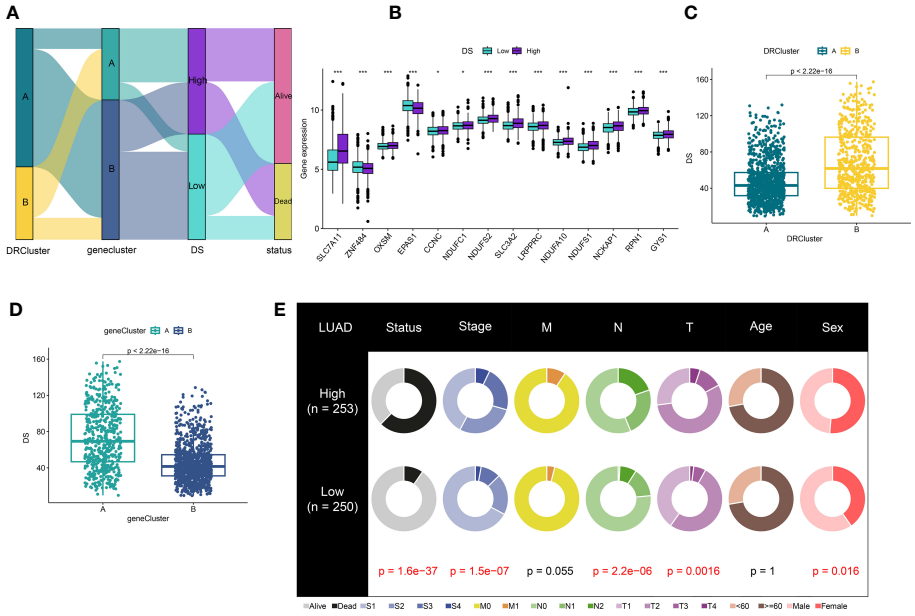

FIGURE 5
Correlation analysis of DS. **(A)** Alluvial diagram of clusters distributions in groups with different DS and survival outcomes **(B)** Expression of DRs between high- and low-DS groups. **(C)** Differences in DS between DRclusters. **(D)** Differences in DS between gene clusters. **(E)** The circular pie chart for the proportion difference of clinical indices. *P < 0.05, ***P < 0.001.

Subsequently, we conducted a univariate Cox regression analysis for DEGs and identified 39 DEGs with prognostic importance for LUAD. To further investigate the heterogeneity of DRs subtypes, we performed unsupervised clustering on 39 DEGs. The 1569 patients with LUAD were also separated into two gene clusters, designated geneCluster A and B (Figure S2). Similar to DRcluster, these genes accurately differentiate LUAD patients, with distinct clusters of genes exhibiting variations in DRs, survival rates, and immune cell infiltration (Figures 3C–F). Following this, the LOOCV framework was used to fit 101 prediction models to both training and testing sets. The C-index for each model was calculated, and based on the model with the highest average C-index (0.713), "Lasso+RSF" was deemed the optimal model (Figures 4A–C, Supplementary Table 5). A DS was calculated for each patient based on the expression of 7 genes (KRT6A, NEIL3, KYNU, ABCC2, SFTPC, CPS1, and INSL4) weighted by their regression coefficients in the model, and patients were divided to high- or low-DS groups based on the median cutoff point of DS (Supplementary Table 6). As evident from the K–M survival analysis, OS rates were significantly diminished in the high-DS group compared to the low-DS group (Figures 4D–G). Moreover, the relationship between different types of patients and their prognoses was analyzed (Figure 5), with results suggesting that a low DS was related to a better prognosis in all patient categories.

Evaluation of the DS

A time-dependent receiver operating characteristic (ROC) curve was employed to assess the validity of DS, as the AUC value for TCGA (0.93–0.96), GSE31210 (0.68–0.79), GSE68465 (0.63–0.66), GSE72094 (0.63–0.72), and meta-cohort (0.71–0.78) (Figures 6A–E). In addition, the C-index of clinical factors in patients with LUAD was determined (Figures 6F–J). Notably, the DS had a higher predictive efficacy than the vast majority of clinical indicators. Subsequently, both DS and clinical indicators were subjected to univariate and multivariate Cox analyses. In all cohorts, the DS was determined to be an independent indicator of OS prognosis (Tables 1–4). In order to determine the prognostic efficacy of DS, we combined 56 previously published LUAD prognostic models and conducted a comparative analysis of each model's C-index. These models were developed using a variety of biologically relevant features, including autophagy, EMT, ferroptosis, hypoxia, necroptosis, glycolysis, and m6A methylation. Accordingly, DS was found to exhibit superior performance relative to the vast majority of models across all cohorts (Figure 7, Supplementary Table 7). Cumulatively, these results, therefore, demonstrate that the DS would be a valuable LUAD prognostic model.

Comparison of the mutations and CNV between DS groups

Using the "maftool" package, a comparison was made between the distribution differences of somatic mutations observed in high- and low-DS groups. (Figures 8A, B). Comparing the frequency of mutants between the high- and low-DS groups, more somatic mutations, both synonymous and nonsynonymous, were observed in the high-DS group (Figures 8C–E). In addition, maftools analysis results showed that 17 genes mutated more frequently in LUAD patients in the high-DS group, including KEAP1, STK11,

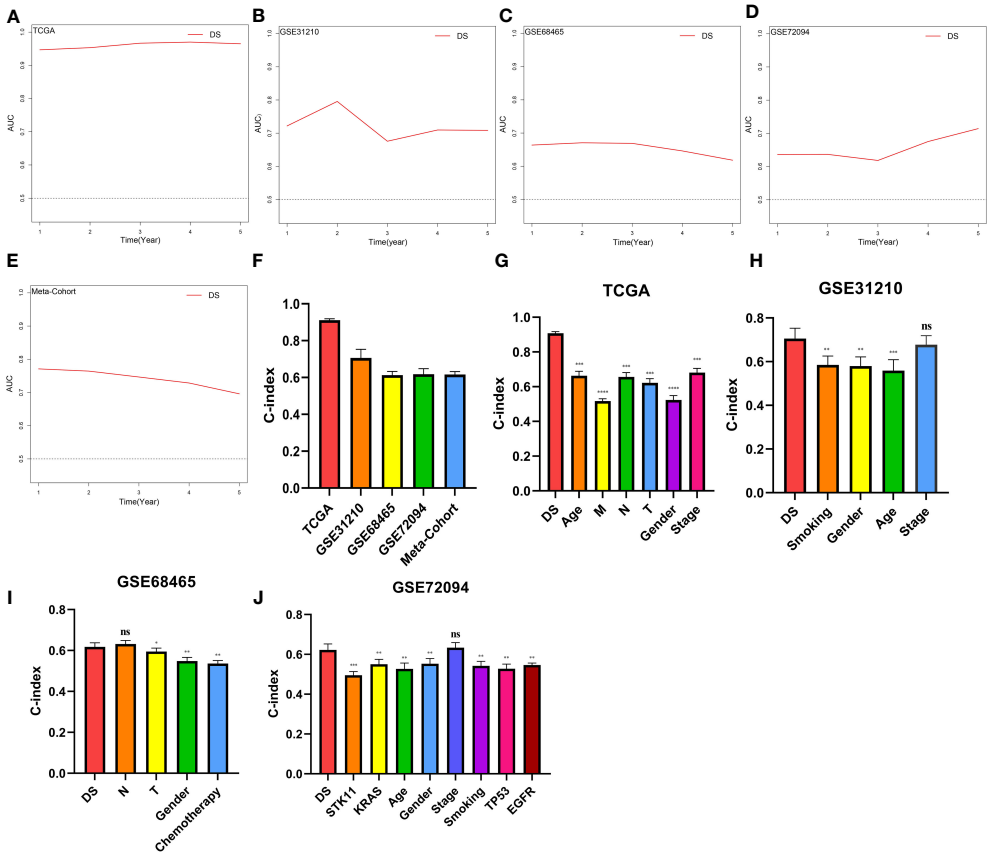

FIGURE 6
Evaluation of the DS. **(A-E)** Time-dependent ROC curves presented with the 1-5 year AUC in TCGA, GSE31210, GSE68465, GSE72094 and meta-cohort. **(F)** The C-index of the CDS for the TCGA, GSE31210, GSE68465, GSE72094 cohorts. **(G-J)** The C-index of the DS and other clinical factors in the TCGA, GSE31210, GSE68465, GSE72094 cohorts. *p < 0.05; **p < 0.01; ***p < 0.001; ****p < 0.0001; ns, not significant.

SMARCA4, TTN, NCKAP5, COL5A2, ANKRD30A, TEX15, PCDH15, GRIN2B, AHNAK, FAT4, FMN2, FAT1, ZNF804B, DOCK2 and COL22A1 (Figure 8F), and there was extensive co-mutation between these genes (Figure 8G). This is consistent with the mutation analysis described above; accordingly, TMB was found to be higher in the high-DS group compared to the low-DS group (Figure 8H). Subsequently, LUAD patients were classified into two mutation groups based on their TMB score. When combining DS and TMB, we discovered that patients with low TMB from the high-DS group had the worst prognosis (Figure 8I). Subsequently, we used the GISTIC 2.0 software to decipher the amplification and deletion of CNA on chromosome. Compared to the high-DS group, the low-DS group had a greater burden of amplification and deletion at both the arm and focal levels (Figure 8J). However, no

TABLE 1 Univariate and multivariate Cox analysis of the clinicopathological features and FA score with OS for TCGA cohort.

	Univariate Cox		Multivariate Cox	
Characteristics	HR(95%CI)	*P* value	HR(95%CI)	*P* value
Stage	1.977(1.586-2.463)	< **0.001**	1.239(0.863-1.779)	0.245
M	1.727(1.18-2.527)	**0.005**	0.969(0.611-1.537)	0.895
N	1.942(1.575-2.394)	< **0.001**	1.23(0.923-1.64)	0.157
T	1.816(1.386-2.38)	< **0.001**	1.267(0.895-1.793)	0.183
Age	1.038(0.822-1.31)	0.754	NA	NA
Sex	1.041(0.847-1.28)	0.7	NA	NA
DS	0.118(0.084-0.165)	< **0.001**	0.136(0.092-0.202)	< **0.001**

Significant value is given in bold.

TABLE 2 Univariate and multivariate Cox analysis of the clinicopathological features and FA score with OS for GSE68465 cohort.

	Univariate Cox		Multivariate Cox	
Characteristics	HR(95%CI)	*P* value	HR(95%CI)	*P* value
N	2.029(1.689-2.438)	< **0.001**	1.92(1.578-2.335)	< **0.001**
T	2.062(1.587-2.68)	< **0.001**	1.851(1.403-2.442)	< **0.001**
Gender	1.262(1.051-1.516)	**0.013**	1.236(1.018-1.5)	**0.032**
Chemotherapy	1.412(1.15-1.734)	< **0.001**	1.279(1.032-1.586)	**0.024**
DS	0.767(0.639-0.92)	**0.004**	0.819(0.678-0.989)	**0.038**

Significant value is given in bold.

significant disparities were observed between the high- and low-DS groups in terms of FGA, FGG, and FGL (Figure 8K). These results indicate a certain degree of correlation between DS and mutations.

TME analysis

In order to evaluate the discriminative potential of the DS subgroup for the TME and its applicability in immunotherapy, we simultaneously evaluated the abundance of immune cell infiltration across multiple samples using four distinct algorithms. Unsurprisingly, as the DS increased, the number of immune cells declined (Figure 9A). Apparently, the activation of key steps in the cancer immunity cycle, such as step 3 (priming_and_activation) and step 4 (CD4 T cell recruiting, Dendritic cell recruiting, Macrophage recruiting, Monocyte recruiting, and T cell recruiting) appeared to be significantly higher in the low-DS group than in the high-DS group (Figure 9B). Subsequently, the expression profile of immune checkpoints in the two DS groups were further evaluated. Accordingly, the analysis revealed that the low-DS group demonstrated elevated expression levels of immune checkpoints, including HHLA2 and CD48 (Figure 9C). Given the observed upregulation of immune-related characteristics in the group with low DS, its underlying biological mechanisms were investigated further. As evident from the findings, DS exhibited correlations with multiple metabolic pathways (Figure 9D). In addition, DS demonstrated a strong correlation with numerous immunotherapeutic strategies (Figure 9D). To investigate the cancer signaling pathways associated with DS, GSVA analysis was performed on high- and low-DS groups. Using a predetermined threshold, we discovered that 16 signature pathways were significantly upregulated in the high-DS group compared to the low-DS group (Figure 9E). GSEA validated that 12 of these pathways were upregulated in high-DS patients, the majority of which are known to be carcinogenic (Figures 9F–I).

Assessment of immunotherapy and chemotherapy

The potential of an immunotherapy response was subsequently predicted for each immune cluster utilizing the TIDE algorithm and submap analysis. Accordingly, lower TIDE scores were observed in the low-DS group, implying a higher sensitivity to immunotherapy in these patients (Figure 10A). Moreover, the submap results indicated that the group with a low DS level was more sensitive to CTLA4 inhibitors (Figure 10B). Although we evaluated an individual's immunotherapy efficacy using two algorithms, it remains critical to directly compare the curative efficacy of immunotherapy cohorts across various DS groups. As a result, four immunotherapy cohorts were included for further analysis. In the IMvigor210 cohort, patients with DR/PR had significantly longer OS compared to patients with SD/PD, whereas the influence of DS on patient prognosis was minimal (Figure 10C). However, patients who responded better to immunotherapy had lower DS levels across all cohorts (Figures 10D–G). Although there were no significant differences in patient survival and DS between the two groups for some cohorts, the propensity for these results was consistent for the other cohorts. In addition, these results demonstrate that the DS was able to predict the efficacy of ICBs and can provide direction for the deployment of immunotherapy.

TABLE 3 Univariate and multivariate Cox analysis of the clinicopathological features and FA score with OS for GSE31210 cohort.

	Univariate Cox		Multivariate Cox	
Characteristics	HR(95%CI)	*P* value	HR(95%CI)	*P* value
Smoking	1.417(0.882-2.277)	0.15	NA	NA
Gender	1.344(0.839-2.152)	0.219	NA	NA
Age	1.263(0.777-2.052)	0.346	NA	NA
Stage	2.774(1.732-4.441)	< **0.001**	2.305(1.417-3.75)	< **0.001**
DS	0.4(0.229-0.7)	**0.001**	0.495(0.278-0.881)	**0.017**

Significant value is given in bold.

TABLE 4 Univariate and multivariate Cox analysis of the clinicopathological features and FA score with OS for GSE72094 cohort.

	Univariate Cox		Multivariate Cox	
Characteristics	HR(95%CI)	*P* value	HR(95%CI)	*P* value
STK11	1.028(0.72-1.469)	0.879	NA	NA
KRAS	0.767(0.588-0.999)	**0.049**	0.911(0.693-1.198)	0.506
Age	1.258(0.836-1.894)	0.27	NA	NA
Gender	0.733(0.564-0.952)	**0.02**	0.746(0.569-0.979)	**0.035**
Stage	1.969(1.477-2.625)	< **0.001**	1.956(1.459-2.623)	< **0.001**
Smoking	1.248(0.694-2.245)	0.459	NA	NA
TP53	0.861(0.645-1.151)	0.313	NA	NA
EGFR	2.58(1.274-5.226)	**0.008**	2.025(0.986-4.159)	0.055
DS	0.549(0.416-0.724)	< **0.001**	0.619(0.465-0.825)	**0.001**

Significant value is given in bold.

Thus, to pinpoint candidate drugs that may exhibit heightened sensitivity in LUAD patients, we conducted drug response predictions using CTRP- and PRISM-derived data. Finally, the cross-correlation of the two pharmacogenomics databases allowed us to predict four drugs or compounds (including SB–743921, ispinesib, cabazitaxel, and gemcitabine) with therapeutic potential in patients (Figures 10H, I).

Single-cell sequencing analysis

To analyze the expression of DS in TME, we used the LUAD single-cell dataset GSE131907 from the GEO database. All the cells were partitioned into 16 clusters using the k-nearest neighbor (KNN) clustering algorithm (Figure 11A). Subsequently, using the "single R" and "copycat" packages to annotate all cells, we were able to identify 9 distinct cellular subtypes, including B cells, endothelial cells, epithelial cells, cancer cells, macrophage cells, monocyte cells, smooth muscle cells, NK cells, and T cells (Figure 11B). Most of these cells are important components of the TME mentioned in the above results. Subsequently, we investigated the single-cell transcriptome localization of 7 genes in DS (Figure 11C). Concurrently, the DS for each cell was calculated, which showed that cells with a high DS predominately resided in the region of cancer cells (Figure 11D). Additionally, the temporal sequence of cancer cellular differentiation was revealed by the analysis of the

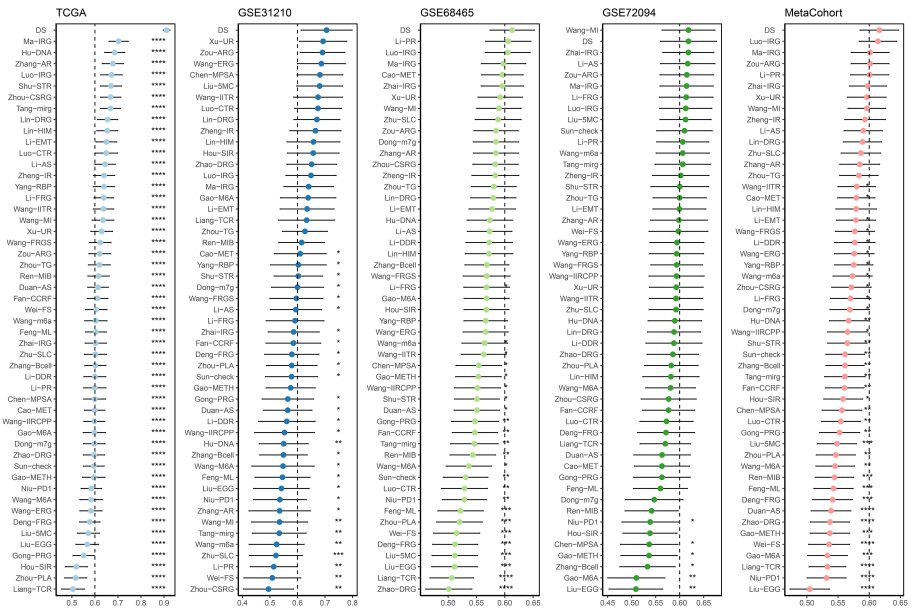

FIGURE 7
C-index analysis between the DS and 56 published signatures in TCGA, GSE31210, GSE68465, GSE72094 and meta-cohort. *p < 0.05; **p < 0.01; ***p < 0.001; ****p < 0.0001; ns, not significant.

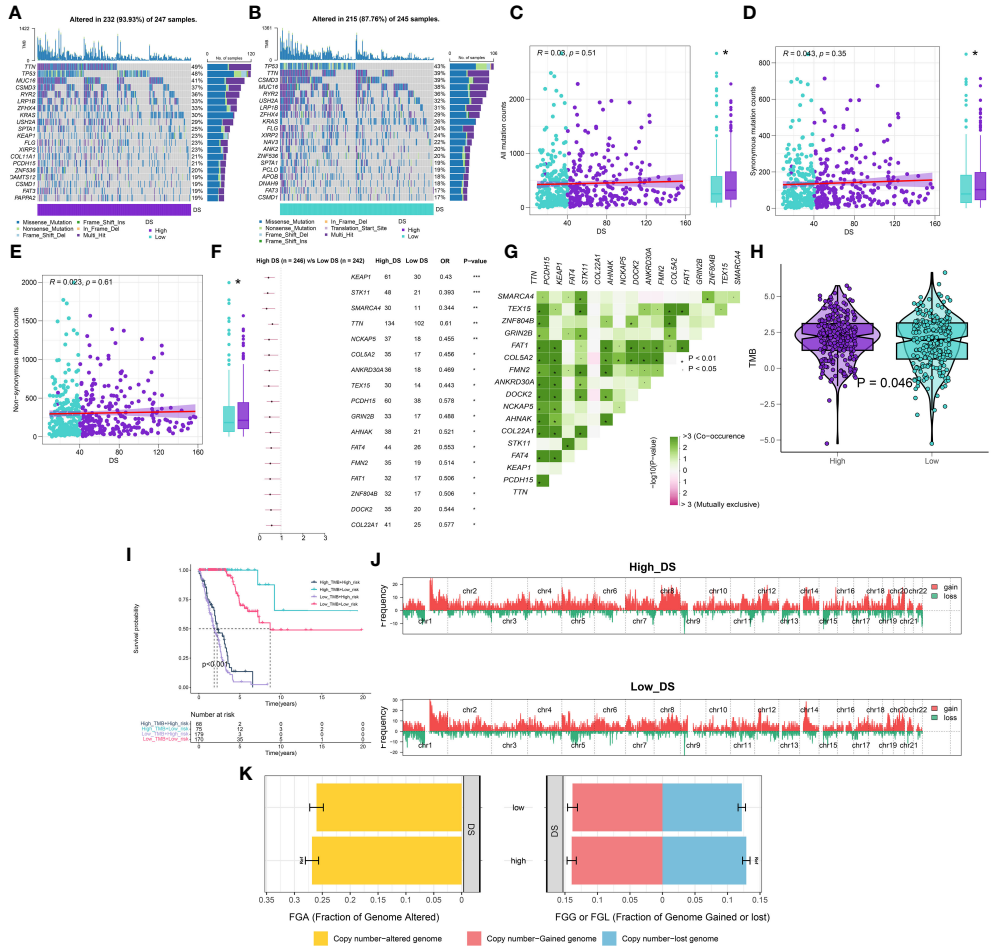

FIGURE 8
Integrated comparisons of somatic mutation and CNVs between high- and low-DS groups in the TCGA cohort. **(A, B)** Visual summary showing common genetic alterations in the high and low-DS groups. **(C-E)** Association between all mutation counts, synonymous mutation counts, nonsynonymous mutation counts, and DS and their distribution in the DS groups. **(F)** Forest plot of gene mutations in the patients. **(G)** Interaction effect of genes mutating differentially in patients. **(H)** Tumor mutation burden between high- and low-DS groups. **(I)** Comprehensive survival analysis based on DS and TMB. **(J)** Gene fragments profiles with amplification (red) and deletion (green) among the DS groups. **(K)** Comparison of the fraction of the genome altered, lost, and gained between the DS groups. *P < 0.05, **P < 0.01, ***P < 0.001.

pseudotime trajectory. Accordingly, low DS cancer cells appear at an earlier pseudotime than high DS cancer cells, which are primarily found in the earliest stages of differentiation (Figures 11E–H).

KYNU evaluation in the LUAD cells

The qRT-PCR experiments were performed on LUAD cell lines to confirm the expression levels of DS genes in LUAD. Our finding discovered that ABCC2, NEIL3, KYNU, and CPS1 exhibited elevated expression in LUAD cell lines, while KRT6A and SFTPC were found to be underexpressed (Figure 12A). In addition, KYNU exhibited the most significant correlation between high expression and unfavorable poor patient prognosis. No reports have documented the role of KYNU in LUAD to date. As a result of these considerations, KYNU was selected as the focus of further experiments. Correspondingly, IHC staining analysis showed that the protein level of KYNU expression was elevated in LUAD tumor tissues relative to paracancerous tissues (Figure 12B). Subsequently, we investigated the function of KYNU in PC-9 and H838 LUAD cell lines through a series of cell-based experiments. Initially, the effect of the siRNA was confirmed via RT-qPCR (Figure 13A). As demonstrated by CCK-8 and clone formation assays, KYNU knockdown inhibits LUAD cell growth and their clone formation capacity (Figures 13B, C). In addition, wound healing and transwell assays confirmed that KYNU knockdown inhibited the cell migration and invasion capabilities of LUAD cells (Figures 13D, E). The precision of these findings corroborated that the expression of KYNU mirrored the variations anticipated through bioinformatic prediction.

Discussion

LUAD persistently remains the principal contributor to cancer-related deaths among all cancer types and poses a substantial threat to global health (39). Prior research has revealed that the onset and

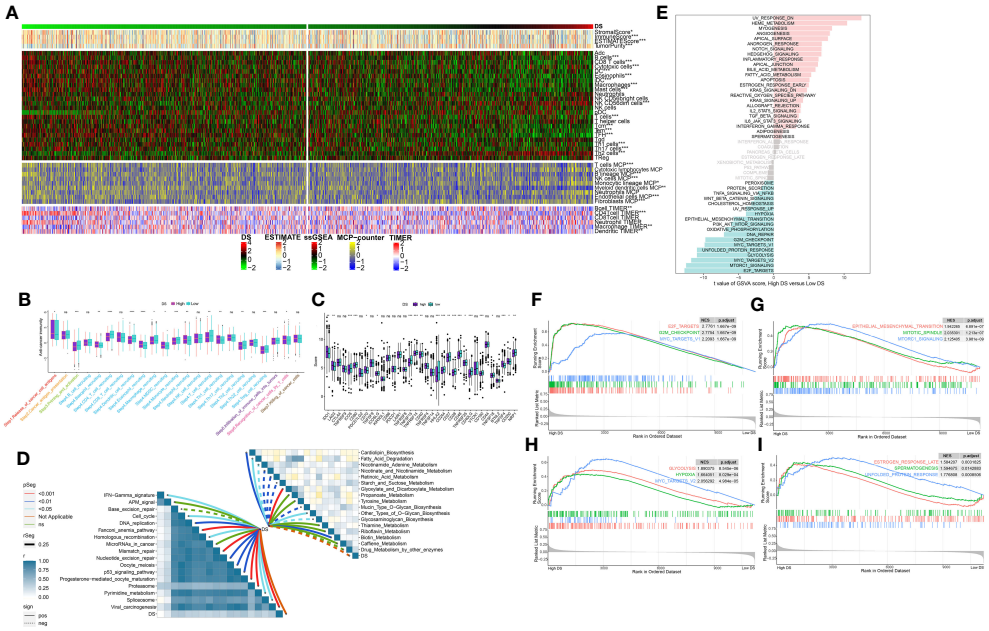

FIGURE 9
Analysis of the TME in different DS groups. **(A)** Differences in immune infiltration status between two DS groups were evaluated by four algorithms. **(B)** The differences of cancer immunity cycle were showed in boxplot between two DS groups. **(C)** The differences of immune checkpoint related genes were showed in boxplot between two DS groups. **(D)** The correlations between the TIIClnc signature score and metabolic immune-related pathways, immune-related pathways based on GSVA of GO and KEGG terms were displayed in butterfly plot. **(E)** The difference in the hallmark gene sets between different DS groups based on GSVA. **(F-I)** The GSEA results for the 12 overlapping upregulated hallmark pathways in terms of the high-DS group. *p < 0.05; **p < 0.01; ***p < 0.001; ****p < 0.0001; ns, not significant.

progression of LUAD involve complex biological mechanisms, such as a multitude of genetic and epigenetic modifications (40, 41). Numerous staging systems have been proposed and utilized for clinical determinations to predict patient prognoses; however, these systems predominantly rely on clinicopathological features, ignoring the critical influence of complex molecular pathogenic processes in the oncogenesis and progression of LUAD (42, 43). As a result, there have been negligible improvements in patient outcomes. Consequently, the identification of superior predictive biomarkers for treatment responsiveness and patient outcomes

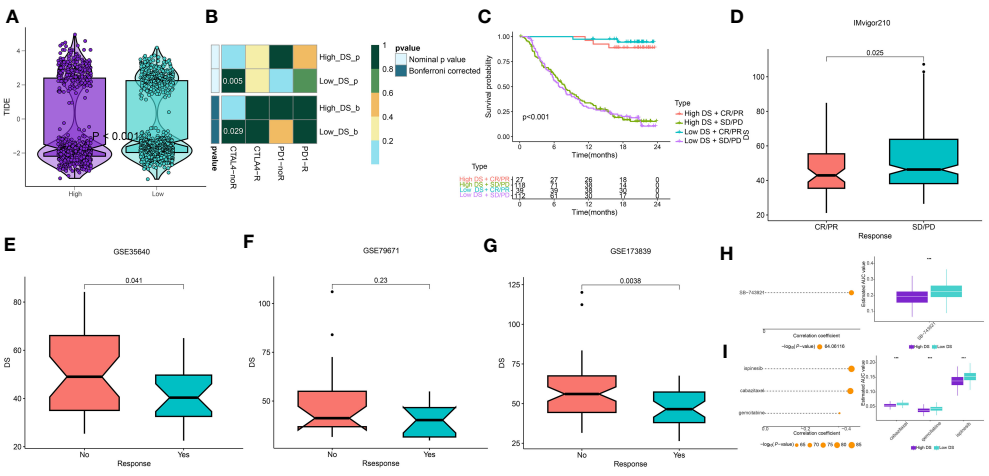

FIGURE 10
Prediction of immunotherapy and chemotherapy response. **(A)** A violin diagram illustrates the variance in TIDE scores among patients with diverse DS. **(B)** A comprehensive submap analysis of the meta-cohort and melanoma patients, inclusive of intricate immunotherapeutic data. **(C)** A Kaplan-Meier plot delineates the survival rates for patients categorized into high- and low-DS groups within the IMvigor cohort. **(D-G)** A box diagram depicts the disparity in DS among patients exhibiting immunotherapy responses in the IMvigor210, GSE35640, GSE79671, and GSE173839 cohorts. **(H, I)** The findings from the correlation study and differential drug response analysis of CTRP-derived pharmaceuticals and PRISM-derived pharmaceuticals are presented. ***P < 0.001.

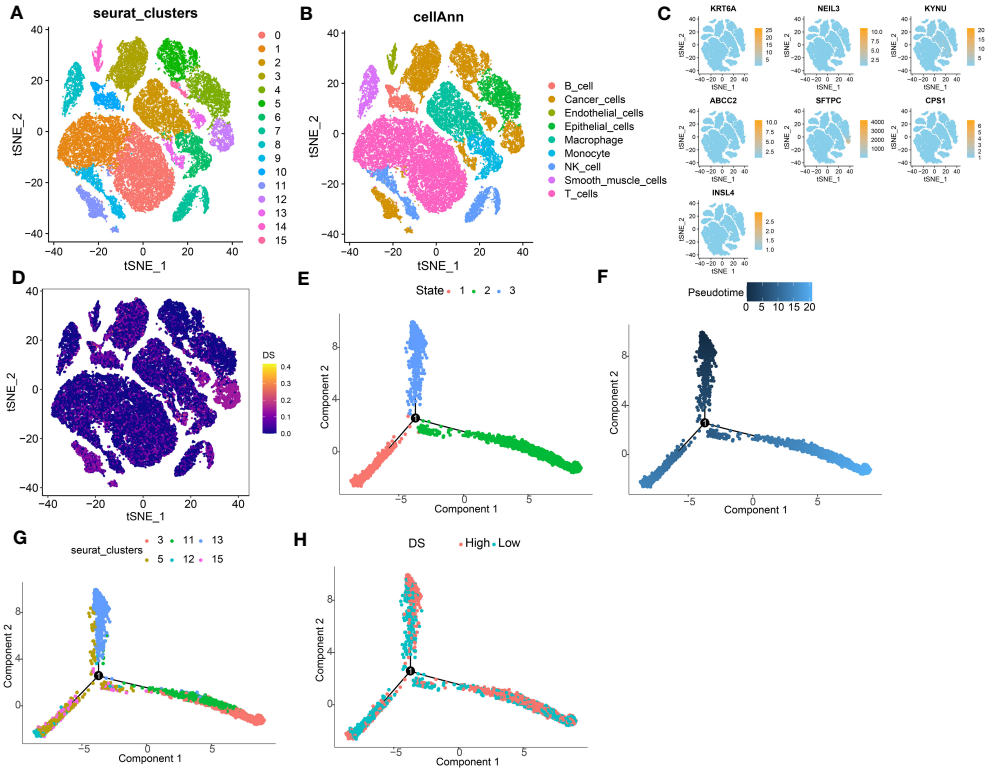

FIGURE 11
Exploration of DS in LUAD scRNA-seq data. **(A)** t-SNE plot colored by 16 cell subpopulations. **(B)** t-SNE plot of the distribution of 9 cell types. **(C, D)** Evaluation of DS gene expression and DS in scRNA-seq data in scRNA-seq data. **(E-H)** Pseudotime trajectory analysis in LUAD cells (Cells are colored based on states, pseudotime, cluster and DS groups.

could be advantageous in optimizing individualized therapeutic strategies and prognostic management for those afflicted with LUAD. Atypical accumulation of intracellular disulfides induces disulfide stress, which results in cellular toxicity and ultimately induces cell death (16, 44). Disulfide bonds are the most important redox-reactive covalent bonds between two cysteine residues within proteins. These bonds are regarded as cellular redox regulators and are intimately linked to the formation of disulfides. Recent studies have revealed that neoplastic cells may also experience disturbances in disulfide metabolism as a result of oxidative stress, a process that can potentially inhibit the proliferation of tumor cells and induce their apoptosis (45, 46). In addition, the disulfides inherent to neoplastic cells may act as conduits, modulating the responsiveness to chemotherapeutic agents and immunotherapy, and possibly serving as prognostic markers (47–79). This suggests that the application of disulfidptosis-focused translational medicine holds considerable promise as a candidate for clinical implementation across an array of human malignancies. Several DRs have been implicated in pathological and physiological processes of a variety of tumor. To counterbalance the oxidative stress induced by their heightened metabolic rate, tumor cells can upregulate the expression of the catalytic subunit SLC7A11 of the Xc−system, thereby maintaining high levels of glutathione (50). In addition, the overexpression of SLC7A11 in glioma cells improves their resistance to oxidative stress and decreases their sensitivity to temozolomide (51). In this regard, SLC3A2 is significantly upregulated in several types of malignant tumor cells, including those of the lung, breast, and prostate (52, 53). Furthermore, SLC3A2 is also an independent prognostic indicator for thymic epithelial tumors and NSCLC (54). Consequently, the overexpression of SLC3A2 contributes to radiotherapy resistance in tumors, indicating that SLC3A2 could surface as a promising clinical prospect in cancer treatment (55). Moreover, models composed of DRs have been established in certain tumor types, demonstrating their potential predictive value for patient prognosis and treatment efficacy (56, 57). These findings indicate that DRs have significant potential for elucidating the molecular mechanisms underlying LUAD and identifying novel biomarkers. Nonetheless, there is a dearth of pertinent research on how DRs influence prognosis, immune infiltration, and clinical response in LUAD.

In this study, we first analyzed the characteristics of DRs in LUAD, including extensive genetic and transcriptional level alterations. The majority of these genes are upregulated in LUAD patients and are associated with a poorer prognosis, suggesting a plausible role for DRs in the pathogenesis of LUAD. Using unsupervised clustering techniques on DRs transcriptomic expression data, we then divided LUAD patients from four distinct cohorts into two subgroups, designated DRcluster A and DRcluster B. In DRcluster B, the majority of DRs were significantly upregulated, indicating relatively active disulfidptosis. Compared to patients in DRcluster A, DRcluster B was associated with an increase in the number of immune cells that infiltrated the

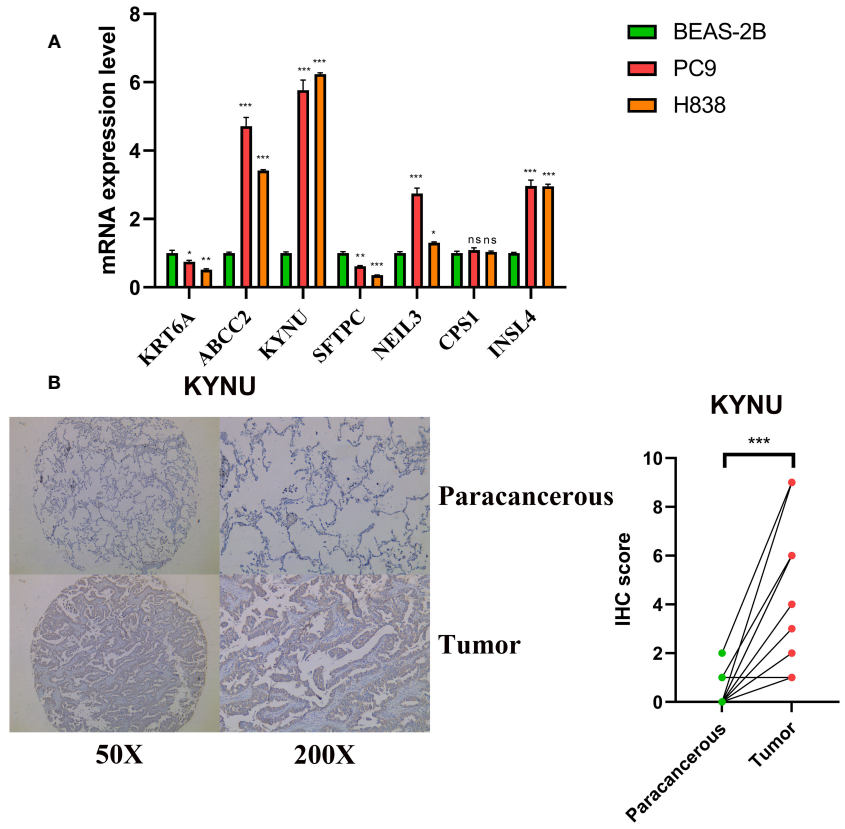

FIGURE 12
Validation of expression levels of DS genes. **(A)** DS genes expression in LUAD and normal cell lines. **(B)** Protein expression levels of KYNU were assessed by IHC. *p < 0.05; **p < 0.01; ***p < 0.001; ns, not significant.

affected tissue. Significant infiltration levels of effector immune cells are critical for a successful immunotherapeutic response. Typically, a higher CD8+ T cell infiltration rate is indicative of a better prognosis for survival. As evidence, a higher concentration of cytotoxic CD8+ T cells permeating the tumor has been linked to superior outcomes for patients with NSCLC (58). This is consistent with our prognosis and analysis results of immune infiltration. As a result, we proceeded to identify 86 DEGs that distinguished the two DRclusters, and based on these DEGs, we formed a pair of gene clusters. Intriguingly, we discovered statistically significant differences in OS, DRs, and TME between gene clusters, revealing a strong correlation between DRclusters and gene clusters. In light of the lack of DRclusters for clinical application and the paucity of biomarkers for prognosis tracking, we developed a robust and effective model by transforming 10 machine learning algorithms into more than 101 combinations and selecting the best performing algorithm determined by the mean C-index across four LUAD cohorts (59). This facilitated the creation of a robust and efficient DR-based prognostic model, suitable for appraising the prognosis of LUAD patients. Ultimately, the combination of LASSO and RSF was deemed the superior model for constructing the DS. Survival analysis utilizing the median value of the DS revealed its association with LUAD prognosis, and concordant results were obtained from three independent cohorts. The AUC at various time points and the C-index suggest that the DS has exceptional clinical efficacy, surpassing the performance of a substantial number of other clinical attributes. Significantly, when compared to the 56 previously reported molecular signatures for LUAD, the predictive performance of the DS is consistently superior in nearly all cohorts examined.

The composition of our DS comprises 7 genes, including KRT6A, NEIL3, KYNU, ABCC2, SFTPC, CPS1, and INSL4. In addition, qRT-PCR analysis revealed that LUAD and human bronchial epithelial cell expression of the majority of genes differed significantly. Numerous identified genes exhibit a strong correlation with the onset and advancement of LC. For instance, overexpression of KRT6A in NSCLC is associated with poor prognosis (60). KRT6A, acting downstream of LSD1, upregulates G6PD and the pentose phosphate pathway flux via the MYC signaling cascade, thereby promoting NSCLC growth and invasion (61). The upregulation of NEIL3 expression in NSCLC tissues and cell lines correlates with clinical progression and a poor prognosis. By partially activating the PI3K/AKT/mTOR signaling pathway, NEIL3 contributes to the progression of NSCLC (62). A recent study demonstrated that SFTPC expression is suppressed in human LUAD tissues and cell lines, and its overexpression inhibits LCcell proliferation *in vitro* and *in vivo* (63). INSL4, via autocrine or paracrine effects, promotes the proliferation and invasion of NSCLC by enhancing the MAPK and AKT signaling pathways. Moreover, INSL4 serves as a detrimental prognostic indicator for patients suffering from NSCLC. Among the

10.3389/fimmu.2023.1233260

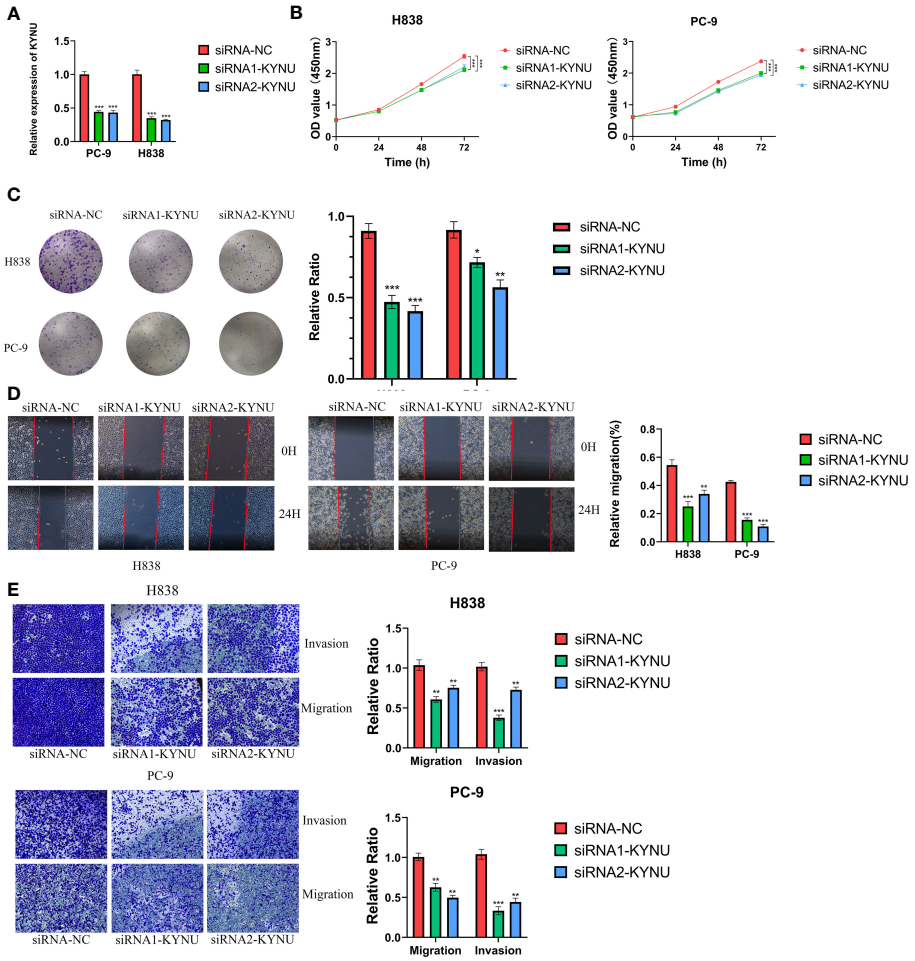

FIGURE 13
(A) The effect of siRNA to knockdown KYNU in LUAD cell lines was measured by RT–qPCR. **(B, C)** The CCK-8 and clone formation assays showed that knockdown of KYNU inhibited the proliferation of LUAD cells. **(D, E)** The wound healing and transwell assays showed that knockdown of KYNU inhibited the migration and invasion of LUAD cells. *P < 0.05; **P < 0.01; ***P < 0.001.

7 genes, IHC confirmed the elevated expression of KYNU in LUAD tissue samples, and the association between high KYNU expressions was notably associated with a shorter OS in the cohort. Moreover, cellular experiments suggest that the knockdown of KYNU can curb the proliferation, invasion, and migration capabilities of LUAD cells, suggesting its oncogenic role in LUAD.

TMB has recently emerged as a promising prognostic biomarker for numerous tumor types. A higher TMB is frequently associated with improved survival outcomes (9). For instance, a study of NSCLC patients revealed that those with elevated TMB levels experienced prolonged OS when subjected to PD-1/PD-L1 antibody therapy (64). In this study, LUAD patients with an escalated DS had elevated TMB. This could be the result of patient heterogeneity or a small sample size. Recently, the proliferation and efficacy of targeted immunotherapies have begun to transform the landscape of cancer treatment (65, 66). Given the complex interaction between the tumor immune microenvironment and host immune responses, there is an urgent need for predictive biomarkers that facilitate individualized therapy. Increased concentrations of CD8+ T cells in the tumor microenvironment correlate with an improved prognosis and increased survival rates among patients with NSCLC (67). Furthermore, the existence of dysfunctional CD8+ T cells within lung tumors and malignant pleural effusions has been documented, thereby diminishing their capacity to mount an effective antitumor response (68). In preclinical studies, NK cell-based therapies have demonstrated the ability to prevent the development of pulmonary metastases (69). Several studies demonstrate that extracorporeal stimulation of autologous Natural Killer (NK) cells with Interleukin-2 (IL-2) in conjunction with adoptive transfer and subcutaneous IL-2 infusions increased overall survival (OS) in a subset of patients with advanced cancers (70). Within the pulmonary environment, neoplasm-associated B lymphocytes can differentiate into plasma cells, thereby producing tumor-specific antibodies capable of recognizing and reacting to tumor-associated antigens (71). Accordingly, the presence of both follicular B cells and tumor-infiltrating plasma cells has been positively correlated with increased longevity in patients with NSCLC, highlighting the protective contribution of plasma cells and antibodies in combating tumor proliferation (72). Moreover, single-cell sequencing analysis

results indicate that high DS cells are primarily located in the tumor cell and B cell regions, suggesting a possible interaction between them. Consistent with previous findings, LUAD patients with a low DS demonstrated a high level of immune cell infiltration, including CD8 cells, NK cells, B cells, dendritic cells, mast cells, and central memory T cells, all of which play crucial roles in either bolster or counter tumor immunity during immunotherapy. Tumor cells characterized by reduced differentiation levels frequently demonstrate accelerated growth rates and heightened invasiveness, often correlating with unfavorable prognoses (73). Pseudotime analysis outcomes revealed a spatial disposition wherein tumor cells exhibiting diminished CDS levels occupied the initial phase of the differentiation trajectory. Conversely, those with elevated CDS levels were situated at the concluding stage of differentiation. Consequently, it becomes evident that CDS levels could potentially be linked to the extent of differentiation as well as invasiveness in tumor cells. In accordance with the tumor immunoediting hypothesis, the high-DS group exhibited greater immunosuppression but decreased immunoreactivity compared to the low-DS group (74). Disparities in the immune infiltrating microenvironment could potentially contribute to cancer progression and result in a poorer prognosis. Elevated IDO1 expression contributes to the development of an immunosuppressive TME by promoting T cell and NK cell inactivation and activating and expanding Tregs and DCs (75, 76). The role of IDO1-mediated tryptophan (TRP) metabolism in resistance to therapies targeting CTLA-4 or PD-1 demonstrates its potential as a promising target to augment existing immunotherapy approaches (77). CD40 is an essential co-stimulatory protein involved in the pro-inflammatory immune activation of antigen-presenting cells like dendritic cells and immunosuppressive macrophages within the cancer landscape (78, 79). Earlier investigations demonstrate that CD40 stimulation, in addition to activating tumor-associated immunosuppressive macrophages and T cells and inhibiting tumor progression (80, 81), also remodels the TME and heightens the tumor's responsiveness to checkpoint blockade therapies in various types of cancer (82, 83). The findings of the current study show that the expression of IDO1 was downregulated in the low-DS group relative to the high-DS group, while CD40 expression was upregulated. In addition, differences in the expression of other immune checkpoints between the two groups suggested immunotherapy would have divergent effects (84). To determine the degree of immunotherapy response in LUAD patients, we evaluated the TIDE and submap algorithms to discovered that low-DS individuals identified by the model may be suitable candidates for immune checkpoint blockade therapies targeting CTLA-4 and PD-1. The scores based on immunotherapy algorithm scores are merely a reflection of theoretical hypotheses and cannot represent the actual efficacy within actual cohorts. For a more comprehensive analysis of the predictive efficacy of DS in immunotherapy, we thus incorporated multiple immunotherapy cohorts. Thus, in predicting therapeutic responses within immunotherapy cohorts, DS exhibits a trend that is consistent with immunotherapy algorithms, as indicated by our findings. These results suggest that a lower DS score may be a potent indicator of immunotherapy response in patients with LUAD.

The efficacy of pharmaceutical interventions is closely correlated with drug sensitivity and individual variation, indicating that personalized therapies based on specific subtypes could reduce the prevalence of ineffective therapies among LUAD patients. An analysis of drug sensitivity differences among LUAD patients with varying DS revealed 4 pharmaceuticals with significantly divergent sensitivities. Subsequent sensitivity projections demonstrated that SB-743921, cabazitaxel, gemcitabine, and ispinesib could potentially serve as superior therapeutic options for individuals with a high DS. Through signaling pathways such as G2M_CHECKPOINT, DNA_REPAIR, and PI3K_AKT_MTOR_SIGNALING, some of these pharmaceuticals exert their antitumor effects, as revealed by our enrichment analyses. Cabazitaxel functions by closely interacting with microtubule proteins, resulting in the inhibition of their depolymerization and consequently the inhibition of cellular mitosis. This mechanism induces cell cycle cessation, resulting in the programmed death or apoptosis of neoplastic cells (85). Recent research revealed that cabazitaxel can induce G2/M phase block and autophagy in LUAD cells by inhibiting the PI3K-AKT-mTOR pathway, indicating its potential as a chemotherapy drug for LUAD patients (86). Gemcitabine is a pyrimidine nucleoside analogue antimetabolite that can inhibit the synthesis and repair of DNA, thereby inducing cellular autophagy and apoptosis (87). When used as a stand-alone treatment, gemcitabine has consistently demonstrated response rates greater than 20% while maintaining a favorable tolerability profile. Moreover, its therapeutic efficacy can be augmented through combination regimens with platinum-based compounds such as cisplatin, thereby synergistically enhancing its overall efficacy (88, 89).

Despite the use of potent open-source data to elucidate two distinct characteristics of LUAD disulfidptosis subtypes and to develop a robust DS evaluation model, this investigation is limited by certain factors. First, this study relies on patient data obtained from publicly available retrospective cohorts and lacks the prospective real-world data required to validate the clinical applicability of the proposed scoring system. In addition, due to financial and resource limitations, we conducted preliminary *in vitro* experiments to investigate the functionality of KYNU in LUAD. The further experimentation and investigation are required for a more complete comprehension of the molecular mechanisms. This study focuses on bioinformatics analysis and preliminary functional investigations to identify possible biomarkers. These limitations will be addressed in future research.

Conclusions

In conclusion, this study identified disulfidptosis-related subgroups and developed a DS for evaluating the prognosis, immune infiltration, mutations, and treatment sensitivity of LUAD patients. Studying disparities in disulfidptosis patterns has deepened our comprehension of both tumor heterogeneity and the intricate complexities within the TME. We have also constructed and validated a DS that accurately predicts patient prognosis and treatment efficacy assessment, offering a potentially powerful new tool for clinical decision-making, patient outcomes, and individualized treatment

strategies. Besides, this study has contributed to advancing the understanding of molecular complexity in LUAD and provides directions and potential avenues for future LUAD research.

Data availability statement

The datasets presented in this study can be found in online repositories. The names of the repository/repositories and accession number(s) can be found in the article/Supplementary Material.

Ethics statement

The studies involving humans were approved by Ethics Committee and Institutional Review Board of the Outdo Biotech. Co., Ltd. (SHYJS-CP-2210035). The studies were conducted in accordance with the local legislation and institutional requirements. The participants provided their written informed consent to participate in this study.

Author contributions

CY and YZ conceived and designed the study. CL and YW performed the collection and assembly of data. YX and CL analyzed the data. YZ and YW performed experiments and wrote the manuscript. All authors read and approved the final manuscript.

Acknowledgments

We thank Bullet Edits Limited for the linguistic editing and proofreading of the manuscript.

Conflict of interest

The authors declare that the research was conducted in the absence of any commercial or financial relationships that could be construed as a potential conflict of interest.

Publisher's note

Supplementary material

The Supplementary Material for this article can be found online at: https://www.frontiersin.org/articles/10.3389/fimmu.2023.1233260/full#supplementary-material

References

1. Torre LA, Bray F, Siegel RL, Ferlay J, Lortet-Tieulent J, Jemal A. Global cancer statistics, 2012. *CA Cancer J Clin* (2015) 65(2):87–108. doi: 10.3322/caac.21262

2. Siegel RL, Miller KD, Fuchs HE, Jemal A. Cancer statistics, 2022. *CA Cancer J Clin* (2022) 72(1):7–33. doi: 10.3322/caac.21708

3. Song C, Wu Z, Wang Q, Wang Y, Guo Z, Li S, et al. A combined two-mRNA signature associated with PD-L1 and tumor mutational burden for prognosis of lung adenocarcinoma. *Front Cell Dev Biol* (2021) 9:634697. doi: 10.3389/fcell.2021.634697

4. Reck M, Heigener DF, Mok T, Soria JC, Rabe KF. Management of non-small-cell lung cancer: recent developments. *Lancet* (2013) 382(9893):709–19. doi: 10.1016/s0140-6736(13)61502-0

5. Miller KD, Nogueira L, Devasia T, Mariotto AB, Yabroff KR, Jemal A, et al. Cancer treatment and survivorship statistics, 2022. *CA Cancer J Clin* (2022) 72(5):409–36. doi: 10.3322/caac.21731

6. Tower J. Programmed cell death in aging. *Ageing Res Rev* (2015) 23(Pt A):90–100. doi: 10.1016/j.arr.2015.04.002

7. Liang C, Zhang X, Yang M, Dong X. Recent progress in ferroptosis inducers for cancer therapy. *Adv Mater* (2019) 31(51):e1904197. doi: 10.1002/adma.201904197

8. Xie Y, Zhu S, Song X, Sun X, Fan Y, Liu J, et al. The tumor suppressor p53 limits ferroptosis by blocking DPP4 activity. *Cell Rep* (2017) 20(7):1692–704. doi: 10.1016/j.celrep.2017.07.055

9. Wang W, Green M, Choi JE, Gijón M, Kennedy PD, Johnson JK, et al. CD8(+) T cells regulate tumour ferroptosis during cancer immunotherapy. *Nature* (2019) 569(7755):270–4. doi: 10.1038/s41586-019-1170-y

10. Rangel M, Kong J, Bhatt V, Khayati K, Guo JY. Autophagy and tumorigenesis. *FEBS J* (2022) 289(22):7177–98. doi: 10.1111/febs.16125

11. Mulcahy Levy JM, Thorburn A. Autophagy in cancer: moving from understanding mechanism to improving therapy responses in patients. *Cell Death Differ* (2020) 27(3):843–57. doi: 10.1038/s41418-019-0474-7

12. Liu X, Nie L, Zhang Y, Yan Y, Wang C, Colic M, et al. Actin cytoskeleton vulnerability to disulfide stress mediates disulfidptosis. *Nat Cell Biol* (2023) 25(3):404–414. doi: 10.1038/s41556-023-01091-2

13. Shin CS, Mishra P, Watrous JD, Carelli V, D'Aurelio M, Jain M, et al. The glutamate/cystine xCT antiporter antagonizes glutamine metabolism and reduces nutrient flexibility. *Nat Commun* (2017) 8:15074. doi: 10.1038/ncomms15074

14. Koppula P, Zhang Y, Shi J, Li W, Gan B. The glutamate/cystine antiporter SLC7A11/xCT enhances cancer cell dependency on glucose by exporting glutamate. *J Biol Chem* (2017) 292(34):14240–9. doi: 10.1074/jbc.M117.798405

15. Goji T, Takahara K, Negishi M, Katoh H. Cystine uptake through the cystine/glutamate antiporter xCT triggers glioblastoma cell death under glucose deprivation. *J Biol Chem* (2017) 292(48):19721–32. doi: 10.1074/jbc.M117.814392

16. Liu X, Olszewski K, Zhang Y, Lim EW, Shi J, Zhang X, et al. Cystine transporter regulation of pentose phosphate pathway dependency and disulfide stress exposes a targetable metabolic vulnerability in cancer. *Nat Cell Biol* (2020) 22(4):476–86. doi: 10.1038/s41556-020-0496-x

17. Leek JT, Johnson WE, Parker HS, Jaffe AE, Storey JD. The sva package for removing batch effects and other unwanted variation in high-throughput experiments. *Bioinformatics* (2012) 28(6):882–3. doi: 10.1093/bioinformatics/bts034

18. Wilkerson MD, Hayes DN. ConsensusClusterPlus: a class discovery tool with confidence assessments and item tracking. *Bioinformatics* (2010) 26(12):1572–3. doi: 10.1093/bioinformatics/btq170

19. Ritchie ME, Phipson B, Wu D, Hu Y, Law CW, Shi W, et al. limma powers differential expression analyses for RNA-sequencing and microarray studies. *Nucleic Acids Res* (2015) 43(7):e47. doi: 10.1093/nar/gkv007

20. Yu G, Wang LG, Han Y, He QY. clusterProfiler: an R package for comparing biological themes among gene clusters. *Omics* (2012) 16(5):284–7. doi: 10.1089/omi.2011.0118

21. Binder H, Allignol A, Schumacher M, Beyersmann J. Boosting for high-dimensional time-to-event data with competing risks. *Bioinformatics* (2009) 25 (7):890–6. doi: 10.1093/bioinformatics/btp088

22. Bair E, Tibshirani R. Semi-supervised methods to predict patient survival from gene expression data. *PloS Biol* (2004) 2(4):E108. doi: 10.1371/journal.pbio.0020108

23. Mayakonda A, Lin DC, Assenov Y, Plass C, Koeffler HP. Maftools: efficient and comprehensive analysis of somatic variants in cancer. *Genome Res* (2018) 28(11):1747–56. doi: 10.1101/gr.239244.118

24. Mermel CH, Schumacher SE, Hill B, Meyerson ML, Beroukhim R, Getz G. GISTIC2.0 facilitates sensitive and confident localization of the targets of focal somatic copy-number alteration in human cancers. *Genome Biol* (2011) 12(4):R41. doi: 10.1186/gb-2011-12-4-r41

25. Chakraborty H, Hossain A. R package to estimate intracluster correlation coefficient with confidence interval for binary data. *Comput Methods Programs BioMed* (2018) 155:85–92. doi: 10.1016/j.cmpb.2017.10.023

26. Charoentong P, Finotello F, Angelova M, Mayer C, Efremova M, Rieder D, et al. Pan-cancer immunogenomic analyses reveal genotype-immunophenotype relationships and predictors of response to checkpoint blockade. *Cell Rep* (2017) 18 (1):248–62. doi: 10.1016/j.celrep.2016.12.019

27. Becht E, Giraldo NA, Lacroix L, Buttard B, Elarouci N, Petitprez F, et al. Estimating the population abundance of tissue-infiltrating immune and stromal cell populations using gene expression. *Genome Biol* (2016) 17(1):218. doi: 10.1186/s13059-016-1070-5

28. Bindea G, Mlecnik B, Tosolini M, Kirilovsky A, Waldner M, Obenauf AC, et al. Spatiotemporal dynamics of intratumoral immune cells reveal the immune landscape in human cancer. *Immunity* (2013) 39(4):782–95. doi: 10.1016/j.immuni.2013.10.003

29. Xu L, Deng C, Pang B, Zhang X, Liu W, Liao G, et al. TIP: A web server for resolving tumor immunophenotype profiling. *Cancer Res* (2018) 78(23):6575–80. doi: 10.1158/0008-5472.Can-18-0689

30. Subramanian A, Tamayo P, Mootha VK, Mukherjee S, Ebert BL, Gillette MA, et al. Gene set enrichment analysis: a knowledge-based approach for interpreting genome-wide expression profiles. *Proc Natl Acad Sci U.S.A.* (2005) 102(43):15545–50. doi: 10.1073/pnas.0506580102

31. Hänzelmann S, Castelo R, Guinney J. GSVA: gene set variation analysis for microarray and RNA-seq data. *BMC Bioinf* (2013) 14:7. doi: 10.1186/1471-2105-14-7

32. Jiang P, Gu S, Pan D, Fu J, Sahu A, Hu X, et al. Signatures of T cell dysfunction and exclusion predict cancer immunotherapy response. *Nat Med* (2018) 24(10):1550–8. doi: 10.1038/s41591-018-0136-1

33. Roh W, Chen PL, Reuben A, Spencer CN, Prieto PA, Miller JP, et al. Integrated molecular analysis of tumor biopsies on sequential CTLA-4 and PD-1 blockade reveals markers of response and resistance. *Sci Transl Med* (2017) 9(379):eaah3560. doi: 10.1126/scitranslmed.aah3560

34. Stuart T, Butler A, Hoffman P, Hafemeister C, Papalexi E, Mauck WM3, et al. Comprehensive integration of single-cell data. *Cell* (2019) 177(7):1888–1902.e21. doi: 10.1016/j.cell.2019.05.031

35. Aran D, Looney AP, Liu L, Wu E, Fong V, Hsu A, et al. Reference-based analysis of lung single-cell sequencing reveals a transitional profibrotic macrophage. *Nat Immunol* (2019) 20(2):163–72. doi: 10.1038/s41590-018-0276-y

36. Gao R, Bai S, Henderson YC, Lin Y, Schalck A, Yan Y, et al. Delineating copy number and clonal substructure in human tumors from single-cell transcriptomes. *Nat Biotechnol* (2021) 39(5):599–608. doi: 10.1038/s41587-020-00795-2

37. Qiu X, Mao Q, Tang Y, Wang L, Chawla R, Pliner HA, et al. Reversed graph embedding resolves complex single-cell trajectories. *Nat Methods* (2017) 14(10):979–82. doi: 10.1038/nmeth.4402

38. Allred DC, Harvey JM, Berardo M, Clark GM. Prognostic and predictive factors in breast cancer by immunohistochemical analysis. *Mod Pathol* (1998) 11(2):155–68.

39. Yang D, Liu Y, Bai C, Wang X, Powell CA. Epidemiology of lung cancer and lung cancer screening programs in China and the United States. *Cancer Lett* (2020) 468:82–7. doi: 10.1016/j.canlet.2019.10.009

40. Kabbout M, Garcia MM, Fujimoto J, Liu DD, Woods D, Chow CW, et al. ETS2 mediated tumor suppressive function and MET oncogene inhibition in human non-small cell lung cancer. *Clin Cancer Res* (2013) 19(13):3383–95. doi: 10.1158/1078-0432.Ccr-13-0341

41. Saji H, Tsuboi M, Shimada Y, Kato Y, Hamanaka W, Kudo Y, et al. Gene expression profiling and molecular pathway analysis for the identification of early-stage lung adenocarcinoma patients at risk for early recurrence. *Oncol Rep* (2013) 29 (5):1902–6. doi: 10.3892/or.2013.2332

42. Westaway DD, Toon CW, Farzin M, Sioson L, Watson N, Brady PW, et al. The International Association for the Study of Lung Cancer/American Thoracic Society/ European Respiratory Society grading system has limited prognostic significance in advanced resected pulmonary adenocarcinoma. *Pathology* (2013) 45(6):553–8. doi: 10.1097/PAT.0b013e32836532ae

43. Rosell R, Carcereny E, Gervais R, Vergnenegre A, Massuti B, Felip E, et al. Erlotinib versus standard chemotherapy as first-line treatment for European patients with advanced EGFR mutation-positive non-small-cell lung cancer (EURTAC): a multicentre, open-label, randomised phase 3 trial. *Lancet Oncol* (2012) 13(3):239–46. doi: 10.1016/s1470-2045(11)70393-x

44. Joly JH, Delfarah A, Phung PS, Parrish S, Graham NA. A synthetic lethal drug combination mimics glucose deprivation-induced cancer cell death in the presence of glucose. *J Biol Chem* (2020) 295(5):1350–65. doi: 10.1074/jbc.RA119.011471

45. Hogg PJ. Biological regulation through protein disulfide bond cleavage. *Redox Rep* (2002) 7(2):71–7. doi: 10.1179/135100002125000299

46. Daly EB, Wind T, Jiang XM, Sun L, Hogg PJ. Secretion of phosphoglycerate kinase from tumour cells is controlled by oxygen-sensing hydroxylases. *Biochim Biophys Acta* (2004) 1691(1):17–22. doi: 10.1016/j.bbamcr.2003.11.004

47. Zhang S, Guo N, Wan G, Zhang T, Li C, Wang Y, et al. pH and redox dual-responsive nanoparticles based on disulfide-containing poly(β-amino ester) for combining chemotherapy and COX-2 inhibitor to overcome drug resistance in breast cancer. *J Nanobiotechnol* (2019) 17(1):109. doi: 10.1186/s12951-019-0540-9

48. Zhang W, Quan Y, Ma X, Zeng L, Li J, Chen S, et al. Synergistic effect of glutathione and IgG4 in immune evasion and the implication for cancer immunotherapy. *Redox Biol* (2023) 60:102608. doi: 10.1016/j.redox.2023.102608

49. Karatas F, Acat M, Sahin S, Inci F, Karatas G, Neselioglu S, et al. The prognostic and predictive significance of serum thiols and disulfide levels in advanced non-small cell lung cancer. *Aging Male* (2020) 23(5):619–28. doi: 10.1080/13685538.2018.1559805

50. Koppula P, Zhuang L, Gan B. Cystine transporter SLC7A11/xCT in cancer: ferroptosis, nutrient dependency, and cancer therapy. *Protein Cell* (2021) 12(8):599–620. doi: 10.1007/s13238-020-00789-5

51. Polewski MD, Reveron-Thornton RF, Cherryholmes GA, Marinov GK, Aboody KS. SLC7A11 overexpression in glioblastoma is associated with increased cancer stem cell-like properties. *Stem Cells Dev* (2017) 26(17):1236–46. doi: 10.1089/scd.2017.0123

52. Digomann D, Kurth I, Tyutyunnykova A, Chen O, Löck S, Gorodetska I, et al. The CD98 heavy chain is a marker and regulator of head and neck squamous cell carcinoma radiosensitivity. *Clin Cancer Res* (2019) 25(10):3152–63. doi: 10.1158/1078-0432.Ccr-18-2951

53. Hasegawa K, Ikeda S, Yaga M, Watanabe K, Urakawa R, Iehara A, et al. Selective targeting of multiple myeloma cells with a monoclonal antibody recognizing the ubiquitous protein CD98 heavy chain. *Sci Transl Med* (2022) 14(632):eaax7706. doi: 10.1126/scitranslmed.aax7706

54. Kanai Y. Amino acid transporter LAT1 (SLC7A5) as a molecular target for cancer diagnosis and therapeutics. *Pharmacol Ther* (2022) 230:107964. doi: 10.1016/j.pharmthera.2021.107964

55. Bajaj J, Konuma T, Lytle NK, Kwon HY, Ablack JN, Cantor JM, et al. CD98-mediated adhesive signaling enables the establishment and propagation of acute myelogenous leukemia. *Cancer Cell* (2016) 30(5):792–805. doi: 10.1016/j.ccell.2016.10.003

56. Zhao S, Wang L, Ding W, Ye B, Cheng C, Shao J, et al. Crosstalk of disulfidptosis-related subtypes, establishment of a prognostic signature and immune infiltration characteristics in bladder cancer based on a machine learning survival framework. *Front Endocrinol (Lausanne)* (2023) 14:1180404. doi: 10.3389/fendo.2023.1180404

57. Wang T, Guo K, Zhang D, Wang H, Yin J, Cui H, et al. Disulfidptosis classification of hepatocellular carcinoma reveals correlation with clinical prognosis and immune profile. *Int Immunopharmacol* (2023) 120:110368. doi: 10.1016/j.intimp.2023.110368

58. Barnes TA, Amir E. HYPE or HOPE: the prognostic value of infiltrating immune cells in cancer. *Br J Cancer* (2017) 117(4):451–60. doi: 10.1038/bjc.2017.220

59. Liu Z, Liu L, Weng S, Guo C, Dang Q, Xu H, et al. Machine learning-based integration develops an immune-derived lncRNA signature for improving outcomes in colorectal cancer. *Nat Commun* (2022) 13(1):816. doi: 10.1038/s41467-022-28421-6

60. Xiao J, Lu X, Chen X, Zou Y, Liu A, Li W, et al. Eight potential biomarkers for distinguishing between lung adenocarcinoma and squamous cell carcinoma. *Oncotarget* (2017) 8(42):71759–71. doi: 10.18632/oncotarget.17606

61. Che D, Wang M, Sun J, Li B, Xu T, Lu Y, et al. KRT6A promotes lung cancer cell growth and invasion through MYC-regulated pentose phosphate pathway. *Front Cell Dev Biol* (2021) 9:694071. doi: 10.3389/fcell.2021.694071

62. Huang H, Hua Q. NEIL3 mediates lung cancer progression and modulates PI3K/AKT/mTOR signaling: A potential therapeutic target. *Int J Genomics* (2022) 2022:8348499. doi: 10.1155/2022/8348499

63. Li B, Meng YQ, Li Z, Yin C, Lin JP, Zhu DJ, et al. MiR-629-3p-induced downregulation of SFTPC promotes cell proliferation and predicts poor survival in lung adenocarcinoma. *Artif Cells Nanomed Biotechnol* (2019) 47(1):3286–96. doi: 10.1080/21691401.2019.1648283

64. Rizvi NA, Hellmann MD, Snyder A, Kvistborg P, Makarov V, Havel JJ, et al. Cancer immunology. Mutational landscape determines sensitivity to PD-1 blockade in non-small cell lung cancer. *Science* (2015) 348(6230):124–8. doi: 10.1126/science.aaa1348

65. Zhou F, Qiao M, Zhou C. The cutting-edge progress of immune-checkpoint blockade in lung cancer. *Cell Mol Immunol* (2021) 18(2):279–93. doi: 10.1038/s41423-020-00577-5

66. Bejarano L, Jordão MJC, Joyce JA. Therapeutic targeting of the tumor microenvironment. *Cancer Discovery* (2021) 11(4):933–59. doi: 10.1158/2159-8290.Cd-20-1808

67. Fumet JD, Richard C, Ledys F, Klopfenstein Q, Joubert P, Routy B, et al. Prognostic and predictive role of CD8 and PD-L1 determination in lung tumor tissue of patients under anti-PD-1 therapy. *Br J Cancer* (2018) 119(8):950–60. doi: 10.1038/s41416-018-0220-9

68. Prado-Garcia H, Romero-Garcia S, Aguilar-Cazares D, Meneses-Flores M, Lopez-Gonzalez JS. Tumor-induced CD8+ T-cell dysfunction in lung cancer patients. *Clin Dev Immunol* (2012) 2012:741741. doi: 10.1155/2012/741741

69. Kim S, Iizuka K, Aguila HL, Weissman IL, Yokoyama WM. *In vivo* natural killer cell activities revealed by natural killer cell-deficient mice. *Proc Natl Acad Sci U.S.A.* (2000) 97(6):2731–6. doi: 10.1073/pnas.050588297

70. Rosenberg SA, Lotze MT, Yang JC, Topalian SL, Chang AE, Schwartzentruber DJ, et al. Prospective randomized trial of high-dose interleukin-2 alone or in conjunction with lymphokine-activated killer cells for the treatment of patients with advanced cancer. *J Natl Cancer Inst* (1993) 85(8):622–32. doi: 10.1093/jnci/85.8.622

71. Germain C, Gnjatic S, Tamzalit F, Knockaert S, Remark R, Goc J, et al. Presence of B cells in tertiary lymphoid structures is associated with a protective immunity in patients with lung cancer. *Am J Respir Crit Care Med* (2014) 189(7):832–44. doi: 10.1164/rccm.201309-1611OC

72. Lohr M, Edlund K, Botling J, Hammad S, Hellwig B, Othman A, et al. The prognostic relevance of tumour-infiltrating plasma cells and immunoglobulin kappa C indicates an important role of the humoral immune response in non-small cell lung cancer. *Cancer Lett* (2013) 333(2):222–8. doi: 10.1016/j.canlet.2013.01.036

73. Ana Kátia S, Teixeira JL, Vasconcelos A. Histopathological profile of patients diagnosed with Malignant tumors assisted in a hospital of reference of Agreste Pernambucano. *Jornal Brasileiro Patologia e Medicina Laboratorial* (2019) 55(1). doi: 10.5935/1676-2444.20190002

74. Hellmann MD, Nathanson T, Rizvi H, Creelan BC, Sanchez-Vega F, Ahuja A, et al. Genomic features of response to combination immunotherapy in patients with advanced non-small-cell lung cancer. *Cancer Cell* (2018) 33(5):843–852.e4. doi: 10.1016/j.ccell.2018.03.018

75. Frumento G, Rotondo R, Tonetti M, Damonte G, Benatti U, Ferrara GB. Tryptophan-derived catabolites are responsible for inhibition of T and natural killer cell proliferation induced by indoleamine 2,3-dioxygenase. *J Exp Med* (2002) 196 (4):459–68. doi: 10.1084/jem.20020121

76. Mellor AL, Keskin DB, Johnson T, Chandler P, Munn DH. Cells expressing indoleamine 2,3-dioxygenase inhibit T cell responses. *J Immunol* (2002) 168(8):3771–6. doi: 10.4049/jimmunol.168.8.3771

77. Holmgaard RB, Zamarin D, Munn DH, Wolchok JD, Allison JP. Indoleamine 2,3-dioxygenase is a critical resistance mechanism in antitumor T cell immunotherapy targeting CTLA-4. *J Exp Med* (2013) 210(7):1389–402. doi: 10.1084/jem.20130066

78. Alexandroff AB, Jackson AM, Paterson T, Haley JL, Ross JA, Longo DL, et al. Role for CD40-CD40 ligand interactions in the immune response to solid tumours. *Mol Immunol* (2000) 37(9):515–26. doi: 10.1016/s0161-5890(00)00079-1

79. Vonderheide RH. CD40 agonist antibodies in cancer immunotherapy. *Annu Rev Med* (2020) 71:47–58. doi: 10.1146/annurev-med-062518-045435

80. von Leoprechting A, van der Bruggen P, Pahl HL, Aruffo A, Simon JC. Stimulation of CD40 on immunogenic human Malignant melanomas augments their cytotoxic T lymphocyte-mediated lysis and induces apoptosis. *Cancer Res* (1999) 59 (6):1287–94.

81. French RR, Chan HT, Tutt AL, Glennie MJ. CD40 antibody evokes a cytotoxic T-cell response that eradicates lymphoma and bypasses T-cell help. *Nat Med* (1999) 5 (5):548–53. doi: 10.1038/8426

82. Ma HS, Poudel B, Torres ER, Sidhom JW, Robinson TM, Christmas B, et al. A CD40 agonist and PD-1 antagonist antibody reprogram the microenvironment of nonimmunogenic tumors to allow T-cell-mediated anticancer activity. *Cancer Immunol Res* (2019) 7(3):428–42. doi: 10.1158/2326-6066.Cir-18-0061

83. Zhang J, Li Y, Yang S, Zhang L, Wang W. Anti-CD40 mAb enhanced efficacy of anti-PD1 against osteosarcoma. *J Bone Oncol* (2019) 17:100245. doi: 10.1016/j.jbo.2019.100245

84. Hiam-Galvez KJ, Allen BM, Spitzer MH. Systemic immunity in cancer. *Nat Rev Cancer* (2021) 21(6):345–59. doi: 10.1038/s41568-021-00347-z

85. Mellado B, Jimenez N, Marin-Aguilera M, Reig O. Diving into cabazitaxel's mode of action: more than a taxane for the treatment of castration-resistant prostate cancer patients. *Clin Genitourin Cancer* (2016) 14(4):265–70. doi: 10.1016/j.clgc.2015.12.030

86. Huo R, Wang L, Liu P, Zhao Y, Zhang C, Bai B, et al. Cabazitaxel-induced autophagy via the PI3K/Akt/mTOR pathway contributes to A549 cell death. *Mol Med Rep* (2016) 14(4):3013–20. doi: 10.3892/mmr.2016.5648

87. Noble S, Goa KL. Gemcitabine. A review of its pharmacology and clinical potential in non-small cell lung cancer and pancreatic cancer. *Drugs* (1997) 54(3):447–72. doi: 10.2165/00003495-199754030-00009

88. Crinò L, Cappuzzo F. Gemcitabine in non-small cell lung cancer. *Expert Opin Pharmacother* (2002) 3(6):745–53. doi: 10.1517/14656566.3.6.745

89. Johnson DH. Gemcitabine for the treatment of non-small-cell lung cancer. *Oncol (Williston Park)* (2001) 15(3 Suppl 6):33–9.

frontiers | Frontiers in Immunology

TYPE Original Research
PUBLISHED 10 November 2023
DOI 10.3389/fimmu.2023.1290968

OPEN ACCESS

EDITED BY
Ines Zidi,
Tunis El Manar University, Tunisia

REVIEWED BY
H. Atakan Ekiz,
Izmir Institute of Technology, Türkiye
Yongxing Lai,
Fujian Medical University, China

*CORRESPONDENCE
Wenzhou Zhang
hnzzzwzx@sina.com
Wenping Song
songwp920@163.com

†These authors have contributed equally to this work

RECEIVED 08 September 2023
ACCEPTED 27 October 2023
PUBLISHED 10 November 2023

CITATION
Li D, Wu X, Cheng C, Liang J, Liang Y, Li H, Guo X, Li R, Zhang W and Song W (2023) A novel prognostic classification integrating lipid metabolism and immune co-related genes in acute myeloid leukemia. *Front. Immunol.* 14:1290968. doi: 10.3389/fimmu.2023.1290968

A novel prognostic classification integrating lipid metabolism and immune co-related genes in acute myeloid leukemia

Ding Li[1,2,3†], Xuan Wu[4,5†], Cheng Cheng[5†], Jiaming Liang[6], Yinfeng Liang[5], Han Li[5], Xiaohan Guo[5], Ruchun Li[5], Wenzhou Zhang[1,2,3*] and Wenping Song[1,2,3*]

[1]Department of Pharmacy, The Affiliated Cancer Hospital of Zhengzhou University and Henan Cancer Hospital, Zhengzhou, China, [2]Henan Engineering Research Center for Tumor Precision Medicine and Comprehensive Evaluation, Henan Cancer Hospital, Zhengzhou, China, [3]Henan Provincial Key Laboratory of Anticancer Drug Research, Henan Cancer Hospital, Zhengzhou, China, [4]Academy of Medical Science, Zhengzhou University, Zhengzhou, China, [5]Department of Internal Medicine, Affiliated Cancer Hospital of Zhengzhou University, Henan Cancer Hospital, Zhengzhou, China, [6]Department of Medicine, The Second Affiliated Hospital of Guangzhou Medical University, Guangzhou, China

Background: As a severe hematological malignancy in adults, acute myeloid leukemia (AML) is characterized by high heterogeneity and complexity. Emerging evidence highlights the importance of the tumor immune microenvironment and lipid metabolism in cancer progression. In this study, we comprehensively evaluated the expression profiles of genes related to lipid metabolism and immune modifications to develop a prognostic risk signature for AML.

Methods: First, we extracted the mRNA expression profiles of bone marrow samples from an AML cohort from The Cancer Genome Atlas database and employed Cox regression analysis to select prognostic hub genes associated with lipid metabolism and immunity. We then constructed a prognostic signature with hub genes significantly related to survival and validated the stability and robustness of the prognostic signature using three external datasets. Gene Set Enrichment Analysis was implemented to explore the underlying biological pathways related to the risk signature. Finally, the correlation between signature, immunity, and drug sensitivity was explored.

Results: Eight genes were identified from the analysis and verified in the clinical samples, including *APOBEC3C*, *MSMO1*, *ATP13A2*, *SMPDL3B*, *PLA2G4A*, *TNFSF15*, *IL2RA*, and *HGF*, to develop a risk-scoring model that effectively stratified patients with AML into low- and high-risk groups, demonstrating significant differences in survival time. The risk signature was negatively related to immune cell infiltration. Samples with AML in the low-risk group, as defined by the risk signature, were more likely to be responsive to immunotherapy, whereas those at high risk responded better to specific targeted drugs.

Conclusions: This study reveals the significant role of lipid metabolism- and immune-related genes in prognosis and demonstrated the utility of these signature genes as reliable bioinformatic indicators for predicting survival in

patients with AML. The risk-scoring model based on these prognostic signature genes holds promise as a valuable tool for individualized treatment decision-making, providing valuable insights for improving patient prognosis and treatment outcomes in AML.

KEYWORDS

acute myeloid leukemia, lipid metabolism, immunotherapy, drug sensitivity, prognostic signature

1 Introduction

Acute myeloid leukemia (AML) is characterized by a clinically, epigenetically, and genetically heterogeneous disease with poor outcomes (1). Despite being initially sensitive to chemotherapy, most patients with AML ultimately experience relapse and die of progressive disease. Therefore, there is an urgent need for alternative treatment solutions. Advances in epigenomic and genomic characterization of AML have paved the way for the development and approval of novel targeted agents (2). Immunotherapy is also a promising strategy for long-term disease control. However, acquired resistance to targeted agents and a low response to immunotherapy still cause treatment failure (3). Thus, novel therapeutic targets and prognostic biomarkers are urgently required to guide clinical practice and predict the survival of patients with AML.

Emerging evidence suggests that metabolic disruptions, particularly those involving certain metabolites and associated pathways, are crucial factors in the development and progression of leukemia. Lipids and their derivatives play critical roles in energy generation and form the structural basis of cellular and organelle membranes. Extensive research conducted over numerous years has explored the impact of lipid metabolism on AML, leading to recent breakthroughs (4). As a lipid category, fatty acids represent an appealing therapeutic target that supports increased biomass, membrane biogenesis, energy production, and lipoprotein generation in dividing AML cells (5). AML is associated with the overexpression and constant activation of sphingosine kinase 1, an enzyme responsible for producing sphingosine 1-phosphate from sphingosine. Remarkably, the inhibition of sphingosine kinase 1 induces apoptosis in AML blasts and leukemic stem cells obtained from patients (6, 7). Consequently, control of lipid metabolism reprogramming has emerged as a promising therapeutic target for enhancing the prognosis of individuals diagnosed with AML. Therefore, we previously constructed a prognostic signature with high specificity and sensitivity for estimating the prognosis of AML patients based on lipid metabolism-related genes (LMRGs) (8). The findings showed that the risk signature had remarkable specificity and sensitivity in estimating the outcomes of AML patients. And, consistent with the findings of other studies, interventions aimed at modulating lipid metabolism have the potential to impact not only tumor cells, but also immune cells (9, 10). We found that the lipid metabolism-related risk signature was closely associated with the immune tumor microenvironment (TME) and response to immunotherapy in AML.

As is same to solid tumor cells, AML cells are capable of developing an immunosuppressive microenvironment in which both adaptive and innate immune responses are profoundly disrupted (11, 12). Emerging evidence indicates that lipids are crucial for driving this dysregulated state. In acidic, hypoxic, and nutrition-deficient TMEs, both the cancer and immune cells tend to depend on the lipids for energy storage, building cellular membranes, and generating signaling molecules. Consequently, the dysregulation of lipid metabolism within the TME can have a profound impact on tumorigenesis, subsequent progression, and metastasis. Within this complex TME, lipids act as double-edged swords capable of either supporting antitumor or promoting pro-tumor immune responses (9, 12). These contradictory results present a dilemma, as simply inhibiting or stimulating a single lipid metabolic pathway within the TME fails to achieve optimal results. The models constructed with a single feature exhibited relatively weaker validity and robustness than those constructed with multiple features. Therefore, there is an urgent need for a comprehensive understanding of a multi-featured signature model specifically tailored for patients with AML, along with an exploration of its prognostic implications.

In this study, we integrated genes related to immunity and lipid metabolism to develop a prognostic signature based on the interactions between antitumor immunity and lipid metabolism.

2 Materials and methods

2.1 Data collection and preparation

The clinical data and RNA-sequencing profile of the patients with AML (Supplementary Table 1) came from The Cancer Genome Atlas (TCGA) database (https://www.cancer.gov/tcga/). Prior to analysis, all transcriptome data for fragments per kilobase of transcript per million mapped reads were log-transformed and subsequently converted to transcripts per million. Baseline features of the AML patients involved in the risk signature are displayed in Supplementary Table 2.

Abbreviations: AML, acute myeloid leukemia; GSEA, Gene Set Enrichment Analysis; IRG, immune-related gene; LMRG, lipid metabolism-related gene; OS, overall survival; exp, expression; ROC, receiver operating characteristic; TCGA, The Cancer Genome Atlas; TIDE, tumor immune dysfunction and exclusion.

For external validation, three independent datasets (GSE12417, GSE37642, and GSE71014) along with the clinical data were acquired from the GEO database, available at https://www.ncbi.nlm.nih.gov/geo/.

2.2 Identification of immune- and lipid metabolism-related prognostic genes

Here, we incorporated a comprehensive approach to identify genes associated with lipid metabolism. Specifically, we included all genes from 34 LMRG sets sourced from the Molecular Signature Database (MsigDB; available at https://www.gsea-msigdb.org/gsea/msigdb/) (13). By considering the intersection of these gene sets, we derived a final set of 1,996 LMRGs. For detailed information regarding the LMRG sets, please refer to Supplementary Table 3. A collection of 1,793 immune-related genes was acquired from the ImmPort database, available at https://www.immport.org/ (14). Details of the immune-related genes (IRGs) are displayed in Supplementary Table 4. The integration of LMRGs and IRGs was performed to conduct a prognostic analysis of AML, and 180 prognostic genes ($p < 0.01$) were acquired for the subsequent analyses.

2.3 Development and validation of a prognostic lipid metabolism and immune co-related signature

A total of 144 samples from the AML cohort in the TCGA database were then randomly divided into the training (N = 72) and validation (N = 72) datasets in a 1:1 ratio. First, we used univariate Cox regression to identify LMRGs and IRGs with prognostic role in the training dataset. Then, least absolute shrinkage and selection operator (LASSO) Cox regression analysis with the R package (version 3.6.1) "glmnet," a novel risk-scoring model with eight genes was developed as follows:

Risk score = expAPOBEC3C × 0.188873061 + expMSMO1 × 0.176721847 + expATP13A2 × 0.096045519 + expSMPDL3B × 0.077828708 + expPLA2G4A × 0.071836509 + expTNFSF15 × 0.027983123 + expIL2RA × 0.022815855 – expHGF × 0.044508523

Subsequently, patients with AML in the training dataset were classified into low-risk group and the high-risk group by the median cutoff risk score. The Kaplan-Meier survival curve was performed to compare the differences between the two risk groups. The receiver operating characteristic (ROC) curves were constructed to assess the validity of the risk signature.

The validity of the risk signature was verified using samples from the GSE12417, GSE37642, and GSE71014 cohorts. The same analyses used for the training dataset were used to calculate the risk scores of samples from the GEO cohorts.

2.4 Clinical correlation and subgroup analyses

To assess the clinical significance and prognostic utility of the risk signature, we extracted the clinical data of 144 patients with AML in the TCGA database, and these variables included age (>= 60 years or < 60 years), gender (female or male), chromosome status (normal or abnormal), and gene mutation (FLT3, NPM1, RAS, and IDH1 mutation or not) (Supplementary Table 5). Then, Kaplan–Meier curves were initially generated to explore the prognostic role of each gene included in the risk signature (15).

2.5 Functional enrichment analysis

The TCGA database contained genomic data from 144 samples in the AML cohort, which were classified into either high-risk or low-risk groups based on their risk score. Using the GSEA v4.1.0 software (https://www.gsea-msigdb.org/gsea/index.jsp), the hallmark gene set (h.all.v7.2.symbols.gmt) was employed for enrichment analysis, with the phenotypic label being the high-risk group versus the low-risk group. The number of permutations used was 1000, while all other settings were set to default values (13). Statistically significant findings were defined as $p < 0.05$ and $q < 0.05$.

2.6 Nomogram construction and assessment

By integrating the risk scores and clinical data of 144 patients with AML in the TCGA database, we constructed nomogram survival models for overall survival (OS) by the "rms" R package, incorporating both univariate and multivariate results. The calibration curve estimate was then adjusted for optimism by using a bootstrap procedure (16). In addition, ROC curves were generated to validate the predictive capacity of the risk signature with clinical characteristics.

A total of 144 patients with AML in the TCGA database were classified into low-risk group and the high-risk group by the median cutoff risk score. The CIBERSORT algorithm was performed to estimate the infiltration levels of various immune cell types (17). Tumor immune dysfunction and exclusion (TIDE) data for AML was acquired from http://tide.dfci.harvard.edu/. The TIDE algorithm was developed to generate TIDE scores and to accurately evaluate the response of immunotherapy agents in patients with cancer (18). Lower TIDE scores indicate better outcomes. The immunotherapy response of each patient was evaluated by the gene expression profiles.

2.8 Pharmaceutical screening

A total of 144 patients with AML in the TCGA database were classified into low-risk group and the high-risk group by the median cutoff risk score. Then, we employed the "pRRophetic" R package in the Genomics of Drug Sensitivity in Cancer (GDSC) database to determine the varying susceptibilities to the drug between high- and low-risk groups. The half maximal inhibitory concentration (IC_{50}) value, which indicates the concentration at which cell growth is inhibited by 50%, was used as a metric of drug sensitivity (19, 20). Stringent filtration conditions ($p < 0.01$) were used.

2.9 Quantitative real-time PCR

Details of the PCR operation was carried out in accordance with previous study (21). Samples of health donor and patients with AML were collected from Henan Cancer Hospital and approved by Medical Ethics Committee of The Affiliated Cancer Hospital of Zhengzhou University (approval no. 2023-KY-0104-001). The PCR primers were purchased from SangonBiotech (Sangon, Zhengzhou, China). And, the primer sequences in this study were showed in the Supplementary Table 6.

3 Results

3.1 Construction of an eight-gene signature with high accuracy of prognosis prediction

Briefly, 1,996 LMRGs and 1,793 IRGs in AML were included, of which 180 candidate prognostic genes were subsequently identified using univariate Cox regression analysis (Figure 1A). LASSO Cox regression analysis finally identified eight crucial genes for lipid metabolism- and immune-related prognostic signatures according to the optimal λ value (Figures 1B, C). Among them, there were five LMRGs (*MSMO1*, *ATP13A2*, *SMPDL3B*, *PLA2G4A*, and *TNFSF15*) and three IRGs (*APOBEC3C*, *IL2RA*, and *HGF*). Except for *HGF*, all other seven signature genes are detrimental factors with a hazard ratio (HR) >1. The risk score for each AML sample in this study was calculated by the formula described in Section 2.3.

The median risk score was regarded as the cut-off value to classify the training TCGA cohort into the high-risk and low-risk groups (Figure 2A). The scatter plot indicated that high-risk patients were significantly associated with a high mortality rate compared to that of low-risk patients (Figure 2B). The gene expression heatmap illustrates that, except for *HGF*, all other seven signature genes were upregulated in the high-risk group (Figure 2C). Kaplan-Meier curve analysis demonstrated that high-risk patients suffered significantly worse survival outcomes than low-risk ones (Figure 2D). The AUC reached 0.807, 0.848, and 0.843 at 1, 3, and 5 years, respectively (Figure 2E). In addition, results for the testing and entire datasets were consistent with those from the training dataset (Figures 3A–E). The above results demonstrated that the potential prognostic signature showed great specificity and sensitivity in estimating the prognosis of AML patients.

3.2 External validation of the risk signature in the GEO cohorts

To validate the predictive reliability of this prognostic signature, we screened and included three GEO datasets as external validation cohorts. After calculating the risk scores for each sample in these datasets, we assigned patients to high- and low-risk groups by the median cut-off value of these scores. Survival analyses performed on all three validation datasets consistently demonstrated that in the high-risk patients with AML experienced significantly worse OS outcomes than the low-risk ones (GSE37642, $p = 0.00041$; GSE71014, $p = 0.0098$; GSE12417, $p = 0.046$) (Figures 4A–C).

3.3 Correlation between the clinical characteristics and prognostic signature

To assess the clinical significance and prognostic utility of the risk signature, Kaplan-Meier curves were initially generated to explore the prognostic role of each gene included in the risk signature. These variables included age (>= 60 years or < 60 years), gender (female or male), chromosome status (normal or abnormal), and gene mutation status (FLT3, NPM1, RAS, and IDH1 mutation or not). The results revealed that regardless of the clinicopathological features, high-risk patients tend to have the worst OS outcomes, indicating the stable performance of the prognostic risk signature (Figures 5A–N).

3.4 Nomogram analysis

Univariate combined with multivariate Cox regression analyses were preformed to explore whether the risk signature and

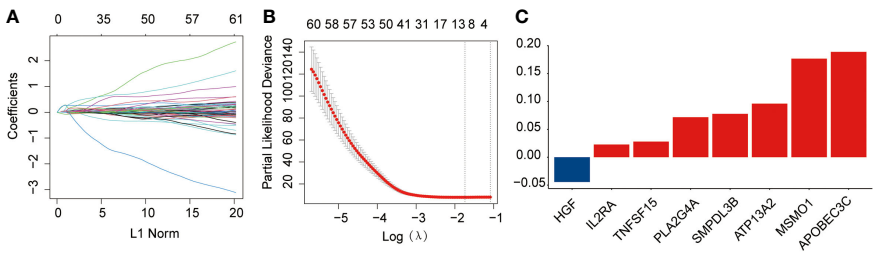

FIGURE 1
Development of the prognostic risk signature in the training dataset. **(A)** The least absolute shrinkage and selection operator (LASSO) model was subjected to ten fold cross-validation for variable selection. **(B)** LASSO coefficient profile of identified crucial genes. **(C)** Coefficient profile of the eight prognostic genes.

10.3389/fimmu.2023.1290968

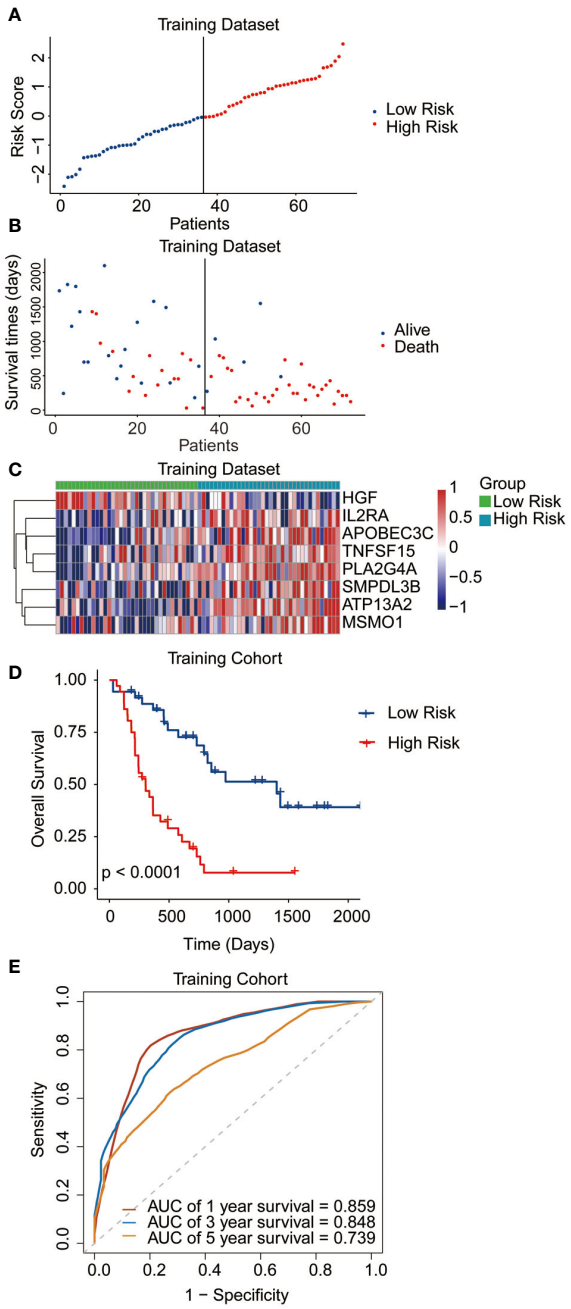

FIGURE 2
Performance of the prognostic signature in the training dataset. **(A)** The risk curve of each AML sample was defined by risk score. **(B)** Scatter plots showing the survival status of each sample. **(C)** Heat map of the expression of the eight selected genes. **(D)** Kaplan-Meier survival curves between the two risk groups. **(E)** The receiver operating characteristic (ROC) curves for overall survival at 1, 3, and 5 years.

clinicopathological parameters, including age, sex, chromosomal status, and gene mutations, were the independent prognostic factors. The results showed that the risk scores (HR = 3.02; 95% CI 2.79-3.25) and age (HR = 2.42; 95% CI 2.2-2.65) were the independent prognostic factors for survival (Figures 6A, B). In addition, a nomogram was developed using age and risk scores to accurately predict the survival rates at 1-, 3-, and 5-year in patients with AML, which suggested that a higher total score suggested worse survival. The result showed that the prognostic signature had the greatest impact on OS (Figure 6C). Meanwhile, the calibration curve demonstrated a strong agreement between the predicted and observed OS at 1-, 3-, and 5-year intervals, indicating the excellent predictive accuracy of the prognostic signature (Figures 6D–F). Furthermore, the 1-, 3-, and 5-year survival ROC analyses showed that the AUCs for the nomogram and risk scores were superior to the other variables, such as age, chromosomal status, sex, as well as FLT3, NPM1, RAS, and IDH1 mutations (Figures 6G–I). These results showed that the nomogram and risk score provided a higher practical value for prognostic prediction than the other variables.

3.5 Biological functions and pathway analysis

GSEA was performed between the two risk groups to identify the underlying biological functions and pathways associated with the risk score. The results indicated that interferon γ, inflammatory, and interferon α responses, as well as TNFα signaling via NF-κB, complement, IL2-STAT5 signaling, IL6-JAK-STAT3 signaling, allograft rejection, hypoxia, and KRAS signaling pathway were enriched, which are central in mediating host responses to inflammation and antitumor immunity (Figure 7).

3.6 Correlation between the prognostic signature and tumor immune microenvironment

As the antitumor immunity-related signaling pathways were significantly enriched in the GSEA analysis, we evaluated the correlation of the prognostic risk signature with immune state in each patient with AML. CIBERSORT algorithm was performed to estimate the infiltration levels of various immune cell types in the TME. The results demonstrated that high-risk patients had a lower fraction of activated dendritic cells, CD56dim NK cells, effector memory CD4 T cells, macrophages, immature B cells, MDSCs, NK cells, NK T cells, neutrophils, T follicular helper cells, plasmacytoid dendritic cells, and type 1 T helper cells (Figure 8A). Then, the immune scores and the TIDE scores of each sample were calculated, and the results demonstrated that the high-risk samples hold lower immune scores and higher TIDE scores than the low-risk samples (Figures 8B, C), indicating that high-risk patients were associated with enhanced tumor immune escape ability. Moreover, we assessed the disparity in the response rates to immunotherapy between the two risk groups. Notably, the samples from the low-risk group exhibited higher immunotherapy response rates than those from the high-risk group (Figure 8D). Based on these outcomes, we ascertained that the risk signature could indicate the immune cell infiltration and the response to immunotherapy in AML.

10.3389/fimmu.2023.1290968

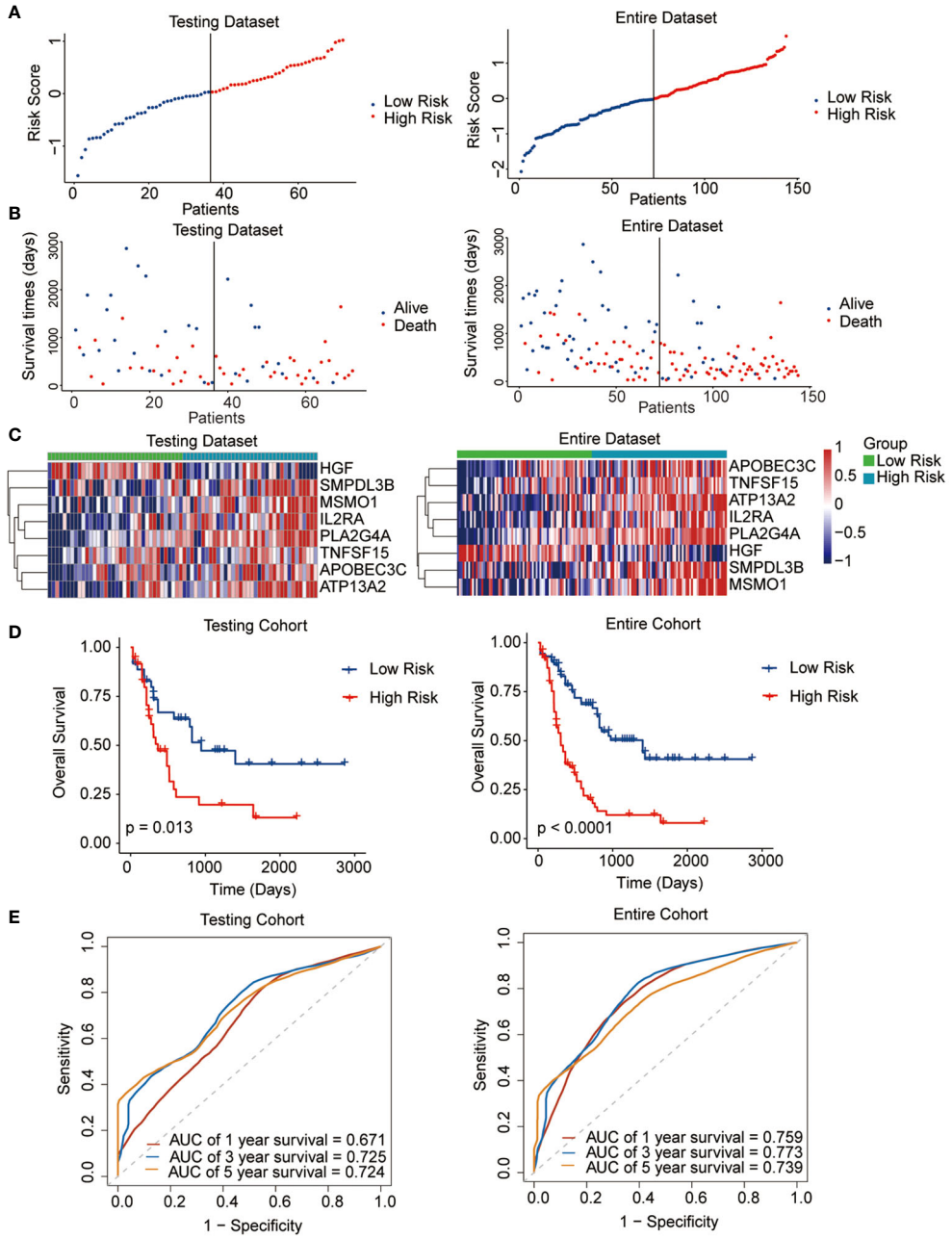

FIGURE 3
Performance of the prognostic signature in the testing and entire datasets. **(A)** The risk curve of each AML sample was defined by risk score. **(B)** Scatter plots showing the survival status of each sample. **(C)** Heat map of the expression of the eight selected genes. **(D)** Kaplan-Meier survival curves between the two risk groups. **(E)** The receiver operating characteristic (ROC) curves for overall survival at 1, 3, and 5 years.

3.7 Drug sensitivity analysis

Thereafter, the pRRophetic package were used to further analyze the sensitivity of antitumor drugs based on the IC_{50} available in the GDSC database for patients with AML (19, 20). In our study, we successfully identified a total of 198 small molecular compounds that exhibited significantly diverse responses between the high-risk and low-risk groups (Supplementary Table 7). The results showed that the high-risk group showed a lower sensitivity to BI2536 (PLK1 inhibitor) and SB-505124 (TGFβR inhibitor), whereas they were sensitive to several other drugs such as AZD2014 (mTOR inhibitor), pictilisib (PI3Kα/δ inhibitor), MK-2206 (Akt inhibitor), dactolisib (dual pan-class I PI3K and mTOR kinase inhibitor), afatinib (EGFR inhibitor), rapamycin (FRAP/mTOR inhibitor), and taselisib (PI3K inhibitor targets PIK3CA mutations), even though none of these is currently used in the treatment of AML (Figure 9). The outcomes of our study offer promising molecular candidates for targeted therapy that can be utilized in the treatment of AML patients.

10.3389/fimmu.2023.1290968

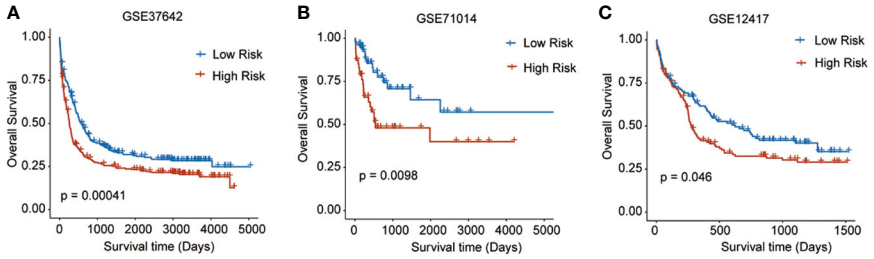

FIGURE 4
Survival analyses performed on all three GEO validation datasets. **(A)** GSE37642: p = 0.00041, **(B)** GSE71014: p = 0.0098, **(C)** GSE12417: p = 0.046).

4 Discussion

Here, we studied the role of LMRGs and IRGs in the prognosis of patients with AML. By analyzing large-scale genomic and clinical datasets from TCGA and GEO databases, we identified an eight-gene signature that demonstrated robust prognostic value and potential clinical applications in AML. We performed additional analysis on the expression of eight signature genes in the high and low-risk groups across multiple cohorts, including TCGA, GSE12417, GSE37642, and GSE71014. The findings demonstrated

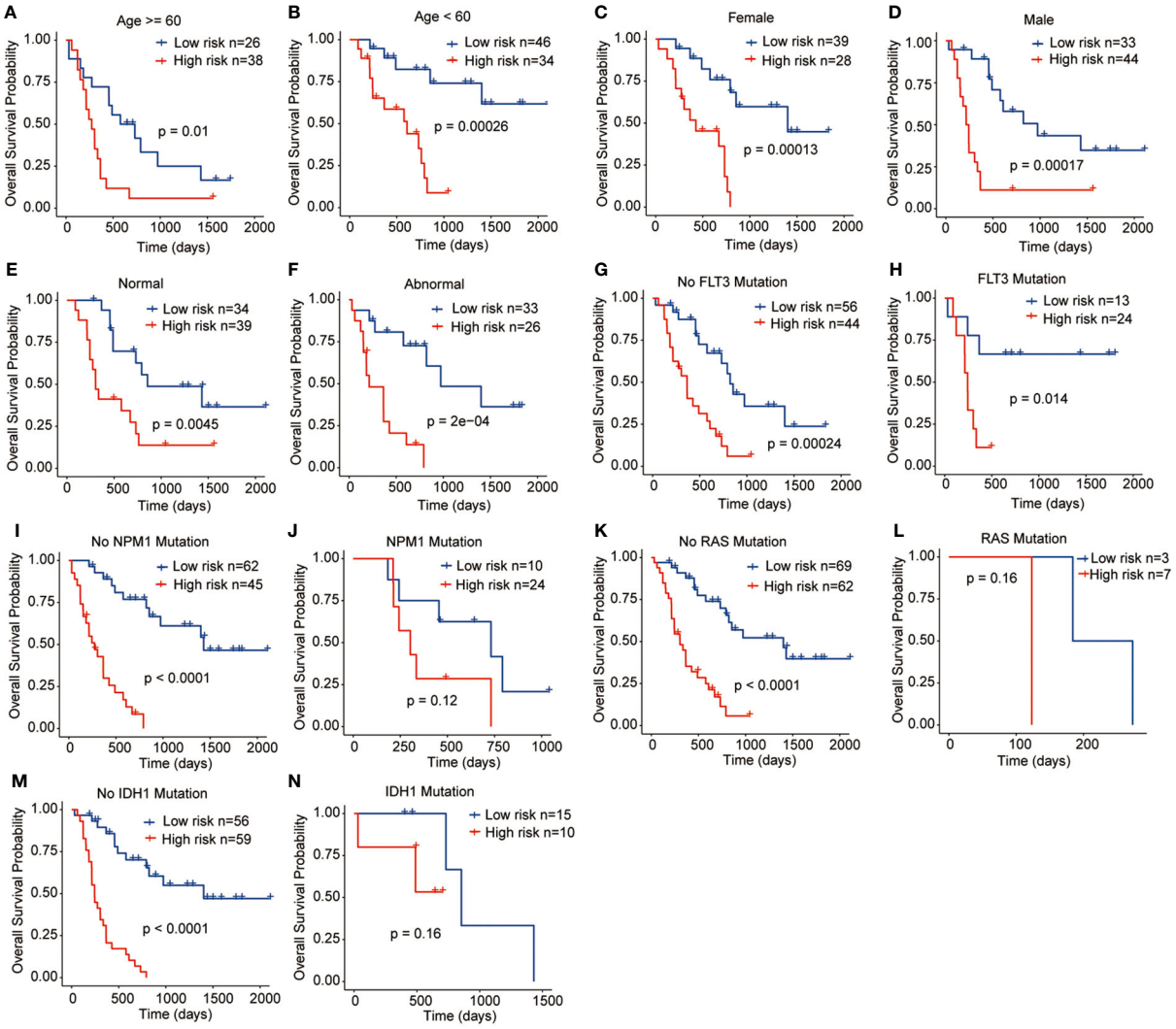

FIGURE 5
Relationships between the prognostic signature and clinicopathological characteristics. **(A)** Age >= 60 years, **(B)** Age < 60 years, **(C)** Female, **(D)** Male, **(E)** Normal chromosome, **(F)** Abnormal chromosome, **(G)** No FLT3 mutation, **(H)** FLT3 mutation, **(I)** No NPM1 mutation, **(J)** NPM1 mutation, **(K)** No RAS mutation, **(L)** RAS mutation, **(M)** IDH1 mutation, **(N)** IDH1 mutation.

10.3389/fimmu.2023.1290968

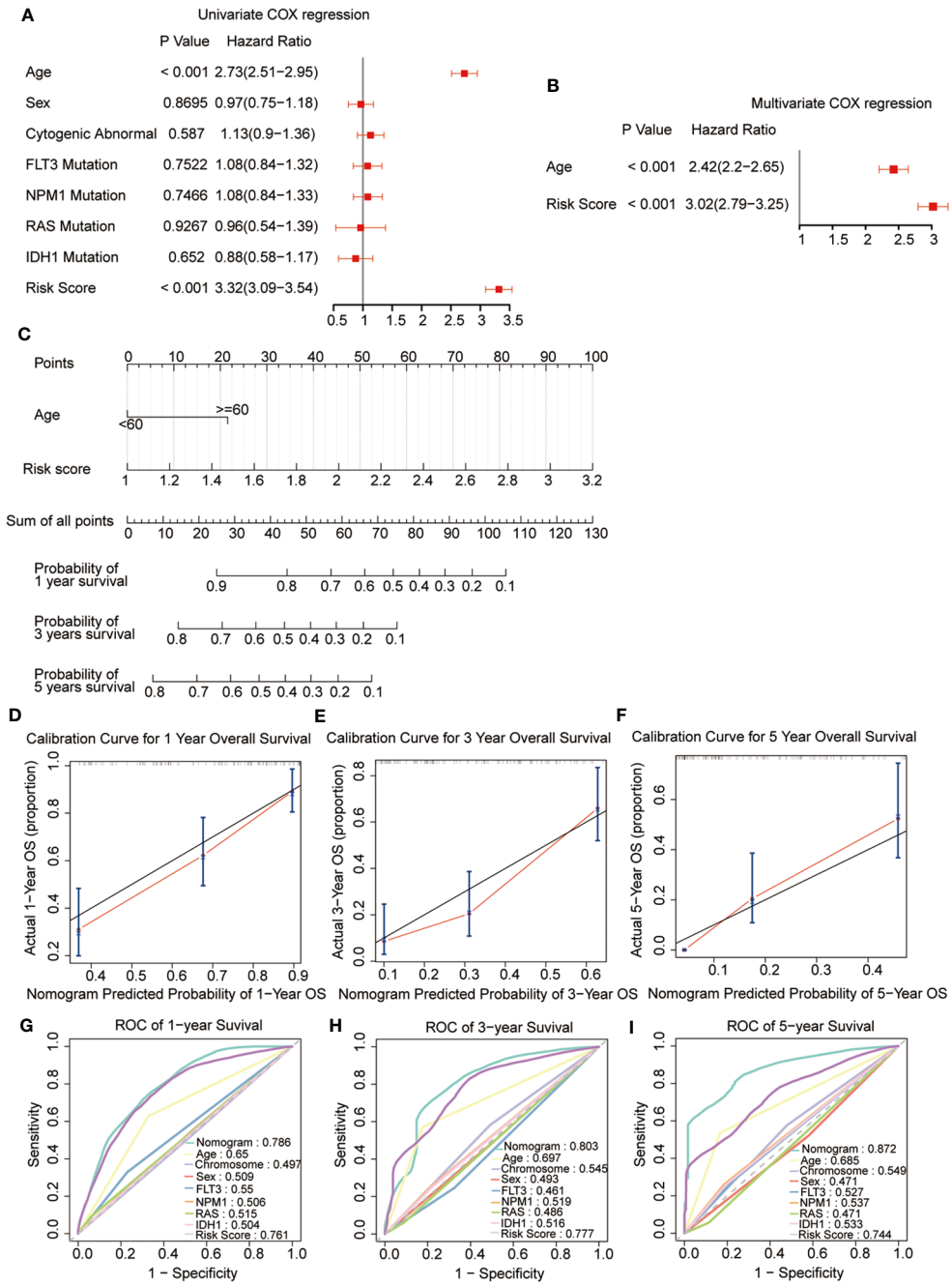

FIGURE 6
Construction and validation of the nomogram. **(A, B)** Univariate and multivariate Cox regression of the prognostic signature and clinical characteristics. **(C)** The developed nomogram to estimate the survival possibilities of patients with AML. **(D-F)** Calibration blots of the agreement between the predicted overall survival and observed overall survival at 1, 3, and 5 years. **(G–I)** The ROC curves for overall survival at 1, 3, and 5 years.

that MSMO1, ATP13A2, SMPDL3B, PLA2G4A, TNFSF15, APOBEC3C, and IL2RA were upregulated in the high-risk group, whereas HGF was downregulated. Survival analysis indicated that patients with high expression of these signature genes, except for HGF, experienced worse OS outcomes. These results provide further evidence that these genes may function as detrimental factors, while HGF may serve as a protective factor (Supplementary Figures 1 and 2). The relative expression of these eight signature genes were also detected in the clinical samples (Supplementary Figure 3).

APOBEC3C is a member of the APOBEC family that plays important but distinct roles in host defense and mediates C-to-T mutagenesis in cancers. A previous study indicated a negative correlation between *APOBEC3C* mRNA expression and base substitution mutations in estrogen receptor-negative breast cancer (22). Qian et al. found that *APOBEC3C* was significantly

10.3389/fimmu.2023.1290968

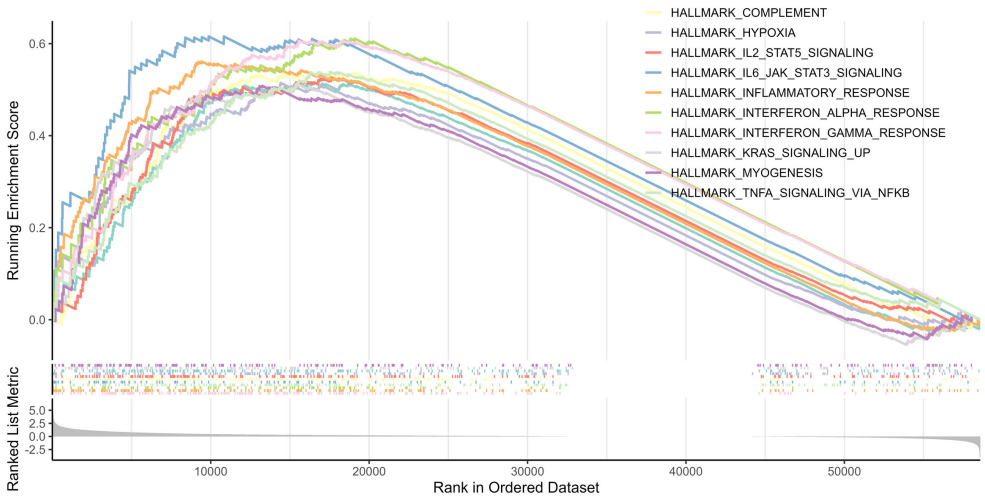

FIGURE 7
Top 10 significantly enriched pathways in the GSEA.

upregulated in pancreatic ductal adenocarcinoma compared with that in normal pancreatic tissues and predicted worse survival rates (23). Jiang et al. found that increased *APOBEC3C* expression was related to hematopoietic stem and progenitor cell proliferation and an increased C-to-T mutational burden during disease progression in patients with myeloproliferative neoplasm (24).

Methylsterol monooxygenase 1 (MSMO1), an intermediate enzyme involved in cholesterol and fatty acid biosynthesis, acts as a novel mediator of chemoresistance in cancer (25). A previous study revealed that MSMO1 plays crucial roles in tumorigenesis and progression and is a promising prognostic biomarker for cervical squamous cell carcinoma (26).

ATPase cation transporting 13A2 (ATP13A2/PARK9), a late endolysosomal transporter, regulates membrane association, cellular α-synuclein multimerization, and externalization and is genetically implicated in neurodegenerative disorders (27). Zhang

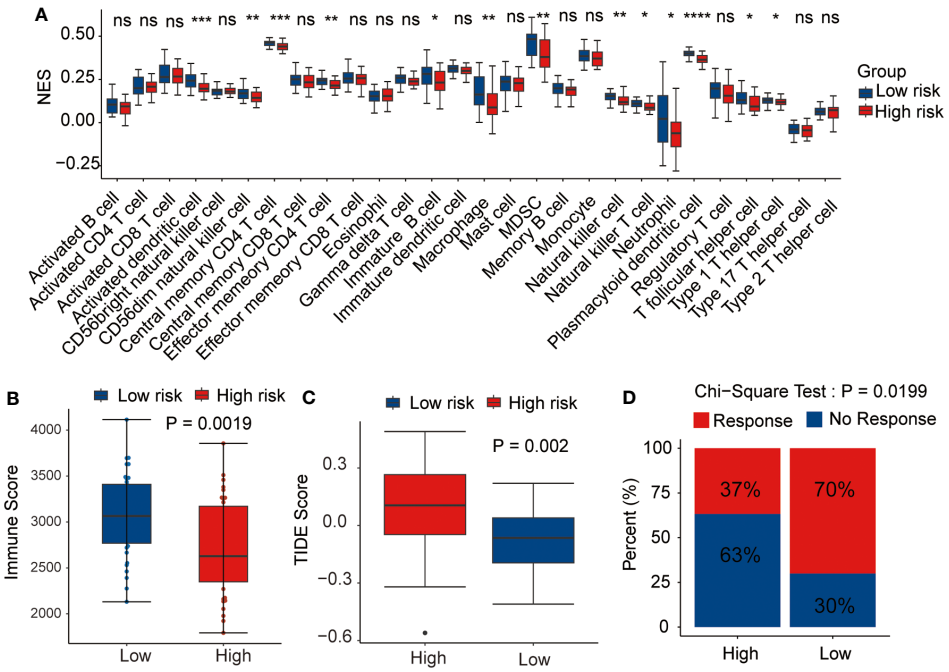

FIGURE 8
Relationship between the prognostic signature and tumor microenvironment. Correlation of the risk score with **(A)** immune infiltration level, **(B)** immune score, **(C)** tumor immune dysfunction and exclusion (TIDE) score, and **(D)** immunotherapy response. *p <0.05, **p <0.01, ***p <0.001, ****p <0.0001, ns, not statistically significant.

10.3389/fimmu.2023.1290968

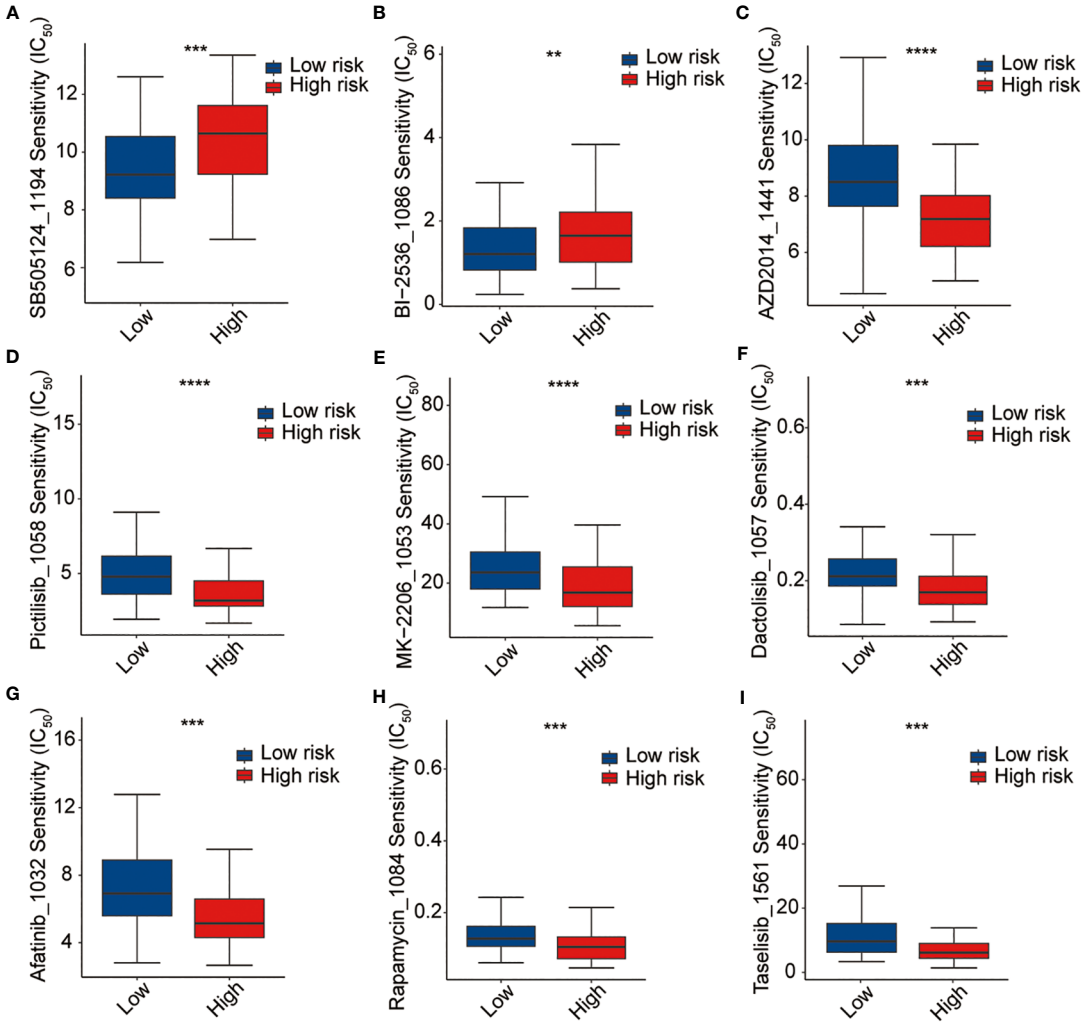

FIGURE 9
Drug sensitivity analysis. **(A)** SB-505124, **(B)** BI2536, **(C)** AZD2014, **(D)** pictilisib, **(E)** MK-2206, **(F)** dactolisib, **(G)** afatinib, **(H)** rapamycin, and **(I)** traselisib. **p <0.01, ***p <0.001, ****p <0.0001.

et al. revealed that ATP13A2 activates the pentose phosphate pathway via the TFEB-PGD axis to facilitate colorectal cancer growth (28).

As the negative regulator of Toll-like receptor signaling, Sphingomyelin Phosphodiesterase Acid Like 3B (SMPDL3B) plays a crucial role in innate immunity and at the interface of membrane biology. Qu et al. demonstrated that SMPDL3B expression indicates poor prognosis and contributes to AML progression (29).

The cytosolic phospholipase, PLA2G4A, is crucial for the pathogenesis of FLT3-ITD-mutated AML (30). Higher PLA2G4A expression results in worse OS and mutations in NRAS, which are known to contribute to the development of myelodysplastic syndrome development (31).

Tumor necrosis family superfamily member 15 (TNFSF15) promotes lymphatic metastasis by upregulating vascular endothelial growth factor-C in a lung cancer mouse model (32). Lu et al. showed that increased TNFSF15 expression indicates worse prognosis in oral cancer (33).

Excessive expression of *IL2RA*, the gene encoding the alpha chain of the interleukin-2 receptor, has been linked to chemotherapy resistance and unfavorable outcomes in AML (34). *IL2RA* enhances cell proliferation and cell cycle activity while suppressing apoptosis in both human AML cell lines and primary cells. In two genetically modified mouse models of AML, *IL2RA* hampered cell differentiation, facilitated stem cell-like characteristics, and was essential for leukemia development. Antibodies targeting *IL2RA* have demonstrated the ability to inhibit leukemic cells without affecting normal hematopoietic cells, and their combined effects with other anti-leukemic agents have shown potential synergy. Consequently, *IL2RA* is a promising therapeutic target in AML because it regulates key processes, such as proliferation, differentiation, apoptosis, stem cell-related properties, and leukemogenesis (35).

As a multifunctional cytokine, hepatocyte growth factor (HGF) regulates cell growth, movement, and tissue regeneration in various epithelial cells (36). HGF binds to its receptor c-Met and activates its kinase activity, initiating signaling pathways such as JAK/STAT3,

PI3K/Akt/NF-κB, and Ras/Raf. Aberrations in the HGF/MET pathway act as diagnostic, predictive, and prognostic biomarkers for cancers (37). HGF has been discovered to regulate the activity of various immune cell types, including B cells, T cells, and natural killer cells, which are important components of the anti-tumor immune response. By enhancing the immune surveillance and anti-tumor effects, HGF may contribute to reducing the risk of AML development or progression. While, it's worth noting that the exact mechanisms by which HGF influences AML risk are still being investigated, and further studies are required to fully reveal its role in the disease. Nonetheless, the association between HGF and a reduced risk in AML highlights the potential importance of this growth factor in the development and treatment of the disease.

The risk score defined by the prognostic signature defined in this study effectively stratified patients with AML into low- and high-risk groups with significantly different survival outcomes. These results are consistent with those of the external validation cohorts from the GEO dataset. Regardless of age, sex, cytogenetic abnormalities, or gene mutations, patients in the high-risk group consistently exhibited worse OS outcomes, further supporting the reliability and generalizability of the prognostic risk signature.

To enhance the clinical utility of our findings, we constructed nomograms that integrated the risk scores derived from the eight-gene signature with other clinical factors. The ROC and calibration curves further confirmed the higher predictive accuracy of the prognostic signature and nomograms compared with the clinical variables, such as age, sex, cytogenetic abnormalities, and gene mutations, indicating their potential as reliable tools for personalized treatment decision-making.

GSEA between the two risk groups sheds light on the underlying biological mechanisms associated with the prognostic signature. Many antitumor immunity-related pathways were enriched, suggesting the involvement of immune dysregulation in AML prognosis. This could lead to the distinction in the immunotherapy response against cancer and the treatment response between the two risk groups.

Then, the correlation between the immune cell infiltration and risk score was explored. The low-risk group showed higher proportions of effector memory CD4 T cells, macrophages, NK cells, NK T cells, T follicular helper cells, Type 1 T helper cells, and other immune cell subtypes. The negative correlation between the immune cell infiltration and risk score suggests that patients in the high-risk group may have impaired immune status. The immune and immune escape scores were then calculated, and the results demonstrated a poorer immune state and stronger immune escape ability in the high-risk group, which may affect the response to immunotherapy. Furthermore, in the high-risk group, there was a notable decrease in the expression level of common immune checkpoints such as PD1, PDL1, PDL2, and CTLA4 (Supplementary Figure 4). These findings indicate that the identified signature holds promise as a valuable tool for assessing the effectiveness of immunotherapy in individuals with AML. Additionally, our prediction results of the immunotherapy response rate further verified this conclusion, which showed that low-risk patients had higher immunotherapy response rates than that of high-risk patients. This finding highlights the potential importance of immune modulation in AML treatment. Future research could focus on understanding the underlying mechanisms that contribute to immune suppression in high-risk patients and explore strategies to enhance immune cell function in these individuals.

In line with the potential impact on the immunotherapy response, we evaluated the sensitivity of AML patients to antitumor drugs using pRRophetic packages. Our results indicated that the high-risk patients exhibited higher sensitivity to some potential drugs. This finding could be relevant for treatment selection and personalized therapeutic approaches in AML as it implies that high-risk patients may be more sensitive to specific antitumor drugs, which targeted to PI3K–AKT–mTOR signaling pathways. PI3K-AKT-mTOR signaling pathway is one of the most abnormal signal pathways in human cancer including AML, which is involved in the control of cell metabolism, proliferation, movement, growth and survival and many other cellular processes (38). Inhibition of PI3K-AKT-mTOR pathway is an important strategy for tumor therapy. However, the effects of these inhibitors seem to vary greatly among patients with AML (39, 40). So far, no clear mutation characteristics or other pathological processes associated with the disease have been detected to predict treatment response. Our results provide a valuable tool for individualized treatment decision-making of these drugs in AML.

It is important to acknowledge the limitations of this study. First, although we utilized large-scale datasets for the analysis, the retrospective nature of the study design may introduce inherent biases. Prospective studies are warranted to validate our findings and to assess the clinical utility of prognostic signatures and nomograms for real-time patient management. Further functional experiments and in-depth mechanistic investigations are required to elucidate the precise roles of the identified LMRGs and IRGs in AML pathogenesis and treatment responses.

In conclusion, our study presents a comprehensive analysis of the prognostic value and clinical implications of an eight-gene signature derived from LMRGs and IRGs in AML. This signature effectively stratified patients into high- and low-risk groups, demonstrating significant differences in survival outcomes and potential implications for immune cell infiltration, treatment response, and drug sensitivity. This opens up avenues for studying the interplay between lipid metabolism and immune dysregulation, which may uncover novel therapeutic targets. Future investigations could explore the manipulation of lipid metabolism pathways as a means to modulate immune responses and improve treatment outcomes in AML. Overall, these findings in this study have several broader implications. They aid in personalized risk assessment for AML patients, guiding treatment decisions towards immunotherapy or targeted drugs based on risk group assignment.

Data availability statement

The datasets presented in this study can be found in online repositories. The names of the repository/repositories and accession number(s) can be found in the article/Supplementary Material.

Ethics statement

The studies involving humans were approved by Medical Ethics Committee of The Affiliated Cancer Hospital of Zhengzhou University. The studies were conducted in accordance with the local legislation and institutional requirements. The ethics committee/institutional review board waived the requirement of written informed consent for participation from the participants or the participants' legal guardians/next of kin because the samples used in this study were the remaining samples obtained in the course of diagnosis and treatment.

Author contributions

DL: Conceptualization, Data curation, Funding acquisition, Investigation, Methodology, Writing – original draft, Writing – review & editing. XW: Conceptualization, Investigation, Resources, Writing – review & editing. CC: Formal analysis, Resources, Validation, Writing – review & editing. JL: Formal analysis, Methodology, Software, Visualization, Writing – review & editing. YL: Formal analysis, Validation, Writing – review & editing. HL: Formal analysis, Validation, Writing – review & editing. XG: Formal analysis, Validation, Writing – review & editing. RL: Formal analysis, Methodology, Writing – review & editing. WZ: Project administration, Resources, Supervision, Writing – review & editing. WS: Conceptualization, Investigation, Project administration, Resources, Supervision, Writing – review & editing.

Funding

The author(s) declare financial support was received for the research, authorship, and/or publication of this article. This study was supported by Henan Provincial Science and Technology Research Project (232102311016) and Henan Provincial Young and Middle-aged Health Science and Technology Innovation Excellent Youth Talent Project (YQRC2023003).

Acknowledgments

We are grateful to the contributors to the public databases used in this study.

Conflict of interest

The authors declare that the research was conducted in the absence of any commercial or financial relationships that could be construed as a potential conflict of interest.

Publisher's note

Supplementary material

The Supplementary Material for this article can be found online at: https://www.frontiersin.org/articles/10.3389/fimmu.2023.1290968/full#supplementary-material

SUPPLEMENTARY FIGURE 1
The relative expression of eight signature genes in the high- and low-risk groups from TCGA, GSE37642, GSE71014, and GSE12417 cohorts. **(A)** APOBEC3C, **(B)** MSMO1, **(C)** ATP13A2, **(D)** SMPDL3B, **(E)**, PLA2G4A, **(F)** TNFSF15, **(G)** IL2RA, **(H)** HGF.

SUPPLEMENTARY FIGURE 2
Correlation of each signature gene and survival in TCGA cohort. **(A)** APOBEC3C, **(B)** MSMO1, **(C)** ATP13A2, **(D)** SMPDL3B, **(E)**, PLA2G4A, **(F)** TNFSF15, **(G)** IL2RA, **(H)** HGF.

SUPPLEMENTARY FIGURE 3
The relative expression of each signature gene in the clinical samples. **(A)** APOBEC3C, **(B)** MSMO1, **(C)** ATP13A2, **(D)** SMPDL3B, **(E)** PLA2G4A, **(F)** TNFSF15, **(G)** IL2RA, **(H)** HGF.

SUPPLEMENTARY FIGURE 4
Correlation of risk score and immune checkpoints. **(A)** PD1, **(B)** PDL1, **(C)** PDL2, **(D)** CTLA4.

References

1. Döhner H, Estey E, Grimwade D, Amadori S, Appelbaum FR, Büchner T, et al. Diagnosis and management of aml in adults: 2017 Eln recommendations from an international expert panel. *Blood* (2017) 129(4):424–47. doi: 10.1182/blood-2016-08-733196

2. Bewersdorf JP, Abdel-Wahab O. Translating recent advances in the pathogenesis of acute myeloid leukemia to the clinic. *Genes Dev* (2022) 36(5-6):259–77. doi: 10.1101/gad.349368.122

3. Vago L, Gojo I. Immune escape and immunotherapy of acute myeloid leukemia. *J Clin Invest* (2020) 130(4):1552–64. doi: 10.1172/jci129204

4. Mishra SK, Millman SE, Zhang L. Metabolism in acute myeloid leukemia: mechanistic insights and therapeutic targets. *Blood* (2023) 141(10):1119–35. doi: 10.1182/blood.2022018092

5. Stevens BM, Jones CL, Pollyea DA, Culp-Hill R, D'Alessandro A, Winters A, et al. Fatty acid metabolism underlies venetoclax resistance in acute myeloid leukemia stem cells. *Nat Cancer* (2020) 1(12):1176–87. doi: 10.1038/s43018-020-00126-z

6. Nguyen TM, Jambhrunkar M, Wong SS, Ross DM, Joyce P, Finnie JW, et al. Targeting acute myeloid leukemia using sphingosine kinase 1 inhibitor-loaded liposomes. *Mol Pharmaceutics* (2023) 20(8):3937–46. doi: 10.1021/acs.molpharmaceut.3c00078

7. Powell JA, Lewis AC, Zhu W, Toubia J, Pitman MR, Wallington-Beddoe CT, et al. Targeting sphingosine kinase 1 induces mcl1-dependent cell death in acute myeloid leukemia. *Blood* (2017) 129(6):771–82. doi: 10.1182/blood-2016-06-720433

8. Li D, Liang J, Yang W, Guo W, Song W, Zhang W, et al. A distinct lipid metabolism signature of acute myeloid leukemia with prognostic value. *Front Oncol* (2022) 12:876981. doi: 10.3389/fonc.2022.876981

9. Yu W, Lei Q, Yang L, Qin G, Liu S, Wang D, et al. Contradictory roles of lipid metabolism in immune response within the tumor microenvironment. *J Hematol Oncol* (2021) 14(1):187. doi: 10.1186/s13045-021-01200-4

10. Zhang HB, Sun ZK, Zhong FM, Yao FY, Liu J, Zhang J, et al. A novel fatty acid metabolism-related signature identifies features of the tumor microenvironment and predicts clinical outcome in acute myeloid leukemia. *Lipids Health Dis* (2022) 21(1):79. doi: 10.1186/s12944-022-01687-x

11. Isidori A, Salvestrini V, Ciciarello M, Loscocco F, Visani G, Parisi S, et al. The role of the immunosuppressive microenvironment in acute myeloid leukemia development and treatment. *Expert Rev Hematol* (2014) 7(6):807–18. doi: 10.1586/17474086.2014.958464

12. Bleve A, Durante B, Sica A, Consonni FM. Lipid metabolism and cancer immunotherapy: immunosuppressive myeloid cells at the crossroad. *Int J Mol Sci* (2020) 21(16):5845. doi: 10.3390/ijms21165845

13. Subramanian A, Tamayo P, Mootha VK, Mukherjee S, Ebert BL, Gillette MA, et al. Gene set enrichment analysis: A knowledge-based approach for interpreting genome-wide expression profiles. *Proc Natl Acad Sci United States America* (2005) 102 (43):15545–50. doi: 10.1073/pnas.0506580102

14. Bhattacharya S, Andorf S, Gomes L, Dunn P, Schaefer H, Pontius J, et al. Immport: disseminating data to the public for the future of immunology. *Immunol Res* (2014) 58(2-3):234–9. doi: 10.1007/s12026-014-8516-1

15. Rich JT, Neely JG, Paniello RC, Voelker CC, Nussenbaum B, Wang EW. A practical guide to understanding Kaplan-Meier curves. *Otolaryngol Head Neck Surg Off J Am Acad Otolaryngol Head Neck Surg* (2010) 143(3):331–6. doi: 10.1016/j.otohns.2010.05.007

16. Hoshino N, Hida K, Sakai Y, Osada S, Idani H, Sato T, et al. Nomogram for predicting anastomotic leakage after low anterior resection for rectal cancer. *Int J Colorectal Dis* (2018) 33(4):411–8. doi: 10.1007/s00384-018-2970-5

17. Chen B, Khodadoust MS, Liu CL, Newman AM, Alizadeh AA. Profiling tumor infiltrating immune cells with Cibersort. *Methods Mol Biol (Clifton NJ)* (2018) 1711:243–59. doi: 10.1007/978-1-4939-7493-1_12

18. Jiang P, Gu S, Pan D, Fu J, Sahu A, Hu X, et al. Signatures of T cell dysfunction and exclusion predict cancer immunotherapy response. *Nat Med* (2018) 24(10):1550–8. doi: 10.1038/s41591-018-0136-1

19. Geeleher P, Cox N, Huang RS. Prrophetic: an R package for prediction of clinical chemotherapeutic response from tumor gene expression levels. *PloS One* (2014) 9(9): e107468. doi: 10.1371/journal.pone.0107468

20. Yang W, Soares J, Greninger P, Edelman EJ, Lightfoot H, Forbes S, et al. Genomics of drug sensitivity in cancer (Gdsc): A resource for therapeutic biomarker discovery in cancer cells. *Nucleic Acids Res* (2013) 41(Database issue):D955–61. doi: 10.1093/nar/gks1111

21. Li D, Yu Z, Wang T, Li Y, Chen X, Wu L. The role of the novel Lincrna Uc002jit.1 in Nf-Kb-mediated DNA damage repair in acute myeloid leukemia cells. *Exp Cell Res* (2020) 391(2):111985. doi: 10.1016/j.yexcr.2020.111985

22. Zhang Y, Delahanty R, Guo X, Zheng W, Long J. Integrative genomic analysis reveals functional diversification of Apobec gene family in breast cancer. *Hum Genomics* (2015) 9:34. doi: 10.1186/s40246-015-0056-9

23. Qian Y, Gong Y, Zou X, Liu Y, Chen Y, Wang R, et al. Aberrant Apobec3c expression induces characteristic genomic instability in pancreatic ductal adenocarcinoma. *Oncogenesis* (2022) 11(1):35. doi: 10.1038/s41389-022-00411-9

24. Jiang Q, Isquith J, Ladel L, Mark A, Holm F, Mason C, et al. Inflammation-driven deaminase deregulation fuels human pre-leukemia stem cell evolution. *Cell Rep* (2021) 34(4):108670. doi: 10.1016/j.celrep.2020.108670

25. Kordias D, Kostara CE, Papadaki S, Verigos J, Bairaktari E, Magklara A. Omics analysis of chemoresistant triple negative breast cancer cells reveals novel metabolic vulnerabilities. *Cells* (2022) 11(17):2719. doi: 10.3390/cells11172719

26. Zheng G, Wang Z, Fan Y, Wang T, Zhang L, Wang M, et al. The clinical significance and immunization of msmo1 in cervical squamous cell carcinoma based on bioinformatics analysis. *Front Genet* (2021) 12:705851. doi: 10.3389/fgene.2021.705851

27. van Veen S, Martin S, Van den Haute C, Benoy V, Lyons J, Vanhoutte R, et al. Atp13a2 deficiency disrupts lysosomal polyamine export. *Nature* (2020) 578 (7795):419–24. doi: 10.1038/s41586-020-1968-7

28. Zhang F, Wu Z, Yu B, Ning Z, Lu Z, Li L, et al. Atp13a2 activates the pentose phosphate pathway to promote colorectal cancer growth though Tfeb-Pgd axis. *Clin Trans Med* (2023) 13(5):e1272. doi: 10.1002/ctm2.1272

29. Qu H, Zhu Y. Smpdl3b predicts poor prognosis and contributes to development of acute myeloid leukemia. *Front Mol Biosci* (2021) 8:695601. doi: 10.3389/fmolb.2021.695601

30. Lai WJ, Chen F, Shu L, Yang XM, Yuan J, Xu JB, et al. Pivotal role of cytosolic phospholipase Pla2g4a in the pathogenesis of Flt3-Itd-mutated acute myeloid leukemia. *Genes Dis* (2023) 10(1):22–5. doi: 10.1016/j.gendis.2022.02.002

31. McGraw KL, Cheng CH, Chen YA, Hou HA, Nilsson B, Genovese G, et al. Non-Del(5q) myelodysplastic syndromes-associated loci detected by Snp-array genome-wide association meta-analysis. *Blood Adv* (2019) 3(22):3579–89. doi: 10.1182/bloodadvances.2019000922

32. Qin T, Huang D, Liu Z, Zhang X, Jia Y, Xian CJ, et al. Tumor necrosis factor superfamily 15 promotes lymphatic metastasis *via* upregulation of vascular endothelial growth factor-C in a mouse model of lung cancer. *Cancer Sci* (2018) 109(8):2469–78. doi: 10.1111/cas.13665

33. Lu HJ, Chuang CY, Su CW, Chen MK, Yang WE, Yeh CM, et al. Role of Tnfsf15 variants in oral cancer development and clinicopathologic characteristics. *J Cell Mol Med* (2022) 26(21):5452–62. doi: 10.1111/jcmm.17569

34. Du W, He J, Zhou W, Shu S, Li J, Liu W, et al. High Il2ra Mrna expression is an independent adverse prognostic biomarker in core binding factor and intermediate-risk acute myeloid leukemia. *J Trans Med* (2019) 17(1):191. doi: 10.1186/s12967-019-1926-z

35. Nguyen CH, Schlerka A, Grandits AM, Koller E, van der Kouwe E, Vassiliou GS, et al. Il2ra promotes aggressiveness and stem cell-related properties of acute myeloid leukemia. *Cancer Res* (2020) 80(20):4527–39. doi: 10.1158/0008-5472.Can-20-0531

36. Zhao Y, Ye W, Wang YD, Chen WD. Hgf/C-Met: A key promoter in liver regeneration. *Front Pharmacol* (2022) 13:808855. doi: 10.3389/fphar.2022.808855

37. Moosavi F, Giovannetti E, Saso L, Firuzi O. Hgf/Met pathway aberrations as diagnostic, prognostic, and predictive biomarkers in human cancers. *Crit Rev Clin Lab Sci* (2019) 56(8):533–66. doi: 10.1080/10408363.2019.1653821

38. Nepstad I, Hatfield KJ, Grønningsæter IS, Reikvam H. The Pi3k-Akt-Mtor signaling pathway in human acute myeloid leukemia (Aml) cells. *Int J Mol Sci* (2020) 21 (8):2907. doi: 10.3390/ijms21082907

39. Nepstad I, Hatfield KJ, Grønningsæter IS, Aasebø E, Hernandez-Valladares M, Hagen KM, et al. Effects of insulin and pathway inhibitors on the Pi3k-Akt-Mtor phosphorylation profile in acute myeloid leukemia cells. *Signal Transduct Target Ther* (2019) 4:20. doi: 10.1038/s41392-019-0050-0

40. Nepstad I, Hatfield KJ, Tvedt THA, Reikvam H, Bruserud Ø. Clonal heterogeneity reflected by Pi3k-Akt-Mtor signaling in human acute myeloid leukemia cells and its association with adverse prognosis. *Cancers* (2018) 10(9):332. doi: 10.3390/cancers10090332

frontiers | Frontiers in Immunology

TYPE Original Research
PUBLISHED 15 November 2023
DOI 10.3389/fimmu.2023.1266843

OPEN ACCESS

EDITED BY
Ines Zidi,
Tunis El Manar University, Tunisia

REVIEWED BY
Jules Zhang-Yin,
Vivalia, Belgium
Flávia Dornelas Kurkowski,
Pontifical Catholic University of Rio Grande do Sul, Brazil

*CORRESPONDENCE
Jiazhong Ren
1084405211@qq.com

RECEIVED 25 July 2023
ACCEPTED 25 October 2023
PUBLISHED 15 November 2023

CITATION
Zhao Y and Ren J (2023) ^{18}F-FAPI-04 PET/CT parameters predict PD-L1 expression in esophageal squamous cell carcinoma. *Front. Immunol.* 14:1266843. doi: 10.3389/fimmu.2023.1266843

^{18}F-FAPI-04 PET/CT parameters predict PD-L1 expression in esophageal squamous cell carcinoma

Yaqing Zhao[1] and Jiazhong Ren[2*]

[1]Department of General Affairs Section, The Second Affiliated Hospital of Shandong University of Traditional Chinese Medicine, Jinan, Shandong, China, [2]Department of Medical Imaging, PET-CT Center, Shandong Cancer Hospital and Institute, Shandong First Medical University and Shandong Academy of Medical Sciences, Jinan, Shandong, China

Purpose: This prospective study examined whether metabolism parameters obtained using the tracer ^{18}F-AlFNOTA-fibroblast activation protein inhibitor (FAPI)-04 (denoted as ^{18}F-FAPI-04) in positron emission tomography/computed tomography (PET/CT) can predict programmed death ligand-1 (PD-L1) expression in patients with locally advanced esophageal squamous cell carcinoma (LA-ESCC).

Patients and methods: The 24 enrolled LA-ESCC patients underwent an ^{18}F-FAPI-04 PET/CT scan. The maximum, mean, peak and standard deviation standard uptake values (SUVmax, SUVmean, SUVpeak and SUVsd), metabolic tumor volume (MTV), and total lesion FAP (TLF) expression of the primary tumor were collected. Additionally, we evaluated PD-L1 expression on cancer cells by immunohistochemistry and immunofluorescence methods. Patients were divided into negative and positive expressions according to the expression of PD-L1 (CPS < 10 and CPS $\geq$ 10), and the variables were compared between the two groups.

Results: The SUVmax, SUVmean, SUVpeak and SUVsd were significantly higher in patients with positive expression than in negative expression (all $p < 0.05$). Receiver operating characteristic curve analysis identified SUVmean (area under the curve [AUC] = 0.882, $p = 0.004$), SUVsd (AUC = 0.874, $p = 0.005$), SUVpeak (AUC = 0.840, $p = 0.010$) and SUVmax (AUC = 0.765, $p = 0.045$) as significant predictors of the PD-L1 positive expression, with cutoff values of 9.67, 1.90, 9.67 and 13.71, respectively. On univariate logistic regression analysis, SUVmean ($p = 0.045$), SUVsd ($p = 0.024$), and SUVpeak ($p = 0.031$) were significantly correlated with the PD-L1 positive expression. On multivariable logistic regression analysis, SUVsd ($p = 0.035$) was an optimum predictor factor for PD-L1 positive expression.

Conclusion: ^{18}F-FAPI-04 PET/CT parameters, including SUVmean, SUVpeak, and SUVsd, correlated with PD-L1 expression in patients with LA-ESCC, and thus SUVsd was an optimum predictor for PD-L1 positive expression, which could help to explore the existence of immune checkpoints and select ESCC candidates for immunotherapy.

KEYWORDS

fibroblast activation protein, positron emission tomography, PD-L1 expression, esophageal carcinoma, 18F-FAPI-04 PET/CT parameters

1 Introduction

Esophageal cancer (EC) is one of the most common malignant tumors of the digestive system in the world, ranking seventh in incidence and sixth in mortality overall in 2020 (1, 2). Esophageal squamous cell carcinoma (ESCC) is the main histological type of esophageal cancer in China. The prognosis for esophageal cancer is poor, with a 5-year survival rate of only 15%-25% worldwide (3). At present, the treatment options available are limited.

With the development and application of immunotherapy, programmed death ligand-1 (PD-L1) has been shown to significantly prolong the overall survival of EC patients with manageable safety (4–6). In 2019, the immune checkpoint inhibitor pembrolizumab was approved by the Food and Drug Administration (FDA) as a second-line therapy to treat patients with locally advanced or metastatic ESCC whose tumors are positively expressing PD-L1 (Combined Positive Score [CPS] ≥10) (5). Immunohistochemistry (IHC) expression of PD-L1 is the most widely used biomarker for predicting the efficacy of esophageal cancer immunotherapy, and accurate and reliable PD-L1 testing is crucial for screening potential beneficiaries of immunotherapy.

Fibroblast activation protein (FAP) is a member of the dipeptidyl peptidase 4 protein family and has both endopeptidase and dipeptidyl peptidase activities. FAP is highly expressed in stromal fibroblasts of more than 90% of epithelial carcinomas (7, 8). Research has shown that high expression of FAP in stromal fibroblasts of breast cancer, colon cancer, esophageal cancer and other malignant tumors is related to poor prognosis (9–11). ^{68}Ga-DOTAFAPI-04 has diagnostic and therapeutic potential in oncologic and nononcologic diseases (12, 13). ^{68}Ga-FAPI-04 has been explored the value of predicting treatment outcomes and prognosis for EC patients (14–16). We previously performed a pilot clinical study in which ^{18}F-FAPI-04, a novel tracer, was safe and offered high specificity for FAP imaging (17). However, the ability of ^{68}Ga-FAPI/^{18}F-FAPI-04 PET/CT to predict PD-L1 expression in EC needs to be validated by prospective studies.

The present study aimed to identify imaging parameters that could predict tumor PD-L1 expression by comparing ^{18}F-FAPI-04 PET/CT parameters between patients with EC classified as negative (CPS < 10) and positive expression (CPS ≥ 10). Identifying patients with PD-L1 positively expressed by imaging will help realize the individualized treatment of tumors and improve prognosis.

2 Methods

2.1 Patients

Potentially eligible locally advanced esophageal squamous cell carcinoma (LA-ESCC) patients were recruited at Shandong Cancer Hospital and Institute from June 2021 to July 2022 (Table 1). All patients volunteered to participate in this study, and the local ethics committee of Shandong Cancer Hospital and Institute approved the prospective study.

Patients were enrolled based on the following criteria: (1) histopathologically confirmed esophageal squamous cell carcinoma(T3~4N0~3M0); (2) age ≥ 18 years; (3) presence of measurable primary tumors;(4) PD-L1 expression assay was conducted and (5) ^{18}F-FAPI-04 PET/CT scanning was performed.

The exclusion criteria included: (1) pregnancy or breastfeeding; and (2) unwillingness to participate or withdraw. The flow chart of research and design is shown in Figure 1.

TABLE 1 Characteristics of enrolled LA-ESCC patients (N=24).

Characteristics		Number of cases (%)
Age (years)	≤60	11 (45.8)
	>60	13 (54.2)
Gender	Male	21 (87.5)
	Female	3 (12.5)
T stage	T3	24 (100.0)
	T4	0 (0.0)
N stage	N0	5 (20.8)
	N1	14 (58.3)
	N2	3 (12.5)
	N3	2 (8.3)
Tumor location	Cervical	0 (0.0)
	Upper	7 (29.2)
	Middle	10 (41.7)
	Lower	7 (29.2)

2.2 ^{18}F-FAPI-04 PET/CT scanning

^{18}F-FAPI-04 was synthesized as described previously (18). Patients were not required to fast or under blood glucose measurement before scanning. After intravenous injection of ^{18}F-FAPI-04 (4.81 MBq/kg), the patients needed to rest for approximately 1 h. Scanning was then performed with two different PET/CT(GE MINI TF Big Bore; Philips Healthcare, Cleveland, OH, USA). Whole-body CT scans were obtained using a low-dose protocol (300 mAs, 120 kV, a 512 × 512 matrix, rotation time of 1.0 s, and pitch index of 0.688; reconstructed with a soft-tissue kernel to a slice thickness of 2 mm) for attenuation correction. PET data were acquired in three-dimensional mode using a 200 × 200 matrix with an imaging time of 1 min per bed position. During image acquisition, the patients maintained normal shallow breathing. Subsequently, after attenuation and correction (Biograph 3D iterative reconstruction software, time of flight [TOF] correction), we viewed attenuation-corrected PET images, CT images, and PET/CT fusion images.

2.3 Imaging analysis

The attenuation-corrected CT images, PET images, and fused PET/CT images were displayed in coronal, sagittal, and transaxial

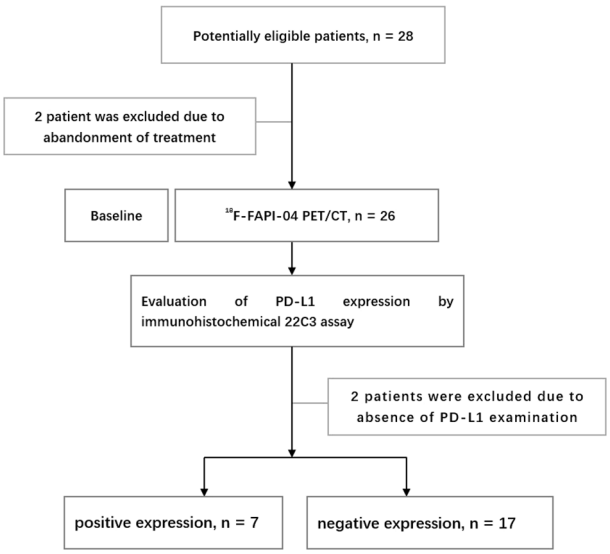

FIGURE 1
Research flowchart.

slices, which were viewed and analyzed on the Nuclear Medicine Information System (Beijing Mozi Healthcare Ltd, Beijing, China). Two experienced PET/CT physicians (J.Z. and J.R., with 18 and 6 years, respectively, of nuclear oncology experience) visually assessed the ^{18}F-FAPI-04 PET/CT images and reached a consensus regarding the image interpretations for primary tumors. Regions of interest were drawn around tumor lesions with higher uptake in transaxial sections, and ^{18}F-FAPI-04 PET/CT parameters were generated by an automated 3-dimensional contouring program with a 30% isocontour. The uptake values in the region of interest were normalised to the injected dose per kilogram of patient body weight, and the standardised uptake values were derived according to the following formula: [measured radioactivity concentration (Bq/mL) × body weight (g)]/injected radioactivity concentration (Bq). Regions of interest were drawn around the primary tumor lesion, and the obtained parameters, including SUVmax, SUVmean, SUVpeak, SUVsd, metabolic tumor volume (MTV), and total lesion FAP expression (TLF), were generated by an automated contouring program provided by the vendor. TLF (total lesion FAP expression) was calculated as the product of the SUVmean of the lesion and the MTV (TLF= SUVmean× MTV). We also measured the SUVmean of 1 cm^3 areas in the ascending aorta, liver and Lumbar 5 (L5) vertebrae. The circular region of interest (ROI) of 1cm3 was drawn in the normal regions of segments VII and VIII of the liver. The average of the liver SUVmean was calculated. The ratio of the SUVmax of the primary tumor to the SUVmean of the normal tissue (blood, liver and L5 vertebrae) is then calculated and is called the tumor to background ratio (TBRblood, TBRliver and TBRbone). For controversial lesions, discussion among the imaging experts with consideration of the results from other imaging modalities proceeded until a final consensus was reached.

2.4 Evaluation of PD-L1 expression by immunohistochemical 22C3 assay

In our study, PD-L1 expression in all patients was obtained by gastroscopic biopsy for pathological tissue of esophageal cancer.

PD-L1 expression was assessed by CPS, which was defined as the number of PD-L1 stained cells (tumor cells, lymphocytes and macrophages) divided by the total number of surviving tumor cells multiplied by 100. The maximum CPS is defined as 100. All other cells, such as tumor-associated plasma cells, neutrophils, normal/non-neoplastic cells, and necrotic cells, were excluded from the evaluation. The cutoff value was determined according to an FDA-approved test and the guidelines of pembrolizumab treatment and separated into two classifications: negative (CPS < 10) and positive expression (CPS ≥ 10) (5, 17). Patients without sufficient viable tumor cells (<100) were excluded. Each slide was blindly given a CPS for PD-L1 expression by two experienced pathologists. Both hematoxylin–eosin (HE) staining and PD-L1 IHC staining were assessed to reach a final CPS value. Two experienced pathologists (D.Z. and H.J., with 25 and 22 years, respectively, of oncology experience) evaluated pathological slides. Each case has a final consistent result after discussion.

2.5 Statistical analysis

Statistical analyzes were performed using SPSS software (version 27.0 for Windows; SPSS INC.). Continuous data were described as the mean ± standard deviation (mean ± SD) or median and interquartile, depending on whether they followed a normal distribution. and non-normally distributed data (including MTV) was expressed as the median and interquartile. Comparisons of normally distributed data between the two groups were performed using a paired two-sample t test, and comparisons of non-normally distributed data between the two groups were performed using the Mann–Whitney U test. Binary logistic regression analyses were performed to ascertain the relationships between ^{18}F-FAPI-04 PET/CT parameters, tumor location, degree of differentiation and PD-L1 expression. Receiver operating characteristic (ROC) curve analysis was used to determine the threshold values with the maximum Youden index of ^{18}F-FAPI-04 PET/CT parameters for PD-L1 positive expression. Spearman rank correlation coefficients were calculated to assess the relationship between ^{18}F-FAPI-04 PET/CT parameters and PD-L1 expression. All tests were two-sided, and a probability of less than 0.05 was considered statistically significant.

3 Results

3.1 Patients' characteristics

From June 2021 to July 2022, 24 patients diagnosed with LA-ESCC based on histological examinations at Shandong Cancer Hospital and Institute were enrolled in this study. The characteristics of the patients are presented in Table 1. Among all patients, 17 patients were classified as negative expression (CPS < 10), and 7 patients as positive expression (CPS ≥ 10). Figure 2 shows

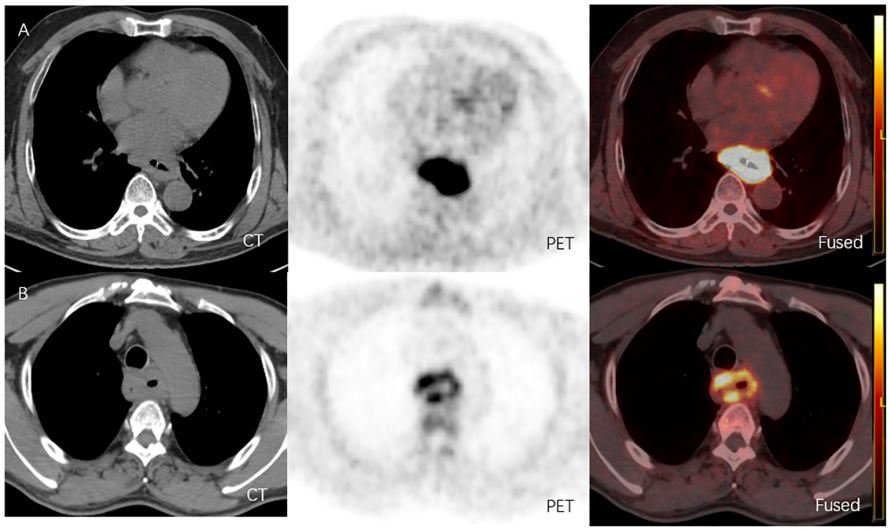

FIGURE 2
(A) 18F-FAPI-04 PET/CT and CT images of a LA-ESCC patient with an outcome classified as PD-L1 positive expression(CPS about 70), with SUVmax 15.36, SUVmean 8.60, SUVpeak 11.02, SUVsd 2.47, MTV 51.52 cm3 and TLF 443.07g. **(B)** 18F-FAPI-04 PET/CT and CT images of a LA-ESCC patient with an outcome classified as PD-L1 positive expression(CPS<1) , with SUVmax 6.45, SUVmean 3.36, SUVpeak 4.51, SUVsd 0.89, MTV 53.99 cm3 and TLF 181.41g.

representative ^{18}F-FAPI-04 PET/CT imaging results for two cases classified as positive and negative PD-L1 expression.

3.2 Quantitative ^{18}F-FAPI-04 PET/CT parameters

The quantitative ^{18}F-FAPI-04 PET/CT parameters SUVmax, SUVmean, SUVpeak, SUVsd, MTV and TLF are shown in Table 2 for all patients, negative (CPS < 10) and positive expression (CPS≥10) patients. SUVmax, SUVmean, SUVpeak, and SUVsd were significantly higher in positive expression patients than in negative (14.13 ± 4.41 vs. 10.61 ± 2.77, p = 0.027; 8.67 ± 1.97 vs. 5.74 ± 1.60, p<0.001; 11.15 ± 2.90 vs.7.77 ± 2.31, p = 0.006 and 2.57 ± 0.48 vs. 1.73 ± 0.59, p = 0.003) (Table 2). None of the other parameters showed a significant difference between negative and positive PD-L1 expression.

3.3 The ability of ^{18}F-FAPI-04 PET/CT parameters to predict PD-L1 expression

ROC curves were generated to evaluate the predictive accuracy of ^{18}F-FAPI-04 PET/CT parameters for identifying negative and positive expression patients (Table 3; Figure 3). The AUC value for SUVmean (AUC = 0.882) was higher than those for SUVsd (AUC =0.874), SUVpeak (AUC =0.840) and SUVmax (AUC=0.765) (Table 3), while the AUC values for all four parameters were significant (p = 0.004, p = 0.005, p = 0.010 and p = 0.045, respectively) (Table 3). The cutoff values for SUVmean, SUVsd, SUVpeak and SUVmax, based on the Youden indexes, were 7.38, 1.90, 9.67 and 13.71, respectively (Table 3).

TABLE 2 Parameters calculated from ^{18}F-FAPI-04 PET/CT scans.

Parameters	All patients (n=24)	Negative expression (n=17)	Positive expression (n=7)	P-value
TBR_{blood}	9.49 ± 0.56	9.08 ± 2.39	10.49 ± 3.52	0.265
TBR_{liver}	9.83 ± 0.84	8.84 ± 3.35	12.23 ± 4.99	0.064
TBR_{bone}	9.76 ± 1.00	9.15 ± 4.17	11.22 ± 6.51	0.360
SUVmax*	11.64 ± 0.74	10.61 ± 2.77	14.13 ± 4.41	0.027
SUVmean*	6.59 ± 0.44	5.74 ± 1.60	8.67 ± 1.97	<0.001
SUVpeak*	8.76 ± 0.59	7.77 ± 2.31	11.15 ± 2.90	0.006
SUVsd*	1.98 ± 0.14	1.73 ± 0.59	2.57 ± 0.48	0.003
MTV (cm^3)	26.55 ± 3.64	18.55 (14.18,37.01)	23.46 (10.46,51.52)	0.930
TLF (g)	182.54 ± 31.73	279.52 ± 246.98	142.62 ± 77.82	0.197

*P < 0.05.

TABLE 3 Areas under the curve for the ability of ^{18}F-FAPI-04 PET/CT parameters to predict PD-L1 expression.

Parameters	AUC	Threshold	p	95%CI		Sensitivity	Specificity
				Lower bound	Upper bound		
SUVmax*	0.765	>13.71	0.045	0.520	1.000	71.43	88.24
SUVmean*	0.882	>7.38	0.004	0.718	1.000	85.71	88.24
SUVpeak*	0.840	>9.67	0.010	0.665	1.000	85.71	82.35
SUVsd*	0.874	>1.90	0.005	0.733	1.000	100	80.59
MTV	0.563	>18.55	0.634	0.269	0.857	71.43	52.94
TLF	0.639	>231.98	0.295	0.344	0.933	57.14	88.24
TBR_{blood}	0.655	>12.848	0.290	0.436	0.835	42.86	100.00
TBR_{liver}	0.706	>12.32	0.124	0.487	0.872	57.14	88.24
TBR_{bone}	0.588	>16.685	0.548	0.371	0.783	28.57	100.00

*P < 0.05.

3.4 Correlations between ^{18}F-FAPI-04 PET/CT parameters and PD-L1 expression

We found a moderate correlation between SUVsd, SUVean, SUVPeak, SUVmax and PD-L1 expression (rs=0.584,p=0.003; rs=0.571,p=0.004; rs=0.511,p=0.011; rs=0.462,p=0.024, respectively). The correlation between ^{18}F-FAPI-04PET/CT biomarkers extracted from tumor lesions and PD-L1 expression is shown in Table 4.

3.5 Associations between ^{18}F-FAPI-04 PET/CT parameters, clinical features and PD-L1 expression

According to univariate logistic regression analyses, SUVmean (p = 0.026), SUVpeak (p = 0.031), and SUVsd (p = 0.024) were independently associated with the PD-L1 expression in LA-ESCC patients (Table 5). Due to the moderate positive correlation among SUVmean, SUVsd and SUVpeak, we only included SUVsd (the

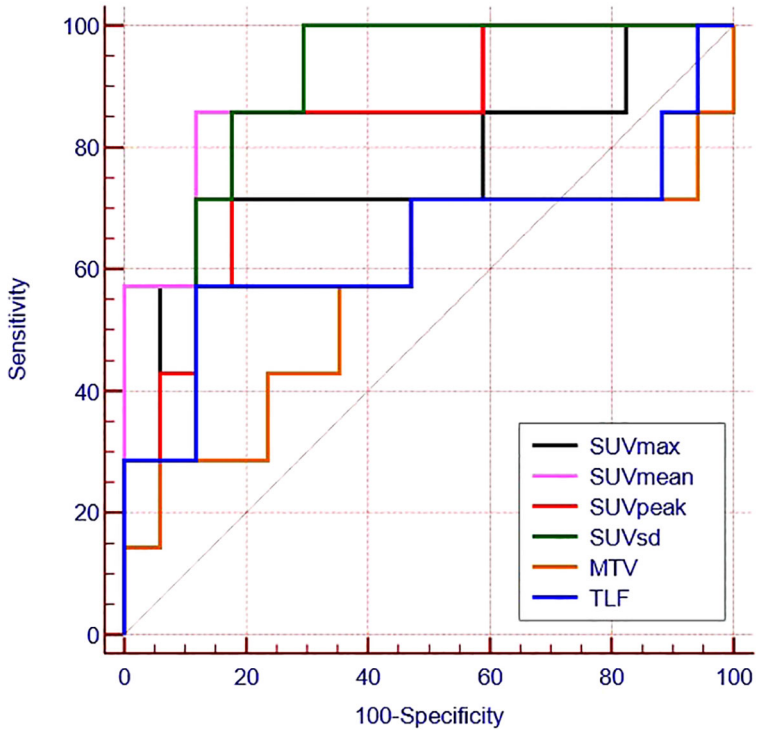

FIGURE 3
Receiver operating characteristic curves for the ability of 18F -FAPI-04 PET/CT parameters to predict PD-L1 expression.

TABLE 4 Correlations between ^{18}F-FAPI-04 PET/CT parameters and PD-L1 expression.

^{18}F-FAPI-04 PET/CT Parameters										
PD-L1 expression		SUVmax*	SUVmean*	SUVpeak*	SUVsd*	MTV	TLF	TBR_{blood}	TBR_{liver}	TBR_{bone}
	rs	0.462	0.571	0.511	0.584	-0.016	0.012	0.205	0.270	0.092
	p	0.024	0.004	0.011	0.003	0.941	0.956	0.337	0.203	0.671

*P < 0.05.

largest correlation coefficient) and TBRliver (p = 0.059) in the multivariate logistic analysis. Finally, only SUVsd (p = 0.035) was an optimum predictor of PD-L1 expression in these patients (Table 5).

4 Discussion

ESCC is the most common type of esophageal cancer, and about 46.8% of ESCC showed positive PD-L1 expression (19). PD-L1 expression in ESCC is an indicator for immunotherapy and a potential prognostic marker for untreated ESCC patients (20, 21). ^{68}Ga-FAPI-04 PET/CT can not only better display the primary tumor and regional lymph nodes, but also the high uptake rate and low background activity of esophageal cancer to facilitate accurate delineation of the target area (22). Therefore, whether parameters from ^{18}F/^{68}Ga-FAPI-04 PET/CT scans can predict PD-L1 expression in esophageal cancer warrants a prospective study.

In 2019, the immune checkpoint inhibitor pembrolizumab was approved by the Food and Drug Administration (FDA) as a second-line therapy to treat patients with locally advanced or metastatic ESCC whose tumors are positively expressing PD-L1 (Combined Positive Score [CPS] ≥10) (22). Therefore, we chose CPS ≥10 as PD-L1 positive expression in our study and investigated PD-L1 expression correlation with parameters of ^{18}F- FAPI-04 PET/CT and clinicopathological characteristics in ESCC.

^{18}F-FDG PET/CT can predict tumor microenvironment and PD-L1 expression in many tumors (14, 23). It has been reported that ^{18}F-FDG PET/CT can provide metabolic information on tumor immune microenvironment in breast cancer and clear cell renal cell carcinoma (23, 24). Many literatures reported that SUVmax of ^{18}F-FDG PET/CT could predict PD-L1 expression in lung adenocarcinomas and squamous cell carcinomas (25, 26). Meanwhile, SUVmax could predict PD-L1 status in cervical cancer (27). These all revealed that the tumor lesion FDG activity (glucose activity) was mainly associated with PD-L1 positive expression.

In our study, the results suggest that specific parameters derived from ^{18}F-FAPI-04 PET/CT scans, particularly SUVmean, SUVpeak, and SUVsd were associated with predicting PD-L1 expression of ESCC. By multivariable logistic regression analysis, SUVsd was an optimum predictor for PD-L1 positive expression in ESCC. SUVsd could reflect intratumoral heterogeneity (28–31). The tumor microenvironment can promote the heterogeneity of tumors, including fibroblasts, vascular and immune cells, and the extracellular matrix (32, 33), which also impacts the PD-L1 expression. Thus, different from the correlation between PD-L1 expression and tumor glucose activity (FDG activity) in ^{18}F-FDG PET/CT imaging, SUVsd was an optimal predictor of PD-L1

TABLE 5 Univariate and multivariate logistic regression analyses of ^{18}F-FAPI-04 PET/CT parameters and clinical factors for predicting PD-L1 expression.

Factor	Univariate analysis		Multivariate analysis	
	OR (95% CI)	p-value	OR (95% CI)	p-value
Differentiation degree	1.20 (0.13-11.05)	0.998	–	–
Location	6.0 (0.52-69.75)	0.152	–	–
SUVmax	1.38 (0.99-1.92)	0.051	–	–
SUVmean *	3.10 (1.14-8.41)	0.026	–	–
SUVpeak *	1.74 (1.05-2.87)	0.031	–	–
SUVsd *	16.93 (1.45-19.87)	0.024	3.182 (1.085-9.334)	0.035
MTV	1.02 (0.97-1.07)	0.386	–	–
TLF	1.00 (1.00-1.02)	0.114	–	–
TBR_{blood}	1.219 (0.865-1.718)	0.257	–	–
TBR_{liver}	1.257 (0.966-1.635)	0.059	0.972 (0.646-1.462)	0.892
TBR_{bone}	1.092 (0.908-1.313)	0.348	–	–

*P < 0.05.
-,This parameter was not multivariate analyzed.

positive expression in ^{18}F-FAPI-04 PET/CT imaging, which may be related to its can reflect tumor microenvironment.

The main limitations of the present study include its single-center design and the relatively small sample size. Further large-scale, multi-center clinical studies are needed to confirm our findings before their clinical application. Additionally, many antibodies in PD-L1 expression detection, such as 22C3, SP263, SP142, etc. We use 22C3 for PD-L1 expression detection in our hospital, and the correlation between other methods for PD-L1 expression and ^{18}F-FAPI-04 PET/CT parameters needs further study. In addition, probably due to the short follow-up period or small sample size, the ^{18}F-FAPI-04 PET/CT parameters could not predict the prognosis of the patients, and we will continue to study this topic.

5 Conclusion

^{18}F-FAPI-04 PET/CT parameters, including SUVmean, SUVpeak, and SUVsd, were associated with PD-L1 expression in patients with LA-ESCC, and thus, SUVsd was an optimal predict for PD-L1 positive expression, which could help to explore the existence of immune checkpoints and select ESCC candidates for immunotherapy.

Data availability statement

The original contributions presented in the study are included in the article/supplementary material. Further inquiries can be directed to the corresponding author.

Ethics statement

The studies involving humans were approved by Tumour Hospital of Shandong First Medical University. The studies were conducted in accordance with the local legislation and institutional requirements. The participants provided their written informed consent to participate in this study.

Author contributions

YZ: Writing – original draft, Data curation. JR: Software, Writing – original draft, Writing – review & editing.

Funding

The author(s) declare that no financial support was received for the research, authorship, and/or publication of this article.

Acknowledgments

We thank experienced nuclear medicine physician J.Z. and pathologist (D.Z. and H.J.,) for their help.

Conflict of interest

The authors declare that the research was conducted in the absence of any commercial or financial relationships that could be construed as a potential conflict of interest.

Publisher's note

References

1. Siegel RL, Miller KD, Fuchs HE, Jemal A. Cancer statistics, 2022. *CA Cancer J Clin* (2022) 72:7–33. doi: 10.3322/caac.21708

2. Sung H, Ferlay J, Siegel RL, Laversanne M, Soerjomataram I, Jemal A, et al. Global cancer statistics 2020: GLOBOCAN estimates of incidence and mortality worldwide for 36 cancers in 185 countries. *CA Cancer J Clin* (2021) 71:209–49. doi: 10.3322/caac.21660

3. Uhlenhopp DJ, Then EO, Sunkara T, Gaduputi V. Epidemiology of esophageal cancer: update in global trends, etiology and risk factors. *Clin J Gastroenterol* (2020) 13:1010–21. doi: 10.1007/s12328-020-01237-x

4. Huang J, Xu J, Chen Y, Zhuang W, Zhang Y, Chen Z, et al. Camrelizumab versus investigator's choice of chemotherapy as second-line therapy for advanced or metastatic oesophageal squamous cell carcinoma (ESCORT): a multicentre, randomised, open-label, phase 3 study. *Lancet Oncol* (2020) 21:832–42. doi: 10.1016/S1470-2045(20)30110-8

5. Kato K, Cho BC, Takahashi M, Okada M, Lin CY, Chin K, et al. Nivolumab versus chemotherapy in patients with advanced oesophageal squamous cell carcinoma refractory or intolerant to previous chemotherapy (ATTRACTION-3): a multicentre, randomised, open-label, phase 3 trial. *Lancet Oncol* (2019) 20:1506–17. doi: 10.1016/S1470-2045(19)30626-6

6. Shah MA, Kojima T, Hochhauser D, Enzinger P, Raimbourg J, Hollebecque A, et al. Efficacy and safety of pembrolizumab for heavily pretreated patients with advanced, metastatic adenocarcinoma or squamous cell carcinoma of the esophagus: the phase 2 KEYNOTE-180 study. *JAMA Oncol* (2019) 5:546–50. doi: 10.1001/jamaoncol.2018.5441

7. Zi F, He J, He D, Li Y, Yang L, Cai Z. Fibroblast activation protein alpha in tumor microenvironment: recent progression and implications (review). *Mol Med Rep* (2015) 11:3203–11. doi: 10.3892/mmr.2015.3197

8. Altmann A, Haberkorn U, Siveke J. The latest developments in imaging of fibroblast activation protein. *J Nucl Med* (2021) 62:160–7. doi: 10.2967/jnumed.120.244806

9. Shi M, Yu DH, Chen Y, Zhao CY, Zhang J, Liu QH, et al. Expression of fibroblast activation protein in human pancreatic adenocarcinoma and its clinicopathological significance. *World J Gastroenterol* (2012) 18:840–6. doi: 10.3748/wjg.v18.i8.840

10. Park H, Lee Y, Lee H, Kim JW, Hwang JH, Kim J, et al. The prognostic significance of cancer-associated fibroblasts in pancreatic ductal adenocarcinoma. *Tumour Biol* (2017) 39:1010428317718403. doi: 10.1177/1010428317718403

11. Saigusa S, Toiyama Y, Tanaka K, Yokoe T, Okugawa Y, Fujikawa H, et al. Cancer-associated fibroblasts correlate with poor prognosis in rectal cancer after chemoradiotherapy. *Int J Oncol* (2011) 38:655–63. doi: 10.3892/ijo.2011.906

12. Mori Y, Dendl K, Cardinale J, Kratochwil C, Giesel FL, Haberkorn U. FAPI PET: fibroblast activation protein inhibitor use in oncologic and nononcologic disease. *Radiology* (2023) 306:e220749. doi: 10.1148/radiol.220749

13. Wang L, Tang G, Hu K, Liu X, Zhou W, Li H, et al. Comparison of (68)Ga-FAPI and (18)F-FDG PET/CT in the evaluation of advanced lung cancer. *Radiology* (2022) 303:191–9. doi: 10.1148/radiol.211424

14. Hu X, Zhou T, Ren J, Duan J, Wu H, Liu X, et al. Response prediction using (18) F-FAPI-04 PET/CT in patients with esophageal squamous cell carcinoma treated with concurrent chemoradiotherapy. *J Nucl Med* (2023) 64:625–31. doi: 10.2967/jnumed.122.264638

15. Zhao L, Pang Y, Chen S, Chen J, Li Y, Yu Y, et al. Prognostic value of fibroblast activation protein expressing tumor volume calculated from [(68) Ga]Ga-FAPI PET/CT in patients with esophageal squamous cell carcinoma. *Eur J Nucl Med Mol Imaging* (2023) 50:593–601. doi: 10.1007/s00259-022-05989-1

16. Liu Q, Shi S, Xu X, Yu X, Song S. The superiority of [(68)Ga]-FAPI-04 over [(18) F]-FDG PET/CT in imaging metastatic esophageal squamous cell carcinoma. *Eur J Nucl Med Mol Imaging* (2021) 48:1248–9. doi: 10.1007/s00259-020-04997-3

17. Wei Y, Zheng J, Ma L, Liu X, Xu S, Wang S, et al. [(18)F]AlF-NOTA-FAPI-04: FAP-targeting specificity, biodistribution, and PET/CT imaging of various cancers. *Eur J Nucl Med Mol Imaging* (2022) 49:2761–73. doi: 10.1007/s00259-022-05758-0

18. Wei Y, Cheng K, Fu Z, Zheng J, Mu Z, Zhao C, et al. [(18)F]AlF-NOTA-FAPI-04 PET/CT uptake in metastatic lesions on PET/CT imaging might distinguish different pathological types of lung cancer. *Eur J Nucl Med Mol Imaging* (2022) 49:1671–81. doi: 10.1007/s00259-021-05638-z

19. Huang Z, Jin Y, Cai X, Chen L, Shen X, Li B, et al. Association of the programmed death ligand-1 combined positive score in tumors and clinicopathological features in esophageal cancer. *Thorac Cancer* (2022) 13:523–32. doi: 10.1111/1759-7714.14285

20. Rong L, Liu Y, Hui Z, Zhao Z, Zhang Y, Wang B, et al. PD-L1 expression and its clinicopathological correlation in advanced esophageal squamous cell carcinoma in a Chinese population. *Diagn Pathol* (2019) 14:6. doi: 10.1186/s13000-019-0778-4

21. Yagi T, Baba Y, Ishimoto T, Iwatsuki M, Miyamoto Y, Yoshida N, et al. PD-L1 expression, tumor-infiltrating lymphocytes, and clinical outcome in patients with surgically resected esophageal cancer. *Ann Surg* (2019) 269:471–8. doi: 10.1097/SLA.0000000000002616

22. Peng D, He J, Liu H, Cao J, Wang Y, Chen Y. FAPI PET/CT research progress in digestive system tumours. *Dig Liver Dis* (2022) 54:164–9. doi: 10.1016/j.dld.2021.07.011

23. Wu C, Cui Y, Liu J, Ma L, Xiong Y, Gong Y, et al. Noninvasive evaluation of tumor immune microenvironment in patients with clear cell renal cell carcinoma using metabolic parameter from preoperative 2-[(18)F]FDG PET/CT. *Eur J Nucl Med Mol Imaging* (2021) 48:4054–66. doi: 10.1007/s00259-021-05399-9

24. Kimura Y, Sasada S, Emi A, Masumoto N, Kadoya T, Arihiro K, et al. (18)F-fluorodeoxyglucose positron emission tomography/computed tomography predicts tumor immune microenvironment function in early triple-negative breast cancer. *Anticancer Res* (2023) 43:127–36. doi: 10.21873/anticanres.16141

25. Wu X, Huang Y, Zhao Q, Wang L, Song X, Li Y, et al. PD-L1 expression correlation with metabolic parameters of FDG PET/CT and clinicopathological characteristics in non-small cell lung cancer. *EJNMMI Res* (2020) 10:51. doi: 10.1186/s13550-020-00639-9

26. Cui Y, Li X, Du B, Diao Y, Li Y. PD-L1 in lung adenocarcinoma: insights into the role of (18)F-FDG PET/CT. *Cancer Manag Res* (2020) 12:6385–95. doi: 10.2147/CMAR.S256871

27. Ji J, Pang W, Song J, Wang X, Tang H, Liu Y, et al. Retrospective analysis of the predictive value of (18)F-FDG PET/CT metabolic parameters for PD-L1 expression in cervical cancer. *Diagnostics (Basel)* (2023) 13:1015. doi: 10.3390/diagnostics13061015

28. Zhou W, Zhou Z, Wen J, Xie F, Zhu Y, Zhang Z, et al. A nomogram modeling (11)C-MET PET/CT and clinical features in glioma helps predict IDH mutation. *Front Oncol* (2020) 10:1200. doi: 10.3389/fonc.2020.01200

29. Yeh R, Trager MH, Rizk EM, Finkel GG, Barker LW, Carvajal RD, et al. FLT-PET at 6 weeks predicts response assessed by CT at 12 weeks in melanoma patients treated with pembrolizumab. *Clin Nucl Med* (2020) 45:267–75. doi: 10.1097/rlu.0000000000002967

30. Ke L, Wu L, Yu J, Meng X. Feasibility of semiquantitative 18F-fluorodeoxyglucose PET/computed tomography in patients with advanced lung cancer for interim treatment evaluation of combining immunotherapy and chemotherapy. *Nucl Med Commun* (2021) 42:1017–23. doi: 10.1097/mnm.0000000000001428

31. Hua T, Zhou W, Zhou Z, Guan Y, Li M. Heterogeneous parameters based on 18F-FET PET imaging can non-invasively predict tumor grade and isocitrate dehydrogenase gene 1 mutation in untreated gliomas. *Quantitative Imaging Med Surgery* (2021) 11:317–27. doi: 10.21037/qims-20-723

32. Ren Q, Zhang P, Lin H, Feng Y, Chi H, Zhang X, et al. A novel signature predicts prognosis and immunotherapy in lung adenocarcinoma based on cancer-associated fibroblasts. *Front Immunol* (2023) 14:1201573. doi: 10.3389/fimmu.2023.1201573

33. Kieffer Y, Hocine HR, Gentric G, Pelon F, Bernard C, Bourachot B, et al. Single-cell analysis reveals fibroblast clusters linked to immunotherapy resistance in cancer. *Cancer Discov* (2020) 10:1330–51. doi: 10.1158/2159-8290.CD-19-1384

frontiers | Frontiers in Immunology

TYPE Original Research
PUBLISHED 15 November 2023
DOI 10.3389/fimmu.2023.1198826

OPEN ACCESS

EDITED BY
Vera Rebmann,
University of Duisburg-Essen, Germany

REVIEWED BY
Taobo Hu,
Peking University People's Hospital, China
Tianyun Long,
University of California, San Diego, United States
Parul Singh,
National Heart, Lung, and Blood Institute (NIH), United States
Shruti Mishra,
Gilead, United States

*CORRESPONDENCE
Zhiyao Ren
zhiyao.ren@ugent.be
Min Ren
renmin@ahmu.edu.cn

†These authors have contributed equally to this work and share first authorship

‡These authors have contributed equally to this work and share last authorship

RECEIVED 02 April 2023
ACCEPTED 31 October 2023
PUBLISHED 15 November 2023

CITATION
Liang J, Wang X, Yang J, Sun P, Sun J, Cheng S, Liu J, Ren Z and Ren M (2023) Identification of disulfidptosis-related subtypes, characterization of tumor microenvironment infiltration, and development of a prognosis model in breast cancer.
Front. Immunol. 14:1198826.
doi: 10.3389/fimmu.2023.1198826

Identification of disulfidptosis-related subtypes, characterization of tumor microenvironment infiltration, and development of a prognosis model in breast cancer

Jiahui Liang[1†], Xin Wang[2†], Jing Yang[1†], Peng Sun[3], Jingjing Sun[1], Shengrong Cheng[4], Jincheng Liu[1], Zhiyao Ren[2*‡] and Min Ren[1*‡]

[1]Department of Breast Surgery, Department of General Surgery, The First Affiliated Hospital of Anhui Medical University, Hefei, Anhui, China, [2]Faculty of Medicine and Health Sciences, Ghent University, Ghent, Belgium, [3]Department of Respiratory and Critical Care Medicine, The First Affiliated Hospital of Anhui Medical University, Hefei, China, [4]Department of Plastic Surgery, The First Affiliated Hospital of Anhui Medical University, Hefei, China

Introduction: Breast cancer (BC) is now the most common type of cancer in women. Disulfidptosis is a new regulation of cell death (RCD). RCD dysregulation is causally linked to cancer. However, the comprehensive relationship between disulfidptosis and BC remains unknown. This study aimed to explore the predictive value of disulfidptosis-related genes (DRGs) in BC and their relationship with the TME.

Methods: This study obtained 11 disulfidptosis genes (DGs) from previous research by Gan et al. RNA sequencing data of BC were downloaded from the Cancer Genome Atlas (TCGA) and Gene Expression Omnibus database (GEO) databases. First, we examined the effect of DG gene mutations and copy number changes on the overall survival of breast cancer samples. We then used the expression profile data of 11 DGs and survival data for consensus clustering, and BC patients were divided into two clusters. Survival analysis, gene set variation analysis (GSVA) and ss GSEA were used to compare the differences between them. Subsequently, DRGs were identified between the clusters used to perform Cox regression and least absolute shrinkage and selection operator regression (LASSO) analyses to construct a prognosis model. Finally, the immune cell infiltration pattern, immunotherapy response, and drug sensitivity of the two subtypes were analyzed. CCK-8 and a colony assay obtained by knocking down genes and gene sequencing were used to validate the model.

Result: Two DG clusters were identified based on the expression of 11DGs. Then, 225 DRGs were identified between them. RS, composed of six genes, showed a significant relationship with survival, immune cell infiltration, clinical characteristics, immune checkpoints, immunotherapy response, and drug sensitivity. Low-RS shows a better prognosis and higher immunotherapy response than high-RS. A nomogram with perfect stability constructed using

signature and clinical characteristics can predict the survival of each patient. CCK-8 and colony assay obtained by knocking down genes have demonstrated that the knockdown of high-risk genes in the RS model significantly inhibited cell proliferation.

Discussion: This study elucidates the potential relationship between disulfidptosis-related genes and breast cancer and provides new guidance for treating breast cancer.

KEYWORDS

breast cancer, disulfidptosis, tumor microenvironments, prognosis, immunotherapy

1 Introduction

In recent years, the incidence of breast cancer in women has continued to grow at a rate of 0.5% per year. By 2022, breast cancer has surpassed lung cancer and has become the world's highest incidence of tumors. According to the latest estimates, there will be 297,790 new breast cancer cases and 43,170 deaths among women in the United States in 2023, making it the leading cause of cancer death among women aged 20-49 (1). Many treatment options for BC have been developed, including surgery, chemotherapy, endocrine therapy, immune antibody (trastuzumab) therapy, and radiotherapy, based on disease stage and pathological characteristics (2, 3). Although the prognosis of breast cancer has improved significantly in the past few decades, even if patients pass standard diagnosis and treatment, 20–30% of BC patients still have distant metastasis, accounting for about 90% of all breast cancer deaths (2).

As a highly complex and heterogeneous disease with different molecular spectrums, breast cancer limits the broad application of classification and standard treatment to some extent. Furthermore, it is difficult to predict the prognosis of BC (2, 4). Therefore, we urgently need to explore the characteristics of the high-risk population of breast cancer patients to obtain the key markers of prognosis and to find potential therapeutic targets to designate individualized treatment to improve the prognosis of patients.

SLC7A11-mediated cystine reduction to cysteine highly depends on the reduced nicotinamide adenine dinucleotide phosphate (NADPH) generated by the glucose–pentose phosphate pathway. Under glucose starvation, the NADPH in SLC7A11-high-expression cells is consumed in large quantities, and the abnormal accumulation of disulfides, such as those in cystine, induces disulfide stress. This causes actin filaments to aggregate and contract rapidly, peeling off the plasma membrane before apparent cell death, called disulfidptosis. During this process, SLC7A11 and SLC3A2, which encode the SLC7A11 chaperone protein, mediate the reduction of ingested cystine to cysteine. Next, the WAVE regulatory complex (WRC) can activate seven subunits of actin-related protein 2 and 3 (Arp2/3) complexes to promote actin polymerization and plate pseudopod formation. This produces a branched cortical actin network under the plasma membrane, thereby stripping actin filaments from the plasma membrane. Nck-related protein 1 encoded by NCKAP1 is a WRC component. Its deletion will reduce the protein levels of other components in the WRC, including WAVE-2, CYFIP 1, Abi 2, and HSPC 300, and inhibit disulfidptosis. Similarly, knocking out the other four components of the WRC will also repress disulfidptosis. Finally, Rac can activate WRC to promote plate pseudopod formation and disulfidptosis. Knockout of the RPN1 gene, which encodes an N-oligosaccharide transferase in the endoplasmic reticulum, will offer UMRC6 cells stronger resistance to disulfidptosis.

However, DRGs have not been demonstrated in the survival prognosis, tumor immune microenvironment, TMB, immunity, and clinical treatment of BC patients. We still lack direct evidence of the predictive ability of DRGs for BC prognosis and immunotherapy. This study aimed to construct a risk score (RS) model based on DRGs to predict the prognosis of BC patients. In this study, TCGA and GEO databases were used to obtain DRGs by analyzing the difference in consensus clustering of DGs. The RS model of DRGs was built using the LASSO-Cox method. Further, we verified that this feature could be used as a reliable, independent predictor of prognosis and immune-sensitive response and could predict the prognosis of BC patients. Through this model, patients were divided into high-risk and low-risk groups. The differences in survival outcomes, tumor immune microenvironment, and immunotherapy response of BC patients were analyzed. According to the differences between groups, drug sensitivity studies were conducted to find sensitive drugs in different populations, and individualized intervention was implemented to improve the prognosis of BC patients.

2 Methods

2.1 Data collection and processing

We downloaded and organized 1,180 samples (1,081 tumor and 99 normal samples) from the TCGA database using the

TCGAbiolinks and SummaryExperiment package in R v.4.2.2 (Supplementary Table 1). We searched the GEO database with "breast cancer" and "survival information" as keywords and screened according to the following criteria: first, all samples were from humans; second, all data sets included matched cancer tissue samples and clinical information; and third, the data set contained at least 200 samples. We downloaded the GSE12276 and GSE20685 gene expression profile, GPL570 platform annotation information, and clinical information using GEOquery, the data transmission tool of the GDC application. Gene expression profiles were standardized using the scaling method provided in the limma R package (5). TCGA and GEO gene expression profile information and clinical data are publicly available and open access. Therefore, no ethical issues were involved. Clinicopathologic features include gender, age, T (tumor) stage, N (lymph node metastasis) status, M (distant metastasis) status, tumor grade, survival status, and survival time. The tumor mutation data were derived from TCGA [GDC (cancer.gov)], and the gene copy number was downloaded from the Xena database (UCSC Xena). We obtained 11 disulfidptosis genes (DGs) from a previous study (6). The workflow of the current study is shown in Figure 1.

2.2 Survival, TMB, and CNV difference analysis between DGs

We used the Limma package using wilcox.test to test the difference in DG expression between tumor and normal samples ($p < 0.05$). R package survival and survminer were used for the survival analysis of DGs. DGs were divided into high- and low-expression groups according to gene expression. The survival differences between the two groups were compared ($p < 0.05$). Tumor mutation burden (TMB) refers to the number of somatic nonsynonymous mutations or all mutations per megabase in the gene region detected by whole exome sequencing or targeted sequencing in a tumor sample (7). Mutation data were downloaded from the Cancer Genome Atlas Breast Cancer (TCGA-BRCA) collection using the GDCquery package with 988 data downloads. According to the data.category = Simple Nucleotide Variation, data.type = Masked Somatic Mutation. The mutation data were analyzed with the R package maftools (8). The mutation probability of DGs in each tumor sample was calculated and analyzed. CNV (Copy Number Variation) is the increase or decrease in the copy number of genomic fragments caused by genome rearrangement. Xena downloaded and collated copy number

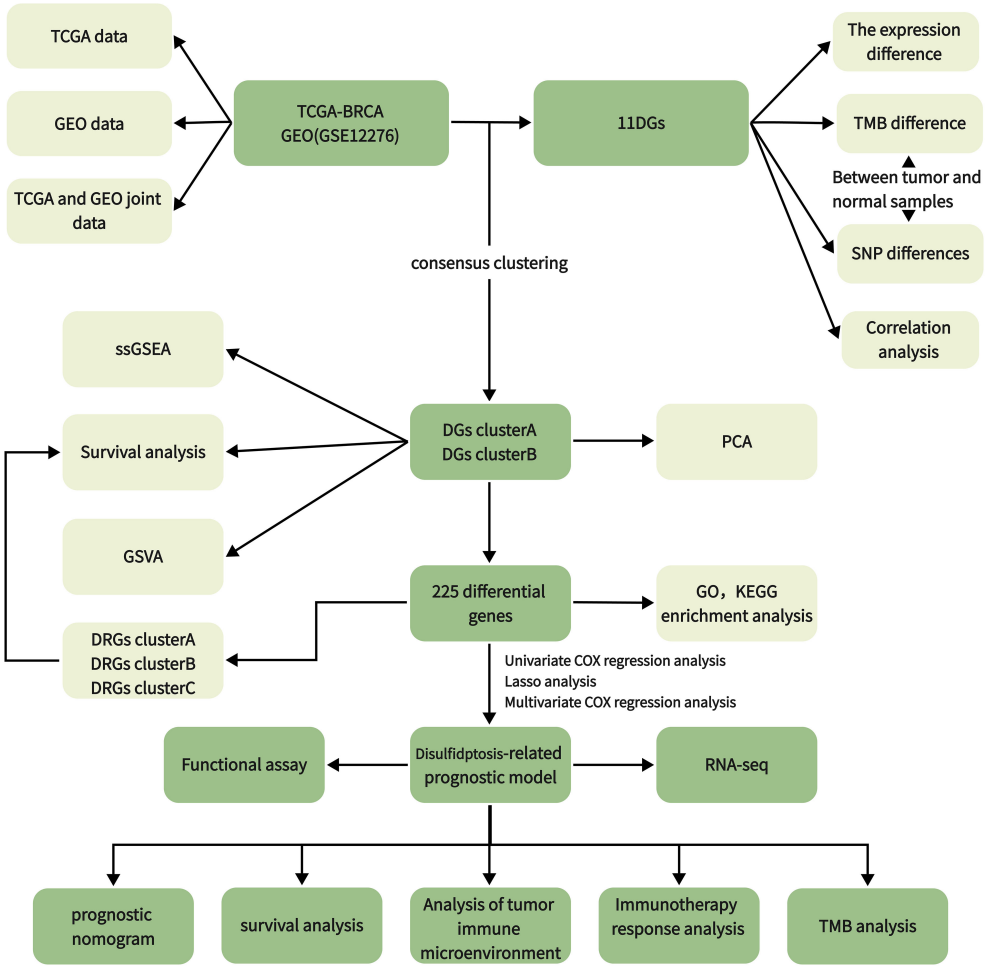

FIGURE 1
Workflow diagram.

variation data and used R-package RCircos to visualize the CNV of DGs.

2.3 Establishment of the disulfidptosis gene cluster

We used the R software package "ConsensusCluster Plus" for consensus clustering analysis and identified clusters of BC patients based on DGs. We set the cluster count (k) between two and nine and selected the optimal k value based on the sum of squared errors (SSE) inflection point. The stability of the DG group was verified by the PCA algorithm. Additionally, Kaplan-Meier survival analysis evaluated the OS of different DG clusters, and the heat map showed the degree of difference in DGs between the two groups.

2.4 TME infiltration and functional enrichment analysis of different clusters

Gene set variation analysis (GSVA) is a particular gene set enrichment method. This method works on single samples and enables pathway-centric analyses of molecular data by performing a conceptually simple but powerful change in the functional unit of analysis from genes to gene sets. We used the GSVA and GSEABase packages to evaluate the pathways enriched in groups A and B. We attempted to explain the reasons for the difference in survival between the groups from the bioinformatics perspective (9). Single sample gene set enrichment analysis (ssGSEA) was used to quantitatively analyze the immune infiltration of the overall sample and to observe the difference in component immune infiltration (10). We used the "limma" R package to analyze the DRGs between the two disulfidptosis clusters ($p < 0.05$, $|\log FC| = 0.585$). Finally, we used the "ggplot2" package. The gene ontology (GO) analysis of DRGs was performed, and the histogram, bubble diagram, and circle diagram were drawn to explore its function and biological process. The Kyoto Encyclopedia of Genes and Genomes (KEGG) pathway enrichment analysis, histogram, and bubble diagram were drawn to explore its function and biological processes.

2.5 Identification of DRGs and construction of the prognostic signature

Before constructing the risk prediction model, we screened the features. First, a univariate Cox model was used to explore the relationship between 225 DRGs and OS of patients. A total of 114 single-factor DRGs related to BC prognosis were obtained. The least absolute shrinkage and selection operator (LASSO) was used to avoid overfitting in the TCGA training cohort (11). The prognostic DRG model was established using multivariate Cox regression analysis and the step Akaike information standard (stepAIC) value. The RS for each patient was calculated by combining the expression of each gene (Ei), LASSO coefficients (Li), and $RS = \Sigma^{n}_{i} Ei * Li$. The patients were divided into high-risk and low-risk groups according to the median RS. Finally, the Kaplan–Meier survival curve was used to analyze the difference in overall survival between the two groups.

The sensitivity and specificity of the prognostic indicators were evaluated using the receiver operating characteristic (ROC) curve and the area under the ROC curve (AUC). A bootstrap method based on 1,000 resamplings was used to obtain the test set (12, 13) to verify the effectiveness of the prediction model. The training set was a combined dataset established using TCGA and GEO based on common genes. In the test set, the AUC of the prognostic model was calculated using the R package "riskRegression." Subsequently, the stability of the ROC model was tested in the separate TCGA and GEO datasets, and the TCGA and GEO joint datasets merged based on common genes. Analyze the relationship between RSs and clinical factors, verify the effectiveness of risk markers, and further compare the survival prediction ability of prognostic factors. The independence of the prognostic model was verified using univariate and multivariate Cox regression analyses by comparing the clinical characteristics of the patients. At the same time, the nomogram was constructed with the Cox regression coefficient of the package "rms," and the calibration curve was drawn.

2.6 Establishment of DRG cluster

We used the "ConsensusCluster Plus" package for consistency clustering analysis and identified clusters of BC patients based on DRGs. We set the cluster count (k) between two and nine and selected the optimal k value based on the sum of the squared errors (SSE) inflection point. The stability of the DG group was verified using a PCA algorithm. Additionally, Kaplan–Meier survival analysis evaluated the OS of different DG clusters, and the heat map showed the difference in DGs between groups.

2.7 Different tumor immune microenvironment patterns with RS

We used the CIBERSORT algorithm to calculate the proportion of tumor-infiltrating immune cells (14). The difference in the proportion of tumor-infiltrating immune cells between the high- and low-risk groups was compared. The ESTIMATE algorithm was used to evaluate the differences in immune, stromal, and tumor purity scores between the high- and low-risk groups. The tumor mutation burden was assessed based on whether the sample was considered high or low risk. Additionally, we used the Maftools package to perform somatic mutation analysis on breast cancer patients to view and analyze somatic mutation data. We also studied the relationship between BC RSs and cancer stem cells.

2.8 The role of RS based on DRGs in predicting drug sensitivity and clinical immune efficacy

For a long time, the research and development of new drugs have been a hot spot in breast cancer treatment. We used the pRRophetic package to calculate the half inhibitory concentration (IC50) of commonly used drugs in breast cancer patients. We screened out

potential drugs with sensitivity differences between the two groups according to the risk level of breast cancer patients ($p < 0.001$) and drew a box plot. We used ggplot2, ggpubr, limma, and reforme2 R software packages to analyze the statistical differences in the expression levels of 79 common ICI-related immunosuppressive molecules (15). Tumor Immune Dysfunction and Exclusion (TIDE) [Tumor Immune Dysfunction and Exclusion (TIDE) (harvard.edu)] is a simple method to predict the immune escape of patients based on the evaluation of the tumor microenvironment using gene expression profiles. Patients with high TIDE scores have a high chance of antitumor immune escape (16). We obtained information on the immune escape ability after submitting the transcriptome data of TCGA-BRCA patients to the website. TCGA is a quantitative scoring scheme developed by developers using machine learning: it is a better predictor of anti-cytotoxic T lymphocyte antigen 4 (CTLA-4) and anti-programmed cell death protein 1 (anti-PD-1) antibody responses. We downloaded BC immunophenotype score (IPS) from TCIA database (https://tcia.at/). In order to predict the sensitivity of immunotherapy, we compared the IPS of high and low risk groups in different immunotherapy decisions (17).

2.9 Cell lines, cell culture, cell transfection, and real-time quantitative PCR

The Tumor Cell Line Comprehensive Analysis Database (DepMap Portal) was utilized to screen for cell lines for further experimental validation (18). Breast cancer cell lines (MDA-MB-468) were obtained from Sichuan Huijixin Biotechnology Co., Ltd. The MDA-MB-468 cells were grown in Dulbecco's Modified Eagle Medium (DMEM) culture medium, supplemented with 10% Fetal Bovine Serum (FBS) in a standard humidified incubator with 5% CO2 at 37°C. The TMEM45A and SHCBP1 specific short hairpin RNAs (shRNAs) were synthesized from Chengdu Youkangjianxing Biotechnology Co., Ltd.

The sequences of shRNAs are as the following: sh- TMEM45A -1: 5′- TGCTGTTGACAGTGAGCGCGGTTAAAGTATTTGAATTTAATAGTGAAGCCACAGATGTATTAAATTCAAATACTTTAACCATGCCTACTGCCTCGGA-3′; sh- TMEM45A -2: 5′- TGCTGTTGACAGTGAGCGCGGTGTACAAAGAGTATTCTGATAGTGAAGCCACAGATGTATCAGAATACTCTTTGTACACCATGCCTACTGCCTCGGA′. sh- SHCBP1 -1: 5′-TGCTGTTGACAGTGAGCGCCACATTGATTTTTCAATTGAATAGTGAAGCCACAGATGTATTCAATTGAAAAATCAATGTGATGCCTACTGCCTCGGA-3′; sh- SHCBP1 -2: 5′- TGCTGTTGACAGTGAGCGCCAGCCAAATGTTGATATTAAATAGTGAAGCCACAGATGTATTTAATATCAACATTTGGCTGATGCCTACTGCCTCGGA -3′.

The knockdown efficiency was evaluated using real-time quantitative PCR (RT-qPCR) after 48 h transfection. The primer sequences used in the experiment are as follows. For the TMEM45A gene, the primers include qpcr-TMEM45A-F (forward primer): TTGGATGCCCACACTATGA and qpcr-TMEM45A-R (reverse primer): TCCATGGTCAAGGAGTTACA. For the SHCBP1 gene, the primers consist of qpcr-SHCBP1-F (forward primer): CTGGAGTTACAGAAGGATGGTG and qpcr-SHCBP1-R (reverse primer): CCATAGAAGCCTGTGGAATGT. After the knockdown of TMEM45A and SHCBP1 in cell line MDA-MB-468, total mRNA from cells was extracted with TRIzol reagent (TaKaRa, Japan). Then, concentration and purity were evaluated by Nanodrop 2000 (Thermo Fisher, USA). After the RNA was reversely transcribed into cDNA with PrimeScript RT kit (TaKaRa, Japan) according to the instructions, SYBR Premix Ex Taq TM kit (TaKaRa, Japan) was applied for RT-qPCR, with β-actin as the endogenous control gene. The RT-qPCR amplification instrument (ABI StepOne Plus) was used to detect the SYBR Green fluorescence signal level after each amplification cycle. Data processing was performed using GraphPad Prism 10.0.0, and T-test was conducted to compare the experimental group to the control group. This supplementary material has been reflected in the preceding text.

2.10 Cell proliferation assay

For three days, proliferation assays were conducted daily on BC cells in 96-well plates using Cell Counting Kit 8 (CCK8) reagent (Beyotime, China). Incubation occurred at 37°C for 2 h, and the plate was analyzed with a microplate reader at 450 nm to measure absorbance.

2.11 Colony formation assays

Approximately 500 cells per well were seeded into a 6-well culture plate and incubated at 37°C for two weeks. After washing with PBS twice, cells were fixed with 4% paraformaldehyde for 15 min and then dyed with crystal violet. Each experiment was repeated three times. ImageJ was used for image analysis to convert images into cellular count data (19). The acquired counts were normalized by dividing them by the corresponding cell count in the control group, yielding percentage data. Data and image processing were performed using GraphPad Prism 10.0.0. The statistical analysis consisted of a t-test conducted on three replicate datasets, comparing the experimental and control groups.

2.12 RNA-seq

Cells were used for RNA sequencing after the knockdown of TMEM45A and SHCBP1 in cell line MDA-MB-468. Approximately 2 μg of total RNA was extracted from each specimen and pretreated with Epicentre Ribo-zeroTM rRNA Removal Kit. Then, the RNA expression profile library was constructed in line with the manufacturer's protocol of NEBNext R Ultratdirectional RNA Library Prep Kit(NEB, USA). The steps are as follows: First, RNA was lysed into small fragments after being treated with NEBNext first strand synthesis reaction buffer at high-temperature treatment, and the first strand cDNA was synthesized using random hexmer primers and M-MULv reverse transcriptase. The second strand dsDNA was then obtained, and the fragment residues were converted into blunt ends by exonuclease or polymerase. Subsequently, the 3'end of each dsDNA fragment was adenylated and connected to the NEBNext adapter with a hairpin structure. After purification using the AMPure XP system (Beckman Coulter, Beverly, USA), 150–200 bp DNA fragments were obtained and sequenced using HiSeq 2500 (Illumina, CA, USA).

2.13 RNA-seq data processing and analysis

FastQC (http://www.bioinformatics.babraham.ac.uk/projects/fastqc/) was utilized to check the sequencing quality of all the sample data trimmed using the FASTX Toolkit. The sequencing reads against the human assembly GRCh37 were mapped using TopHat (v 2.0.9). We perform differential analysis using the gene expression matrix in counts format. We employed the R package edgeR to perform differential analysis between snSHCBP1 and NC, as well as snTMEM45A and NC, using predetermined criteria (fold change > 1, padj < 0.05). Following this analysis, we created volcano plots to visualize the differential expression of genes. We conducted an intersection analysis to identify genes that exhibited consistent differential expression in both replicates. Subsequently, we performed Gene Ontology (GO) and Kyoto Encyclopedia of Genes and Genomes (KEGG) enrichment analyses (p-value < 0.05) on the genes found in the intersection.

3 Results

3.1 11DGs in breast cancer: expression, genetic variants, and prognostic values

We analyzed the differences between 11 DGs in breast cancer and normal breast tissue samples. Except for NCKAP1, other genes significantly differed between tumor and normal groups ($p < 0.05$). The expression levels of SLC3A2, RPN1, BRK1, ACTR2, ACTR3, RAC1, SLC7A11, and WASF2 in the tumor samples were higher than those in the normal samples. On the other hand, the expression levels of WASF2, CYFIP1, and ABI2 in the normal samples were higher (Figure 2A). Of the 911 breast cancer samples of TCGA, 33 samples had DG mutations. The genes with the highest mutation frequencies were NCKAP1 and CYFIP1. Still, no base mutation was found in WASF2 (Figure 2B). The location and copy number changes of DGs on chromosomes are shown in Figure 2C. Among them, SLC3A2, BRK1, ABI2, ACTR2, NCKAP1, RAC1, RPN1, SLC7A11, and ACTR3 are upregulated in breast cancer, while CYFIP1 and WASF2 were downregulated. COX regression analysis and K-M survival analysis were performed on the expression of 11 DGs and the survival time of patients, and the tumor samples were divided into high- and low-risk groups according to the median value of a single gene. It can be concluded that SLC7A11, SLC3A2, RPN1, NCKAP1, BRK1, ACTR2, ACTR3, and RAC1 are single-factor genes that can predict the survival of patients ($p < 0.05$, Supplementary Table 2). The survival analysis was statistically significant, and the gene expression was negatively correlated with the survival time (Figure 2D). The 11 DGs positively regulated each other (Figure 2E).

3.2 Clusters of DGs identified in breast cancer

We performed a consistent cluster analysis of the expression levels of 11 DGs to explore their roles in the occurrence and development of breast cancer. Among the clustering variables, k = 2 had better clustering stability, the highest intra-group correlation, and the lowest inter-group correlation (Figures 3A–C). Therefore, we divided all tumor samples into clusters A (n = 339) and B (n = 850). PCA showed a significant interval between the two groups (Figure 3D). Survival analysis between groups A and B showed that the prognosis of group A was significantly better than that of group B, and the survival difference between the two groups was statistically significant ($p < 0.05$, Figure 3E). Additionally, the heat map between the two AB groups showed significant differences in the expression of 11 DGs between the two groups, especially between the SLC7A11 groups (Figure 3F).

3.3 TME infiltration and functional enrichment analysis of different clusters

The samples in the A and B groups were analyzed using GSVA. From Figure 4A, it can be seen that group B was more active in arachidonic acid metabolism and taurine and hypotaurine metabolism pathways than group A. At the same time, group A was active in nonhomologous end connections, ubiquitin-mediated proteolysis, and other pathways. We performed a single sample gene set enrichment analysis (ssGSEA) on groups A and B. From Figure 4B, we can see Activated.B.cell, Activated.CD8.T.cell, CD56dim.natural.killer.cell, Eosinophil, MDSC, Macrophage, Mast.cell, Monocyte. Natural.killer.cell, Neutrophil, Plasmacytoid.dendritic.cell, T.follicular.helper.cell, Type.1.T.helper.cell, and Type.17.T.helper.cell were highly expressed in Cluster A and Activated.CD4.T.cell, Activated.dendritic.cell, Gamma.delta.T.cell, Immature.B.cell, Immature.dendritic.cell, Regulatory.T.cell, and Type.2.T.helper.cell were highly expressed in cluster B. We found 225 differential genes between groups A and B to explore the differences in biological processes between groups A and B according to the DG grouping.

We performed GO and KEGG enrichment analyses on these differential genes. As shown in Figures 4C, D, DRGs are mainly enriched in the nuclear division, chromosome segregation, and nuclear chromosome segregation in biological processes (BP). In addition, DRGs were primarily enriched in the spindle, chromosomal region, and condensed chromosome. Regarding molecular function, DRGs were mainly enriched in microtubule binding, tubulin binding, and ATP hydrolysis activity. We also performed a KEGG enrichment analysis to explore the differential genes in the pathway. The most enriched pathways were in the cell cycle. Cytokine–cytokine receptor interaction and human papillomavirus infection were the most significant enrichments in the cell cycle, PPAR signaling pathway, and ECM–receptor interaction (Figures 4E, F).

3.4 Clusters of DRGs identified in breast cancer

Based on a consensus cluster analysis of 225 DRGs, the relationship between disulfidptosis and BRCA subtypes was explored. K = 3 is the appropriate choice for the most stable aggregation (Figures 5A–D). Therefore, we divided all tumor samples into three subgroups: cluster A (n = 525), cluster B (n = 379), and cluster C (n = 285). 11DGs exhibit significant differences among clusters A, B, and C (Figure 5E). Figure 5F shows that the prognosis of group A is the best, followed by group B,

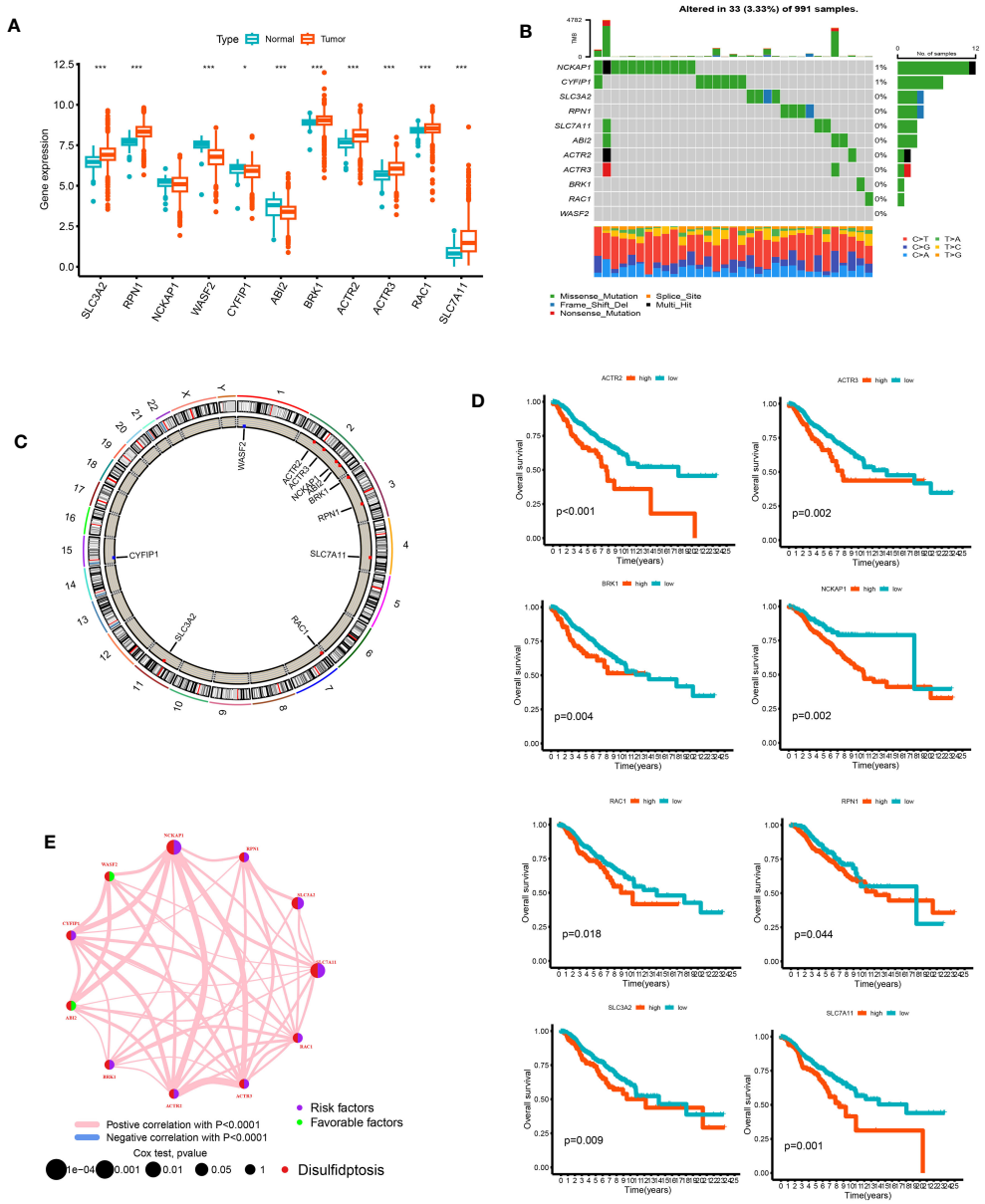

FIGURE 2
The analysis of 11 DGs' expression and association in the TCGA cohort. **(A)** The expression of the 11 DGs in BC tissues and healthy breast tissues (*p<0.05; ***p< 0.001). **(B)** Data on the frequency of DGs' mutations for 991 BC patients. **(C)** The sites of CNV variation in DGs on the 23 chromosomes. **(D)** The relationship between 8 DGs and overall s survival. **(E)** The interactions between DGs in BC (the red and blue strings denote positive and negative correlation, respectively; the intensity of the correlation is indicated by the color shades).

and the prognosis of group C is relatively poor. From Figure 5G, it can be seen that there were significant differences in the expression levels of DRGs between different clusters. The samples of DRG cluster A were mostly in cluster A of 11 DGs, and the survival prognosis of these two clusters was significantly better than that of other groups.

3.5 Creating and confirming the predictive RS

We used univariate Cox regression analysis to extract 114 DRGs associated with BC prognosis in the preliminary screening (Supplementary Table 3). Using the LASSO regression algorithm, 14 BC-related genes were identified based on the minimum partial likelihood of the best λ value and deviation (Figures 6A, B, Supplementary Table 4). Multivariate Cox regression analysis was performed on these 14 genes, and a risk model consisting of six genes was obtained (Figure 6C). Among them, SHCBP and TMEM45A were molecules that improved prognosis. PIGR, IGLV6-57, TCN1, and GFRA1 were risk factors. The molecular formula of the model was as follows: RS = (0.1917 * SHCBP1 + 0.0836 * TMEM45A–0.0721 * PIGR–0.1633 * IGLV6–57–0.0489 * TCN1-0.0676 * GFRA1). In the bootstrap set, AUC at one year was 0.767, AUC at three years was 0.717, and AUC at five years was 0.694 (Figure 6D, Supplementary

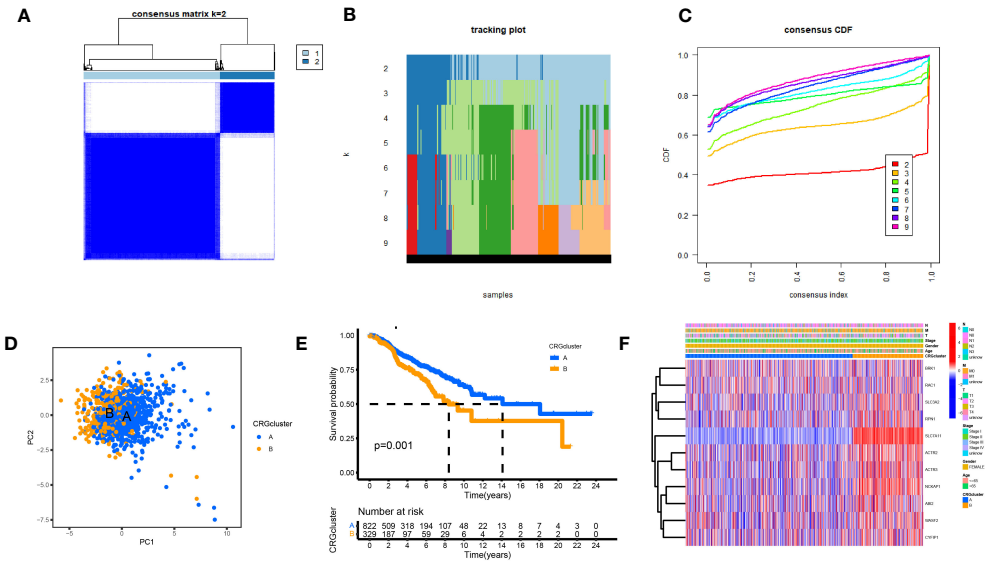

FIGURE 3
Biological and clinicopathological characteristics of DG subtypes. **(A)** The consensus matrix's heatmap of two clusters (κ = 2). **(B)** tracking plot. **(C)** Consensus CDF. **(D)** A considerable transcriptome divergence between the two subtypes is seen by PCA analysis. **(E)** Subtype-specific Kaplan-Meier OS curves. **(F)** DGs expression levels and clinicopathological traits vary across subtypes.

Table 5). Besides, we used the GEO database GSE20685 for external data verification. The AUC values of breast cancer patients predicted by our model were 0.743, 0.650, and 0.615 at one, three, and five years, respectively (Figure 6E). We validated it separately in the GEO dataset: AUC at one year was 0.762, AUC at three years was 0.734, AUC at five years was 0.758, AUC at one year was 0.771, AUC at three years was 0.712, and AUC at five years was 0.652 in TCGA. In the combined dataset of TCGA and GEO, the AUC at one year was 0.766. The AUC at three years was 0.716, and the AUC at five years was 0.686 (Figures 6F–H). BC patients were randomly selected for scoring, total point = point (T) + point (N) + point (RS) + point (stage) + point (age) below by combining RS and clinicopathological features, using the nomogram (a quantitative method), as shown in Figure 6I. The total score corresponds to the scale in the figure. It can predict 1-year, 3-year, and 5-year OS of BC patients. The calibration curve showed adequate consistency between the predicted values of the 1-year, 3-year, and 5-year OS nomograms and the actual observed values (Figure 6J).

3.6 Dividing the high- and low-risk groups and observing their distribution in clusters

The patients in the TCGA, GEO, and total datasets were divided into high-risk and low-risk groups according to the median RS value. The differences between the groups were compared. Figure 7A shows that the genes (SLC7A11, SLC3A2, BRK1, ACTR2, ACTR3, RPN1, and NCKAP1) have the K-M survival analysis between the high- and low-risk groups showed that the survival differences between the high- and low-risk groups were statistically different ($p < 0.001$) in the TCGA dataset, GEO dataset, combined dataset and external validation of the GEO database. The prognosis of the significantly high-risk group was poor (Figure 7B). Seven of the 11 disulfide death genes showed significant differences in gene expression between high-risk and low-risk individuals (Figure 7C). Figure 7D illustrates the proportion of surviving and dying patients in two RS high and low groups, two DGs, and three DRG subtypes. Figures 7E, F show the RS distribution of two DG subtypes and three DRG subtypes, respectively. The PCA diagram shows that RS has an adequate grouping function (Figure 7G).

3.7 Different immune landscapes in the two risk groups

The CIBERSORT algorithm evaluated the relationship between RS and the relative number of immune cells. RS was positively correlated with the number of immune cells, such as Macrophages M0 and M2, Dendritic cells resting, Mast cells activated, B cells memory, NK cells resting, T cells CD4 memory resting, B cells naïve, Mast cells resting, and Monocytes. The expression of immune cells, such as dendritic cells activated, Plasma cells, Macrophages M1, and T cells CD8, was negatively correlated ($p < 0.05$). The stromal score, immune score, and ESTIMATE score of the high-risk group were higher. The difference between the groups was statistically significant (Figure 8A). Our study also examined the association between six genes and the number of immune cells (Figure 8B). According to our research, these six genes affect most immune cells. By observing the mutation frequency of each tumor sample and the mutation frequency of the gene, the TMB difference between the high- and low-risk groups was compared. From Figures 8C, D, it can be seen that the TMB of patients in the high-risk group is higher than that in the low-risk group, RS is positively correlated with TMB, and CRGsClusteA is significantly enriched in the low-risk area.

The TMB survival curve showed that patients with low TMB had a better prognosis (Figure 8E). Compared with other groups, BC patients with low risk and low TMB had the best prognoses (Figure 8F). The

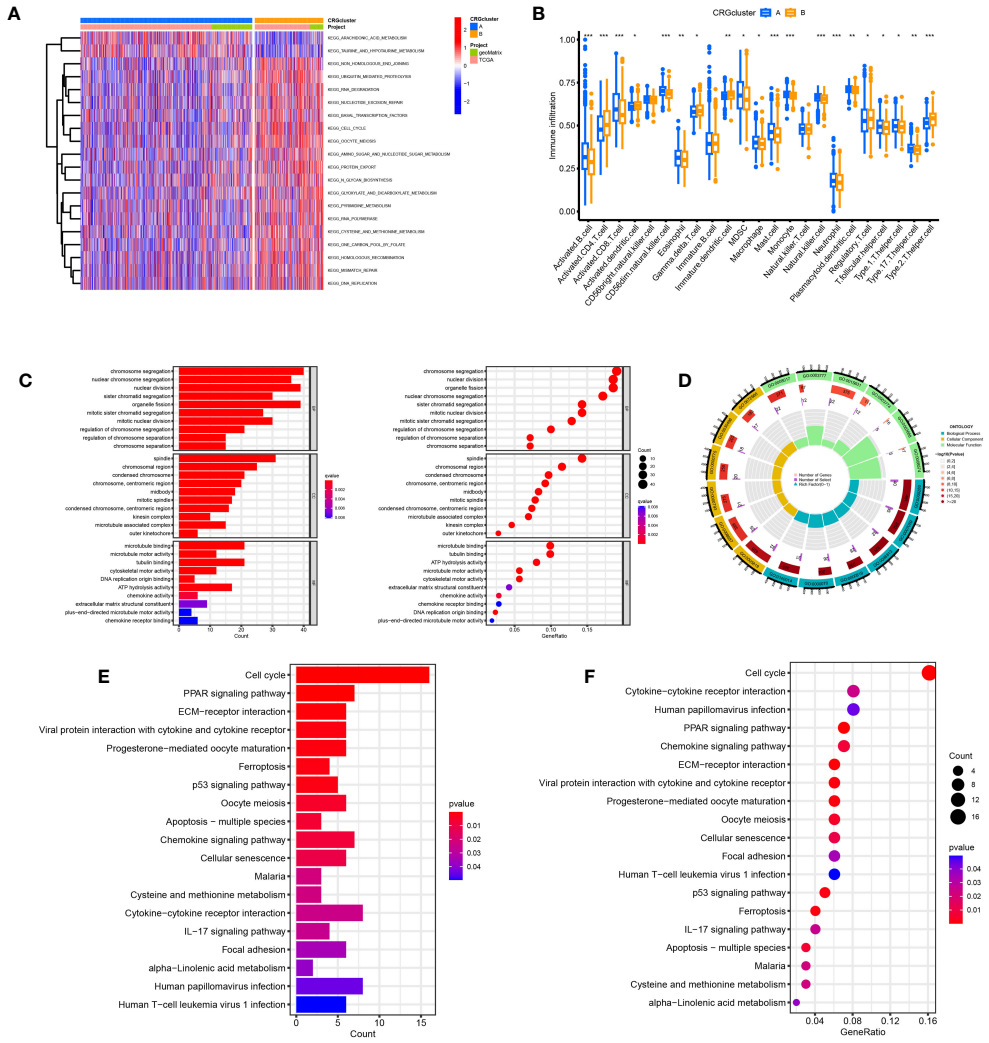

FIGURE 4
Disulfidptosis subtypes linked to TME invasion. **(A)** GSVA of two disulfidptosis subtype-related cellular pathways (Red means activated and blue means inhibited). **(B)** Correlations between immune cell infiltration levels in the two subtypes associated with disulfidptosis. **(C, D)** The GO function enrichment analyses. **(E, F)** The KEGG function enrichment analyses.

mutation rate of the low-risk group was 85.81% (Figure 8G). The mutation rate of the high-risk group was 85.78% (Figure 8H). The waterfall diagram shows that the mutation genes in the high- and low-risk groups are mainly PIK3 CA, TP53, TTN, CDH1, GATA3, MUC16, and MAP3K1, and the mutation rates of these genes are different in the high- and low-risk groups. PIK3CA had the highest mutation frequency in the low-risk samples, while TP53 had the highest in the high-risk groups. The mutation probability of TP53 in the high-risk group was 43%, while the mutation frequency of TP53 in the low-risk group was only 29%.

3.8 Drug sensitivity and different immunotherapy responses in the two risk groups

There was a positive correlation between RS and stem cells. The higher the RS, the higher the content of stem cells ($p < 0.05$) (Figure 9A). The TIDE score of the high-risk group was lower than that of the low-risk group, and the tumor immune escape ability was weak (Figure 9B). The ESTIMATE results showed that the stromal immunity and estimated scores of the high-risk group were low (Figure 9C). The drug treatment of breast cancer has broad research prospects and has attracted much attention. Therefore, the IC50 value of chemotherapeutic drugs for BC was calculated, and the relationship between RS and drug resistance was analyzed. We noted that in addition to docetaxel (microtubule depolymerization inhibitors) and parthenolide (NF-κB inhibitors) in high-risk patients with lower IC50. In contrast, other drugs [ABT.888 (Veliparib, PARP inhibitors)], AG.014699 (Rucaparib, PARP inhibitors), AMG.706 (Motesanib, VEGFR inhibitors), ATRA, AUY922 (Luminespib, HSP90 inhibitors), GDC0941 (Pictilisib, PI3K inhibitors), Metformin, Methotrexate, Nilotinib, Nutlin.3a (MDM2 inhibitors), Roscovitine, Temsirolimus, and Tipifarnib) had lower IC50 in low-risk patients (Figure 9D). We performed immune checkpoint analysis on high-risk and low-risk groups to explore the precise use of immune checkpoint

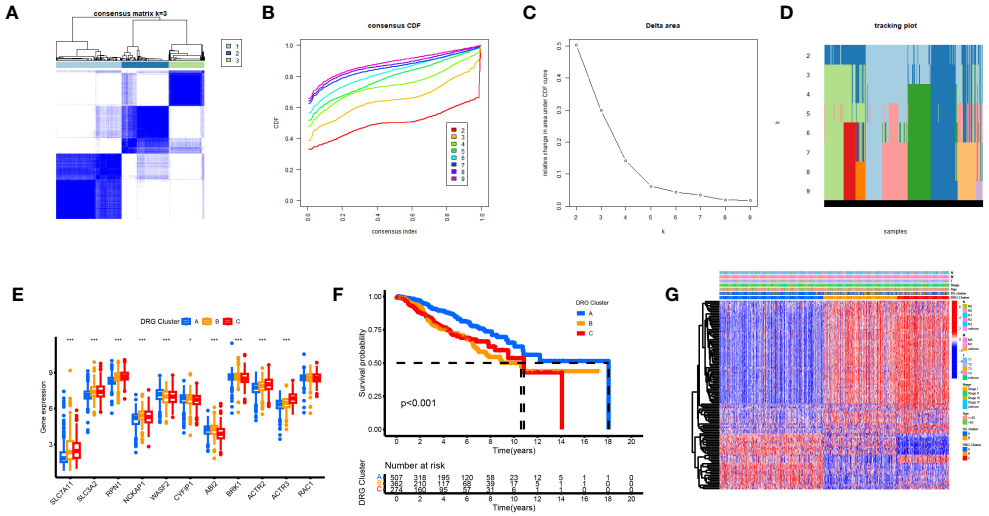

FIGURE 5
Biological and clinicopathological characteristics of DRG subtypes. **(A)** The consensus matrix's heatmap of two clusters (κ = 3). **(B)** Consensus CDF **(C)** Delta area. **(D)** tracking plot Consensus CDF. **(E)** DRGs expression levels and clinicopathological traits vary across subtypes. **(F)** Subtype-specific Kaplan-Meier OS curves. **(G)** DRGs expression levels and clinicopathological traits vary across subtypes.

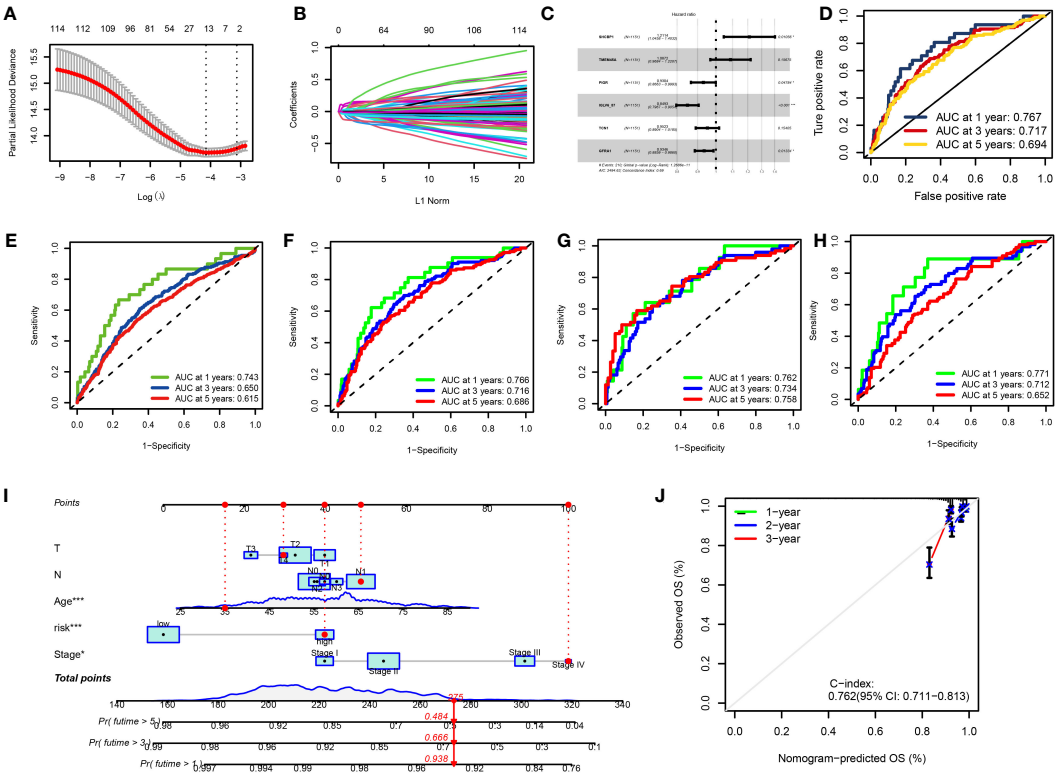

FIGURE 6
(A, B) LASSO variable trajectory plot for 1,000 cross validations **(A)** and LASSO coefficient profile **(B)**. **(C)** Forest Plot for Multifactorial Cox Regression Analysis. **(D)** ROC curves and AUCs for 1-, 3-, and 5-year survival rates. **(E)** ROC curves and AUCs for 1-, 3-, and 5-year survival rates in another independent GEO dataset. **(F)** ROC curves and AUCs for 1-, 3-, and 5-year survival rates in the TCGA and GEO merged datasets. **(G)** ROC curves and AUCs for 1-, 3-, and 5-year survival rates in TCGA datasets. **(H)** ROC curves and AUCs for 1-, 3-, and 5-year survival rates in GEO datasets. **(I)** The nomogram used to calculate the survival rates of 1-, 3-, and 5-years for patients with BC. **(J)** Calibration curve for nomograms.

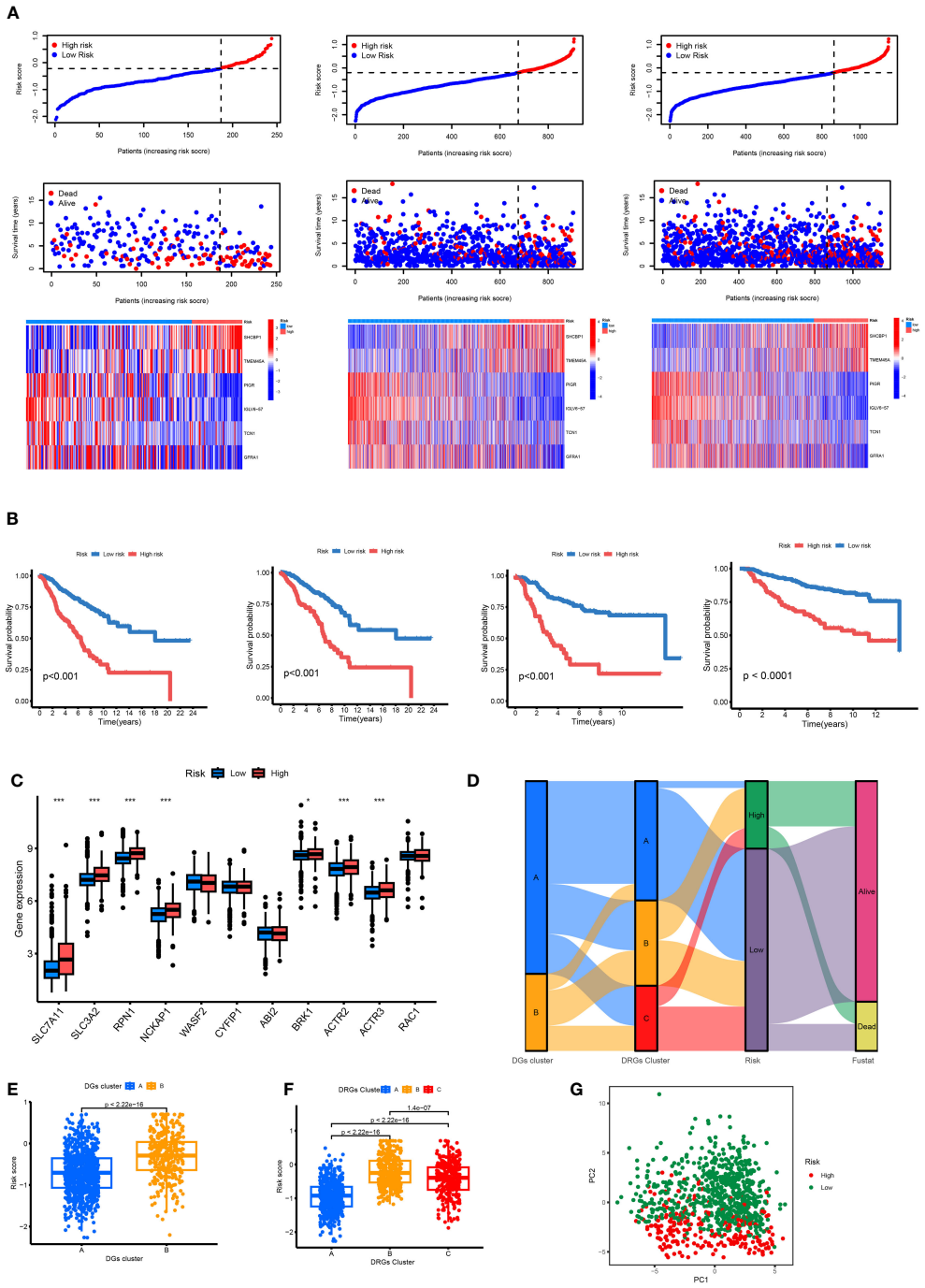

FIGURE 7
(A) Ranked dot, scatter plots and heat map of the model gene expressions in the TCGA and GEO merged datasets, TCGA datasets and GEO datasets. **(B)** Kaplan–Meier analyses of the OS between the TCGA and GEO merged datasets, TCGA datasets, GEO datasets and another independent GEO dataset. **(C)** RS score differences in eleven DGs. *p < 0.05, ***p < 0.001. **(D)** The subtype distributions among groups, risk scores and survival outcomes. **(E)** Variations in risk scores among DGs subtypes. **(F)** Variations in risk scores among CRGs subtypes. **(G)** Through PCA analysis, it can be seen that there are large transcriptome differences between high and low groups.

inhibitors (ICI) in breast cancer patients. Except for the high expression of the PVR gene in the high-risk group, the other immune checkpoint genes were increased in the low-risk group. The IPS of the low-risk group was significantly higher than that of the high-risk group, and the immunotherapy efficacy of the low-risk group was better (Figure 9E).

3.9 Knockdown of TMEM45A and SHCBP1 inhibited BC cell proliferation

We conducted a search on the DepMap Portal to assess the expression levels of TMEM45A and SHCBP1 in various breast

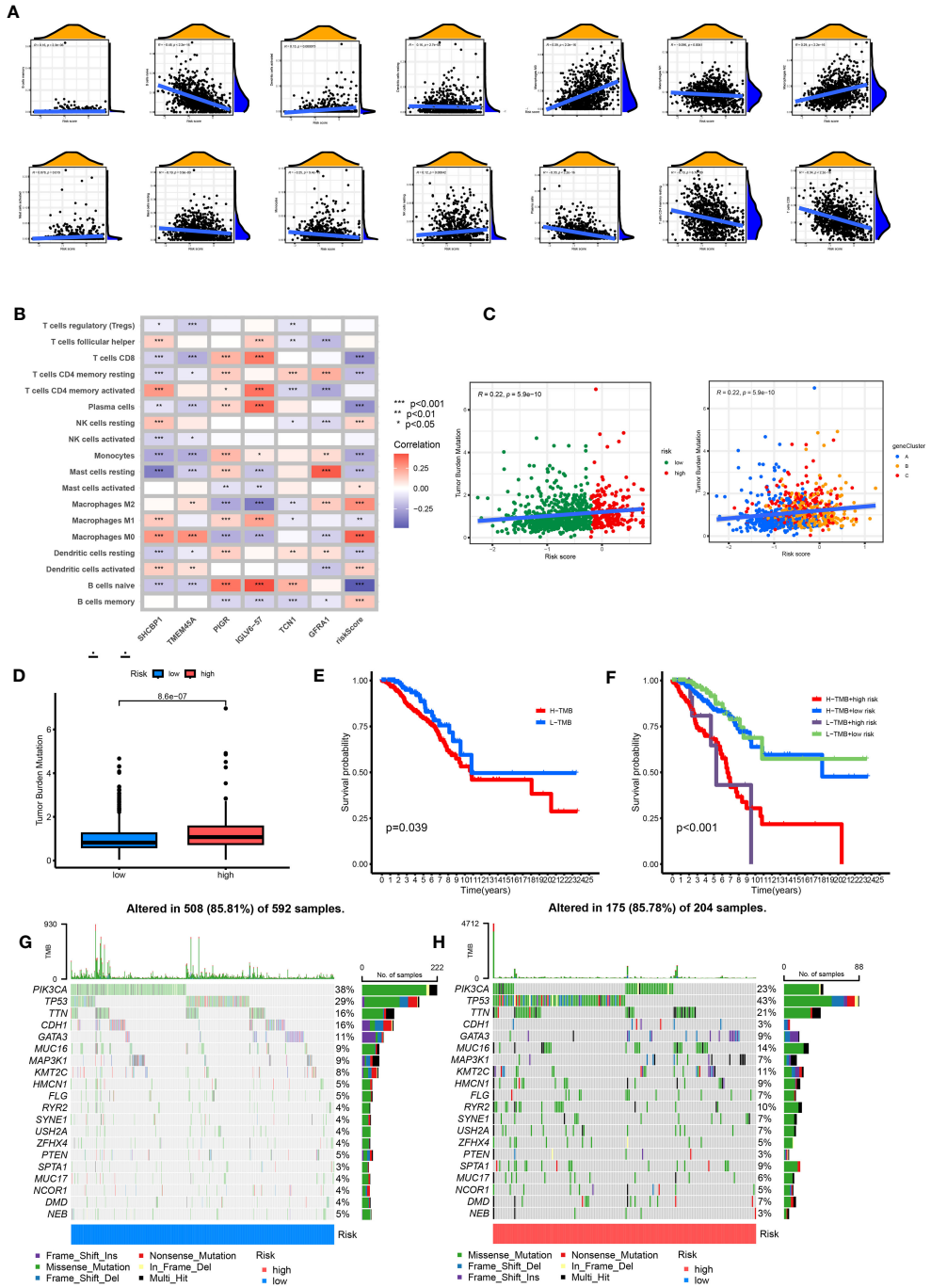

FIGURE 8
Comprehensive analysis of the risk scores in BC. **(A)** Correlations between immune cell types and risk score. **(B)** The six genes from the proposed model are correlated with the number of immune cells. **(C)** risk score and TMB spearman correlation analysis. **(D)** The differences in TMB between high- and low-risk groups. **(E)** Kaplan–Meier survival curves of BC patients between the H-TMB and L-TMB groups. **(F)** Kaplan–Meier survival curves of BC patients across H-TMB + high risk, H-TMB + low risk, L-TMB + high risk, and L-TMB + low risk. TMB, tumor mutational burden; H, high; L, low. **(G, H)** The somatic mutation features waterfall plot determined by high and low risk scores. One patient was represented by each column. The correct number represented each gene's frequency of mutation, and the upper barplot displayed TMB. The proportion of each variant type was displayed in the right barplot.

cancer cell lines. Ultimately, we observed that these two genes exhibited significantly high expression in the MDA-MB-468 cell line (Supplementary Figure 1). In our study, we constructed a predictive model using six dual sulfur death-related genes. We selected the high-risk genes TMEM45A and SHCBP1 in our model to validate the potential for targeted gene therapy. TCGA and GEO data analyses revealed that TMEM45A and SHCBP1 were highly expressed in breast cancer. Therefore, we knocked down TMEM45A and SHCBP1 and further investigated the role of TMEM45A and SHCBP1 in MDA-MB-468 breast cancer cells *in vitro*.

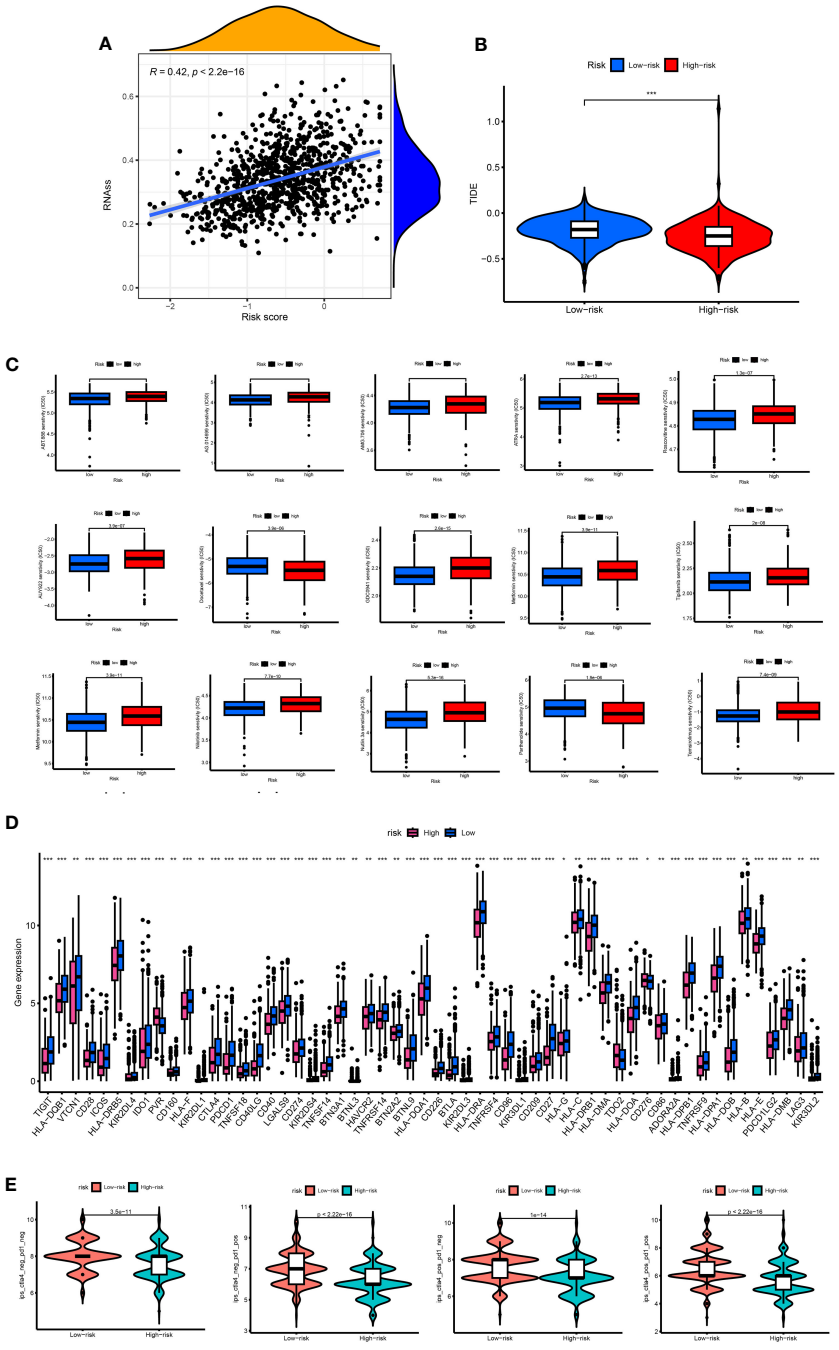

FIGURE 9
(A) Associates between the CSC index and the risk score. **(B)** TIDE score between high- and low-risk group. **(C)** The boxplots for the drug sensitivity analysis. **(D)** Differential expression analysis of the immune checkpoint genes between the high-risk and low-risk groups. IC50, the half-maximal inhibitory concentration; *, $p < 0.05$; **, $p < 0.01$; ***, $p < 0.001$. **(E)** The difference between anti-PD1 treatment and anti-CTLA-4 treatment between high and low risk groups.

First, we established MDA-MB-468 shTMEM45A and shSHCBP1 cell lines through lentiviral transduction. As shown in Figure 10A, the knockdown of TMEM45A and SHCBP1 in MDA-MB-468 was satisfactory. We further investigated the impact of TMEM45A and SHCBP1 knockdown on the functionality of breast cancer cells through CCK-8 and colony formation assays to determine their effects on BRCA cell proliferation.

As expected, the CCK-8 assay (Figure 10B) showed that the knockdown of TMEM45A and SHCBP1 in MDAMB468 similarly inhibited the proliferation of breast cancer cells. The colony formation assays (Figure 10C, D) demonstrated that the knockdown of TMEM45A and SHCBP1 significantly and independently inhibited cell proliferation ($p < 0.05$). These results collectively indicate that TMEM45A and SHCBP1 influence the proliferation of BC cells.

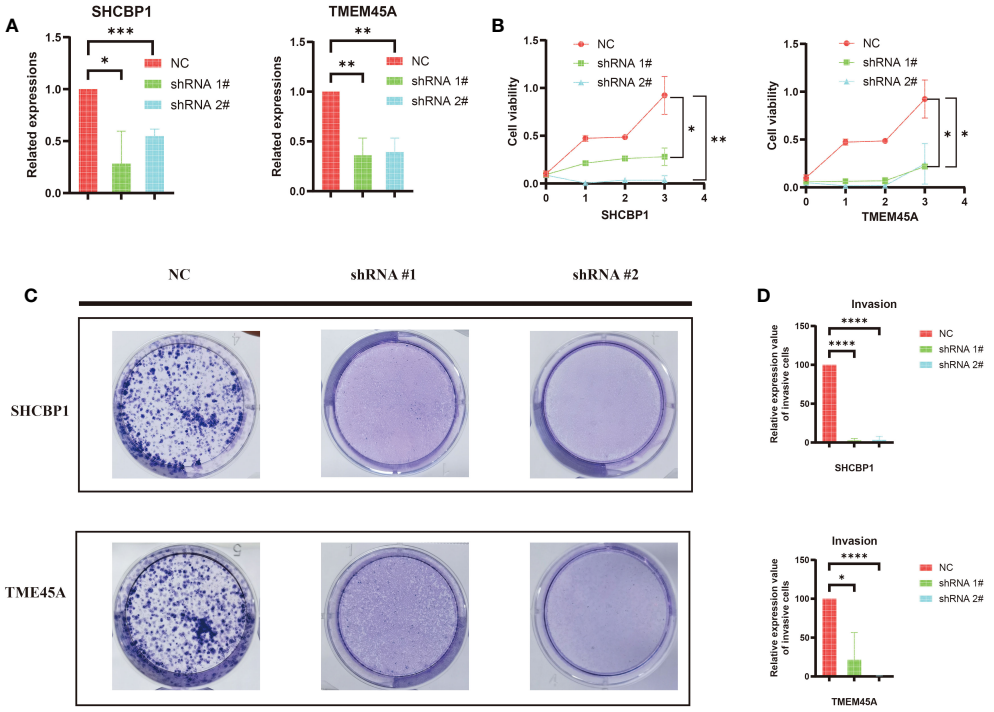

FIGURE 10
(A) The efficiency of silencing TMEM45A and SHCBP1 was indicated by RT-qPCR in MDA-MB-468 cell lines. **(B)** The MTT assay revealed that, in comparison to the control group, the proliferation capability of the MDA-MB-468 cell line with TMEM45A and SHCBP1 knockdown significantly diminished. **(C, D)** The clonogenic assay revealed that the depletion of TMEM45A and SHCBP1 attenuated the proliferative capacity of MDA-MB-468 cells. The data is presented as the mean from at least three independent experiments. (*p<0.05; **p<0.01; ***p< 0.001; ****p< 0.0001).

3.10 Sequencing and functional enrichment analysis

The knockdown of SHCBP1 and TMEM45A was achieved by generating shSHCBP1_1, shSHCBP1_2, shTMEM45A_1, and shTMEM45A_2. Differential analysis was conducted using the average counts from three replicate sequencing experiments (Supplementary Table 6). shSHCBP1_1 exhibited differential expression in 1171 genes (687 upregulated, 484 downregulated) compared to the NC group, while shSHCBP1_2 showed differential expression in 593 genes (421 upregulated, 172 downregulated) compared to the NC group (Figures 11A–C). shTMEM45A_1 exhibited differential expression in 7710 genes (3896 upregulated, 3814 downregulated) compared to the NC group, while shSHCBP1_2 showed differential expression in 7272 genes (3683 upregulated, 3589 downregulated) compared to the NC group (Figures 11F–H). We identified the intersecting genes in the upregulated and downregulated gene sets from the two independent replicate experiments and subjected these genes to GO and KEGG enrichment analyses (Figures 11D, E, I, J).

4 Discussion

Regulated cell death (RCD) is a type of cell death controlled by specific molecular pathways and regulated by genetic or pharmacological manipulation (20). Recently, disulfidptosis has been defined as a new RCD. Previous studies have suggested that SLC7A11-mediated cystine intake is critical in promoting glutathione biosynthesis and inhibiting oxidative stress and ferroptosis. Subsequently, SLC7A11 was found to significantly promote cell death under glucose starvation (21–23). Subsequently, it was found that SLC7A11-mediated reduction of cystine to cysteine was highly dependent on the reduced nicotinamide adenine dinucleotide phosphate (NADPH) produced by the glucose–pentose phosphate pathway (24). Recently, Liu et al. proposed that disulfidptosis is an abnormal accumulation of disulfides, such as cystine, which induces disulfide stress, causes disulfide bond cross-linking and cytoskeleton contraction of the actin cytoskeleton, and ultimately induces cell death6. Not only does RCD play a key role in body development and cell homeostasis, but its dysregulation is also causally linked to many diseases, including cancer. Escape from cell death is considered to be one of the core markers of cancer. The importance of other RCDs in BC has been revealed, but the role of disulfidptosis in BC remains unclear (25–29). Our study explored the importance of disulfidptosis in predicting the prognosis, survival time, immunotherapy response, and chemosensitivity of BC patients. This result may lay the foundation for precisely treating BC breast protrusion-related diseases.

We first performed a differential gene expression analysis, gene copy number mutation between tumor and normal tissues, and tumor mutation load analysis on 11 DGs. We found that, except for NCKAP1, the remaining DGs had significant expression differences

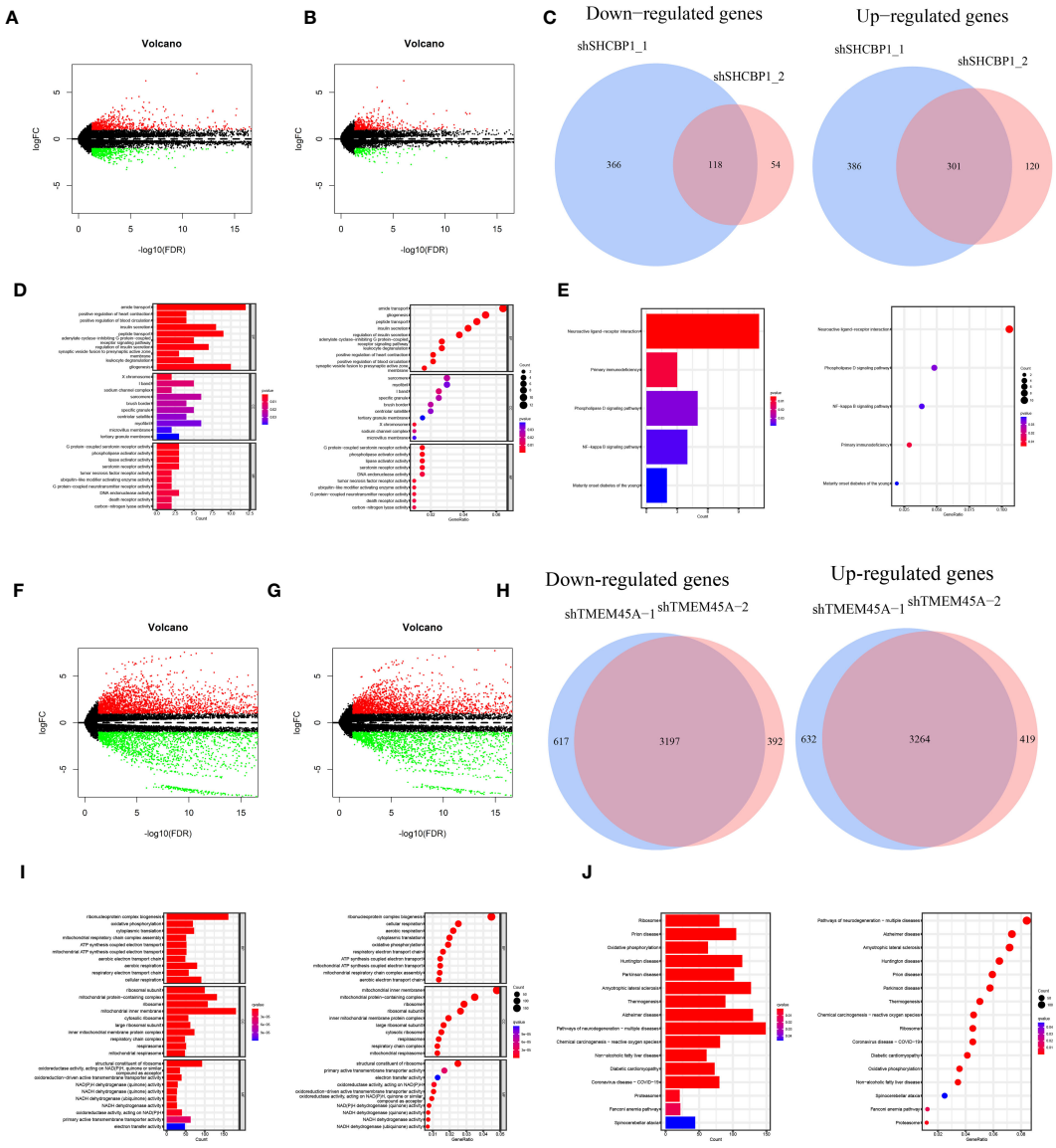

FIGURE 11
The volcano plot displays the differentially expressed genes between shSHCBP1_1 **(A)** and shSHCBP1_2 **(B)** compared to the NC group. **(C)** The Venn diagram shows the overlap in differentially expressed genes between shSHCBP1_1 and shSHCBP1_2 compared to the NC group. **(D, E)** GO and KEGG Enrichment Analysis of Overlapping Differentially Expressed Genes in shSHCBP1_1 and shSHCBP1_2 vs. NC. The volcano plot displays the differentially expressed genes between shTMEM45A_1 **(F)** and shTMEM45A_2 **(G)** compared to the NC group. **(H)** The Venn diagram shows the overlap in differentially expressed genes between shTMEM45A_1 and shTMEM45A_2 compared to the NC group. **(I, J)** GO and KEGG Enrichment Analysis of Overlapping Differentially Expressed Genes in shTMEM45A_1 and shTMEM45A_2 vs. NC.

between the two groups. Most of them had increased gene expression in breast cancer, meaning these genes may be involved in some BC generation and development processes. In addition to the decrease in CYFIP1 and WASF2 gene copy numbers in tumor samples, the copy number of other DGs increased to varying degrees, consistent with the decline in CYFIP1 and WASF2 gene expression in BC patients. It has been reported that ABI2 can promote the growth and metastasis of HCC. In BC patients, the ABI2 gene copy number increased. Still, gene expression decreased, indicating that there may be other mechanisms in the body, such as methylation, acetylation, ubiquitination, and so on, to regulate ABI2 expression. Among the 911 breast cancer mutation data samples, only 33 had DG mutations. The highest mutation probability was 1% for NCKAP1 and CYFIP1. DGs showed more specific genetic stability than the 53% mutation rate of high-mutation genes, such as TP53 and PIK3CA (30). K-M survival analysis showed that the expression levels of SLC7A11, SLC3A2, RPN1, NCKAP1, BRK1, ACTR2, ACTR3, and RAC1 could independently predict the prognosis of patients ($p < 0.05$). Among these 11 DGs, SLC7A11 can affect non-small cell lung cancer (31), renal cell carcinoma (32), prostate cancer progression through ferroptosis, and WASF2 is associated with poor ovarian cancer prognosis (33). These results further indicate that DGs play an important role in the development and progression of tumors.

Consensus clustering is a standard unsupervised clustering method for cancer subtype classification research. It can distinguish samples into several subtypes according to different omics datasets to find new disease subtypes or compare different subtypes (34–36). We consistently clustered 11 prognostic DGs in the TCGA and GEO breast cancer data and identified two DG clusters. The OS of BC patients was statistically different between the two clusters, and the OS of group A was longer than that of group B. GSVA analysis showed that some pathways were enriched differently between the two DG groups, such as arachidonic acid metabolism, ubiquitin-mediated proteolysis, and taurine and hypotaurine metabolism. The ssGSEA analysis showed that most of the immune cells in group A were widely enriched and infiltrated, which may inhibit tumor cells through an immune response. In contrast, the lack of immune cells and immunosuppression in group B may be related to the poor prognosis of patients. PCA analysis showed a considerable difference between groups A and B.

A total of 225 DRGs were obtained, and GO and KEGG enrichment analyses were performed on these genes. GO analysis showed that these DRGs were mainly enriched in microtubule binding, tubulin binding, and other biological behaviors closely related to the construction of the cytoskeleton. Therefore, it can be speculated that these DRGs may mediate changes in the cytoskeleton and cause cell death, which is consistent with previous studies 6. Furthermore, through KEGG enrichment analysis, these differential genes were mainly enriched in signal transduction pathways, such as the cell cycle, PPAR signaling pathway, ECM-receptor interaction, and other pathways, indicating that intercellular interaction may be a critical link in disulfidptosis-induced cell death.

One-hundred-and-fourteen of the 225 differential genes were associated with BC prognosis. According to the expression of these 114 DRGs, breast cancer was divided into three subtypes by consensus clustering. The prognosis of group A was the best, followed by group B, and the prognosis of group C was relatively poor. In this study, we further developed six DRGs (SHCBP, TMEM45A, PIGR, IGLV6-57, TCN1, GFRA1) to construct RS to predict the prognosis of BC patients and used TCGA, GEO separated and TCGA and GEO joint databases to evaluate the prognostic value of RS through a survival curve, RS map, survival state map, and heatmap. RS = (0.1917 * SHCBP1 + 0.0836 * TMEM45A-0.0721 * PIGR-0.1633 * IGLV6-57-0.0489 * TCN1-0.0676 * GFRA1). SHCBP1 has been previously reported as an immune-related biomarker for cancer diagnosis and prognosis and a potential therapeutic target for tumor immunotherapy (37). Jing et al. proposed that TMEM45A can be used as an oncogene in ovarian cancer and that inhibition of TMEM45A may be a therapeutic strategy for ovarian cancer. Wichitra et al. proposed that M1 macrophages can cause high expression of PIGR in breast cancer cells, and high expression of polymeric immunoglobulin receptor (PIGR) in breast cancer is associated with an increased 5-year survival rate (38), indicating that PIGR may be a protective factor for breast cancer. IGLV6-57 is also widely used in cancer diagnosis (39). TCN1 may play a carcinogenic role in colorectal cancer by regulating the ITGB4 signaling pathway leading to cytoskeleton damage and promoting cell death (40). This type of cell death may be disulfidptosis. Sunil Bhakta et al. proposed that GFRA1 is associated with targeted therapy for hormone receptor–positive breast cancer (41). The six genes constructing the model are inseparable from regulating tumor life activities.

The area under the ROC curve (AUC) was used to evaluate the predictive ability of RS for patient prognosis (42). A considerable AUC indicates that the model has good classification ability and can compare features (43). The AUC of our model was 0.762, 0.734, and 0.758 at one year, three years, and five years, respectively, which was significantly higher than most prediction models. We integrated all the essential information of a series of prognostic models, including author, year, and genetic characteristics, and constructed AUC to verify the diagnostic performance of the model. After comparison, we found that our model had the best diagnostic performance (Table 1). Table 1 shows a metabolic-related 4-gene prognostic model with AUCs of 0.764, 0.689, and 0.612 for 1-year, 3-year, and 5-year, respectively (44). Another pyroptosis model consisted of 16 genes with AUC of 0.756, 0.752, and 0.723 for 1, 3, and 5 years (45). Its diagnostic value is almost the same as our model, but it is composed of 16 genes, while our model has only six genes that can be better applied in clinical practice. In two cuproptosis-related prognostic models, 1-year, 3-year, and 5-year AUC values were 0.685, 0.678, and 0.678 (46), and for another 1-, 3-, and 5-year model, the AUCs were 0.554, 0.527, and 0.649 (47). The AUC of the

TABLE 1 The area under the ROC curve (AUC) showed the sensitivity and specificity of the known gene signatures in predicting the prognosis of BC patients.

Article	Year	RCD	Model Gene	AUC
Our	2023	Disulfidptosis	6	0.762 (1-year), 0.734 (3-year), 0.758 (5-year)
Lu, Liu, and Zhang 2022 (44)	2022	Metabolic	4	0.764 (1-year), 0.689 (3-year), 0.612 (5-year)
Chen, Luo, et al., 2022 (45)	2022	Pyroptosis	16	0.756 (1-year), 0.752 (3-year), 0.723 (5-year)
Li et al., 2022 (46)	2022	Cuproptosis	6	0.685 (1-year), 0.678 (3-year), 0.678 (5-year)
Sha et al., 2022 (47)	2022	Cuproptosis	2	0.554 (1-year), 0.527 (3-year), 0.649 (5-year)
Zhu et al., 2022 (48)	2022	Ferroptosis	6	0.821 (1-year), 0.678 (3-year), 0.651 (5-year)
Yu et al., 2022 (49)	2022	Necroptosis	6	0.701 (1-year), 0.716 (2-year), 0.708 (3-year)
Chen, Yang, et al., 2022 (50)	2022	Necroptosis	7	0.731 (1-year), 0.643 (3-year), 0.641 (5-year)

ferroptosis model constructed by Zhu et al. was 0.821, 0.678, and 0.651 in 1-, 3-, and 5-years (48). The AUCs of the ferroptosis model produced by Zhu et al. were 0.821, 0.678, and 0.651 in 1-, 3-, and 5-year models. Although it had a good prediction effect in the first year, our model AUC was above 0.734, which was more stable. We also list other models more concerned with short-term survival rates, such as the AUC of the necroptosis-related model at 1-, 2-, and 3-year patients, which were 0.701, 0.716, and 0.708 (49). The AUC of the necroptosis-related prognostic model constructed by Chen et al. in 1-, 3-, and 5-year patients were 0.731, 0.643, and 0.641, respectively (50). Our prognostic model has adequate predictive value. Our model involves only six genes, while other models tend to have more genes. To a certain extent, our RS model is more convenient to use. The C-index of the nomogram was 0.762 (95% CI: 0.711–0.813), indicating that the predicted results of 1-, 3-, and 5-year patients were consistent with the actual results. The expression of DGs in the high-risk group was significantly increased, suggesting that genes have an adverse effect on the prognoses of patients. Therefore, the prognostic model constructed by DRGs is reliable and accurate. On the other hand, it also shows the critical role of DGs in the occurrence, development, and life processes of tumors. In summary, the model we constructed can be considered a suitable prognostic signal, and its mechanism of action in BC deserves further exploration and verification.

Subsequently, we found the immune factors that determined the prognoses of the high- and low-risk groups through the immune analysis of the patients. The high-risk group had a large number of macrophage M2 cell infiltrations. Macrophages M2 increase is associated with tumor growth and poor prognosis of cancer 48, and are considered essential biomarkers in cancer diagnosis and a potential target for cancer treatment (51, 52). T cells CD8 is a significant member of the low-risk group. In previous reports, T cell CD8 can prevent tumor growth and promote immune response and immunotherapy (53). This may be one of the reasons for the survival difference between high- and low-risk groups. The TMB study showed that PIK3CA had the highest mutation frequency in the low-risk samples, while TP53 had the highest mutation frequency in the high-risk groups. The mutation rate of TP53 in patients with an increased risk of BC is 43%, while the mutation rate of TP53 in patients with low risk is only 29%. Previous studies have reported that the mutation of the TP53 gene is related to the poor therapeutic effect and prognosis of BC (54, 55), confirming the poor prognosis of patients with a high TP53 mutation rate in our high-risk group.

Tumor treatment is an essential field of concern. Through IC 50 screening analysis of potential chemical drugs, we realized that low-risk patients might be more sensitive to chemotherapy, ABT.888 (Veliparib, PARP inhibitors), AG.014699 (Rucaparib, PARP inhibitors), AMG.706 (Motesanib, VEGFR inhibitors), ATRA, and AUY922 (Luminespib, HSP90 inhibitors). GDC0941 (Pictilisib, PI3K inhibitors), Metformin, Methotrexate, Nilotinib, Nutlin.3a (MDM2 inhibitors), Roscovitine, Temsirolimus, Tipifarnib, and other drugs had a lower IC50 in the low-risk group. High-risk patients resisted PARP and VEGFR inhibitors and other drugs and were sensitive to docetaxel (a microtubule depolymerization inhibitor) and parthenolide (NF-κB inhibitors). Immunotherapy also occupies a crucial position in the treatment of BC patients. The ESTIMATE results showed that the stromal immunity and estimated scores of the high-risk group were low. The TIDE analysis showed that the TIDE immune escape score of the high-risk group was low. The combination of PD-1 and PDL-1 caused T cells to lose the ability to attack cancer cells, resulting in the immune escape of tumor cells. The expression of immune checkpoint genes, such as PD-1 and PDL-1, in high-risk patients, was low, which may be the reason for the low TIDE immune escape score in the high-risk group. However, based on the difference in immune checkpoints between the high- and low-risk groups, distinguished by the RS model constructed by DRGs, we found that the expression of immune checkpoint genes in the high-risk group was significantly lower than that in the low-risk group. It is speculated that patients in the low-risk group are more likely to induce an antitumor immune response through immune genes, thus benefiting from immunotherapy, which is consistent with the high Stromal Score, Immune Score, and ESTIMATE Score results of the low-risk population in the previous article. TMB is a reliable biomarker for predicting treatment outcomes in cancer patients treated with ICI (56, 57). This is consistent with our earlier results that 'RS is significantly associated with TMB. Patients in the high-risk group had higher TMB, antitumor immune dysfunction, poor ICI treatment, and poor prognosis. In summary, combined with drug sensitivity and immune efficacy analysis, we predict that low-risk patients will benefit more from combining chemotherapy and immunotherapy, providing a basis for individualized treatment of BC patients. More drugs are worthy of selection and development for low-risk patients. The effects of chemotherapy and immunotherapy in the high-risk group were poor. The high expression of disulfidptosis genes (e.g., SLC3A2, RPN1, BRK1, ACTR2, ACTR3, SLC7A11, and NCKAP1) in the KM analysis of breast cancer indicated the poor prognosis of patients. The difference analysis between the high- and low-risk groups differed. These genes were highly expressed in the high-risk group. Through our study, targeted therapy of the disulfidptosis gene will benefit the high-risk group.

In addition, we conducted *in vitro* validation through cell formation assays and CCK-8 on the high-risk genes (TMEM45A and SHCBP1) within the RS model. This initial validation provided preliminary evidence of the feasibility of utilizing these two genes for targeted therapy in breast cancer (BC). Subsequently, we conducted cellular sequencing following the gene knockout of TMEM45A and SHCBP1 to infer their roles in the biological mechanisms.

This study systematically analyzed the role of disulfidptosis-related genes in the prognosis of breast cancer and their correlation with the tumor microenvironment and clinical characteristics and constructed a better prognosis prediction model. The model performs well in predicting the survival outcome, tumor immune microenvironment, and immunotherapy response of BC patients. Furthermore, it expounds on its correlation with TMB, immunity, and clinical treatment (chemotherapy and immunotherapy), providing a reference for individualized and precise breast cancer treatment. Finally, Experimental validation and sequencing were also conducted to substantiate these findings.

5 Conclusion

This study has the following contributions. First, this study is the first to identify the subtypes associated with disulfidptosis and to create a predictive model based on breast cancer DRGs. Although disulfidptosis differs from other recognized cell death methods, it may provide new therapeutic possibilities for cancer treatment. Second, a variety of different technologies and databases are used to improve the reliability of the results. We also defined subtypes associated with disulfidptosis and created a predictive model for the screening and testing processes. Finally, we first proposed a disulfidptosis gene-targeted therapy for high-risk BC groups. We intend to gather further patient samples during subsequent clinical investigations to substantiate the dependability of our model.

Data availability statement

The datasets presented in this study can be found in online repositories. The names of the repository/repositories and accession number(s) can be found within the article/Supplementary Materials. The sequencing raw data is stored in the GEO database under GSE246486.

Ethics statement

Ethical approval was not required for the studies on humans in accordance with the local legislation and institutional requirements because only commercially available established cell lines were used.

Author contributions

JHL, ZR, and MR designed and conceived this project; XW and JY completed these experiments; JS, JHL, and XW interpreted and analyzed the data; JHL and JCL revised the manuscript. All authors contributed to the article and approved the submitted version.

Funding

The author(s) declare financial support was received for the research, authorship, and/or publication of this article. This study was supported by Wu Jieping Medical Foundation (No. 320.6750.2020-7-1), Anhui Provincial Natural Science Foundation (No. 2308085MH276), Anhui Medical University Clinical Science Foundation (No. 2021xkj140). Research Fund of Anhui Institute of translational medicine (No. 2022zhyx-C29).

Acknowledgments

We acknowledge TCGA and GEO database for providing their platforms and contributors for uploading their meaningful datasets.

Conflict of interest

The authors declare that the research was conducted in the absence of any commercial or financial relationships that could be construed as a potential conflict of interest.

Publisher's note

Supplementary material

The Supplementary Material for this article can be found online at: https://www.frontiersin.org/articles/10.3389/fimmu.2023.1198826/full#supplementary-material

References

1. Siegel RL, Miller KD, Wagle NS, Jemal A. Cancer statistics, 2023. *CA Cancer J Clin* (2023) 73(1):17–48. doi: 10.3322/caac.21763

2. Waks AG, Winer EP. Breast cancer treatment: A review. *Jama* (2019) 321(3):288–300. doi: 10.1001/jama.2018.19323

3. Britt KL, Cuzick J, Phillips KA. Key steps for effective breast cancer prevention. *Nat Rev Cancer* (2020) 20(8):417–36. doi: 10.1038/s41568-020-0266-x

4. Perou CM, Sørlie T, Eisen MB, van de Rijn M, Jeffrey SS, Rees CA, et al. Molecular portraits of human breast tumours. *Nature* (2000) 406(6797):747–52. doi: 10.1038/35021093

5. Lohr M, Hellwig B, Edlund K, Mattsson JS, Botling J, Schmidt M, et al. Identification of sample annotation errors in gene expression datasets. *Arch Toxicol* (2015) 89(12):2265–72. doi: 10.1007/s00204-015-1632-4

6. Liu X, Nie L, Zhang Y, Yan Y, Wang C, Colic M, et al. Actin cytoskeleton vulnerability to disulfide stress mediates disulfidptosis. *Nat Cell Biol* (2023) 25(3):404–14. doi: 10.1038/s41556-023-01091-2

7. Zhang C, Li Z, Qi F, Hu X, Luo J. Exploration of the relationships between tumor mutation burden with immune infiltrates in clear cell renal cell carcinoma. *Ann Transl Med* (2019) 7(22):648. doi: 10.21037/atm.2019.10.84

8. Mayakonda A, Lin DC, Assenov Y, Plass C, Koeffler HP. Maftools: efficient and comprehensive analysis of somatic variants in cancer. *Genome Res* (2018) 28(11):1747–56. doi: 10.1101/gr.239244.118

9. Hänzelmann S, Castelo R, Guinney J. GSVA: gene set variation analysis for microarray and RNA-seq data. *BMC Bioinf* (2013) 14:7. doi: 10.1186/1471-2105-14-7

10. Jin Y, Wang Z, He D, Zhu Y, Chen X, Cao K. Identification of novel subtypes based on ssGSEA in immune-related prognostic signature for tongue squamous cell carcinoma. *Cancer Med* (2021) 10(23):8693–707. doi: 10.1002/cam4.4341

11. Friedman JH, Hastie T, Tibshirani R. Regularization paths for generalized linear models *via* coordinate descent. *J Stat Softw* (2010) 33(1):1missing22. doi: 10.18637/jss.v033.i01

12. Shi X, Li Y, Pan S, Liu X, Ke Y, Guo W, et al. Identification and validation of an autophagy-related gene signature for predicting prognosis in patients with esophageal squamous cell carcinoma. *Sci Rep* (2022) 12(1):1960. doi: 10.1038/s41598-022-05922-4

13. Liu XS, Pompey KT. Bootstrap estimate of bias for intraclass correlation. *J Appl Meas* (2020) 21(1):101–8.

14. Newman AM, Liu CL, Green MR, Gentles AJ, Feng W, Xu Y, et al. Robust enumeration of cell subsets from tissue expression profiles. *Nat Methods* (2015) 12 (5):453–7. doi: 10.1038/nmeth.3337

15. Hu FF, Liu CJ, Liu LL, Zhang Q, Guo AY. Expression profile of immune checkpoint genes and their roles in predicting immunotherapy response. *Brief Bioinform* (2021) 22(3). doi: 10.1093/bib/bbaa176

16. Jiang P, Gu S, Pan D, Fu J, Sahu A, Hu X, et al. Signatures of T cell dysfunction and exclusion predict cancer immunotherapy response. *Nat Med* (2018) 24(10):1550–8. doi: 10.1038/s41591-018-0136-1

17. Charoentong P, Finotello F, Angelova M, Mayer C, Efremova M, Rieder D, et al. Pan-cancer immunogenomic analyses reveal genotype-immunophenotype relationships and predictors of response to checkpoint blockade. *Cell Rep* (2017) 18 (1):248–62. doi: 10.1016/j.celrep.2016.12.019

18. Tsherniak A, Vazquez F, Montgomery PG, Weir BA, Kryukov G, Cowley GS, et al. Defining a cancer dependency map. *Cell* (2017) 170(3):564–76. doi: 10.1016/j.cell.2017.06.010

19. Grishagin IV. Automatic cell counting with ImageJ. *Anal Biochem* (2015) 473:63–5. doi: 10.1016/j.ab.2014.12.007

20. Galluzzi L, Vitale I, Aaronson SA, Abrams JM, Adam D, Agostinis P, et al. Molecular mechanisms of cell death: recommendations of the Nomenclature Committee on Cell Death 2018. *Cell Death Differ* (2018) 25(3):486–541. doi: 10.1038/s41418-017-0012-4

21. Shin CS, Mishra P, Watrous JD, Carelli V, D'Aurelio M, Jain M, et al. The glutamate/cystine xCT antiporter antagonizes glutamine metabolism and reduces nutrient flexibility. *Nat Commun* (2017) 8:15074. doi: 10.1038/ncomms15074

22. Koppula P, Zhang Y, Shi J, Li W, Gan B. The glutamate/cystine antiporter SLC7A11/xCT enhances cancer cell dependency on glucose by exporting glutamate. *J Biol Chem* (2017) 292(34):14240–9. doi: 10.1074/jbc.M117.798405

23. Goji T, Takahara K, Negishi M, Katoh H. Cystine uptake through the cystine/glutamate antiporter xCT triggers glioblastoma cell death under glucose deprivation. *J Biol Chem* (2017) 292(48):19721–32. doi: 10.1074/jbc.M117.814392

24. Liu X, Olszewski K, Zhang Y, Lim EW, Shi J, Zhang X, et al. Cystine transporter regulation of pentose phosphate pathway dependency and disulfide stress exposes a targetable metabolic vulnerability in cancer. *Nat Cell Biol* (2020) 22(4):476–86. doi: 10.1038/s41556-020-0496-x

25. Hanahan D, Weinberg RA. Hallmarks of cancer: the next generation. *Cell* (2011) 144(5):646–74. doi: 10.1016/j.cell.2011.02.013

26. Zhu L, Tian Q, Jiang S, Gao H, Yu S, Zhou Y, et al. A novel ferroptosis-related gene signature for overall survival prediction in patients with breast cancer. *Front Cell Dev Biol* (2021) 9:670184. doi: 10.3389/fcell.2021.670184

27. Hu T, Zhao X, Zhao Y, Cheng J, Xiong J, Lu C. Identification and verification of necroptosis-related gene signature and associated regulatory axis in breast cancer. *Front Genet* (2022) 13:842218. doi: 10.3389/fgene.2022.842218

28. Xu L, Hu Y, Liu W. Pyroptosis-mediated molecular subtypes are characterized by distinct tumor microenvironment infiltration characteristics in breast cancer. *J Inflammation Res* (2022) 15:345–62. doi: 10.2147/jir.S349186

29. Wang D, Wei G, Ma J, Cheng S, Jia L, Song X, et al. Identification of the prognostic value of ferroptosis-related gene signature in breast cancer patients. *BMC Cancer* (2021) 21(1):645. doi: 10.1186/s12885-021-08341-2

30. Lang GT, Jiang YZ, Shi JX, Yang F, Li XG, Pei YC, et al. Characterization of the genomic landscape and actionable mutations in Chinese breast cancers by clinical sequencing. *Nat Commun* (2020) 11(1):5679. doi: 10.1038/s41467-020-19342-3

31. Lu X, Kang N, Ling X, Pan M, Du W, Gao S. MiR-27a-3p promotes non-small cell lung cancer through SLC7A11-mediated-ferroptosis. *Front Oncol* (2021) 11:759346. doi: 10.3389/fonc.2021.759346

32. Li YZ, Zhu HC, Du Y, Zhao HC, Wang L. Silencing lncRNA SLC16A1-AS1 Induced Ferroptosis in Renal Cell Carcinoma Through miR-143-3p/SLC7A11 Signaling. *Technol Cancer Res Treat* (2022) 21:15330338221077803. doi: 10.1177/15330338221077803

33. Yang X, Ding Y, Sun L, Shi M, Zhang P, He A, et al. WASF2 serves as a potential biomarker and therapeutic target in ovarian cancer: A pan-cancer analysis. *Front Oncol* (2022) 12:840038. doi: 10.3389/fonc.2022.840038

34. Shao W, Yang Z, Fu Y, Zheng L, Liu F, Chai L, et al. The pyroptosis-related signature predicts prognosis and indicates immune microenvironment infiltration in gastric cancer. *Front Cell Dev Biol* (2021) 9:676485. doi: 10.3389/fcell.2021.676485

35. Chen D, Huang H, Zang L, Gao W, Zhu H, Yu X. Development and verification of the hypoxia- and immune-associated prognostic signature for pancreatic ductal adenocarcinoma. *Front Immunol* (2021) 12:728062. doi: 10.3389/fimmu.2021.728062

36. Coleman S, Kirk PDW, Wallace C. Consensus clustering for Bayesian mixture models. *BMC Bioinf* (2022) 23(1):290. doi: 10.1186/s12859-022-04830-8

37. Wang N, Zhu L, Wang L, Shen Z, Huang X. Identification of SHCBP1 as a potential biomarker involving diagnosis, prognosis, and tumor immune microenvironment across multiple cancers. *Comput Struct Biotechnol J* (2022) 20:3106–19. doi: 10.1016/j.csbj.2022.06.039

38. Asanprakit W, Lobo DN, Eremin O, Bennett AJ. M1 macrophages evoke an increase in polymeric immunoglobulin receptor (PIGR) expression in MDA-MB468 breast cancer cells through secretion of interleukin-1β. *Sci Rep* (2022) 12(1):16842. doi: 10.1038/s41598-022-20811-6

39. Miao Y, Wang J, Ma X, Yang Y, Mi D. Identification prognosis-associated immune genes in colon adenocarcinoma. *Biosci Rep* (2020) 40(11). doi: 10.1042/bsr20201734

40. Zhu X, Jiang X, Zhang Q, Huang H, Shi X, Hou D, et al. TCN1 deficiency inhibits the Malignancy of colorectal cancer cells by regulating the ITGB4 pathway. *Gut Liver* (2022) 17(3):412–29. doi: 10.5009/gnl210494

41. Bhakta S, Crocker LM, Chen Y, Hazen M, Schutten MM, Li D, et al. An anti-GDNF family receptor alpha 1 (GFRA1) antibody-drug conjugate for the treatment of hormone receptor-positive breast cancer. *Mol Cancer Ther* (2018) 17(3):638–49. doi: 10.1158/1535-7163.Mct-17-0813

42. Zhang D, Li Y, Yang S, Wang M, Yao J, Zheng Y, et al. Identification of a glycolysis-related gene signature for survival prediction of ovarian cancer patients. *Cancer Med* (2021) 10(22):8222–37. doi: 10.1002/cam4.4317

43. Lv W, Yu H, Han M, Tan Y, Wu M, Zhang J, et al. Analysis of tumor glycosylation characteristics and implications for immune checkpoint inhibitor's efficacy for breast cancer. *Front Immunol* (2022) 13:830158. doi: 10.3389/fimmu.2022.830158

44. Lu J, Liu P, Zhang R. A metabolic gene signature to predict breast cancer prognosis. *Front Mol Biosci* (2022) 9:900433. doi: 10.3389/fmolb.2022.900433

45. Chen H, Luo H, Wang J, Li J, Jiang Y. Identification of a pyroptosis-related prognostic signature in breast cancer. *BMC Cancer* (2022) 22(1):429. doi: 10.1186/s12885-022-09526-z

46. Li Z, Zhang H, Wang X, Wang Q, Xue J, Shi Y, et al. Identification of cuproptosis-related subtypes, characterization of tumor microenvironment infiltration, and development of a prognosis model in breast cancer. *Front Immunol* (2022) 13:996836. doi: 10.3389/fimmu.2022.996836

47. Sha S, Si L, Wu X, Chen Y, Xiong H, Xu Y, et al. Prognostic analysis of cuproptosis-related gene in triple-negative breast cancer. *Front Immunol* (2022) 13:922780. doi: 10.3389/fimmu.2022.922780

48. Zhu J, Chen Q, Gu K, Meng Y, Ji S, Zhao Y, et al. Correlation between ferroptosis-related gene signature and immune landscape, prognosis in breast cancer. *J Immunol Res* (2022) 2022:6871518. doi: 10.1155/2022/6871518

49. Yu H, Lv W, Tan Y, He X, Wu Y, Wu M, et al. Immunotherapy landscape analyses of necroptosis characteristics for breast cancer patients. *J Transl Med* (2022) 20 (1):328. doi: 10.1186/s12967-022-03535-z

50. Chen F, Yang J, Fang M, Wu Y, Su D, Sheng Y. Necroptosis-related lncRNA to establish novel prognostic signature and predict the immunotherapy response in breast cancer. *J Clin Lab Anal* (2022) 36(4):e24302. doi: 10.1002/jcla.24302

51. Cha YJ, Koo JS. Role of tumor-associated myeloid cells in breast cancer. *Cells* (2020) 9(8). doi: 10.3390/cells9081785

52. Komohara Y, Jinushi M, Takeya M. Clinical significance of macrophage heterogeneity in human Malignant tumors. *Cancer Sci* (2014) 105(1):1–8. doi: 10.1111/cas.12314

53. Farhood B, Najafi M, Mortezaee K. CD8(+) cytotoxic T lymphocytes in cancer immunotherapy: A review. *J Cell Physiol* (2019) 234(6):8509–21. doi: 10.1002/jcp.27782

54. Olivier M, Hollstein M, Hainaut P. TP53 mutations in human cancers: origins, consequences, and clinical use. *Cold Spring Harb Perspect Biol* (2010) 2(1):a001008. doi: 10.1101/cshperspect.a001008

55. Takahashi S, Fukui T, Nomizu T, Kakugawa Y, Fujishima F, Ishida T, et al. TP53 signature diagnostic system using multiplex reverse transcription-polymerase chain reaction system enables prediction of prognosis of breast cancer patients. *Breast Cancer* (2021) 28(6):1225–34. doi: 10.1007/s12282-021-01250-z

56. Addeo A, Friedlaender A, Banna GL, Weiss GJ. TMB or not TMB as a biomarker: That is the question. *Crit Rev Oncol Hematol* (2021) 163:103374. doi: 10.1016/j.critrevonc.2021.103374

57. Cao D, Xu H, Xu X, Guo T, Ge W. High tumor mutation burden predicts better efficacy of immunotherapy: a pooled analysis of 103078 cancer patients. *Oncoimmunology* (2019) 8(9):e1629258. doi: 10.1080/2162402x.2019.1629258

frontiers | Frontiers in Immunology

TYPE Original Research
PUBLISHED 17 January 2024
DOI 10.3389/fimmu.2023.1301157

OPEN ACCESS

EDITED BY
Ines Zidi,
Tunis El Manar University, Tunisia

REVIEWED BY
Melissa A. Reimers,
Washington University in St. Louis, United States
Murat Akand,
University Hospitals Leuven, Belgium

*CORRESPONDENCE
Yuyan Zhu
yyzhu@cmu.edu.cn
Meng Yu
yumeng@cmu.edu.cn

RECEIVED 24 September 2023
ACCEPTED 29 December 2023
PUBLISHED 17 January 2024

CITATION
Xu Y, Sun X, Liu G, Li H, Yu M and Zhu Y (2024) Integration of multi-omics and clinical treatment data reveals bladder cancer therapeutic vulnerability gene combinations and prognostic risks. *Front. Immunol.* 14:1301157. doi: 10.3389/fimmu.2023.1301157

Integration of multi-omics and clinical treatment data reveals bladder cancer therapeutic vulnerability gene combinations and prognostic risks

Yan Xu[1], Xiaoyu Sun[2], Guangxu Liu[1], Hongze Li[1], Meng Yu[3,4]* and Yuyan Zhu[1]*

[1]Department of Urology, The First Hospital of China Medical University, Shenyang, China, [2]Department of Pharmacology, School of Pharmacy, China Medical University, Shenyang, China, [3]Department of Laboratory Animal Science, China Medical University, Liaoning, Shenyang, China, [4]Key Laboratory of Transgenetic Animal Research, China Medical University, Liaoning, Shenyang, China

Background: Bladder cancer (BCa) is a common malignancy of the urinary tract. Due to the high heterogeneity of BCa, patients have poor prognosis and treatment outcomes. Immunotherapy has changed the clinical treatment landscape for many advanced malignancies, opening new avenues for the precise treatment of malignancies. However, effective predictors and models to guide clinical treatment and predict immunotherapeutic outcomes are still lacking.

Methods: We downloaded BCa sample data from The Cancer Genome Atlas to identify anti-PD-L1 immunotherapy-related genes through an immunotherapy dataset and used machine learning algorithms to build a new PD-L1 multidimensional regulatory index (PMRI) based on these genes. PMRI-related column-line graphs were constructed to provide quantitative tools for clinical practice. We analyzed the clinical characteristics, tumor immune microenvironment, chemotherapy response, and immunotherapy response of patients based on PMRI system. Further, we performed function validation of classical PMRI genes and their correlation with PD-L1 in BCa cells and screening of potential small-molecule drugs targeting PMRI core target proteins through molecular docking.

Results: PMRI, which consists of four anti-PD-L1 immunotherapy-associated genes (*IGF2BP3, P4HB, RAC3*, and *CLK2*), is a reliable predictor of survival in patients with BCa and has been validated using multiple external datasets. We found higher levels of immune cell infiltration and better responses to immunotherapy and cisplatin chemotherapy in the high PMRI group than in the low PMRI group, which can also be used to predict immune efficacy in a variety of solid tumors other than BCa. Knockdown of *IGF2BP3* inhibited BCa cell proliferation and migration, and *IGF2BP3* was positively correlated with PD-L1 expression. We performed molecular docking prediction for each of the core proteins comprising PMRI and identified 16 small-molecule drugs with the highest affinity to the target proteins.

Conclusions: Our PD-L1 multidimensional expression regulation model based on anti-PD-L1 immunotherapy-related genes can accurately assess the prognosis of patients with BCa and identify patient populations that will benefit from immunotherapy, providing a new tool for the clinical management of intermediate and advanced BCa.

KEYWORDS

bladder cancer, regulation of PD-L1 expression, prognosis, immunotherapy efficacy, molecular docking

Background

Bladder cancer (BCa) is the tenth most common malignancy worldwide and has the sixth highest incidence in men, with approximately 573,000 new cases and 213,000 cancer-related deaths annually worldwide (1). Patients with muscle-invasive bladder cancer (MIBC) have a poor prognosis, with an overall five-year survival rate of 40–50%. For patients with limited MIBC, neoadjuvant chemotherapy combined with radical cystectomy is the primary treatment modality, whereas only palliative systemic chemotherapy or immunotherapy is used for metastatic BCa (2). BCa is considered an immunotherapy-responsive tumor, immune checkpoint inhibition therapy targeting the immunosuppressive microenvironment has revolutionized cancer treatment (3). However, only a fraction of patients has experienced lasting benefits from immune checkpoint inhibitors, limiting the use of these promising strategies in clinical practice (3, 4). Therefore, there is an urgent need to identify reliable molecular biomarkers to predict the response to checkpoint blockade and improve the clinical efficacy of these therapies.

Research on potential biomarkers for BCa immunotherapy has focused on two aspects, (i) tumor cell-related markers, such as intratumoral heterogeneity (ITH), tumor mutational burden (TMB), intrinsic molecular subtypes (IMS), DNA damage repair (DDR), intrinsic molecular subtypes, gene expression profile (GEP); (ii) tumor microenvironment-related markers, such as tumor-infiltrating lymphocytes (TIL), intrinsic molecular subtypes (IMS), GEP. Damage response (DDR), intrinsic molecular isoforms, GEP. (iii) Markers related to tumor microenvironment, such as tumor infiltrating lymphocyte (tumor-infiltrating lymphocyte TIL), programmed cell death protein (PD-1/PD-L1), gastrointestinal microbiota (5, 6). However, owing to the high heterogeneity of BCa, there is currently no biomarker with sufficient clinical evidence to justify its routine use. Therefore, there is a need to understand the role of immunotherapy in BCa based on immunotherapy-related genes and to identify reliable features to predict the prognosis of patients with BCa and their response to immunotherapy and chemotherapy.

The expression of programmed cell death ligand 1 (PD-L1), an important immunosuppressive protein on the surface of tumor cells, is regulated at multiple levels, including genomic alterations (amplification or translocation), epigenetic modifications (methylation of histones or CpG islands and histone acetylation), transcriptional regulation (inflammatory stimulation and oncogenic signaling), post-transcriptional regulation (miRNA, 3'-UTR, RAS and angiotensin II status regulation), post-translational modifications (ubiquitination, glycosylation, phosphorylation and palmitoylation) (7). The pathways, proteins, and cytokines involved in the regulation of PD-L1 expression are complex and diverse; however, all of these regulatory pathways could be novel ways to treat tumors. In the past few years, ICIs blocking the PD-1/PD-L1 pathway have emerged as therapeutic approaches that can improve the overall survival of patients with mUC, but they are effective with PD-L1 inhibitor therapy only in some patients. Consequently, it is of great clinical significance to investigate the regulatory mechanisms of PD-L1 expression in depth (3). Notably, clinical prediction models constructed to integrate the regulatory mechanisms of PD-L1 expression are lacking. Therefore, exploring PD-L1 expression regulation models can help predict the efficacy of anti-PD-1/PD-L1 immunotherapy in patients with BCa to help them choose the treatment strategies.

In current study,we identified four genes that regulate PD-L1 expression in different dimensions based on the screening of immunotherapy-related genes from an immunotherapy dataset and combined them with machine learning methods to construct a therapeutically guided PD-L1 Multidimensional Regulation Index (PMRI). The different forms of validation all suggest that the PD-L1 multidimensional expression regulation model can accurately assess the prognosis of patients with BCa and identify possible patient populations benefiting from immunotherapy and chemotherapy.

Materials and methods

Obtaining sequence data from BCa patients and identifying anti-PD-L1 immunotherapy-related genes

We downloaded expression profile data, corresponding clinical information and pathological sections from The Cancer Genome

Atlas (TCGA) (https://portal.gdc.cancer.gov/) database for BCa patients, and raw RNA-seq data were normalized to fragments per kilobase million (FPKM). The GSE13507, GSE32894, GSE31684 and GSE48075 cohorts were obtained from the Gene Expression Omnibus (GEO) (https://cancergenome.nih.gov/) database. We also downloaded the IMvigor210 immunotherapy data cohort, a group of expression profile data and corresponding clinical information for patients treated with anti-PD-L1 antibody (atezolizumab) for uroepithelial carcinoma (8). After receiving anti-PD-L1 antibody immunotherapy, patients were classified into the following four categories based on response: complete remission (CR), partial remission (PR), stable disease (SD), and progressive disease (PD), and we set CR and PR in the IMvigor210 dataset as the group responding to PD-L1 blockers and SD and PD as the group not responding to PD-L1 blockers. Genes differentially expressed in response to anti-PD-L1 immunotherapy were identified by comparing the response and non-response groups by the R package "DESeq2" at a threshold (p-value < 0.05), after which we used WGCNA to obtain the module with the highest correlation to the CR group and thus the anti-PD-L1 immunotherapy-related genes.

Unsupervised clustering

Based on the red module genes obtained from the above WGCNA, we performed consensus clustering using the R package "ConsensusClusterPlus" to identify BCa subtypes (9).

Construction and validation of PD-L1 multidimensional regulatory index and histological validation at the protein level

We performed differential expression analysis of the modular genes with the highest correlation with the CR group between tumor and normal tissues with a threshold of logFC > 1 and fdr < 0.01. Genes associated with prognosis in BCa patients were subsequently screened by univariate cox regression analysis with a threshold of p-value < 0.005, and finally multifactorial cox regression analysis was used to construct a PD-L1 multidimensional regulatory index (PMRI). PMRI was obtained for each BCa patient according to the following formula: PD-L1 multidimensional regulatory index (PMRI) = Coef(Gene1) × Expr(Gene1) + Coef(Gene2) × Expr(Gene2) +…… + Coef(Gene n) × Expr(Gene n). Where Expr(Gene n) represents the expression of a particular gene and Coef(Gene n) represents the coefficient obtained from multifactorial Cox analysis of genes. GSE13507, GSE32894, GSE31684 and GSE48075 cohorts were eliminated for batch effects and combined as an external validation cohort.

Based on Kaplan-Meier method and subject operating characteristic curve (ROC) to study TCGA cohort and GSE13507, GSE32894, GSE31684, and GSE48075 cohorts to validate the prognostic value of PMRI. We combined the commonly used clinicopathological features to construct column line plots and compared the validity of the column line plots by plotting 1-, 3-, and 5-year calibration curves as well as ROC curves. We further searched the Human Protein Atlas database (https://www.proteinatlas.org/) (10) to obtain histological validation of *CLK2, IGF2BP3, P4HB* and *RAC3* at the protein level between bladder tumor tissue and normal bladder tissue.

Gene set enrichment analysis and immuno-infiltration analysis

GSEA was performed by the R package "clusterProfiler" to evaluate the major enrichment pathways in the high-risk group, and the HALLMARK, c5GO and c2KEGG gene sets were set as the enriched gene sets with the screening conditions of |NES| > 1, nominal p-value<0.05. The sample replacement test was performed 1000 times, so gene sets were obtained from the MSigDb database (https://www.gsea-msigdb.org/gsea/msigdb/) download.

Tumor purity, stromal score, immune score and ESTIMATE score (10) were calculated for each BCa patient using the "ESTIMATE" package in the R program. A single sample gene set enrichment analysis (ssGSEA) algorithm was also used to study the level of immune infiltration based on different immune cell types between the high PMRI and low PMRI groups. Lymphocyte scores in pathological sections were graded using a semi-quantitative scoring system (0-5) to describe tumor inflammation.

Analysis of drug treatment response and immunotherapy response

We derived IC50 by ProPhetic algorithm to assess drug response to common chemotherapy treatments for BCa, comparing drug sensitivity to chemotherapy treatments in patients with high and low PMRI. We also downloaded gene expression of cancer cells to different drugs from Genomics For Drug Sensitivity in Cancer (GDSC) database (https://www.cancerrxgene.org/) (11) and the Cancer Treatment Response Portal (CTRP) database (https://portals.broadinstitute.org/ctrp/) (12) to download the gene expression data of cancer cells to different drugs to analyze the gene expression of *CLK2, IGF2BP3, P4HB* and *RAC3* in relation to drug sensitivity.

The response of BCa patients to immunotherapy was assessed by the Tumor Immune Dysfunction and Exclusion (TIDE) algorithm score in the TIDE database (http://tide.dfci.harvard.edu/) (13), and the immune escape potential between high and low PMRI groups was investigated using the Wilcoxon trial (TIDE score), with high TIDE scores often associated with poorer immunotherapy response and stronger immune escape potential. We also extracted clinical information from the IMvigor210 dataset (atezolizumab) to assess the analysis of differences between anti-PD-L1 immunotherapy groups (responders or non-responders) between high/low PMRI (8). These results were used to assess the predictive value of PMRI on the effect of immune checkpoint therapy.

Molecular docking simulation

We used MOE software to screen small molecule drugs that bind to the target proteins and perform molecular docking simulations. We downloaded the protein structures of the target targets (CLK2-6KHE, IGF2BP3-6GX6, P4HB-7ZSC and RAC3-2QME) from the PDB database and small molecule drugs were obtained from the zinc15 database of FDA approved drugs and subjected to energy minimization. We set LigX to 7 at pH and 300 K to optimize the protonation state and hydrogen orientation of the protein, and finally simulated the binding pose of IGF2BP3, RAC3, CLK2 and P4HB to small molecule drugs by docking.

Cell culture

We purchased and used human BCa cell lines T24 and UM-UC3 from the Shanghai Cell Bank of the Chinese Academy of Sciences. T24 and UM-UC3 cells were cultured in medium containing 5% fetal bovine serum against the wall. Cells were cultured at 37°C with 5% CO2.

Small interfering RNA transfection

The purchased siRNA was transfected with lipo3000. T24 and UM-UC3 cells were pre-plated into 6-well cell culture plates and transfected when cell fusion reached about 70%. First, 7.5 μL of 20 μM siRNA solution and 125 μL of serum-free medium were mixed well and incubated for 5 min at room temperature; 7.5 μL of Lipo3000 and 125 μL of serum-free medium were mixed well and incubated for 5 min at room temperature. The two solutions were then mixed together and incubated for 15 min. Finally, the mixture was added to the cells and the 6-well plate was shaken gently in an "8" motion to mix the transfection solution into the medium. The cells were incubated for 48 hours and then analyzed for transfection efficiency. *IGF2BP3*-specific siRNA sequences are: si-*IGF2BP3*#1, 5'-GCTGGAGCTTCAATTAAGA-3'; si-*IGF2BP3*#2, 5'-CCTTGAAAGTAGCCTATAT-3'.

Protein blotting

Total cell lysates were extracted, normalized and attenuated for electrophoresis. Proteins were separated by SDS-PAGE and transferred to PVDF membranes. The membranes were then blocked in 3% bovine serum albumin at room temperature, incubated overnight with primary antibody, and then incubated with secondary antibody.

RNA extraction and real-time PCR

A total of 14 BCa specimens were collected at the First Hospital of China Medical University (Shenyang, China), and all samples were rapidly frozen at -80°C immediately after collection. total RNA was prepared from 14 BCa tissues by Trizol reagent (Invitrogen) and reverse transcribed in PrimeScript RT premix (Takara). The primer sequences for *IGF2BP3* and *PD-L1* primer sequences are shown in Supplementary Table S1.

Cell Counting Kit-8 cell activity assay and EdU cell proliferation assay

CCK8 and EdU were used to detect cell viability. The digested cells were washed and resuspended and then counted using a cell counting plate, and the counts were averaged three times. T24 and UM-UC3 cells transfected with si-*IGF2BP3* were spread in 96-well plates, after which 2000 cells were inoculated into each well, and 6 replicate wells were set up for each group, and five groups of 0h, 24h, 48h, 72h and 96h were set up. At 0h, 24h, 48h, 72h and 96h, 10 μl of CCK8 solution was added to each well and mixed thoroughly with a pipette gun, followed by incubation in a tinfoil-wrapped light-proof treatment in an incubator at 37°C for 4 h. The absorbance values of each well at 450 nm were measured and counted under light-proof conditions using a multi-mode enzyme marker. The si-*IGF2BP3*-transfected T24 and UM-UC3 cells were inoculated in 24-well plates, and each well was incubated with EdU medium for 2 h. The cells were washed twice with PBS. Cell fixation solution (PBS containing 4% paraformaldehyde) was added to each well and fixed at room temperature for 30 min, after which the glycine decolorization shaker was added and incubated for 5 min before discarding the glycine solution and adding 100 μl of permeant decolorization shaker with slow shaking permeation. After that, staining reaction solution was added to each well under light-proof treatment. Images were examined using fluorescence microscopy. Each experiment was repeated three times.

Cell migration capacity assay

Wound-healing and Transwell assays were performed to determine cell invasion ability. Parallel lines were drawn on the bottom surface of six-well plates using marker pens, T24 and UM-UC3 cells were resuspended and the plates were spread, and the next day a straightedge was used to create scratches than using a 10 μl gun tip with the direction of the scratch perpendicular to the marker line, after which the cells were washed 3 times with PBS to wash away the floating cells, and after 72 h the cells were removed and photographed under a microscope. Transfected T24 and UM-UC3 cells were collected and starved in serum-free medium for 4h to remove the effect of serum. The cells were digested with trypsin and resuspended in serum-free incomplete medium, followed by the addition of the above cell suspension in the upper chamber of the Transwell and complete medium containing 10% fetal bovine serum in the lower chamber for 48 h. The Transwell was washed three times with PBS, and the cells adhering to the lower membrane were fixed with 4% paraformaldehyde and stained with crystal violet. Each experiment was repeated three times.

Statistical analysis

Survival curves were plotted using the Kaplan-Meier method to compare survival differences between the two groups Correlations were assessed using Spearman correlation analysis. P-values ≤0.05 were considered statistically significant. All statistical analyses were performed by R. Experimental data were processed and plotted using Image J and GraphPad software. The workflow of this study is shown in Supplementary Figure S1.

Results

Identification of anti-PD-L1 immunotherapy-related genes in BCa

We performed a difference analysis of the IMvigor210 dataset between the groups responding to PD-L1 blockers (CR and PR groups) and those non-responding to PD-L1 blockers (SD and PD groups) with a threshold of p-value less than 0.05, and obtained 3301 genes and constructed a volcano plot (Figure 1A). To identify the modules with the highest correlation with the complete response group (CR group), we applied WGCNA to the TCGA-BLCA dataset to construct a co-expression network and finally aggregated the 3301 genes obtained above into 6 modules (Figure 1B) with an optimal soft threshold of 4 to ensure a scale-free topology (Figure 1C). The correlations between the module feature genes and multiple variables were obtained by calculating the Pearson correlation coefficient (PCC), where the red module was significantly positively correlated with the CR composition (PCC=0.25, P=2E-06) (Figure 1D). We then performed GO and KEGG enrichment analysis of the genes in the red module, and the results showed that they are mainly involved in the cell cycle, DNA replication, and the pathway of DNA unwinding helicase activity (Figure 1E).

Identification of anti-PD-L1 immunotherapy-associated Clusters and differences in immune microenvironment and immunotherapy response among different Clusters

We performed a cluster analysis of BCa patients in the TCGA cohort using the red module genes obtained after WGCNA analysis, and the results showed that the BCa patients in the TCGA cohort could be well divided into two clusters, and there was good internal stability and consistency between the two clusters (Supplementary Figure S2A). Kaplan-Meier curves showed that patients in Cluster1 group had significantly worse prognosis than Cluster2 group ($p < 0.05$) (Supplementary Figure S2B). Comparison of the differences in immune microenvironment between the two Clusters by the ESITIMATE algorithm showed that Cluster 2 had a higher ESITIMATE score, immune score, stromal score and lower tumor purity compared to Cluster 1 (Supplementary Figure S2C). The CIBERSORT algorithm showed a significant difference in immune cell infiltration between the two Clusters. Significantly different, with a significantly higher proportion of CD8 T cells in Cluster 2 than in Cluster 1 ($p < 0.05$) (Supplementary Figure S2D).

Construction and validation of PD-L1 multidimensional regulatory index

We performed differential and prognostic analyses on the red module genes obtained from the WGCNA analysis, after which in order to construct a risk model associated with PD-L1 immunotherapy and its derived PD-L1 multidimensional regulatory index (PMRI), we used multifactorial Cox analysis to screen four genes with independent prognostic value to construct the PMRI, which were *IGF2BP3* (HR= 1.225, 95% CI=1.026-1.463, P=0.025), *P4HB* (HR=1.573, 95% CI=1.170-2.113, P=0.003), *RAC3* (HR=1.256, 95% CI=1.054-1.496, P=0.011) and *CLK2* (HR=0.614, 95% CI=0.456-0.825, P=0.001)(The coefficients obtained from the multifactorial Cox analysis of the four genes in PMRI were 0.203 for *IGF2BP3*, 0.453 for *P4HB*, 0.228 for *RAC3* and -0.488 for *CLK2* (Figures 2A, B). We compared the expression levels of *IGF2BP3, P4HB, RAC3* and *CLK2* in TCGA BCa tissues and normal tissues, and the results showed that all four genes were significantly upregulated in tumor tissues (Figure 2C). We also obtained immunohistochemical staining results of *CLK2, IGF2BP3, P4HB* and *RAC3* from the HPA database in normal and BCa tissues, demonstrating that these four genes were highly expressed in BCa tissues (Figure 2D).

PD-L1 multidimensional modulation index predicts the prognosis of BCa patients

Kaplan-Meier curves showed that the high PMRI group had a worse prognosis in the OS phase compared to the low PMRI group ($p < 0.05$) (Figure 3A). To assess the prognostic predictive validity of PMRI, we obtained the GSE13507, GSE32894, GSE31684, and GSE48075 cohorts as a validation cohort, and the results showed that the mortality rate was significantly higher in the high-PMRI group than in the low-PMRI group ($p < 0.05$), suggesting that PMRI has a better prognostic predictive value at OS stage (Figure 3B). The results by univariate and multivariate regression analysis showed that PMRI was an independent risk factor (Figures 3C, D). We also performed a difference analysis of different common clinical characteristics in the high/low PMRI group, and the results showed that Cluster, grading and BCa subtypes were significantly different in the high/low PMRI group ($p < 0.05$) (Figure 3E). Analysis of PMRI index and clinical trait stratified survival curves showed that PMRI could significantly differentiate the prognosis of each clinical subgroup, with patients in the high PMRI group having a had a poorer prognosis (Supplementary Figure S3).

We also obtained the characteristics of currently published prognostic models for BCa and compared them with the prognostic prediction accuracy of the PMRI in this study, and the results showed that the PMRI outperformed other prognostic models in predicting BCa patients (Figure 3F; Supplementary

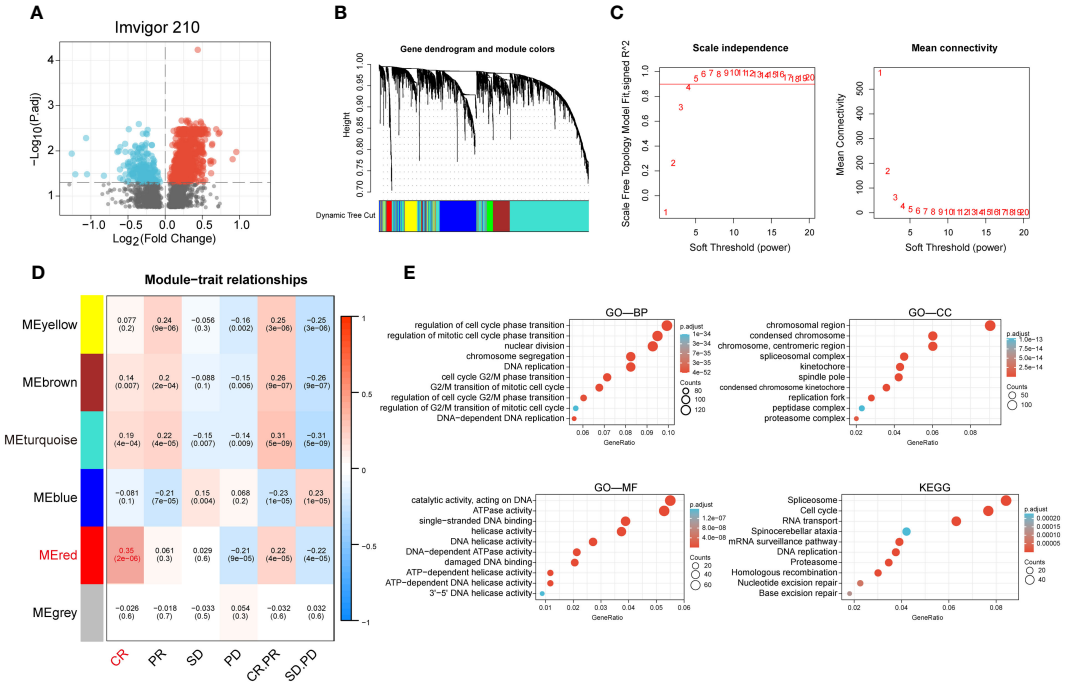

FIGURE 1
Identification of anti-PD-L1 immunotherapy-related genes in BCa. **(A)** Volcano plot of anti-PD-L1 blocker antibodies (CR and PR groups) versus anti-PD-L1 antibody non-responsive groups (SD and PD groups) for differential analysis. **(B)** Cluster dendrogram of 3301 genes with significant differences. **(C)** Selection of optimal soft threshold power over a wide range. **(D)** Tabular cells showing Pearson correlation coefficients with p-values between modular feature genes and multiple variables. **(E)** GO enrichment analysis and KEGG enrichment analysis of the red module genes.

Figure S4), (14–20).The area under the ROC curve (AUC) can be used to analyze the validity of the PMRI prognostic prediction, and the AUCs at 1, 3 and 5 years were 0.709, 0.663 and 0.623, and the 1-year AUC was better than other clinical features in predicting patient survival, suggesting that this PMRI can better predict the short- and long-term survival of BCa patients (Figures 3G, H). Finally, we constructed column line graphs based on the PMRI and other clinical features (age and clinical stage) from multivariate analysis, with the PMRI accounting for the major part of the total column line graph score (Figure 3I). The calibration curve showed that the 1-, 3-, and 5-year column line plots exhibited good predictive accuracy compared to the reference line (Figure 3J). These results above suggest that PMRI can accurately and reliably predict the survival outcome of BCa patients.

PD-L1 multidimensional regulatory index predicts pan-cancer prognosis

To explore the prevalence of PMRI in other cancers, we used the model equation for PMRI described above to calculate PMRI values for patients with other cancer types in TCGA and to plot Kaplan-Meier survival curves for the high/low PMRI groups. For Overall Survival (OS), patients in the high PMRI group in KIRP, LGG, LUAD, MESO, PCPG, SARC, THCA, and UCEC had a poorer prognosis, while patients in the low PMRI group in LAML had a poorer prognosis (Figure 4A). For Disease Specific Survival (DSS), patients in the high PMRI group in BLCA, KIRC, KIRP, LGG, MESO, SARC, SKCM, THCA, and UCEC had poorer Disease Specific Survival. The patients in the low PMRI group in CESC had poorer Disease-Specific Survival (Figure 4B). For Disease Free Interval (DFI), patients in the high PMRI group in BLCA, LGG, SARC and UCEC had shorter Disease Free Interval, while patients in the low PMRI group in ESCA had shorter Disease Free Interval (Figure 4C). For Progression Free Interval (PFI), patients in the high PMRI group had shorter Progression Free Interval in BLCA, KIRP, LGG, MESO, SARC, SKCM and UCEC, while patients in the low PMRI group had shorter Progression Free Interval in CESC and PRAD. Progression Free Interval in CESC and PRAD (Figure 4D). The above results suggest that PMRI has a good effect in predicting prognosis not only in BCa but also in other cancers.

Correlation of gene set enrichment analysis and PD-L1 multidimensional regulatory index with the tumor microenvironment

To explore the cancer signaling pathways associated with PMRI, we performed GSEA analysis in the high PMRI and low PMRI groups, and the results showed that the high PMRI group was significantly enriched in HYPOXIA, IL2_STAT5_SIGNALING, IL6_JAK_STAT3_SIGNALING, INFLAMMATORY_ RESPONSE, INTERFERON_GAMMA_RESPONSE, MTORC1_SIGNALING, and PI3K_AKT_MTOR_SIGNALING signaling pathways, and the above signaling pathways are involved in the regulation of

10.3389/fimmu.2023.1301157

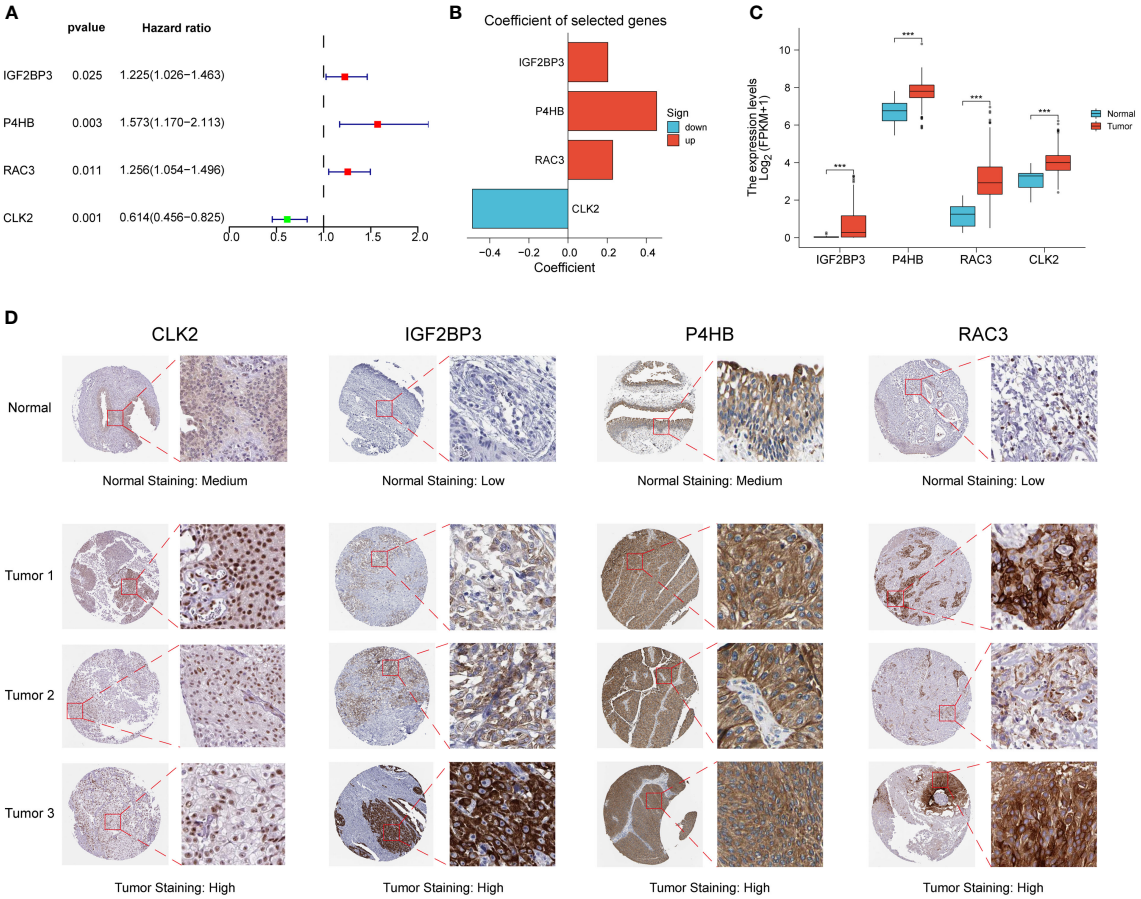

FIGURE 2
Construction of PD-L1 multidimensional regulatory index and validation of immunohistochemical staining results. **(A)** Forest plots of four PMRIs obtained by multifactorial Cox analysis. **(B)** Constructed histograms of four gene coefficients composed of PMRI. **(C)** Comparison of the expression levels of *IGF2BP3, P4HB, RAC3* and *CLK2* in TCGA BCa tissues and normal tissues. **(D)** Immunohistochemical staining results of CLK2, IGF2BP3, P4HB and RAC3 in normal and BCa tissues. *p < 0.05, **p < 0.01, ***p < 0.001.

PD-L1 expression levels, so it can be confirmed that PMRI is closely related to PD-L1 expression levels (21) (Figure 5A). In addition, by performing GO and KEGG enrichment analysis on the high PMRI group, the results showed that high PMRI was closely associated with immune cell infiltration (Figure 5B).

We used the ESTIMATE algorithm to assess immune cell infiltration in the tumor microenvironment of BCa patients, and the results showed that patients in the high PMRI group had significantly higher TME scores (ESTIMATE score, immune score and stromal score) and significantly lower tumor purity scores than those in the low PMRI group, indicating that compared to the low PMRI group, patients in the high PMRI group had a higher percentage of immune and stromal cell infiltration ratio was higher and tumor purity was lower in the high PMRI group compared to the low PMRI group (Figure 5C). The results of immune-related function analysis by ssGSEA algorithm showed that HLA and immune checkpoint expression were significantly higher in the high PMRI group than in the low PMRI group (Figure 5D). We then compared the expression of common HLA molecules, immunostimulatory genes and immunosuppressive genes in the high/low PMRI group, and most common HLA molecules, immunostimulatory genes and immunosuppressive genes were highly expressed in the high PMRI group, such as PD-L1, PD-1 and CTLA-4 (Figures 5E–G). We confirmed the higher level of immune cell infiltration in patients in the high PMRI group (TCGA-XF-AAMX) than in patients in the low PMRI group (TCGA-ZF-A9R7) by TCGA pathological sections (Figures 5H, I). Taken together, the results suggest that our patients in the high PMRI group may correspond to BCa hot tumors while those in the low PMRI group may correspond to BCa cold tumors.

Association of PD-L1 multidimensional modulation index with immunotherapy efficacy

We used the IMvigor 210 database to analyze the immunotherapy response in the high/low PMRI population, and the results showed that the PMRI scores of those who responded to anti-PD-L1 antibodies were significantly higher than those who did not respond to anti-PD-L1 antibodies, indicating that high PMRI

10.3389/fimmu.2023.1301157

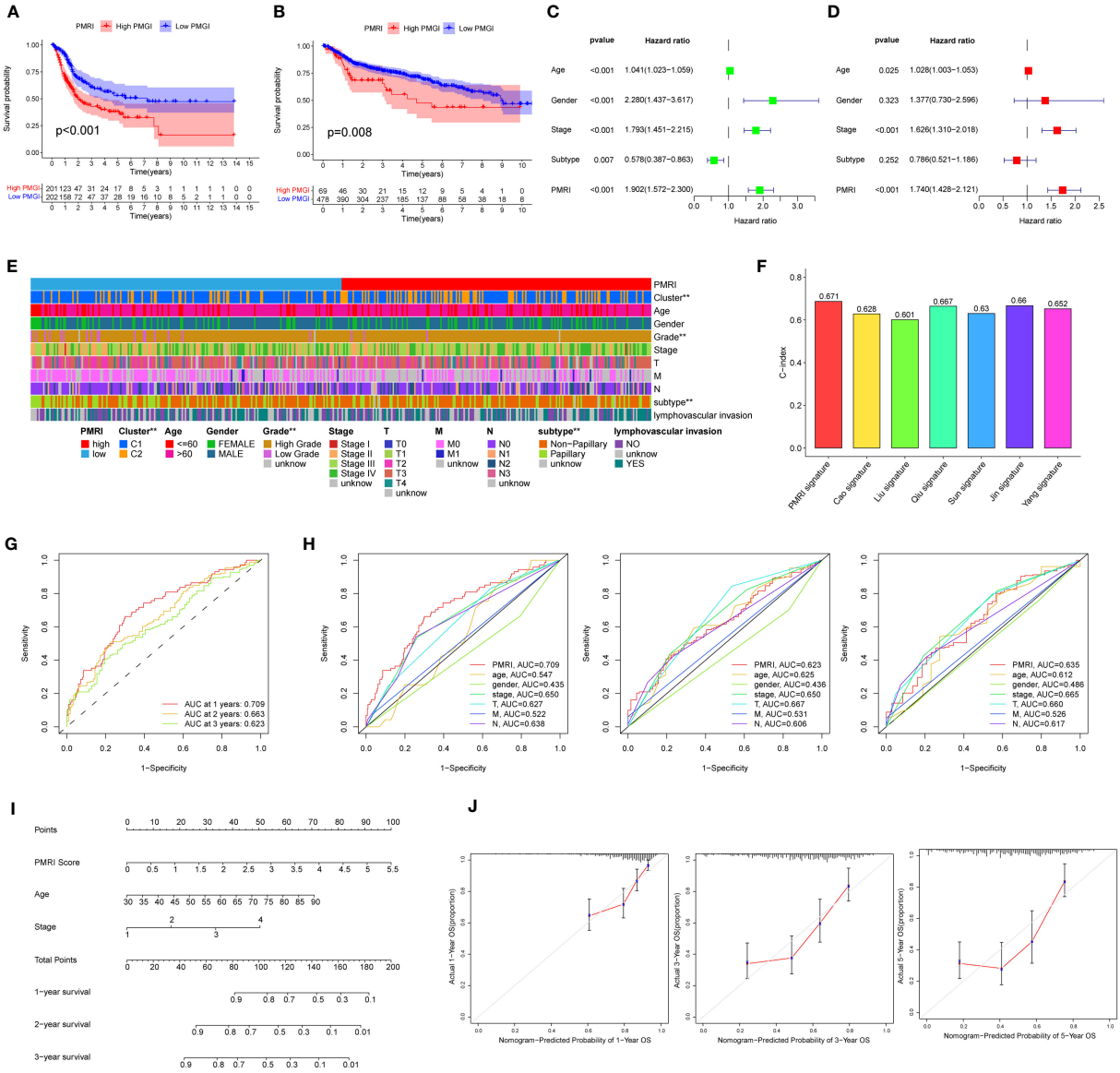

FIGURE 3
Association of PD-L1 multidimensional regulatory indices with clinical traits and construction of line plots. **(A)** Kaplan-Meier survival curves for the TCGA cohort. **(B)** Kaplan-Meier survival curves for the GSE13507, GSE32894, GSE31684 and GSE48075 cohorts. **(C, D)** Univariate and multivariate regression analyses. **(E)** Common clinical characteristics (Cluster, age, sex, grade, stage, T, M, N, BCa subtype and whether lymphovascular invasion) were analyzed for differences in the high/low PMRI group. **(F)** Histogram of PMRI index compared with other BCa prognostic indices. **(G)** ROC curves of PMRI at 1, 3 and 5 years. **(H)** AUC comparison of PMRI with other clinical traits at 1, 3 and 5 years. **(I)** Column line graphs constructed based on PMRI, age, and clinical stage. **(J)** Calibration curves for 1-year, 3-year and 5-year overall survival. *p < 0.05, **p < 0.01, ***p < 0.001.

scores were strongly associated with better immunotherapy outcomes (Figure 6A). We also determined the difference in expression of the four genes that construct the PMRI score between the responding and non-responding groups, and the results showed that all four genes (*IGF2BP3, CLK2, P4HB* and *RAC3*) were significantly more highly expressed in those who responded to anti-PD-L1 antibodies (Figure 6B). In addition, higher expression levels of the immune checkpoints *PD-1, PD-L1* and *CTLA-4* in the high PMRI group and a significant positive correlation between PMRI score and expression of *PD-1, PD-L1* and *CTLA-4* were strongly associated with a good prognosis in the OS phase of BCa (Figures 6C–E). Patients with lower TIDE scores were more likely to benefit from immunotherapy (13) and high PMRI group had a significantly higher TIDE score than the low PMRI group, and it can be inferred that the high PMRI group responded better to immunotherapy (Figure 6F). In addition, we found significant differences in MSI and TMB between the high/low PMRI groups (Figures 6G, H). Finally, we assessed the value of PMRI score in predicting the efficacy of immunotherapy by PMRI scoring in cancer patients in pan-cancer, and the results showed significant differences in TIDE scoring between the low PMRI scoring group and the high PMRI group in BRCA, CSC, ESCA,

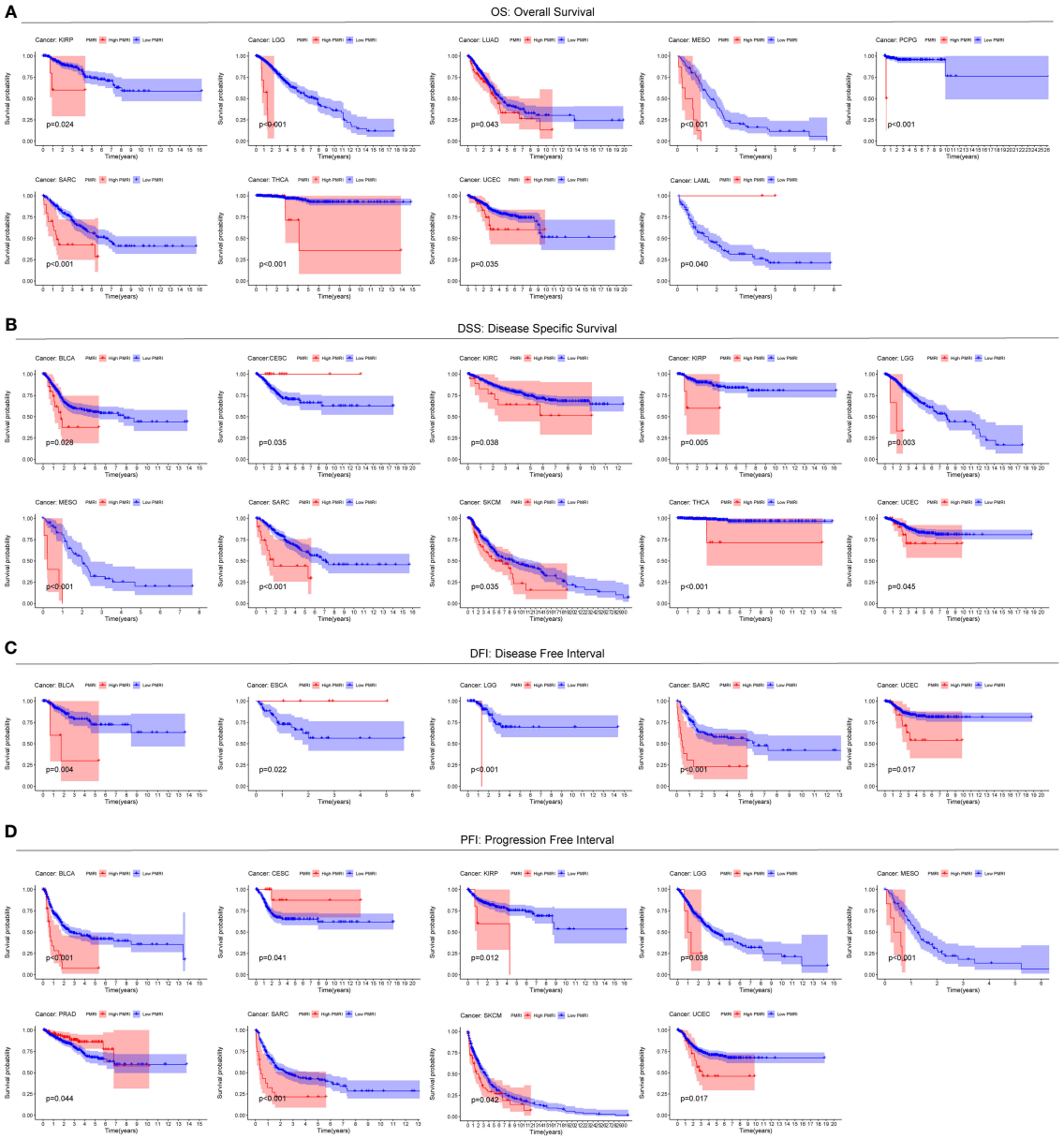

FIGURE 4
Predictive value of PMRI in other cancers. Using Kaplan-Meier survival curve analysis, patients in the high PMRI group and low PMRI group were compared in pan-cancer for Overall Survival (OS) **(A)**, Disease Specific Survival (DSS) **(B)**, Disease Free Interval (DFI) **(C)**, and Progression Free Interval (PFI) **(D)**.

HNSC, LGG, LUAD, LUSC, PAAD, TGCT, THCA, and UCEC, suggesting that PMRI scores can also be used to assess immunotherapy efficacy in pan-cancer in addition to in BLCA (Figure 6I). In addition, we collected genes that have been currently reported to be positively associated with immune efficacy and negatively associated with immune efficacy and analyzed them for association with PMRI (22–24). The results showed that PMRI was significantly positively associated with positive immune efficacy-related genes (*MSH2, MSH6, NRAS* and *POLD1*) and negatively associated with negative immune efficacy-related genes (*STK11*) (Figure 6J). The above results suggest that PMRI can predict the effect of immunotherapy and that patients in the high PMRI group have a better effect on immunotherapy.

Association between PD-L1 multidimensional modulation index and chemotherapy response and common drug sensitivity

To guide the clinical use of drugs in BCa patients, we analyzed the response to common BCa chemotherapeutic drugs in the high PMRI and PMRI groups, and the IC50 was negatively correlated with patients' sensitivity to the drugs. The results showed that patients in the high PMRI group were more effective in treatment with Cisplatin, while the low PMRI group was more effective in treatment with Gefitinib and Methotrexate treatment was more effective (Supplementary Figure S5A). We collected data from the TCGA

10.3389/fimmu.2023.1301157

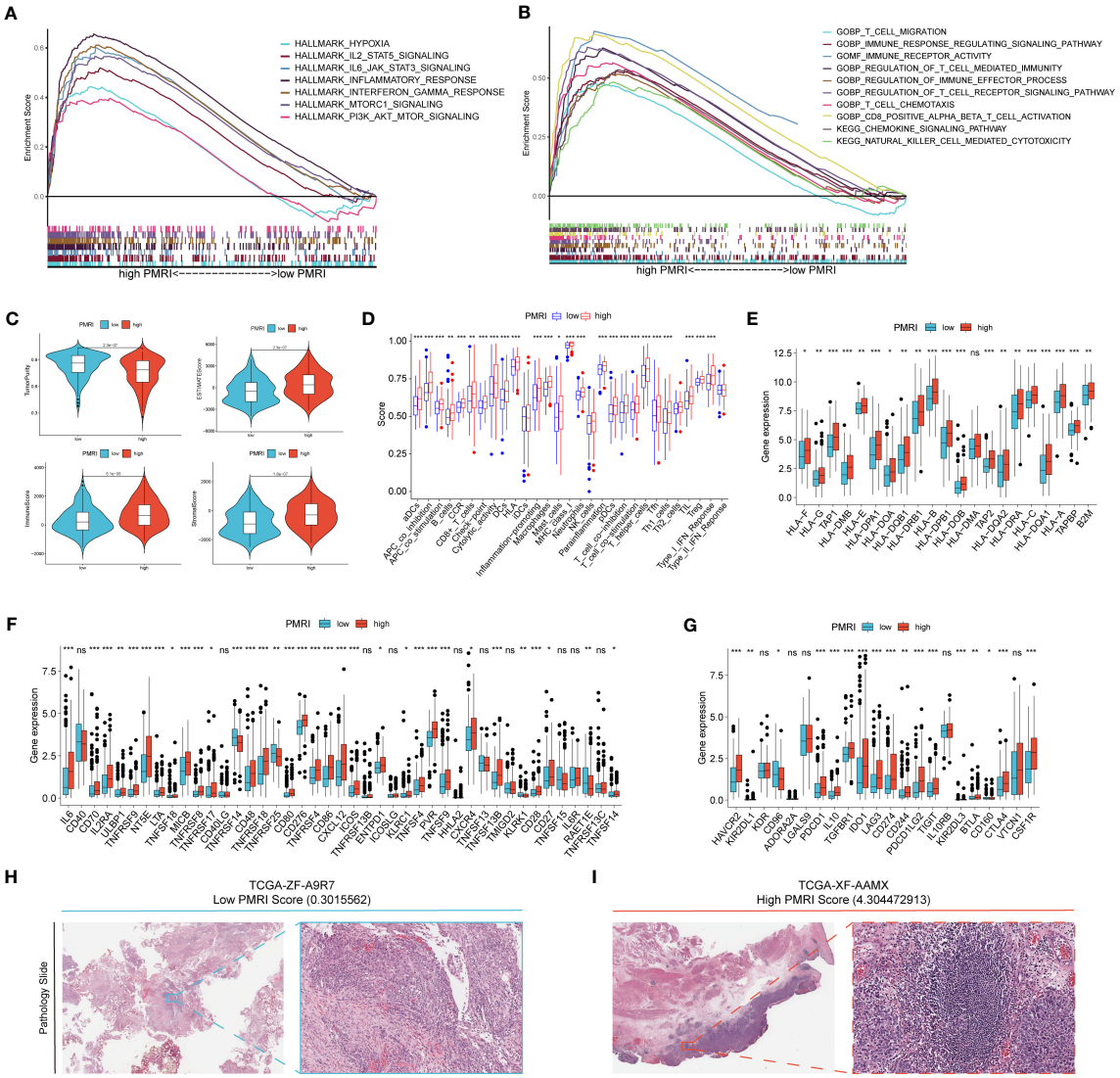

FIGURE 5
Correlation analysis of GSEA and tumor microenvironment. **(A, B)** GSEA analysis of patients in the high PMRI group. **(C)** Comparison of tumor purity, ESTIMATE score, immune score and stromal score between patients in the high PMRI group and low PMRI group. **(D)** Comparison of immune-related functions between patients in the high PMRI group and low PMRI group. **(D)** Comparison of HLA molecule **(E)**, immunostimulatory gene **(F)** and immunosuppressive gene **(G)** expression between patients in the high PMRI group and low PMRI group. Level of immune cell infiltration in TCGA pathological sections of patients in the low PMRI group **(H)** and patients in the high PMRI group **(I)**. *p < 0.05, **p < 0.01, ***p < 0.001, ns, Non Significance.

cohort to analyze the difference in PMRI scores between the cisplatin-responsive group and the non-responsive group. The results showed that the PMRI score in the cisplatin-responsive group (CR&PR) was significantly higher than that in the cisplatin-non-responsive group (PD&SD) (Supplementary Figure S5B). In addition, the relationship between drug sensitivity and mRNA expression of *P4HB, IGF2BP3, RAC3* and *CLK2* was analyzed by GDSC and CTRP databases, with positive correlation representing gene expression associated with drug resistance and negative correlation representing genes associated with drug sensitivity. The results of both databases showed that the mRNA expression of *P4HB* correlated with most chemotherapeutic drug resistance, and the mRNA expression of *CLK2* correlated with most chemotherapeutic drug sensitivity (Supplementary Figures S5C, D). These results suggest that PMRI is an effective indicator for predicting the efficacy of commonly used chemotherapy drugs (cisplatin and methotrexate) in BCa, and can be used as a potential therapeutic target for BCa chemotherapy.

Small molecule drug candidate prediction for core target proteins

Molecular docking is a structure-based computational algorithm for compound screening. We obtained the protein structures of IGF2BP3, RAC3, CLK2 and P4HB from the PDB database for molecular docking with 1379 FDA-approved small molecule drugs. Showing the top four small molecules with the highest binding power to the IGF2BP3 binding pocket (Nonoxynol-9, Cobicistat, Valrubicin, and Indinavir) (Figures 7A–D), the top four small molecules with the highest binding power to the RAC3

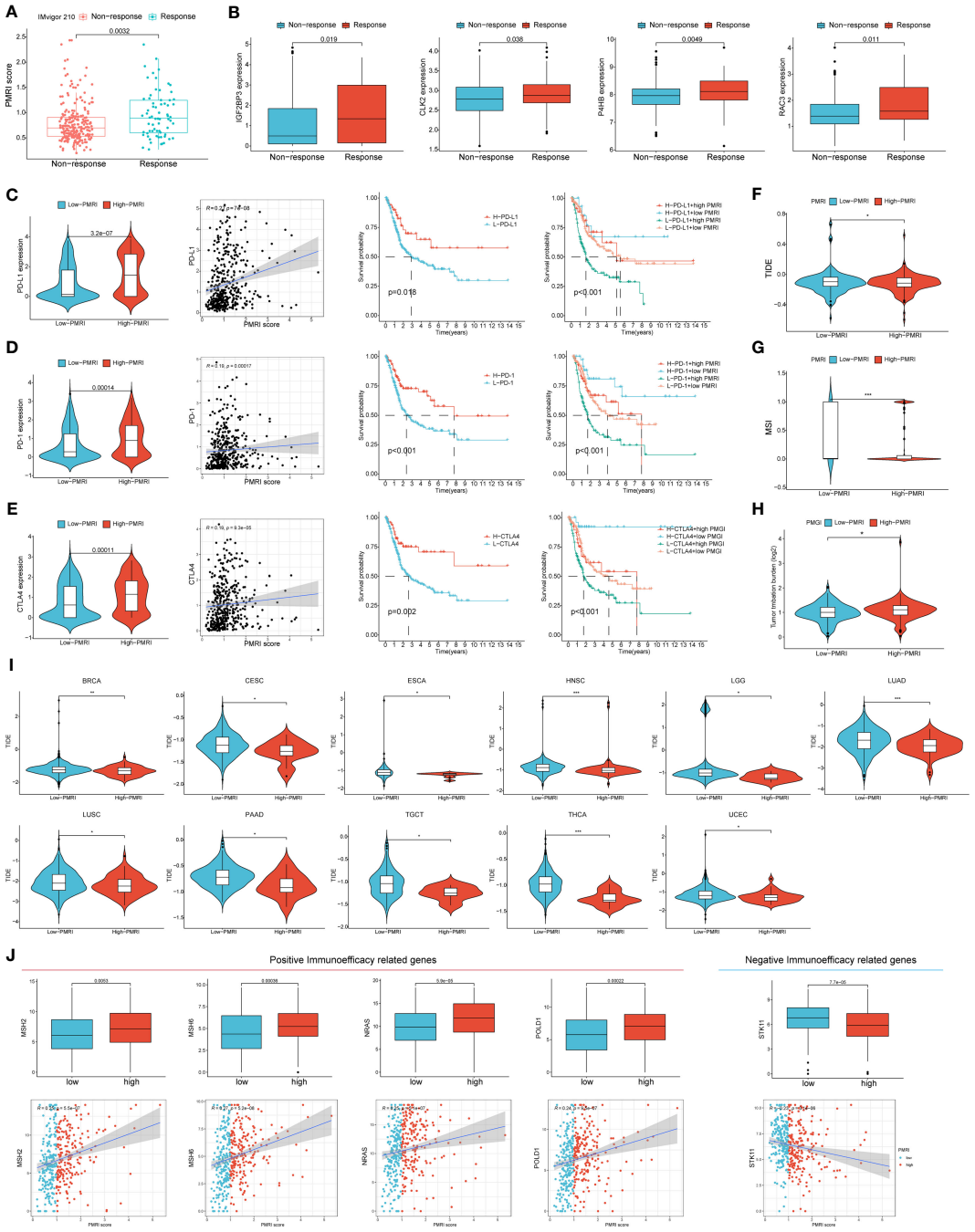

FIGURE 6
PD-L1 multidimensional modulation index in response to immunotherapy. **(A)** Box plots of PMRI scores in the responding and non-responding groups. **(B)** Differences in *IGF2BP3, CLK2, P4HB* and *RAC3* expressions between the responding and non-responding groups. **(C–E)** Differences in *PD-1, PD-L1* and *CTLA-4* expression between high/low PMRI groups, correlation of PMRI with PD-1, PD-L1 and CTLA-4 expression and prognostic correlation of PMRI with *PD-1, PD-L1* and *CTLA-4*. Differences in TIDE score **(F)**, MSI **(G)** and TMB **(H)** between the high PMRI group and low PMRI group. **(I)** PMRI scores are used to assess immunotherapy efficacy in pan-cancer. **(J)** Association of PMRI index with genes related to positive/negative immune efficacy. *p < 0.05, **p < 0.01, ***p < 0.001.

binding pocket (Tessalon, Cobicistat, Nonoxynol-9, and Gadofosveset) (Figures 7E–H), the top four small molecules with the highest pocket binding to CLK2 (Saquinavir, Amaryl, Trypan Blue, and Irinotecan) (Figures 7I–L), and the top four small molecules with the highest pocket binding to P4HB The top four small molecules with the highest pocket binding (Gadofosveset, Propantheline, Tessalon and Cobicistat) (Figures 7M–P). For example, Cobicistat (ZINC000085537014) forms hydrogen bonds with IGF2BP3 amino acid residues Glu-69, Ser-58 and Arg-79, where Glu-69 and Ser-58 act as hydrogen bond acceptors and Arg-79 as a hydrogen bond donor. In addition, these small molecules form van der Waals (VDW) interactions with residues around the protein receptor, contributing to the binding between the small molecules and IGF2BP3, RAC3, CLK2 and P4HB.

Knockdown of *IGF2BP3* inhibits proliferation and migration of BCa and *IGF2BP3* positively correlates with PD-L1

To investigate the role of *IGF2BP3* in BCa cells, two siRNAs (*IGF2BP3*-1, *IGF2BP3*-2) were designed to silence *IGF2BP3* expression in T24 and UM-UC3 cells. The expression of IGF2BP3 after knockdown was verified by protein blotting, and the results showed that the above two siRNAs could effectively knock down the expression of *IGF2BP3* (Supplementary Figures S6A, B). We then performed CCK8, EdU, wound healing and Transwell experiments on T24 and UM-UC3 cells transfected with si-*IGF2BP3*, respectively. The CCK8 results showed that the proliferation ability of T24 and UM-UC3 cells in the NC group was significantly higher than that of both si-*IGF2BP3* groups at 24, 48, 72 and 96 h ($p < 0.05$, Figures 8A, B). The results by EdU staining assay showed that knockdown of *IGF2BP3* gene had significantly lower proliferative capacity for T24 and UM-UC3 cells than the NC group ($p < 0.05$, Figures 8C, D). Both wound healing assay and Transwell assay results showed that the migratory ability of T24 and UM-UC3 cells with low expression of *IGF2BP3* was significantly reduced ($p < 0.05$, Figures 8E–H). The above results suggest that knockdown of *IGF2BP3* expression can inhibit the proliferation and migration of BCa cells.

We then collected 14 BCa tissue samples to investigate the correlation between IGF2BP3 and *PD-L1*, and found a significant positive correlation between *IGF2BP3* and *PD-L1* (R=0.596, P value=0.024, Figure 8I). We found a significant decrease in the protein level of *PD-L1* after silencing *IGF2BP3* expression in T24 and UM-UC3 cells by WB experiments (Figures 8J, K; Supplementary Figures S6C, D). In addition, we constructed a pattern diagram of the relationship between the four genes constructing the PMRI index and PD-L1 (Figure 8L).

Discussion

Advanced or metastatic BCa is an aggressive malignancy associated with poor long-term survival outcomes (17, 25, 26). Immune checkpoint inhibitors targeting programmed cell death 1 (PD-1) or PD-L1 have recently been shown to be effective in patients with BCa (27). Therefore, more accurate and reliable immunotherapy-related markers are needed to predict survival status and immunotherapy response in patients with BCa. In this study, we established a PMRI constructed from four anti-PD-L1 immunotherapy-related genes (*IGF2BP3, P4HB, RAC3*, and *CLK2*) based on an anti-PD-L1 immunotherapy dataset. We found an association between high PMRI not only with poor prognosis in patients with BCa, but also with therapeutic strategies that could help differentiate and predict the efficacy of immunotherapy in patients with BCa, and thus improve patient prognosis. *In vitro* experiments and preliminary virtual screening further identified the biological functions and potential druggability of PMRI. Thus, our PMRI can predict the prognostic risk and immunotherapy response of BCa. The derived PMRI can be used as a new indicator to predict BCa prognosis and immunotherapy benefits, and may provide valuable insights to find new BCa treatment strategies.

An important finding of this study was the exploration of the therapeutic potential for BCa from the new perspective of PD-L1 expression co-regulation patterns. To determine whether PMRI can predict the efficacy of anticancer immunotherapy in patients with BCa, we compared the expression levels of common immune checkpoints and HLA molecules between the high and low PMRI groups and found that the majority were significantly upregulated in the high PMRI group, with *PD-1, PD-L1*, and *CTLA-4* expression levels significantly correlated with PMRI scores. The results showed that the TIDE scores in the high PMRI group were significantly lower than those in the low PMRI group, suggesting that ICI immunotherapy is more effective in treating the high PMRI population. We also scored PMRI for TIDE immune efficacy in pan-cancer, demonstrating that it can be used not only as a potential biomarker to predict BCa immunotherapy response and screen suitable patients, but also for predicting immunotherapy efficiency in pan-cancer. Consistent with the TIDE score results, there were significant differences in PMRI scores between the responding and non-responding groups of uroepithelial cancer patients in response to PD-L1 therapy in the IMvigor 210 cohort, with the responding group having higher PMRI scores, validating the efficacy of anti-PD-L1 immunotherapy for patients in the high PMRI score group. However, we predicted the response of BCa patients to treatment with common chemotherapeutic agents based on the IC50 values of the drugs. Additionally, we calculated the association between gene expression and drug sensitivity, and found that common chemotherapeutic agents (e.g., cisplatin and gemcitabine) also differed significantly between PMRI subgroups. These results suggest that we constructed the PMRI as a valid indicator to assess the response of patients with BCa to immunotherapy and chemotherapy, to accurately assess the prognosis of patients, and to identify the patient population that will benefit from immunotherapy.

Current predictive biomarkers for PD-1/PD-L1 inhibitors include predictors, such as TMB, MSI, PD-L1, IFN-γ, TIL, and serum markers (IL-6/IL-8/LDH/CRP/B2M) (5). The other cytokines and serum markers predict the efficacy of immunotherapy in terms of the immune microenvironment. In our study, we constructed a PMRI based on immunotherapy datasets and from the perspective of the multifaceted regulation of *PD-L1* expression in cancer cells and found that it not only correlated significantly with TMB and MSI, but also validated its effectiveness in predicting immunotherapy efficacy in patients with BCa using the TIDE algorithm and external immunotherapy datasets. Our results strongly suggest that the pathways involved in regulating *PD-L1* expression may also be considered as candidate reference factors for the comprehensive treatment of intermediate and advanced bladder tumors.

The four genes ultimately included in the PMRI were significantly and highly expressed in patients in the anti-PD-L1 immunotherapy response group. Insulin-like growth factor 2 mRNA-binding protein 3 (IGF2BP3) is an RNA-binding protein (RBP). Researchers found that IGF2BP3 can act as a *PD-L1* mRNA reader, recognizing and regulating the stability of METTL3-mediated m6A-modified *PD-L1* mRNA in a METTL3-dependent manner to prevent *PD-L1* mRNA degradation (28). The *P4HB* gene encodes a protein disulfide isomerase (PDI) and endoplasmic reticulum oxidase 1 (ERO1) that are involved in the protein folding process of the endoplasmic

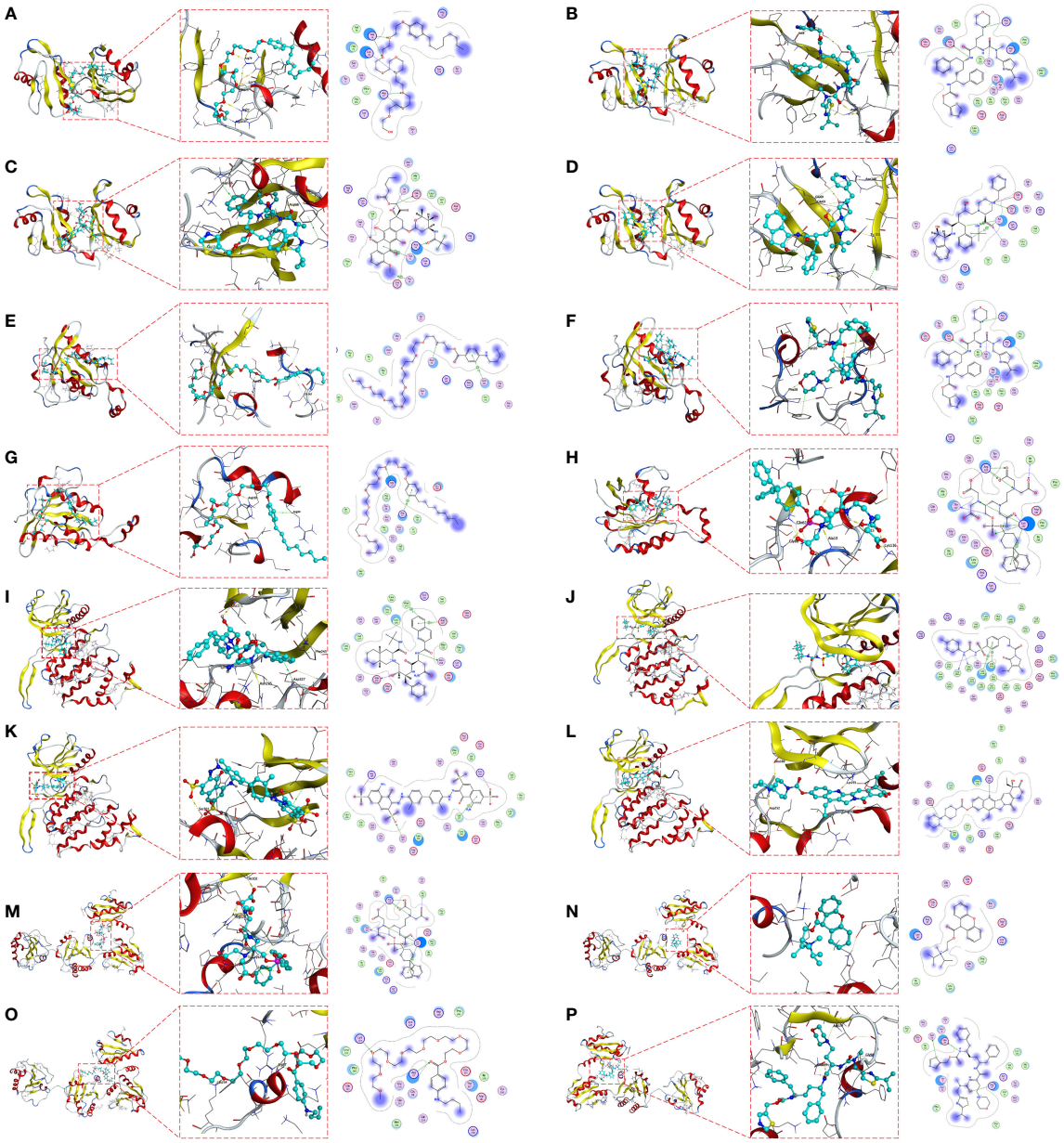

FIGURE 7
Molecular docking pose. Screening of candidate small molecules for target proteins using molecular docking. Docking poses of IGF2BP3 active pocket with Nonoxynol-9 **(A)**, Cobicistat **(B)**, Valrubicin **(C)** and Indinavir **(D)** are shown. Docking poses of RAC3 active pocket with Tessalon **(E)**, Cobicistat **(F)**, Nonoxynol-9 **(G)** and Docking poses of the CLK2 active pocket with Saquinavir **(I)**, Amaryl **(J)**, Trypan Blue **(K)** and Irinotecan **(L)**. Docking poses of the P4HB active pocket with Gadofosveset **(M)**, Propantheline **(N)**, Tessalon **(O)** and Cobicistat **(P)** in docked position. On the left is the overall structure of IGF2BP3, RAC3, CLK2 and P4HB with small molecule drugs, where the small molecules are embedded into the protein. In the middle is a detailed diagram of the interaction between IGF2BP3, RAC3, CLK2 and P4HB with small molecule drugs, where the hydrogen bonds are shown as yellow dashed lines. On the right is a 2D interaction diagram between IGF2BP3, RAC3, CLK2 and P4HB and small molecule drugs, where green arrows indicate side chain hydrogen bonding interactions, blue arrows indicate main chain hydrogen bonding interactions, and hexagons represent residues interacting with aromatic hydrocarbons.

reticulum. Moreover, researchers found that PDI and ERO1, acting in concert, could promote oxidative protein folding of PD-L1 in the endoplasmic reticulum thereby enhancing PD-L1 expression (29, 30). Cancer cells have been reported to utilize the JAK-STAT signaling pathway to increase *PD-L1* mRNA expression, whereas *RAC3* overexpression can activate JAK/STAT signaling through the PYCR1 axis to regulate PD-L1 expression, and thus suppress tumor immunity to provide favorable conditions for BCa progression (21, 31). Similarly, the binding of Wnt ligands to activated EGFR induces β-catenin/TCF/LEF to form a complex with the PD-L1 promoter region and induces *PD-L1* mRNA expression in tumor cells. *CLK2* has been reported to increase *PD-L1* mRNA expression to evade T-cell attack via the Wnt/β-catenin/TCF/LEF pathway (32, 33). The anti-PD-L1 immunotherapy-related genes are closely related to the transcriptional, post-transcriptional, and protein stability regulation of PD-L1 in cancer cells. Consistent with these observations, we validated the function of classical PMRI genes and their relevance to PD-L1 expression in BCa cells. The results showed that IGF2BP3

10.3389/fimmu.2023.1301157

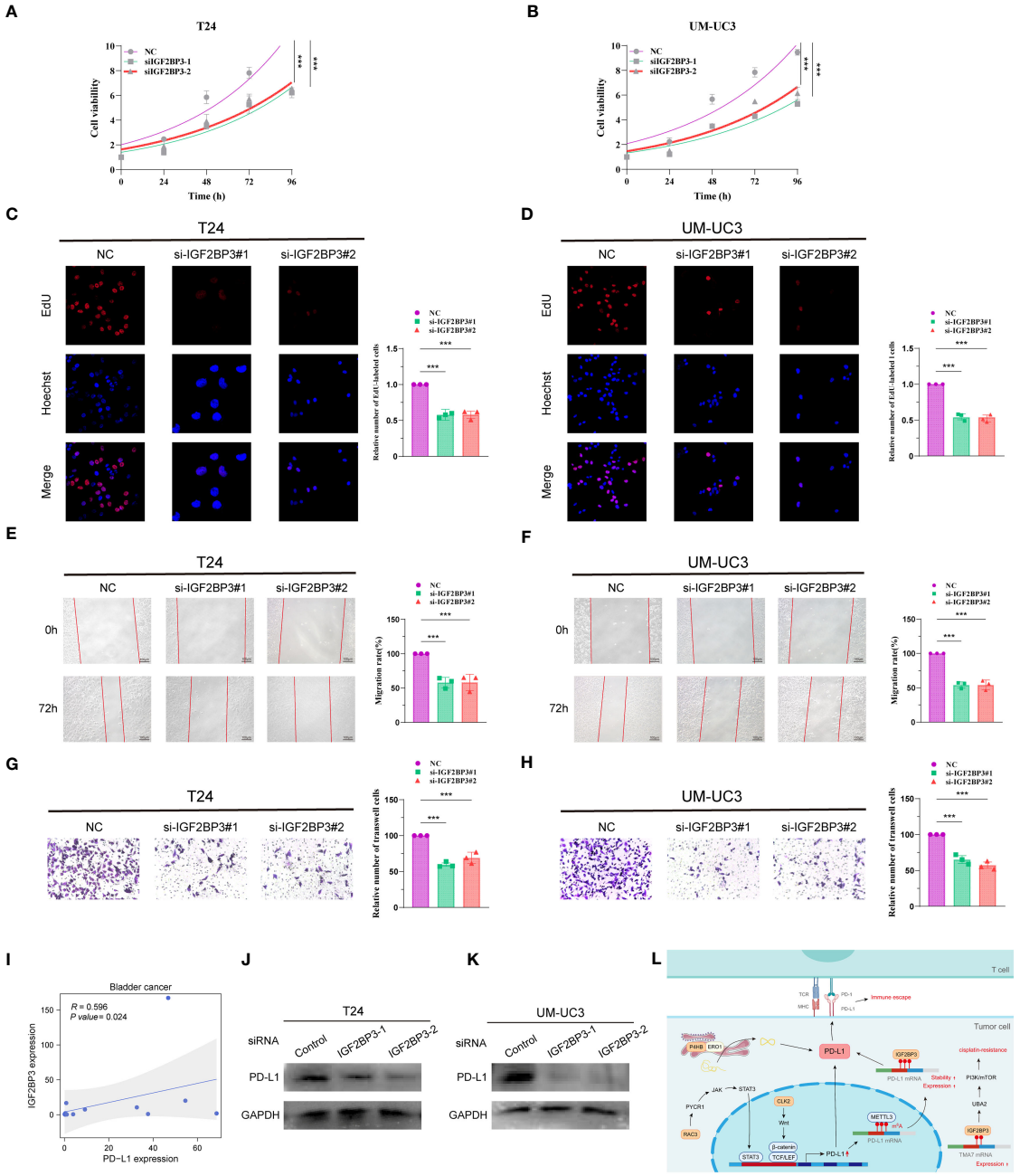

FIGURE 8
Knockdown of *IGF2BP3* inhibits BCa cell proliferation and migration and *IGF2BP3* correlates with PD-L1. CCK8 viability assay **(A, B)**, EdU cell proliferation capacity assay **(C, D)**, wound healing capacity assay **(E, F)** and transwell cell migration capacity **(G, H)** in T24 and UM-UC3 cells transfected with two si-*IGF2BP3*, respectively. **(I)** qPCR assay of *IGF2BP3* and *PD-L1* correlation in 14 BCa tissues. **(J, K)** PD-L1 protein expression levels in T24 and UM-UC3 cells after siRNA transfection. **(L)** PMRI index gene and PD-L1 correlation pattern plot. *p < 0.05, **p < 0.01, ***p < 0.001.

promoted the proliferation and migration of BCa cells and positively regulated *PD-L1* expression. These results suggest that anti-PD-L1 immunotherapy-related genes and their derived PMRI are closely associated with PD-L1 expression and tumor immunity in cancer cells. PMRI genes from DNA induction, transcriptional, translational, and post-translational modifications of PD-L1 expression. The synergistic regulation of PD-L1 expression by PMRI genes from DNA induction, transcriptional, translational, and post-translational modifications may have potential value in therapeutic evaluation and translational research.

As another application of PITI efficacy prediction, we demonstrated the feasibility of a structure-based approach for identifying candidate small-molecule drugs that target core proteins. We used *IGF2BP3, RAC3, CLK2*, and *P4HB* as small-molecule drug targets and screened potential small-molecule drugs by molecular docking from the zinc database of Food and Drug Administration (FDA)-approved drugs using MOE software. Valrubicin is among the top four small-molecule drugs with the highest affinity for IGF2BP3, and it has been reported in clinical trials for superficial BCa chemotherapy, demonstrating that

valrubicin is effective in ablating tumors remaining in the bladder after incomplete transurethral resection of bladder tumors and in preventing and delaying bladder tumor recurrence (34). A clinical trial of cobicistat, which has a strong affinity to RAC3, was conducted for the treatment of human immunodeficiency virus exposure prophylaxis (35). Irinotecan is among the top four small-molecule drugs with the highest binding affinity to the CLK2 binding pocket, and it has been widely used in clinical trials for solid tumors, such as colorectal, pancreatic, and biliary tract cancers (36–38). Furthermore, Gadofosveset, which is known to have a P4HB-docking pocket with the highest affinity, was reported in clinical trials in combination with MR angiography for the treatment of peripheral vascular disease; results showed that at 0.03 mmol/kg it was not only safe and effective for MR angiography of occlusive disease of the main iliac artery, but also had improved accuracy over non-enhanced MR angiography (39). Although the specific mechanisms of these candidate small-molecule compounds remain to be explored in depth, our findings suggest that they have great potential for anti-PD-L1 immunotherapy in BCa, especially in the population of BCa patients with high PMRI scores.

Although our constructed PMRI can closely respond to and predict the prognosis, chemotherapy sensitivity, and immunotherapy efficacy of BCa and many other cancers, this study has some limitations. First, the data for our analysis were obtained from public databases, which may have led to a case-selection bias. In addition, there is a need to collect large amounts of clinical case-data for evaluation to further validate the accuracy of our findings. Finally, further *in vivo* and *in vitro* experiments are required to validate the specific molecular mechanisms of the genes involved in the construction of the PMRI in BCa progression.

Conclusion

In summary, based on the comprehensive analysis of multiple aspects of BCa by PMRI constructed from anti-PD-L1 immunotherapy-related genes, we found that PMRI could effectively predict the prognosis and immunotherapeutic effects in patients with BCa. This study identified novel prognoses, therapeutic biomarker combinations, and potential therapeutic targets for anti-PD-L1 immunotherapy, providing useful insights for future research on BCa treatment strategies. In the era of cancer immunotherapy, exploring co-regulation patterns of PD-L1 expression and their oncological therapeutic potential provides new perspectives for clinical diagnosis, individualized comprehensive treatment, and translational research of BCa.

Data availability statement

The original contributions presented in the study are included in the article/Supplementary Material. Further inquiries can be directed to the corresponding authors.

Ethics statement

Ethical approval was not required for the studies on humans in accordance with the local legislation and institutional requirements because only commercially available established cell lines were used.

Author contributions

YX: formal analysis, data curation, conceptualization, experiment, writing—original draft. XYS: formal analysis, visualization, writing—original draft. GXL: software, investigation, writing—original draft. HZL: investigation, writing—original draft. MY: software, supervision, data curation, conceptualization, experiment, writing—review and editing. YYZ: conceptualization, writing—review and editing, supervision, project administration, funding acquisition. All authors contributed to the article and approved the submitted version.

Funding

The author(s) declare financial support was received for the research, authorship, and/or publication of this article. This work was supported by Xisike-Pilot Cancer Research Foundation (grants 20201030) and Applied Basic Research Program of Liaoning Province in 2023 (grants 2023010409133159830).

Conflict of interest

The authors declare that the research was conducted in the absence of any commercial or financial relationships that could be construed as a potential conflict of interest.

Publisher's note

Supplementary material

The Supplementary Material for this article can be found online at: https://www.frontiersin.org/articles/10.3389/fimmu.2023.1301157/full#supplementary-material

References

1. Sung H, Ferlay J, Siegel RL, Laversanne M, Soerjomataram I, Jemal A, et al. Global cancer statistics 2020: GLOBOCAN estimates of incidence and mortality worldwide for 36 cancers in 185 countries. *CA: Cancer J Clin* (2021) 71(3):209–49. doi: 10.3322/caac.21660

2. Patel VG, Oh WK, Galsky MD. Treatment of muscle-invasive and advanced bladder cancer in 2020. *CA: Cancer J Clin* (2020) 70(5):404–23. doi: 10.3322/caac.21631

3. Pardoll DM. The blockade of immune checkpoints in cancer immunotherapy. *Nat Rev Cancer* (2012) 12(4):252–64. doi: 10.1038/nrc3239

4. Zhang Y, Zhang Z. The history and advances in cancer immunotherapy: understanding the characteristics of tumor-infiltrating immune cells and their therapeutic implications. *Cell Mol Immunol* (2020) 17(8):807–21. doi: 10.1038/s41423-020-0488-6

5. Sznol M, Chen L. Antagonist antibodies to PD-1 and B7-H1 (PD-L1) in the treatment of advanced human cancer. *Clin Cancer Res* (2013) 19(5):1021–34. doi: 10.1158/1078-0432.CCR-12-2063

6. Arzimanoglou II, Gilbert F, Barber HR. Microsatellite instability in human solid tumors. *Cancer* (1998) 82(10):1808–20. doi: 10.1002/(SICI)1097-0142(19980515)82:10<1808::AID-CNCR2>3.0.CO;2-J

7. Yi M, Niu M, Xu L, Luo S, Wu K. Regulation of PD-L1 expression in the tumor microenvironment. *J Hematol Oncol* (2021) 14(1):10. doi: 10.1186/s13045-020-01027-5

8. Rosenberg JE, Hoffman-Censits J, Powles T, van der Heijden MS, Balar AV, Necchi A, et al. Atezolizumab in patients with locally advanced and metastatic urothelial carcinoma who have progressed following treatment with platinum-based chemotherapy: a single-arm, multicentre, phase 2 trial. *Lancet (London England)* (2016) 387(10031):1909–20. doi: 10.1016/S0140-6736(16)00561-4

9. Wilkerson MD, Hayes DN. ConsensusClusterPlus: a class discovery tool with confidence assessments and item tracking. *Bioinf (Oxford England)* (2010) 26 (12):1572–3. doi: 10.1093/bioinformatics/btq170

10. Uhlén M, Fagerberg L, Hallström BM, Lindskog C, Oksvold P, Mardinoglu A, et al. Proteomics. Tissue-based map of the human proteome. *Sci (New York NY)* (2015) 347(6220):1260419.

11. Yang W, Soares J, Greninger P, Edelman EJ, Lightfoot H, Forbes S, et al. Genomics of Drug Sensitivity in Cancer (GDSC): a resource for therapeutic biomarker discovery in cancer cells. *Nucleic Acids Res* (2013) 41(Database issue):D955–61.

12. Basu A, Bodycombe NE, Cheah JH, Price EV, Liu K, Schaefer GI, et al. An interactive resource to identify cancer genetic and lineage dependencies targeted by small molecules. *Cell* (2013) 154(5):1151–61. doi: 10.1016/j.cell.2013.08.003

13. Jiang P, Gu S, Pan D, Fu J, Sahu A, Hu X, et al. Signatures of T cell dysfunction and exclusion predict cancer immunotherapy response. *Nat Med* (2018) 24(10):1550–8. doi: 10.1038/s41591-018-0136-1

14. Jin K, Qiu S, Jin D, Zhou X, Zheng X, Li J, et al. Development of prognostic signature based on immune-related genes in muscle-invasive bladder cancer: bioinformatics analysis of TCGA database. *Aging* (2021) 13(2):1859–71. doi: 10.18632/aging.103787

15. Liu J, Ma H, Meng L, Liu X, Lv Z, Zhang Y, et al. Construction and external validation of a ferroptosis-related gene signature of predictive value for the overall survival in bladder cancer. *Front Mol Biosci* (2021) 8:675651. doi: 10.3389/fmolb.2021.675651

16. Qiu H, Hu X, He C, Yu B, Li Y, Li J. Identification and validation of an individualized prognostic signature of bladder cancer based on seven immune related genes. *Front Genet* (2020) 11:12. doi: 10.3389/fgene.2020.00012

17. Xu Y, Xia Z, Sun X, Wei B, Fu Y, Shi D, et al. Identification of a glutamine metabolism reprogramming signature for predicting prognosis, immunotherapy efficacy, and drug candidates in bladder cancer. *Front Immunol* (2023) 14:1111319. doi: 10.3389/fimmu.2023.1111319

18. Sun J, Yue W, You J, Wei X, Huang Y, Ling Z, et al. Identification of a novel ferroptosis-related gene prognostic signature in bladder cancer. *Front Oncol* (2021) 11:730716. doi: 10.3389/fonc.2021.730716

19. Yang L, Li C, Qin Y, Zhang G, Zhao B, Wang Z, et al. A novel prognostic model based on ferroptosis-related gene signature for bladder cancer. *Front Oncol* (2021) 11:686044. doi: 10.3389/fonc.2021.686044

20. Sun X, Li S, Lv X, Yan Y, Wei M, He M, et al. Immune-related long non-coding RNA constructs a prognostic signature of ovarian cancer. *Biol Procedures Online* (2021) 23(1):24. doi: 10.1186/s12575-021-00161-9

21. Cha JH, Chan LC, Li CW, Hsu JL, Hung MC. Mechanisms controlling PD-L1 expression in cancer. *Mol Cell* (2019) 76(3):359–70. doi: 10.1016/j.molcel.2019.09.030

22. Miao D, Margolis CA, Gao W, Voss MH, Li W, Martini DJ, et al. Genomic correlates of response to immune checkpoint therapies in clear cell renal cell carcinoma. *Sci (New York NY)* (2018) 359(6377):801–6. doi: 10.1126/science.aan5951

23. Kato S, Goodman A, Walavalkar V, Barkauskas DA, Sharabi A, Kurzrock R. Hyperprogressors after immunotherapy: analysis of genomic alterations associated with accelerated growth rate. *Clin Cancer Res* (2017) 23(15):4242–50. doi: 10.1158/1078-0432.CCR-16-3133

24. Remon J, Passiglia F, Ahn MJ, Barlesi F, Forde PM, Garon EB, et al. Immune checkpoint inhibitors in thoracic Malignancies: review of the existing evidence by an IASLC expert panel and recommendations. *J Thorac Oncol* (2020) 15(6):914–47. doi: 10.1016/j.jtho.2020.03.006

25. Sternberg CN, de Mulder PH, Schornagel JH, Théodore C, Fossa SD, van Oosterom AT, et al. Randomized phase III trial of high-dose-intensity methotrexate, vinblastine, doxorubicin, and cisplatin (MVAC) chemotherapy and recombinant human granulocyte colony-stimulating factor versus classic MVAC in advanced urothelial tract tumors: European Organization for Research and Treatment of Cancer Protocol no. *30924*. *J Clin Oncol* (2001) 19(10):2638–46. doi: 10.1200/JCO.2001.19.10.2638

26. Dyrskjøt L, Hansel DE, Efstathiou JA, Knowles MA, Galsky MD, Teoh J, et al. Bladder cancer. *Nat Rev Dis Primers* (2023) 9(1):58.

27. Powles T, Eder JP, Fine GD, Braiteh FS, Loriot Y, Cruz C, et al. MPDL3280A (anti-PD-L1) treatment leads to clinical activity in metastatic bladder cancer. *Nature.* (2014) 515(7528):558–62. doi: 10.1038/nature13904

28. Wan W, Ao X, Chen Q, Yu Y, Ao L, Xing W, et al. METTL3/IGF2BP3 axis inhibits tumor immune surveillance by upregulating N(6)-methyladenosine modification of PD-L1 mRNA in breast cancer. *Mol Cancer* (2022) 21(1):60. doi: 10.1186/s12943-021-01447-y

29. Shergalis AG, Hu S, Bankhead A 3rd, Neamati N. Role of the ERO1-PDI interaction in oxidative protein folding and disease. *Pharmacol Ther* (2020) 210:107525. doi: 10.1016/j.pharmthera.2020.107525

30. Tanaka T, Kutomi G, Kajiwara T, Kukita K, Kochin V, Kanaseki T, et al. Cancer-associated oxidoreductase ERO1-α promotes immune escape through up-regulation of PD-L1 in human breast cancer. *Oncotarget* (2017) 8(15):24706–18. doi: 10.18632/oncotarget.14960

31. Cheng C, Song D, Wu Y, Liu B. RAC3 promotes proliferation, migration and invasion *via* PYCR1/JAK/STAT signaling in bladder cancer. *Front Mol Biosci* (2020) 7:218. doi: 10.3389/fmolb.2020.00218

32. Du L, Lee JH, Jiang H, Wang C, Wang S, Zheng Z, et al. β-Catenin induces transcriptional expression of PD-L1 to promote glioblastoma immune evasion. *J Exp Med* (2020) 217(11):e20191115. doi: 10.1084/jem.20191115

33. Zhou HB, Yang L, Liu SF, Xu XH, Chen Z, Li YX, et al. CDC Like Kinase 2 plays an oncogenic role in colorectal cancer *via* modulating the Wnt/β-catenin signaling. *Neoplasma* (2022) 69(3):657–69. doi: 10.4149/neo_2022_220206N138

34. Newling DW, Hetherington J, Sundaram SK, Robinson MR, Kisbenedek L. The use of valrubicin for the chemoresection of superficial bladder cancer – a marker lesion study. *Eur Urology* (2001) 39(6):643–7. doi: 10.1159/000052521

35. Gantner P, Hessamfar M, Souala MF, Valin N, Simon A, Ajana F, et al. Elvitegravir-cobicistat-emtricitabine-tenofovir alafenamide single-tablet regimen for human immunodeficiency virus postexposure prophylaxis. *Clin Infect Dis* (2020) 70 (5):943–6.

36. Kopetz S, Guthrie KA, Morris VK, Lenz HJ, Magliocco AM, Maru D, et al. Randomized trial of irinotecan and cetuximab with or without vemurafenib in BRAF-mutant metastatic colorectal cancer (SWOG S1406). *J Clin Oncol* (2021) 39(4):285–94. doi: 10.1200/JCO.20.01994

37. Wang-Gillam A, Hubner RA, Siveke JT, Von Hoff DD, Belanger B, de Jong FA, et al. NAPOLI-1 phase 3 study of liposomal irinotecan in metastatic pancreatic cancer: Final overall survival analysis and characteristics of long-term survivors. *Eur J Cancer (Oxford Engl 1990)* (2019) 108:78–87. doi: 10.1016/j.ejca.2018.12.007

38. Yoo C, Kim KP, Jeong JH, Kim I, Kang MJ, Cheon J, et al. Liposomal irinotecan plus fluorouracil and leucovorin versus fluorouracil and leucovorin for metastatic biliary tract cancer after progression on gemcitabine plus cisplatin (NIFTY): a multicentre, open-label, randomised, phase 2b study. *Lancet Oncol* (2021) 22 (11):1560–72. doi: 10.1016/S1470-2045(21)00486-1

39. Perreault P, Edelman MA, Baum RA, Yucel EK, Weisskoff RM, Shamsi K, et al. MR angiography with gadofosveset trisodium for peripheral vascular disease: phase II trial. *Radiology* (2003) 229(3):811–20. doi: 10.1148/radiol.2293021180

Glossary

ACC	Adrenocortical carcinoma
BCa	Bladder cancer
CLK2	CDC Like Kinase 2
BLCA	Bladder Urothelial Carcinoma
BRCA	Breast invasive carcinoma
CESC	Cervical squamous cell carcinoma and endocervical adenocarcinoma
CHOL	Cholangiocarcinoma
COAD	Colon adenocarcinoma
CNV	Copy number variation
CTLA4	Cytotoxic T-lymphocyte-associated protein 4
DLBC	Lymphoid Neoplasm Diffuse Large B-cell Lymphoma
DSS	Disease-free survival
ESCA	Esophageal carcinoma
GBM	Glioblastoma multiforme
GDSC	Genomics of Drug Sensitivity in Cancer
GEO	Gene Expression Omnibus
GO	Gene Ontology
GSEA	gene set enrichment analysis
GTEx	Genotype-Tissue Expression Program
HNSC	Head and Neck squamous cell carcinoma
HR	Hazard Ratio
IC50	half maximal inhibitory concentration
ICB	Immune checkpoint blockade
IGF2BP3	Insulin Like Growth Factor 2 MRNA Binding Protein 3
KEGG	Kyoto Encyclopedia of Genes and Genomes
KICH	Kidney Chromophobe
KIRC	Kidney renal clear cell carcinoma
KIRP	Kidney renal papillary cell carcinoma
KM	Kaplan–Meier
LAG3	Lymphocyte Activating 3
LAML	Acute Myeloid Leukemia
LGG	Brain Lower Grade Glioma
LIHC	Liver hepatocellular carcinoma
LUAD	Lung adenocarcinoma
LUSC	Lung squamous cell carcinoma
MESO	Mesothelioma
NES	Normalized enrichment score
OS	Overall survival

(Continued)

Continued

OV	Ovarian serous cystadenocarcinoma
P4HB	Prolyl 4-Hydroxylase Subunit Beta
PAAD	Pancreatic adenocarcinoma
PCPG	Pheochromocytoma and Paraganglioma
PD-1	Programmed cell death 1
PD-L1	Programmed cell death 1 ligand 1
PFS	Progression-free survival
PMRI	PD-L1 multidimensional regulatory index
PPI	protein–protein interaction
PRAD	Prostate adenocarcinoma
RAC3	Rac Family Small GTPase 3
READ	Rectum adenocarcinoma
ROC	Receiver Operating Characteristic
SARC	Sarcoma
SKCM	Skin Cutaneous Melanoma
ssGSEA	single-sample gene set enrichment analysis
STAD	Stomach adenocarcinoma
TCGA	The Cancer Genome Atlas
TGCT	Testicular Germ Cell Tumors
THCA	Thyroid carcinoma
THYM	Thymoma
TIDE	tumor immune dysfunction and exclusion
TP53	Tumor Protein P53
TMB	Tumor mutation burden
UCEC	Uterine Corpus Endometrial Carcinoma
UCS	Uterine Carcinosarcoma
UVM	Uveal Melanoma
WGCNA	Weighted Gene coexpression Network Analysis

frontiers | Frontiers in Immunology

TYPE Original Research
PUBLISHED 05 February 2024
DOI 10.3389/fimmu.2024.1332492

OPEN ACCESS

EDITED BY
Vera Rebmann,
University of Duisburg-Essen, Germany

REVIEWED BY
Cui Youbin,
First Affiliated Hospital of Jilin University, China
Martin Leu,
University Medical Center Göttingen, Germany

*CORRESPONDENCE
Ming-Qiang Kang
9199115045@fjmu.edu.cn
Wan-Li Lin
wanlilin2020@163.com
Rong-Yu Xu
xry641127@sina.com
Zhi-Nuan Hong
hongzhinuan@163.com

†These authors have contributed equally to this work and share first authorship

‡These authors have contributed equally to this work

RECEIVED 03 November 2023
ACCEPTED 17 January 2024
PUBLISHED 05 February 2024

CITATION
Xie S-H, Yang L-T, Zhang H, Tang Z-L, Lin Z-W, Chen Y, Hong Z-N, Xu R-Y, Lin W-L and Kang M-Q (2024) Adjuvant therapy provides no additional recurrence-free benefit for esophageal squamous cell carcinoma patients after neoadjuvant chemoimmunotherapy and surgery: a multi-center propensity score match study. *Front. Immunol.* 15:1332492. doi: 10.3389/fimmu.2024.1332492

Adjuvant therapy provides no additional recurrence-free benefit for esophageal squamous cell carcinoma patients after neoadjuvant chemoimmunotherapy and surgery: a multi-center propensity score match study

Shu-Han Xie[1,2†], Li-Tao Yang[1,2,3†], Hai Zhang[1,2,4†], Zi-Lu Tang[5,6†], Zhi-Wei Lin[1,2], Yi Chen[1,2], Zhi-Nuan Hong[1,7,8,9*‡], Rong-Yu Xu[5,6*‡], Wan-Li Lin[4*‡] and Ming-Qiang Kang[1,7,8,9*‡]

[1]Department of Thoracic Surgery, Fujian Medical University Union Hospital, Fuzhou, Fujian, China, [2]The Graduate School of Fujian Medical University, Fuzhou, Fujian, China, [3]Department of Thoracic Surgery, Baoji Traditional Chinese Medicine Hospital, Baoji, Shaanxi, China, [4]Department of Thoracic Surgery, Gaozhou People's Hospital, Gaozhou, Guangdong, China, [5]Department of Thoracic Surgery, Quanzhou First Hospital, Quanzhou, Fujian, China, [6]Department of Thoracic Surgery, Quanzhou First Hospital Affiliated to Fujian Medical University, Quanzhou, Fujian, China, [7]Key Laboratory of Cardio-Thoracic Surgery (Fujian Medical University), Fujian Province University, Fuzhou, Fujian, China, [8]Key Laboratory of Gastrointestinal Cancer (Fujian Medical University), Ministry of Education, Fuzhou, Fujian, China, [9]Fujian Key Laboratory of Tumor Microbiology, Fujian Medical University, Fuzhou, Fujian, China

Purpose: The need for adjuvant therapy (AT) following neoadjuvant chemoimmunotherapy (nICT) and surgery in esophageal squamous cell cancer (ESCC) remains uncertain. This study aims to investigate whether AT offers additional benefits in terms of recurrence-free survival (RFS) for ESCC patients after nICT and surgery.

Methods: Retrospective analysis was conducted between January 2019 and December 2022 from three centers. Eligible patients were divided into two groups: the AT group and the non-AT group. Survival analyses comparing different modalities of AT (including adjuvant chemotherapy and adjuvant chemoimmunotherapy) with non-AT were performed. The primary endpoint was RFS. Propensity score matching(PSM) was used to mitigate inter-group patient heterogeneity. Kaplan-Meier survival curves and Cox regression analysis were employed for recurrence-free survival analysis.

Results: A total of 155 nICT patients were included, with 26 patients experiencing recurrence. According to Cox analysis, receipt of adjuvant therapy emerged as an independent risk factor(HR:2.621, 95%CI:[1.089,6.310], P=0.032), and there was statistically significant difference in the Kaplan-Meier survival curves between non-AT and receipt of AT in matched pairs (p=0.026). Stratified analysis revealed AT bring no survival benefit to patients with pathological complete response(p=

0.149) and residual tumor cell(p=0.062). Subgroup analysis showed no significant difference in recurrence-free survival between non-AT and adjuvant chemoimmunotherapy patients(P=0.108). However, patients receiving adjuvant chemotherapy exhibited poorer recurrence survival compared to non-AT patients (p= 0.016).

Conclusion: In terms of recurrence-free survival for ESCC patients after nICT and surgery, the necessity of adjuvant therapy especially the adjuvant chemotherapy, can be mitigated.

KEYWORDS

adjuvant therapy, neoadjuvant chemoimmunotherapy, esophageal cancer, propensity score matching, recurrence-free survival

1 Introduction

Esophageal cancer accounts for approximately 50% of cancer cases in China, with over 90% diagnosed as esophageal squamous cell carcinoma (ESCC) (1, 2). Esophagectomy plays a pivotal role in the treatment of locally advanced esophageal squamous cell carcinoma (3). However, surgery alone often results in substantial recurrence and metastasis, with rates ranging from 43.3% to 50.0% (4).

Currently, the standard treatment for locally advanced ESCC involves minimally invasive esophagectomy following neoadjuvant therapy (5). However, the standard neoadjuvant therapy for locally advanced ESCC remains uncertain. Neoadjuvant chemoradiotherapy (nCRT) is commonly used in Western countries, while neoadjuvant chemotherapy (nCT) is extensively used in China and Japan (6) (7). Despite availability of these treatments, the survival of ESCC patients following neoadjuvant therapy is poor due to high recurrence rates and limited long-term survival. The 10-year results from the CROSS trial show a 63.6% disease-free survival rate in the nCRT group, with a 24.3% distant metastasis rate (8). Therefore, there is an urgent need for more effective systemic therapies to improve long-term survival outcomes. Previous study indicates enhanced prognosis in patients receiving nCRT following the addition of adjuvant chemotherapy(aCT) (9). Additionally, neoadjuvant chemoimmunotherapy (nICT) has emerged as a promising and innovative approach for locally advanced ESCC in recent years. Our center has conducted a single-arm phase II clinical trial to evaluate the safety and efficacy of nICT in the treatment of locally advanced ESCC (LA-ESCC) (10). Furthermore, the combination of pembrolizumab (a PD-1 inhibitor) with chemotherapy has been recommended as a first-line treatment for advanced EC (11). The NICE phase-II study demonstrated a 78.1% 2-year recurrence-free survival rate and a 67.9% overall survival rate after nICT (12). The CheckMate577 study revealed that adjuvant immunotherapy following nCRT and esophagectomy significantly extended median disease-free survival to 11.0 months, highlighting the therapeutic advantage of immunotherapy as a systemic treatment option (13).

However, it is imperative to elucidate whether adjuvant therapy, including aCT and adjuvant chemoimmunotherapy(aICT), is indispensable following nICT. Considering the long-term immune memory effect of immunotherapeutic agents (14, 15), we propose that postoperative adjuvant treatment might not be necessary for improved recurrence-free survival in esophageal cancer patients undergoing nICT.

Abbreviations: nCT, neoadjuvant chemotherapy; nCRT, neoadjuvant chemoradiotherapy; nICT, neoadjuvant chemoimmunotherapy; aIT, adjuvant immunotherapy; aICT, adjuvant chemoimmunotherapy; aCT, adjuvant chemotherapy; AT, adjuvant therapy; LA-ESCC, locally advanced ESCC; PSM, propensity score matching; MIE, minimally invasive esophagectomy; RFS, recurrence-free survival; ESCC, esophageal squamous cell cancer.

2 Methods

2.1 Patient selection

This study retrospectively enrolled patients who underwent esophagectomy at three centers(Fujian Medical University Union Hospital, Quanzhou First Hospital and Gaozhou People's Hospital) between January 1, 2019, and December 30, 2022. The inclusion criteria of this study were as follows: 1. Patients diagnosed with $cT_{3\text{-}4a}N_{any}M_0$ or $cT_{1\text{-}2}N_+M_0$ ESCC; 2. receiving at least one cycle of nICT without restrictions on the chemotherapy regimen and type of immunodrug; 3. undergoing radical resection(R0 resection); and 4. provided complete clinical and pathological information. The exclusion criteria were as follows: 1. Patients diagnosed with esophageal adenocarcinoma or other pathological type; 2. patients who underwent only exploratory surgery or jejunostomy; and 3. patients who received radiotherapy before or after surgery. The

patient selection procedure is summarized in the flowchart (Figure S1).

2.2 Treatment protocols

Diagnostic and clinical staging procedures included gastroscopy, contrast-enhanced computed tomography of the neck, chest, and upper abdomen, as well as neck ultrasound. Positron emission computed tomography was performed when necessary.

The chemotherapy regimen primarily consisted of platinum in combination with paclitaxel or docetaxel, administered every three weeks. Common neoadjuvant chemotherapy regimens involved cisplatin(60 mg/m^2) on day 1, followed by nab-paclitaxel(125 mg/m^2) on days 1 and 8, or docetaxel(75 mg/m^2) with cisplatin(60 mg/m^2) on day 1. Following neoadjuvant chemotherapy, PD-1 monoclonal antibodies were administered, including camrelizumab, pembrolizumab, sintilimab, tislelizumab, or toripalimab, as detailed in our previous studies (16, 17). Generally, PD-1 inhibitors were administered every three weeks, including sintilimab at a dosage of 200 mg, toripalimab at a dosage of 240 mg, pembrolizumab at a dosage of 200 mg, tislelizuma at a dosage of 200 mg and camrelizumab at a dosage of 200 mg.

Suitable candidates for curative esophagectomy, without contraindications, typically underwent the procedure 4-8 weeks after the last dose of neoadjuvant therapy. Esophagectomy with standard 2-field or 3-field lymphadenectomy and gastric reconstruction was performed. Neck lymphadenectomy was conducted if preoperative imaging indicated suspected neck lymph node enlargement.

Postoperative adjuvant therapy was not mandatory and was applied depending on a comprehensive assessment of pathological outcomes, treatment preferences, physical condition, and physician evaluation. Adjuvant therapy regimens in this study included chemotherapy(aCT), immunotherapy(aIT), or a combination of both(aICT).

Dosages and cycles were determined by expert oncologists and thoracic surgeons, and adjusted as needed for drug-related toxicities, patient tolerance, or tumor response to treatment.

2.3 Follow-up and outcomes measure

In accordance with the NCCN and CSCO guideline, ESCC patients were subjected to regular follow-up examinations every 3 to 6 months within the initial two-year period. Subsequently, follow-ups were conducted at 6-month intervals from the third to fifth year, and annually thereafter. Commonly, the follow-up methods included outpatient visits and telephone interviews. Computed tomography (CT) scans is widely used as a routine examination method to monitor for recurrence of the disease during the follow-up period. If deemed necessary and possible, a PET-CT scan or biopsy will be conducted. Follow-up times were defined from the date of surgery to recurrence or the last date of follow-up. The cut-off date of the last follow-up was October 28, 2023. The follow-up endpoint in this study is recurrence-free survival, defined as the duration from surgical resection to the occurrence of local recurrence or distal metastasis. Moreover, we investigated recurrence patterns among patients after nICT. Locoregional recurrences were defined as cancer reappearance within the esophagus, at the surgical anastomosis site, or in adjacent regional lymph nodes. Distant recurrences were defined as cancer recurrence in distant organs or beyond the operative field.

2.4 Relevant definitions

In this study, Propensity score matching (PSM) was performed to assess the impact of adjuvant therapy and its specific regimens on survival outcomes in distinct groups of ESCC patients. For matching cohort 1, ESCC patients with AT was compared with patients without AT. Subsequent analyses, represented by matching cohorts 2 and 3, investigated the survival advantage of specific adjuvant therapy modes compared to the absence of any adjuvant therapy. Notably, patients with adjuvant chemotherapy was compared with patients without any adjuvant therapy in matching cohort 2. Similarly, patients with adjuvant chemoimmunotherapy was compared with patients without any adjuvant therapy in matching cohort 3. Statistical analysis flow is depicted in Figure 1.

Additionally, The 11-month landmark method was implemented to re-evaluate the role of AT in the nICT group by excluding patients without positive outcome events and a follow-up period of no exceeding 11 months post-surgery (18–20).

2.5 Statistical analyses

Categorical data were presented as counts and percentages, compared using Chi-square or Fisher's exact tests. PSM reduced bias from confounders, generating scores via logistic regression and nearest neighbor matching without replacement (caliper: 0.05). Matching parameters included pCR, ypT, ypN statuses. Matching cohorts 1 and 3 had a 1:1 ratio, cohort 2 a 1:2 ratio. Survival differences were analyzed using Kaplan-Meier curves and log-rank tests. In addition, Cox regression was performed to evaluate risk factors (variables with $p< 0.05$ in univariate analysis were included in the multivariate analysis, using LR stepwise regression method). The reverse Kaplan-Meier method was used to calculate the median follow-up duration. In this study, the statistical test values were calculated using the chi-square test. Data were analyzed using SPSS (v25) and R (v4.3.1). Statistical significance was set at $P < 0.05$.

3 Results

3.1 Baseline characteristic of ESCC patients in the nICT group

Our study included a total of 155 patients from three centers. The study consisted of 125 males (80.6%) and 30 females (19.4%).

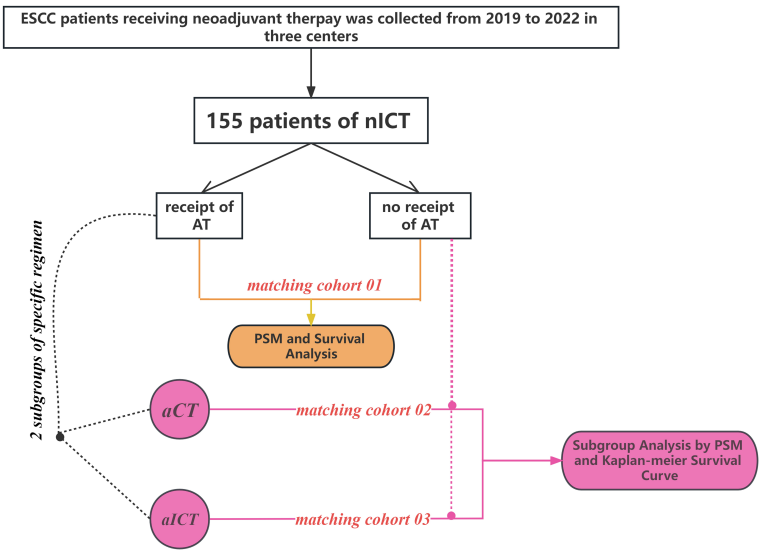

FIGURE 1
The flowchart illustrates the statistical analysis process in this study.

Among them, 77 patients(49.6%) received AT. All patients took a TP or DP for their neoadjuvant chemotherapy regimen. Within the AT recipients, only 20 patients receive adjuvant chemotherapy and 10 patients received adjuvant immunotherapy (aIT), while 47 patients take aICT as their adjuvant therapy regimen. The median follow-up duration of this study was 23 months (95%CI: 20.95-25.05; range:2-48 months). Detailed information about patients in nICT group is presented in Table 1.

3.2 Survival comparison between AT recipients and non-AT patients in the nICT group before and after PSM

A comparison of baseline characteristics between the AT and non-AT patient populations is detailed in Table 2. Before PSM, AT recipients had a worse RFS compared to patients without AT (p=0.027). Similarly, Kaplan-Meier curve analysis and log-rank tests indicated statistically significant differences between patients who received AT and those who did not after PSM (p=0.026), as shown in Figure 2.

Subsequently, Cox regression analysis was conducted in unmatched pairs to analyze the risk factors affecting the RFS of nICT patients. In univariate Cox analysis, ypN status, ypT status, smoking history and AT were identified as the significant influencing factor for RFS in nICT patients. While, AT(HR:2.621, 95%CI: [1.089,6.310], P=0.032) and ypN status were significant independent risk factor for RFS in multivariate Cox analysis, as shown in Table 3.

In stratified analysis, it was observed that patients with pathological complete response showed no statistically significant differences in prognosis based on the receipt of AT(p=0.072 in unmatched pairs; p= 0.149 in matched pairs), as shown in Figures 3A, B. Similarly, among patients with residual tumor cell (non-pCR), the receipt of AT did not result in statistically significant differences in prognosis(p=0.142 in unmatched pairs; p= 0.062 in matched pairs), as shown in Figures 3C, D.

3.3 11-month landmark analysis of the role of AT in the recipients of nICT

In landmark analysis, patients without positive outcome events and a follow-up period of no more than 11 months post-surgery was excluded. The AT recipients have worse recurrence-free survival compared to patients without AT in both pre-PSM and after-PSM cohorts(P=0.024; p= 0.011, respectively), as is shown in Figure 4. The matching parameters in this landmark analysis including Sex, pCR, ypT and ypN status. Detailed baseline information about patients on landmark method basis is presented in Table 4.

3.4 Subgroup analysis of survival comparison between patients of non-AT and two modalities of AT

In the nICT group, both before and after PSM, patients receiving aCT exhibited poorer prognosis in terms of recurrence-free survival compared to non-AT patients (p=0.008;p= 0.016, respectively), as shown in Figures 5A, B. Detailed baseline information for these two matched pairs before and after matching is presented in Table 5.

Conversely, no statistically significant differences were observed between non-AT patients and those receiving aICT before and after PSM (p=0.232; p= 0.108, respectively), as illustrated in Figures 5C, D. The baseline information for non-AT and aICT patients before and after matching is presented in Table 6.

10.3389/fimmu.2024.1332492

TABLE 1 Clinicopathological Characteristics of patients in nICT group.

Clinicopathological characteristic	N (%)
Sex	
male	125 (80.6%)
female	30 (19.4%)
Age	
≤65	122 (78.7%)
>65	33 (21.3%)
BMI	
<18.5	18 (11.6%)
18.5-23.9	106 (68.4%)
≥24	31 (20.0%)
Smoking history	
no	66 (42.6%)
yes	89 (57.4%)
Tumor location	
upper	14 (9.0%)
middle	90 (58.1%)
lower	51 (32.9%)
Regimen of nCT	
TP/DP	155 (100.0%)
Others	0 (0%)
Type of immunodrug	
sintilimab	34 (21.9%)
toripalimab	14 (9.0%)
pembrolizumab	30 (19.4%)
tislelizumab	11 (7.1%)
camrelizumab	66 (42.6%)
Cycle of neoadjuvant therapy	
≤2	121 (78.1%)
>2	34 (21.9%)
Adjuvant therapy	
no	78 (50.3%)
yes	77 (49.7%)
Type of adjuvant therapy	
aCT	20 (26.0%)
aICT	47 (61.0%)
aIT	10 (13.0%)
Regimen of chemotherapy in aCT and aICT	
TP/DP	65 (97.0%)
Others*	2 (3.0%)
Stage	
I	67 (43.2%)
II	24 (15.5%)
IIIa	22 (14.2%)
IIIb	38 (24.5%)
IVa	4 (2.6%)
ypT stage	
T_0	47 (30.3%)
T_1	31 (20.0%)
T_2	22 (14.2%)
T_3	55 (35.5%)
ypN stage	
N_0	91 (58.7%)
N_1	38 (24.5%)
N_2	22 (14.2%)
N_3	4 (2.6%)
Pathological response	
non-pCR	119 (76.8%)
pCR	36 (23.2%)

nCT, neoadjuvant chemotherapy; aICT, adjuvant chemoimmunotherapy; aCT, adjuvant chemotherapy; aIT, adjuvant immunotherapy; pCR, pathological complete response. TP/DP: paclitaxel combined with platinum-based chemotherapy or docetaxel combined with platinum-based chemotherapy.
*2 patients take platinum +5-FU as adjuvant chemotherapy regimen.

3.5 Recurrence patterns

Within the nICT group, 26 patients experienced recurrence. The median time to recurrence was 12.5 months. Specifically, 14 patients had locoregional recurrences, 11 patients had distant metastasis, and 1 patients experienced both locoregional recurrence and distant metastasis. Additionally, 2 patients developed supraclavicular lymph node metastasis, classified as a locoregional recurrence in our study, as shown in Figure 6.

4 Discussion

In recent years, immunotherapy has increasingly been used for esophageal cancer patients, especially those with locally advanced stages. However, the necessity and benefits of adjuvant therapy for ESCC patients after nICT and surgery remain contentious in international medical consensus. Given the reported finding that nICT does not increase postoperative complications (21), our study is keen to investigate the prognostic factors influencing the survival

TABLE 2 Characteristics comparison of AT and non-AT patients in nICT group before and after matching.

	Before PSM		Statistics value	P value	After PSM		Statistics value	P value
	non-AT	AT			non-AT	AT		
Sex			5.762	0.016			3.576	0.059
male	57 (73.1%)	68 (88.3%)			44 (74.6%)	52 (88.1%)		
female	21 (26.9%)	9 (11.7%)			15 (25.4%)	7 (11.9%)		
Age			1.774	0.183			0.837	0.360
≤65	58 (74.4%)	64 (83.1%)			45 (76.3%)	49 (83.1%)		
>65	20 (25.6%)	13 (16.9%)			14 (23.7%)	10 (16.9%)		
BMI			0.952	0.621			1.943	0.379
<18.5	11 (14.1%)	7 (9.1%)			9 (15.3%)	5 (8.5%)		
18.5-23.9	52 (66.7%)	54 (70.1%)			42 (71.2%)	42 (71.2%)		
≥24	15 (19.2%)	16 (20.8%)			8 (13.6%)	12 (20.3%)		
Smoking history			1.514	0.219			0.555	0.456
no	37 (47.4%)	29 (37.7%)			27 (45.8%)	23 (39.0%)		
yes	41 (52.6%)	48 (62.3%)			32 (54.2%)	36 (61.0%)		
Tumor location			5.704	0.058			1.950	0.377
upper	4 (5.1%)	10 (13.0%)			4 (6.8%)	7 (11.9%)		
middle	52 (66.7%)	38 (49.4%)			37 (62.7%)	30 (50.8%)		
lower	22 (28.2%)	29 (37.7%)			18 (30.5%)	22 (37.3%)		
Cycle of nICT			0.539	0.463			0.457	0.499
≤2	59 (75.6%)	62 (80.5%)			45 (76.3%)	48 (81.4%)		
>2	19 (24.4%)	15 (19.5%)			14 (23.7%)	11 (18.6%)		
Stage			6.325	0.175			0.000	1.000
I	39 (50.0%)	28 (36.4%)			27 (45.8%)	27 (45.8%)		
II	13 (16.7%)	11 (14.3%)			11 (18.6%)	11 (18.6%)		
IIIa	9 (11.5%)	13 (16.9%)			9 (15.3%)	9 (15.3%)		
IIIb	14 (17.9%)	24 (31.2%)			12 (20.3%)	12 (20.3%)		
IVa	3 (3.8%)	1 (1.3%)			0 (0%)	0 (0%)		
ypT stage			2.945	0.400			0.000	1.000
T_0	27 (34.6%)	20 (26.0%)			17 (28.8%)	17 (28.8%)		
T_1	14 (17.9%)	17 (22.1%)			14 (23.7%)	14 (23.7%)		
T_2	13 (16.7%)	9 (11.7%)			8 (13.6%)	8 (13.6%)		
T_3	24 (30.8%)	31 (40.3%)			20 (33.9%)	20 (33.9%)		
ypN stage			6.210	0.093			0.000	1.000
N_0	52 (66.7%)	39 (50.6%)			38 (64.4%)	38 (64.4%)		
N_1	14 (17.9%)	24 (31.2%)			14 (23.7%)	14 (23.7%)		
N_2	9 (11.5%)	13 (16.9%)			7 (11.9%)	7 (11.9%)		
N_3	3 (3.8%)	1 (1.3%)			0 (0%)	0 (0%)		

(Continued)

TABLE 2 Continued

	Before PSM		Statistics value	P value	After PSM		Statistics value	P value
	non-AT	AT			non-AT	AT		
Pathological response			2.183	0.140			0.000	1.000
non-pCR	56 (71.8%)	63 (81.8%)			45 (76.3%)	45 (76.3%)		
pCR	22 (28.2%)	14 (18.2%)			14 (23.7%)	14 (23.7%)		

nICT, neoadjuvant chemoimmunotherapy; pCR, pathological complete response; AT, adjuvant chemotherapy.

of esophageal cancer patients undergoing nICT and evaluate the necessity of adjuvant therapy and different AT modalities (including aCT and aICT) in order to better guide the selection of treatment and surveillance model after nICT and surgery. In this study, data from three centers of 155 nICT cases were analyzed. After propensity score matching, there were no statistically significant differences observed in baseline characteristics between patients who received AT and those who did not. According to the Cox analysis and Kaplan-Meier curve analysis, the addition of adjuvant therapy significantly compromised the recurrence-free survival rate of ESCC following nICT in our study. These findings suggest that the administration of adjuvant therapy had a detrimental impact on recurrence-free survival following nICT and the unnecessity of AT in this patient population. This aligns with prior research indicating patients receiving adjuvant therapy exhibited a significantly diminished disease-free survival following resection and neoadjuvant chemoradiation, in comparison to those not undergoing adjuvant therapy (22).

Previous studies have reported that ESCC patients with a pathological complete response have higher 5-year overall survival than incomplete responders (23). The correlation between pathological response and prognosis influences the choice of postoperative treatment. However, the recommendation of adjuvant therapy for ESCC patients exhibiting diverse pathological responses remains a subject of ongoing controversy (9, 24). Therefore, stratified analysis was conducted in our study to evaluate survival outcomes of AT among patients achieving pCR and those with residual pathological tumor cells (ypT+ status or/and ypN+ status) after nICT. Interestingly, AT did not significantly enhance recurrence-free survival benefits for pCR cases, indicating that these individuals can adopt a "watch and see" follow-up strategy, consistent with the current postoperative follow-up strategy (25, 26). However, in cases with incomplete response, the survival advantages of AT were still not found to be statistically significant. Previous studies have demonstrated that the administration of postoperative chemotherapy does not confer any additional survival benefit to patients with lymph node metastasis following neoadjuvant chemotherapy, which aligns with our study (27). The clinical trial CheckMate-577 showed that nivolumab, as an adjuvant agent, can lead to longer disease-free survival for patients with residual pathological tumors after nCRT and surgery. However, there is insufficient evidence and research to substantiate the necessity of AT in ESCC patients who had received nICT and exhibit positive postoperative pathological findings. Previous research has demonstrated that, in comparison to as adjuvants, immune checkpoint inhibitors (ICIs) offer distinct advantages as neoadjuvant therapy for eradicating distant metastases (28). This potentially explains the improved recurrence-free survival observed in nICT cases without AT of our study, even in cases of lymph node metastasis or residual tumor cells.

Administration of different adjuvant therapy regimens may exert varying benefits in terms of recurrence-free survival of ESCC patients. Therefore, whether different adjuvant therapy regimens (aCT and aICT) could confer survival benefits to nICT cases was analyzed. In this study, the patients receiving aICT did not show any statistically significant differences compared to those without any AT. However, it was noted that recipients of aCT exhibited inferior survival rates compared to non-AT individuals following nICT and surgery in both pre-match and post-match cohorts, suggesting the absence of requirement for aCT. Previous research conducted by Yan demonstrated that postoperative adjuvant chemotherapy is not necessary for reducing recurrence

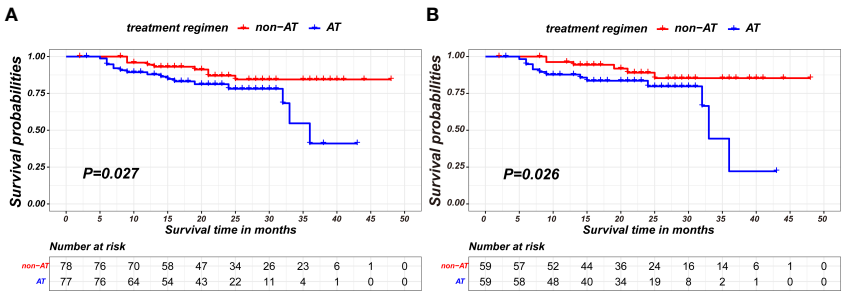

FIGURE 2
Kaplan-Meier survival curves of recurrence-free survival between non-AT and AT recipients in the nICT group before PSM **(A)** and after PSM **(B)**.

10.3389/fimmu.2024.1332492

TABLE 3 Univariate and multivariate Cox analysis for recurrence-free survival in a unmatched population.

	Univariate Cox analysis			Multivariate Cox analysis		
	HR	95%CI	P value	HR	95%CI	P value
Sex			0.112			
male	1.000					
female	0.310	[0.073,1.313]				
age			0.187			
≤65	1.000					
>65	0.377	[0.089,1.604]				
smoking history			0.042			
no	1.000					
yes	2.469	[1.034,5.894]				
BMI			0.451			
<18.5	1.000					
18.5-23.9	3.325	[0.444,24.933]	0.242			
>24	3.855	[0.474,31.364]	0.207			
Location			0.171			
Upper	1.000					
Middle	0.527	[0.146,1.909]	0.330			
lower	1.163	[0.323,4.181]	0.817			
Cycle of nICT			0.399			
≤2	1.000					
>2	1.484	[0.593,3.716]				
Receipt of AT			0.033			0.032
No	1.000			1.000		
Yes	2.460	[1.075,5.626]		2.621	[1.089,6.310]	
ypT stage			0.198			
T_0	1.000					
T_1	2.368	[0.668,8.397]	0.182			
T_2	1.686	[0.377,7.536]	0.494			
T_3	3.270	[1.065,10.037]	0.038			
ypN stage			0.005			0.014
N_0	1.000			1.000		
N_1	1.448	[0.525,3.992]	0.475	1.185	[0.424,3.312]	0.746
N_2	3.624	[1.427,9.206]	0.007	3.019	[1.173,7.771]	0.022
N_3	9.514	[2.021,44.791]	0.004	14.087	[2.821,70.342]	0.001
Pathological response			0.050			
non-pCR	1.000					
pCR	0.236	[0.056,0.998]				

nICT, neoadjuvant chemoimmunotherapy; AT, adjuvant chemotherapy; pCR, pathological complete response.

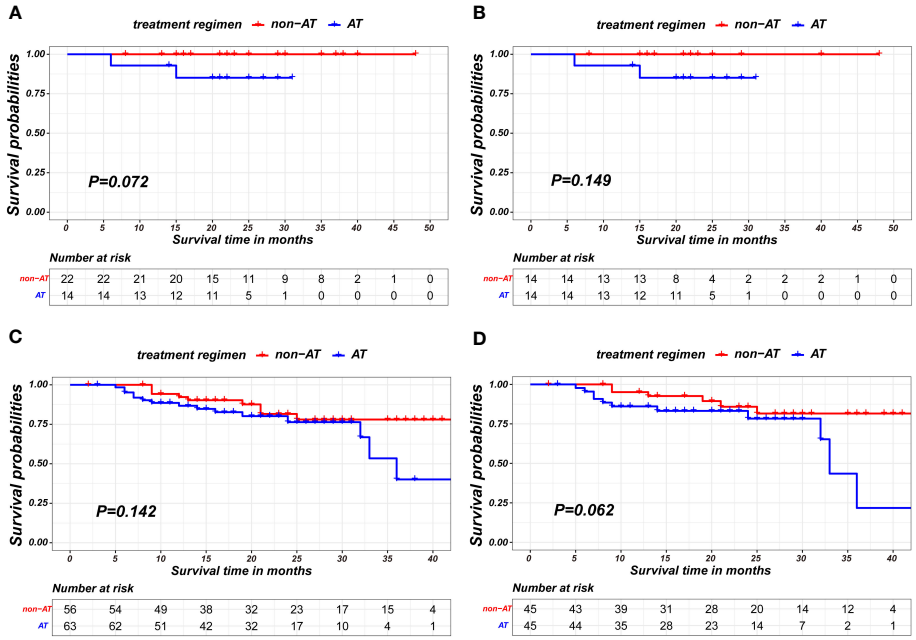

FIGURE 3
Kaplan-Meier survival curves of recurrence-free survival between non-AT and AT recipient in subgroup of pCR patients in unmatched pairs **(A)**, pCR patients in matched pairs **(B)**, non-pCR patients in unmatched pairs **(C)** and non-pCR patients in matched pairs **(D)**.

in patients who have undergone neoadjuvant chemotherapy and a trend towards inferior disease-free survival was observed in patients who underwent adjuvant therapy (29), aligning with our study's perspective on the need for adjuvant chemotherapy following neoadjuvant therapy. In addition, it is widely acknowledged that not all patients derive benefits from chemotherapy. Considering the potential impact of esophagectomy on patients, factors such as impaired postoperative food intake and swallowing ability, physiological and psychological stress, as well as postoperative complications, compromise the immune system of individuals with esophageal cancer after surgery (30–32). Consequently, the adverse effects of chemotherapy may further impede an already compromised immune system's capacity to effectively recognize and target cancer cells, thereby diminishing the efficacy of chemotherapy or immunotherapy and leading to cancer recurrence. In addition, administration of neoadjuvant therapy may potentially suppress the responsiveness of patients towards subsequent systemic therapy post-surgery (33, 34). In this study, we identified adjuvant therapy and higher ypN status as independent risk factors of recurrence in ESCC patients following nICT and surgery. Furthermore, subgroup analysis revealed that patients receiving adjuvant chemotherapy exhibited a poorer prognosis compared to those who did not receive any adjuvant therapy. This may be due to the outweighing side effects of chemotherapy compared to its survival benefit. These findings suggest that in our clinical practice, a close follow-up strategy is preferable over continued administration of adjuvant therapy, particularly chemotherapy, for patients undergoing nICT and surgery.

For the recurrence pattern in nICT patients, the proportion of local recurrence and distant metastasis was 54% and 46%, respectively. However, the majority of patients with distant recurrence had bone metastases and respiratory system metastases, suggesting that in

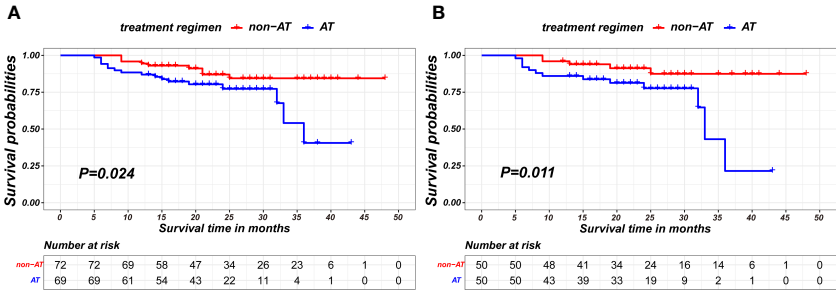

FIGURE 4
Kaplan-Meier survival curves of recurrence-free survival between non-AT and aCT patients on the 11-month landmark basis before PSM **(A)** and after PSM **(B)**.

10.3389/fimmu.2024.1332492

TABLE 4 Characteristics comparison of AT patients and non-AT patients in the nICT group on the landmark basis before and after matching.

	Before PSM		Statistics value	P value	After PSM		Statistics value	P value
	non-AT	AT			non-AT	AT		
Sex			7.076	0.008			0.102	0.749
male	52 (72.2%)	62 (89.9%)			44 (88.0%)	45 (90.0%)		
female	20 (27.8%)	7 (10.1%)			6 (12.0%)	5 (10.0%)		
Age			1.302	0.254			0.071	0.790
≤65	55 (76.4%)	58 (84.1%)			41 (82.0%)	42 (84.0%)		
>65	17 (23.6%)	11 (15.9%)			9 (18.0%)	8 (16.0%)		
BMI			0.971	0.615			1.903	0.399
<18.5	10 (13.9%)	6 (8.7%)			6 (12.0%)	3 (6.0%)		
18.5-23.9	48 (66.7%)	48 (69.6%)			37 (74.0%)	36 (72.0%)		
≥24	14 (19.4%)	15 (21.7%)			7 (14.0%)	11 (22.0%)		
Smoking history			1.684	0.194			0.042	0.838
no	36 (50.0%)	27 (39.1%)			19 (38.0%)	20 (40.0%)		
yes	36 (50.0%)	42 (60.9%)			31 (62.0%)	30 (60.0%)		
Tumor location			4.453	0.108			2.346	0.309
upper	4 (5.6%)	9 (13.0%)			3 (6.0%)	7 (14.0%)		
middle	48 (66.7%)	35 (50.7%)			32 (64.0%)	26 (52.0%)		
lower	20 (27.8%)	25 (36.2%)			15 (30.0%)	17 (34.0%)		
Cycle of nICT			0.016	0.900			0.000	1.000
≤2	58 (80.6%)	55 (79.7%)			40 (80.0%)	40 (80.0%)		
>2	14 (19.4%)	14 (20.3%)			10 (20.0%)	10 (20.0%)		
Stage			4.779	0.320			1.053	1.000
I	36 (50.0%)	27 (39.1%)			24 (48.0%)	24 (48.0%)		
II	12 (16.7%)	10 (14.5%)			10 (20.0%)	9 (18.0%)		
IIIa	8 (11.1%)	9 (13.0%)			6 (12.0%)	6 (12.0%)		
IIIb	13 (18.1%)	22 (31.9%)			10 (20.0%)	10 (20.0%)		
IVa	3 (4.2%)	1 (1.4%)			0 (0%)	1 (2.0%)		
ypT stage			2.312	0.510			0.083	0.994
T_0	25 (34.7%)	19 (27.5%)			16 (32.0%)	16 (32.0%)		
T_1	13 (18.1%)	14 (20.3%)			9 (18.0%)	10 (20.0%)		
T_2	12 (16.7%)	8 (11.6%)			8 (16.0%)	8 (16.0%)		
T_3	22 (30.6%)	28 (40.6%)			17 (34.0%)	16 (32.0%)		
ypN stage			4.371	0.239			1.015	1.000
N_0	48 (66.7%)	37 (53.6%)			34 (68.0%)	33 (66.0%)		
N_1	12 (16.7%)	19 (27.5%)			10 (20.0%)	10 (20.0%)		
N_2	9 (12.5%)	12 (17.4%)			6 (12.0%)	6 (12.0%)		
N_3	3 (4.2%)	1 (1.4%)			0 (0%)	1 (2.0%)		
Pathological response			1.488	0.223			0.000	1.000

(Continued)

TABLE 4 Continued

	Before PSM		Statistics value	P value	After PSM		Statistics value	P value
	non-AT	AT			non-AT	AT		
non-pCR	51 (70.8%)	55 (79.7%)			36 (72.0%)	36 (72.0%)		
pCR	21 (29.2%)	14 (20.3%)			14 (28.0%)	14 (28.0%)		

nICT, neoadjuvant chemoimmunotherapy; AT, adjuvant chemotherapy; pCR, pathological complete response.

addition to routine CT examination, PET/CT or bone scintigraphy may help to facilitate early detection of distant metastasis.

To the best of our knowledge, this study represents the first analysis of the survival benefit associated with adjuvant therapy in ESCC patients with nICT following surgery. According to previous research, the median time to recurrence for ESCC after nCRT is approximately 11 months (35–37), which is similar with our study. Therefore, the follow-up period in this study is adequate to reflect the effectiveness of adjuvant treatment for ESCC for recurrence. Additionally, to further mitigate the potential bias caused by shorter follow-up durations compared to the median recurrence time, a sensitivity analysis(landmark method) was conducted on patients with follow-up durations exceeding 11 months. The results of this landmark analysis mirrored those of the primary analysis, suggesting that the observed lack of benefit from adjuvant therapy is robust and reliable.

Despite the implementation of rigorous inclusion and exclusion criteria, as well as propensity score matching to ensure baseline comparability, the inherent limitations of a retrospective study design may introduce some degree of bias. Additionally, the majority of patients in our study were treated with the TP/DP regimen-based protocol for neoadjuvant and adjuvants and received no more than two cycles of treatment. Consequently, conducting subgroup analysis regarding chemotherapy regimens and cycles was not feasible in this study. We are currently making efforts to collaborate with more institutions to expand our database and plan to conduct subgroup analyses in future studies. Since the incidence of ESCC is more than 90% in Asian populations, it is important to note that this study specifically focused on patients diagnosed with esophageal squamous cell carcinoma; thus, the applicability of our research findings to patients with adenocarcinoma remains uncertain.

Conclusion

In terms of recurrence-free survival, the need for postoperative adjuvant therapy can be reduced for patients who have undergone nICT and surgery. Meanwhile, the adverse effects of postoperative adjuvant chemotherapy for patients already receiving nICT appear to outweigh its therapeutic benefits in preventing recurrence. A well-designed prospective study on a large scale is necessary to validate these findings.

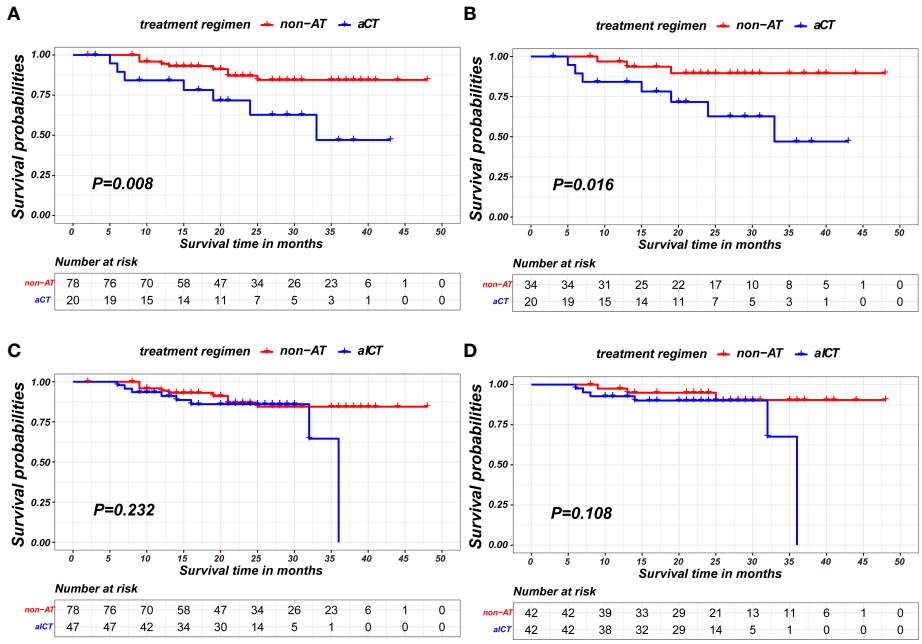

FIGURE 5
Kaplan-Meier survival curves of recurrence-free survival between patients of non-AT and two modalities of AT: **(A)** comparison of patients of non-AT with aCT before PSM; **(B)** comparison of patients of non-AT with aCT after PSM; **(C)** comparison of patients of non-AT with aICT before PSM; **(D)** comparison of patients of non-AT with aICT after PSM).

10.3389/fimmu.2024.1332492

TABLE 5 Characteristics comparison of aCT patients and non-AT patients before and after matching.

	Before PSM		Statistics value	P value	After PSM		Statistics value	P value
	non-AT	aCT			non-AT	aCT		
Sex			4.395	0.038			3.847	0.072
male	57 (73.1%)	19 (95.0%)			25 (73.5%)	19 (95.0%)		
female	21 (26.9%)	1 (5.0%)			9 (26.5%)	1 (5.0%)		
Age			1.004	0.389			0.064	1.000
≤65	58 (74.4%)	17 (85.0%)			28 (82.4%)	17 (85.0%)		
>65	20 (25.6%)	3 (15.0%)			6 (17.6%)	3 (15.0%)		
BMI			1.244	0.681			5.111	0.101
<18.5	11 (14.1%)	1 (5.0%)			5 (14.7%)	1 (5.0%)		
18.5-23.9	52 (66.7%)	15 (75.0%)			28 (82.4%)	15 (75.0%)		
≥24	15 (19.2%)	4 (20.0%)			1 (2.9%)	4 (20.0%)		
Smoking history			1.965	0.161			1.518	0.218
no	37 (47.4%)	6 (30.0%)			16 (47.1%)	6 (30.0%)		
yes	41 (52.6%)	14 (70.0%)			18 (52.9%)	14 (70.0%)		
Tumor location			1.857	0.523			1.888	0.543
upper	4 (5.1%)	0 (0%)			3 (8.8%)	0 (0%)		
middle	52 (66.7%)	12 (60.0%)			18 (52.9%)	12 (60.0%)		
lower	22 (28.2%)	8 (40.0%)			13 (38.2%)	8 (40.0%)		
Cycle of nICT			0.267	0.606			0.078	0.780
≤2	59 (75.6%)	14 (70.0%)			25 (73.5%)	14 (70.0%)		
>2	19 (24.4%)	6 (30.0%)			9 (26.5%)	6 (30.0%)		
Stage			7.180	0.158			0.499	0.931
I	39 (50.0%)	6 (30.0%)			12 (35.3%)	6 (30.0%)		
II	13 (16.7%)	3 (15.0%)			6 (17.6%)	3 (15.0%)		
IIIa	9 (11.5%)	2 (10.0%)			4 (11.8%)	2 (10.0%)		
IIIb	14 (17.9%)	9 (45.0%)			12 (35.3%)	9 (45.0%)		
IVa	3 (3.8%)	0 (0%)			0 (0%)	0 (0%)		
ypT stage			4.697	0.217			0.193	1.000
T_0	27 (34.6%)	4 (20.0%)			8 (23.5%)	4 (20.0%)		
T_1	14 (17.9%)	5 (25.0%)			9 (26.5%)	5 (25.0%)		
T_2	13 (16.7%)	1 (5.0%)			2 (5.9%)	1 (5.0%)		
T_3	24 (30.8%)	10 (50.0%)			15 (44.1%)	10 (50.0%)		
ypN stage			4.989	0.196			0.470	0.872
N_0	52 (66.7%)	9 (45.0%)			18 (52.9%)	9 (45.0%)		
N_1	14 (17.9%)	7 (35.0%)			9 (26.5%)	7 (35.0%)		
N_2	9 (11.5%)	4 (20.0%)			7 (20.6%)	4 (20.0%)		
N_3	3 (3.8%)	0 (0%)			0 (0%)	0 (0%)		
Pathological response			1.461	0.227			0.064	1.000

(Continued)

TABLE 5 Continued

	Before PSM		Statistics value	P value	After PSM		Statistics value	P value
	non-AT	aCT			non-AT	aCT		
non-pCR	56 (71.8%)	17 (85.0%)			28 (82.4%)	17 (85.0%)		
pCR	22 (28.2%)	3 (15.0%)			6 (17.6%)	3 (15.0%)		

nICT, neoadjuvant chemoimmunotherapy; aCT, adjuvant chemotherapy; AT, adjuvant chemotherapy; pCR, pathological complete response.

TABLE 6 Characteristics comparison of aICT patients and non-AT patients before and after matching.

	Before PSM		Statistics value	P value	After PSM		Statistics value	P value
	non-AT	aICT			non-AT	aICT		
Sex			2.442	0.118			1.235	0.266
male	57 (73.1%)	40 (85.1%)			32 (76.2%)	36 (85.7%)		
female	21 (26.9%)	7 (14.9%)			10 (23.8%)	6 (14.3%)		
Age			1.254	0.263			0.283	0.595
≤65	58 (74.4%)	39 (83.0%)			32 (76.2%)	34 (81.0%)		
>65	20 (25.6%)	8 (17.0%)			10 (23.8%)	8 (19.0%)		
BMI			0.902	0.637			2.349	0.329
<18.5	11 (14.1%)	4 (8.5%)			6 (14.3%)	3 (7.1%)		
18.5-23.9	52 (66.7%)	34 (72.3%)			32 (76.2%)	31 (73.8%)		
≥24	15 (19.2%)	9 (19.1%)			4 (9.5%)	8 (19.0%)		
Smoking history			0.090	0.765			0.048	0.827
no	37 (47.4%)	21 (44.7%)			20 (47.6%)	19 (45.2%)		
yes	41 (52.6%)	26 (55.3%)			22 (52.4%)	23 (54.8%)		
Tumor location			6.187	0.045			1.191	0.601
upper	4 (5.1%)	8 (17.0%)			3 (7.1%)	6 (14.3%)		
middle	52 (66.7%)	23 (48.9%)			25 (59.5%)	22 (52.4%)		
lower	22 (28.2%)	16 (34.0%)			14 (33.3%)	14 (33.3%)		
Cycle of nICT			1.595	0.207			1.844	0.175
≤2	59 (75.6%)	40 (85.1%)			31 (73.8%)	36 (85.7%)		
>2	19 (24.4%)	7 (14.9%)			11 (26.2%)	6 (14.3%)		
Stage			6.142	0.216			0.000	1.000
I	39 (50.0%)	19 (40.4%)			19 (45.2%)	19 (45.2%)		
II	13 (16.7%)	5 (10.6%)			5 (11.9%)	5 (11.9%)		
IIIa	9 (11.5%)	9 (19.1%)			7 (16.7%)	7 (16.7%)		
IIIb	14 (17.9%)	14 (29.8%)			11 (26.2%)	11 (26.2%)		
IVa	3 (3.8%)	0 (0%)			0 (0%)	0 (0%)		
ypT stage			0.641	0.887			0.000	1.000
T_0	27 (34.6%)	15 (31.9%)			13 (31.0%)	13 (31.0%)		
T_1	14 (17.9%)	9 (19.1%)			9 (21.4%)	9 (21.4%)		
T_2	13 (16.7%)	6 (12.8%)			6 (14.3%)	6 (14.3%)		

(Continued)

10.3389/fimmu.2024.1332492

TABLE 6 Continued

	Before PSM		Statistics value	P value	After PSM		Statistics value	P value
	non-AT	aICT			non-AT	aICT		
T_3	24 (30.8%)	17 (36.2%)			14 (33.3%)	14 (33.3%)		
ypN stage			5.997	0.113			0.000	1.000
N_0	52 (66.7%)	24 (51.1%)			24 (57.1%)	24 (57.1%)		
N_1	14 (17.9%)	14 (29.8%)			12 (28.6%)	12 (28.6%)		
N_2	9 (11.5%)	9 (19.1%)			6 (14.3%)	6 (14.3%)		
N_3	3 (3.8%)	0 (0%)			0 (0%)	0 (0%)		
Pathological response			0.739	0.390			0.000	1.000
non-pCR	56 (71.8%)	37 (78.7%)			32 (76.2%)	32 (76.2%)		
pCR	22 (28.2%)	10 (21.3%)			10 (23.8%)	10 (23.8%)		

nICT, neoadjuvant chemoimmunotherapy; aICT, adjuvant chemoimmunotherapy; AT, adjuvant chemotherapy; pCR, pathological complete response.

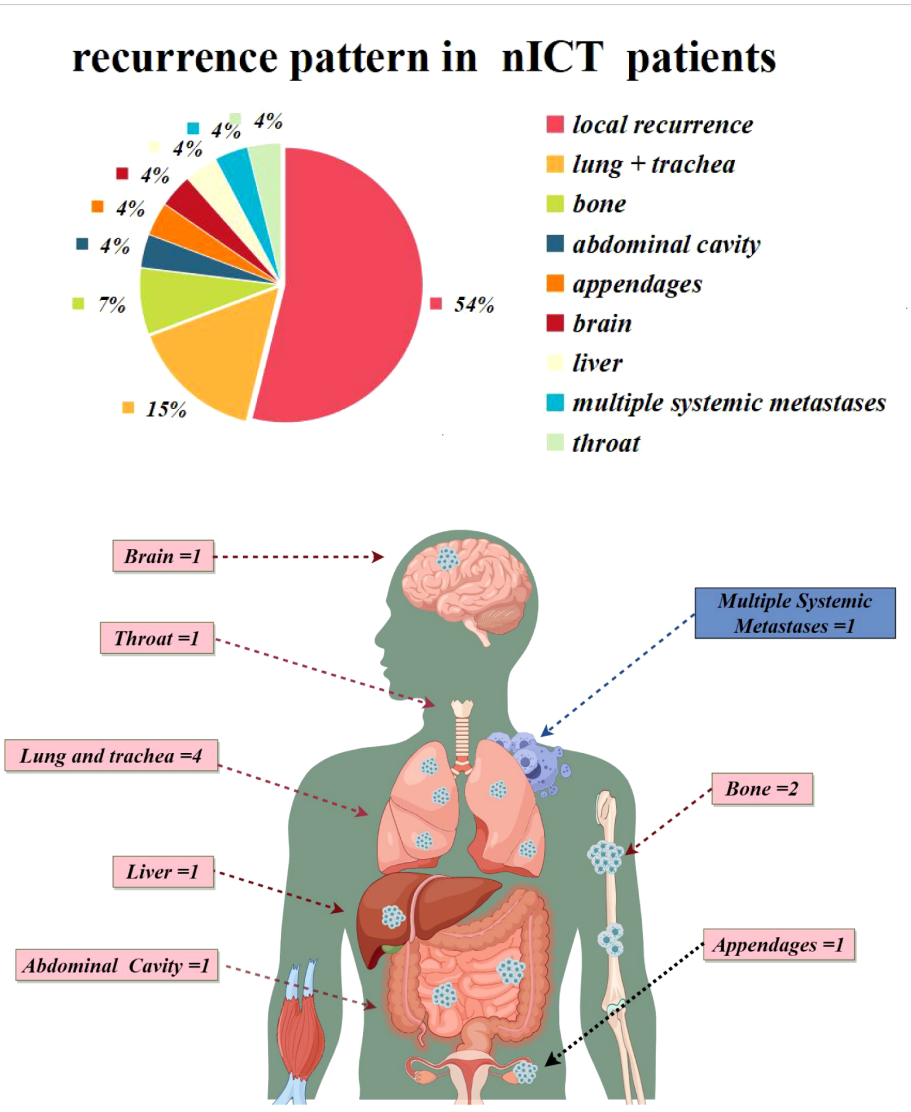

FIGURE 6
Recurrence patterns in the nICT group.

Data availability statement

The raw data supporting the conclusions of this article will be made available by the authors at reasonable request.

Ethics statement

The studies involving humans were approved by Fujian Medical University Union Hospital (Project identification code: 2023KY241). The studies were conducted in accordance with the local legislation and institutional requirements. The ethics committee/institutional review board waived the requirement of written informed consent for participation from the participants or the participants' legal guardians/next of kin because this is a retrospective study.

Author contributions

SX: Conceptualization, Data curation, Formal analysis, Methodology, Software, Supervision, Writing – original draft, Writing – review & editing. LY: Conceptualization, Data curation, Formal analysis, Methodology, Writing – original draft, Writing – review & editing. HZ: Data curation, Formal analysis, Investigation, Writing – original draft. ZT: Data curation, Investigation, Writing – original draft. ZL: Data curation, Investigation, Software, Writing – original draft. YC: Data curation, Investigation, Software, Writing – original draft. ZH: Conceptualization, Data curation, Supervision, Writing – review & editing. RX: Conceptualization, Data curation, Supervision, Writing – review & editing. WL: Conceptualization, Data curation, Supervision, Writing – review & editing. MK: Conceptualization, Data curation, Supervision, Writing – review & editing.

Funding

The author(s) declare that no financial support was received for the research, authorship, and/or publication of this article.

Acknowledgments

We express our sincere appreciation for the technical support provided by Figdraw. The authors express their gratitude to Figdraw for providing an online drawing platform. Finally, we express huge gratitude towards Frontier in Immunology for providing us with this opportunity to check our manuscript again.

Conflict of interest

The authors declare that the research was conducted in the absence of any commercial or financial relationships that could be construed as a potential conflict of interest.

Publisher's note

All claims expressed in this article are solely those of the authors and do not necessarily represent those of their affiliated organizations, or those of the publisher, the editors and the reviewers. Any product that may be evaluated in this article, or claim that may be made by its manufacturer, is not guaranteed or endorsed by the publisher.

Supplementary material

The Supplementary Material for this article can be found online at: https://www.frontiersin.org/articles/10.3389/fimmu.2024.1332492/full#supplementary-material

References

1. Li J, Xu J, Zheng Y, Gao Y, He S, Li H, et al. Esophageal cancer: idemiology, risk factors and screening. *Chin J Cancer Res* (2021) 33(5):535–47. doi: 10.21147/j.issn.1000-9604.2021.05.01

2. He F, Wang J, Liu L, Qin X, Wan Z, Li W, et al. Esophageal cancer: trends in incidence and mortality in China from 2005 to 2015. *Cancer Med* (2021) 10(5):1839–47. doi: 10.1002/cam4.3647

3. Lagergren J, Smyth E, Cunningham D, Lagergren P. Oesophageal cancer. *Lancet.* (2017) 390(10110):2383–96. doi: 10.1016/S0140-6736(17)31462-9

4. Ajani JA, D'Amico TA, Bentrem DJ, Chao J, Corvera C, Das P, et al. Esophageal and esophagogastric junction cancers, version 2.2019, NCCN clinical practice guidelines in oncology. *J Natl Compr Canc Netw* (2019) 17(7):855–83. doi: 10.6004/jnccn.2019.0033

5. van Hagen P, Hulshof MC, van Lanschot JJ, Steyerberg EW, van Berge Henegouwen MI, Wijnhoven BP, et al. Preoperative chemoradiotherapy for esophageal or junctional cancer. *N Engl J Med* (2012) 366(22):2074–84. doi: 10.1056/NEJMoa1112088

6. Kadono T, Yamamoto S, Hirose T, Ikeda G, Ohara A, Itoyama M, et al. Safety and short-term efficacy of preoperative FOLFOX therapy in patients with resectable esophageal squamous cell carcinoma who are ineligible for cisplatin. *Esophagus.* (2023) 20(1):109–15. doi: 10.1007/s10388-022-00951-4

7. Nishiwaki N, Noma K, Kunitomo T, Hashimoto M, Maeda N, Tanabe S, et al. Neoadjuvant chemotherapy for locally advanced esophageal cancer comparing cisplatin and 5-fluorouracil versus docetaxel plus cisplatin and 5-fluorouracil: a propensity score matching analysis. *Esophagus.* (2022) 19(4):626–38. doi: 10.1007/s10388-022-00934-5

8. Yang H, Liu H, Chen Y, Zhu C, Fang W, Yu Z, et al. Long-term efficacy of neoadjuvant chemoradiotherapy plus surgery for the treatment of locally advanced esophageal squamous cell carcinoma: the NEOCRTEC5010 randomized clinical trial. *JAMA Surg* (2021) 156(8):721–9. doi: 10.1001/jamasurg.2021.2373

9. Park SY, Kim HK, Jeon YJ, Lee J, Cho JH, Choi YS, et al. The role of adjuvant chemotherapy after neoadjuvant chemoradiotherapy followed by surgery in patients with esophageal squamous cell carcinoma. *Cancer Res Treat* (2023) 55(4):1231–9. doi: 10.4143/crt.2022.1417

10. Zhang Z, Hong ZN, Xie S, Lin W, Lin Y, Zhu J, et al. Neoadjuvant sintilimab plus chemotherapy for locally advanced esophageal squamous cell carcinoma: a single-arm, single-center, phase 2 trial (ESONICT-1). *Ann Transl Med* (2021) 9(21):1623. doi: 10.21037/atm-21-5381

11. Smyth EC, Gambardella V, Cervantes A, Fleitas T. Checkpoint inhibitors for gastroesophageal cancers: dissecting heterogeneity to better understand their role in first-line and adjuvant therapy. *Ann Oncol* (2021) 32(5):590–9. doi: 10.1016/j.annonc.2021.02.004

12. Yang Y, Liu J, Liu Z, Zhu L, Chen H, Yu B, et al. Two-year outcomes of clinical N2-3 esophageal squamous cell carcinoma after neoadjuvant chemotherapy and immunotherapy from the phase 2 NICE study. *J Thorac Cardiovasc Surg* (2023) S0022-5223(23):00782–1. doi: 10.1016/j.jtcvs.2023.08.056

13. Yarchoan M, Johnson BA 3rd, Lutz ER, Laheru DA, Jaffee EM. Targeting neoantigens to augment antitumour immunity. *Nat Rev Canc* (2017) 17(9):569. doi: 10.1038/nrc.2017.74

14. Pauken KE, Torchia JA, Chaudhri A, Sharpe AH, Freeman GJ. Emerging concts in PD-1 checkpoint biology. *Semin Immunol* (2021) 52:101480. doi: 10.1016/j.smim.2021.101480

15. He J, Hu Y, Hu M, Li B. Development of PD-1/PD-L1 pathway in tumor immune microenvironment and treatment for non-small cell lung cancer. *Sci R* (2015) 5:13110. doi: 10.1038/sr13110

16. Gao L, Hong ZN, Wu L, Yang Y, Kang M. Residual tumor model in esophageal squamous cell carcinoma after neoadjuvant immunochemotherapy: Frequently involves the mucosa and/or submucosa. *Front Immunol* (2022) 13:1008681. doi: 10.3389/fimmu.2022.1008681

17. Hong ZN, Gao L, Weng K, Huang Z, Han W, Kang M. Safety and feasibility of esophagectomy following combined immunotherapy and chemotherapy for locally advanced esophageal squamous cell carcinoma: A propensity score matching analysis. *Front Immunol* (2022) 13:836338. doi: 10.3389/fimmu.2022.836338

18. Brandão M, Martins-Branco D, De Angelis C, Vuylsteke P, Gelber RD, Van Damme N, et al. Surgery of the primary tumor in patients with de novo metastatic breast cancer: a nationwide population-based retrospective cohort study in Belgium. *Breast Cancer Res Treat* (2023) 203:351–63. doi: 10.1007/s10549-023-07116-6

19. Mazzarella L, Giugliano F, Nicolo E, Esposito A, Crimini E, Tini G, et al. Immune-related adverse event likelihood score identifies "Pure" IRAEs strongly associated with outcome in a phase I-II trial population. *Oncologist* (2023), oyad239. doi: 10.1093/oncolo/oyad239

20. Heymach JV, Harpole D, Mitsudomi T, Taube JM, Galffy G, Hochmair M, et al. Perioperative durvalumab for resectable non-small-cell lung cancer. *N Engl J Med* (2023) 389:18. doi: 10.1056/NEJMoa2304875

21. Hong Z, Xu J, Chen Z, Xu H, Huang Z, Weng K, et al. Additional neoadjuvant immunotherapy does not increase the risk of anastomotic leakage after esophagectomy for esophageal squamous cell carcinoma: a multicenter retrospective cohort study. *Int J Surg* (2023) 109(8):2168–78. doi: 10.1097/JS9%0000000000487

22. Li X, Luan S, Yang Y, Zhou J, Shang Q, Fang P, et al. Trimodal therapy in esophageal squamous cell carcinoma: role of adjuvant therapy following neoadjuvant chemoradiation and surgery. *Cancers (Basel)* (2022) 14(15):3721. doi: 10.3390/cancers14153721

23. Al-Kaabi A, van der Post RS, van der Werf LR, Wijnhoven BPL, Rosman C, Hulshof MCCM, et al. Impact of pathological tumor response after CROSS neoadjuvant chemoradiotherapy followed by surgery on long-term outcome of esophageal cancer: a population-based study. *Acta Oncol* (2021) 60(4):497–504. doi: 10.1080/0284186X.2020.1870246

24. Gao H, Wang Y, Jiang Z, Shi G, Hu S, Ai J, et al. Association of survival with adjuvant radiotherapy for pN0 esophageal cancer. *Aging (Albany NY)* (2023) 15 (8):3158–70. doi: 10.18632/aging.204677

25. Network NCC. *NCCN clinical practice guidelines in oncology (NCCN guidelines): esophageal and esophagogastric junction cancers. Version 4.2020*. The National Comprehensive Cancer Network: Plymouth Meeting, PA (2020).

26. Stahl M, Mariette C, Haustermans K, Cervantes A, Arnold DESMO Guidelines Working Group. Oesophageal cancer: ESMO Clinical Practice Guidelines for diagnosis, treatment and follow-up. *Ann Oncol* (2013) 24 Suppl 6:vi51–6. doi: 10.1093/annonc/mdt342

27. Stiles BM, Christos P, Port JL, Lee PC, Paul S, Saunders J, et al. Predictors of survival in patients with persistent nodal metastases after preoperative chemotherapy for esophageal cancer. *J Thorac Cardiovasc Surg* (2010) 139(2):387–94. doi: 10.1016/j.jtcvs.2009.10.003

28. Liu J, Blake SJ, Yong MC, Harjunpää H, Ngiow SF, Takeda K, et al. Improved efficacy of neoadjuvant compared to adjuvant immunotherapy to eradicate metastatic disease. *Cancer Discovery* (2016) 6(12):1382–99. doi: 10.1158/2159-8290.CD-16-0577

29. Yan W, Zhao P, Fu H, Lin Y, Li Z, Dai L, et al. Survival after induction chemotherapy and esophagectomy is not improved by adjuvant chemotherapy. *Ann Thorac Surg* (2019) 108(5):1505–13. doi: 10.1016/j.athoracsur.2019.04.106

30. Shiozaki A, Fujiwara H, Okamura H, Murayama Y, Komatsu S, Kuriu Y, et al. Risk factors for postoperative respiratory complications following esophageal cancer resection. *Oncol Lett* (2012) 3(4):907–12. doi: 10.3892/ol.2012.589

31. van Sandick JW, Gisbertz SS, ten Berge IJ, Boermeester MA, van der Pouw Kraan TC, Out TA, et al. Immune responses and prediction of major infection in patients undergoing transhiatal or transthoracic esophagectomy for cancer. *Ann Surg* (2003) 237(1):35–43. doi: 10.1097/00000658-200301000-00006

32. Kubo Y, Miyata H, Sugimura K, Shinno N, Asukai K, Hasegawa S, et al. Prognostic implication of postoperative weight loss after esophagectomy for esophageal squamous cell cancer. *Ann Surg Oncol* (2021) 28(1):184–93. doi: 10.1245/s10434-020-08762-6

33. Ji Y, Du X, Zhu W, Yang Y, Ma J, Zhang L, et al. Efficacy of concurrent chemoradiotherapy with S-1 vs radiotherapy alone for older patients with esophageal cancer: A multicenter randomized phase 3 clinical trial. *JAMA Oncol* (2021) 7 (10):1459–66. doi: 10.1001/jamaoncol.2021.2705

34. Cheraghi A, Barahman M, Hariri R, Nikoofar A, Fadavi P. Comparison of the pathological response and adverse effects of oxaliplatin and capecitabine versus paclitaxel and carboplatin in the neoadjuvant chemoradiotherapy treatment approach for esophageal and gastroesophageal junction cancer: A randomized control trial study. *Med J Islam Repub Iran* (2021) 35:140. doi: 10.47176/mjiri.35.140

35. Sugiyama M, Morita M, Yoshida R, Ando K, Egashira A, Takefumi O, et al. Patterns and time of recurrence after complete resection of esophageal cancer. *Surg Today* (2012) 42(8):752–8. doi: 10.1007/s00595-012-0133-9

36. Dresner SM, Griffin SM. Pattern of recurrence following radical oesophagectomy with two-field lymphadenectomy. *Br J Surg* (2000) 87(10):1426–33. doi: 10.1046/j.1365-2168.2000.01541.x

37. Nakagawa S, Kanda T, Kosugi S, Ohashi M, Suzuki T, Hatakeyama K. Recurrence pattern of squamous cell carcinoma of the thoracic esophagus after extended radical esophagectomy with three-field lymphadenectomy. *J Am Coll Surg* (2004) 198(2):205–11. doi: 10.1016/j.jamcollsurg.2003.10.005

frontiers | Frontiers in Oncology

TYPE Original Research
PUBLISHED 23 February 2024
DOI 10.3389/fonc.2024.1325514

OPEN ACCESS

EDITED BY
Vera Rebmann,
University of Duisburg-Essen, Germany

REVIEWED BY
Akira Umemura,
Iwate Medical University, Japan
Yuhan Zhang,
Chinese Academy of Medical Sciences and Peking Union Medical College, China

*CORRESPONDENCE
Huanwei Zheng
13323119317@163.com

†These authors have contributed equally to this work and share first authorship

RECEIVED 21 October 2023
ACCEPTED 05 February 2024
PUBLISHED 23 February 2024

CITATION
Wang H, Cao X, Meng P, Zheng C, Liu J, Liu Y, Zhang T, Li X, Shi X, Sun X, Zhang T, Zuo H, Wang Z, Fu X, Li H and Zheng H (2024) Machine learning-based identification of colorectal advanced adenoma using clinical and laboratory data: a phase I exploratory study in accordance with updated World Endoscopy Organization guidelines for noninvasive colorectal cancer screening tests.
Front. Oncol. 14:1325514.
doi: 10.3389/fonc.2024.1325514

Machine learning-based identification of colorectal advanced adenoma using clinical and laboratory data: a phase I exploratory study in accordance with updated World Endoscopy Organization guidelines for noninvasive colorectal cancer screening tests

Huijie Wang[1†], Xu Cao[1†], Ping Meng[2], Caihua Zheng[2], Jinli Liu[2], Yong Liu[1], Tianpeng Zhang[3], Xiaofang Li[1], Xiaoyang Shi[1], Xiaoxing Sun[1], Teng Zhang[4], Haiying Zuo[5], Zhichao Wang[5], Xin Fu[6], Huan Li[6] and Huanwei Zheng[2*]

[1]Department of Endoscopy, Shijiazhuang Traditional Chinese Medicine Hospital, Shijiazhuang, China, [2]Department of Gastroenterology, Shijiazhuang Traditional Chinese Medicine Hospital, Shijiazhuang, China, [3]Department of Anus & Intestine Surgery, Shijiazhuang Traditional Chinese Medicine Hospital, Shijiazhuang, China, [4]Institute of Traditional Chinese Medicine, North China University of Science and Technology, Tangshan, China, [5]Graduate School, Hebei North University, Zhangjiakou, China, [6]Research and Development Department, Wuhan Metware Biotechnology Co., Ltd, Wuhan, China

Objective: The recent World Endoscopy Organization (WEO) guidelines now recognize precursor lesions of colorectal cancer (CRC) as legitimate screening targets. However, an optimal screening method for detecting advanced adenoma (AA), a significant precursor lesion, remains elusive.

Methods: We employed five machine learning methods, using clinical and laboratory data, to develop and validate a diagnostic model for identifying patients with AA (569 AAs vs. 3228 controls with normal colonoscopy). The best-performing model was selected based on sensitivity and specificity assessments. Its performance in recognizing adenoma-carcinoma sequence was evaluated in line with guidelines, and adjustable thresholds were established. For comparison, the Fecal Occult Blood Test (FOBT) was also selected.

Results: The XGBoost model demonstrated superior performance in identifying AA, with a sensitivity of 70.8% and a specificity of 83.4%. It successfully detected 42.7% of non-advanced adenoma (NAA) and 80.1% of CRC. The model-transformed risk assessment scale provided diagnostic performance at different positivity thresholds. Compared to FOBT, the XGBoost model better identified AA and NAA, however, was less effective in CRC.

Conclusion: The XGBoost model, compared to FOBT, offers improved accuracy in identifying AA patients. While it may not meet the recommendations of some organizations, it provides value for individuals who are unable to use FOBT for various reasons.

KEYWORDS

advanced colorectal adenoma, machine learning, non-invasive test, risk assessment, adjustable thresholds

1 Introduction

Colorectal cancer (CRC) represents a significant threat to residents of China, contributing substantially to the societal burden (1). In China, CRC-related new cases and deaths account for 9.87% and 8.01% of all malignant tumor incidence and mortality, respectively (2). Addressing this public health challenge effectively is of paramount importance (3).

The goal of CRC screening is to reduce mortality and morbidity by identifying treatable CRC cases and precursor lesions, while minimizing health risks and individual burdens (4). In 2023, the CRC Screening Committee of the World Endoscopy Organization (WEO) issued guidelines for evaluating novel non-invasive screening tests for CRC. These guidelines recommend a dual-step screening process, starting with a non-invasive test and, if positive, followed by a colonoscopy. The non-invasive test should be capable of identifying individuals with an increased likelihood of CRC or advanced precursor lesions (5). Advanced adenoma (AA), an important precursor lesion, is currently considered to carry a significantly elevated risk (6). Although the fecal immunochemical test (FIT) is currently the most widely used non-invasive test, its sensitivity for early detection of CRC, especially AA, remains suboptimal (7). As a result, there is an urgent need for more accurate and non-invasive screening strategies that can identify AA, thereby improving survival rates among CRC patients (8).

Recent clinical guidelines from the Asian Pacific Gastroenterology and Digestive Endoscopy highlight the superiority of combining biomarkers over single biomarkers for detecting colorectal neoplasia (8). Machine learning, based on feature combinations, has emerged as a powerful and effective method for predictive analytics. Its successful application in diagnosis, prediction, and treatment selection has received considerable recognition (9). Routine medical laboratory tests are widely used in China and have become an essential part of modern healthcare (10). The results of these tests may contain more information than even the most experienced clinician can discern, making them suitable for analysis through artificial intelligence to uncover subtle interrelationships (11).

Predictive and diagnostic models based on routine clinical and laboratory data have been developed for various cancers (12–15). However, they often exhibit low sensitivity for AAs due to their non-specific symptoms and distinct risk factors compared to those of CRC (16).

The CRC Screening Committee of the WEO outlines a four-phase evaluation process for new tests, starting with Phase I studies involving limited cohorts or case-control studies (5). Based on this premise, we conducted a Phase I exploratory case-control study using clinical and laboratory data. The aim is to construct a machine-learning diagnostic model for identifying AA and to assess its ability to meet the objectives of non-invasive screening tests, as outlined in the WEO guidelines. These objectives include diagnostic performance regarding the adenoma-carcinoma sequence, adjustable thresholds of positivity, and comparison with validated non-invasive screening tests.

2 Materials and methods

2.1 Study design and population

We conducted a retrospective case-control study, comprising a case group with AA (17) and a control group with normal colonoscopies. The objective was to develop (train) and validate (test) a model for diagnosing AA. AA is defined as an adenoma that exhibits any of the following characteristics: size ≥ 1 cm, presence of tubulovillous or villous components, or high-grade dysplasia. The model was constructed based on features obtained as part of routine clinical care, which included demographic characteristics, lifestyle factors, and clinical features (including comorbidities and laboratory indicators). We ensured that data from at least one laboratory test were available within one month before the colonoscopy. In addition, we validated the outcome model in other populations including non-advanced adenoma (NAA) and CRC. NAA refers to an adenoma that does not meet the definition of AA. All subjects were identified using colonoscopy and pathohistological diagnoses obtained from medical records between April 2015 and June 2022. The exclusion criteria were as follows: a history of colorectal surgery, incomplete medical records, substandard bowel preparation, a colonoscopy that did not reach the cecum, and cases that did not meet the standards of data quality control (QC) (Detail for Figure 1). Specifically, the exclusion criteria

for CRC did not include substandard bowel preparation and whether the colonoscope reached the cecum.

The retrospective study received approval from the Ethics Committee of Shijiazhuang Traditional Chinese Medicine Hospital (NO.20220919029), and the requirements for informed consent were waived due to the retrospective nature of the study.

2.2 Data collection

The present study collected demographic characteristics (age, sex, and marital status), smoking and drinking information (including never, former, and current usage), comorbid conditions, and laboratory test results (routine blood and urine tests, fecal occult blood test [FOBT], biochemistry, tumor markers, and coagulation function). Notably, qualitative FOBT is more prevalent in Chinese hospitals than quantitative FIT. The FOBT method employed in this study was immunocolloid gold (the FOBT was considered positive when the hemoglobin level was greater than or equal to 0.2 μg/ml diluent).

Detailed test methods for laboratory data included in the machine learning analyses were presented in Supplementary Table 1.

2.3 Feature screening

During the data QC process, we retained the features of interest and excluded features with a missing rate exceeding 20% or samples with a missing rate exceeding 50%. For continuous variables with missing values in features retained after QC, we imputed them using k-nearest neighbors (KNN, K = 15). Missing values in categorical variables with a missing rate of less than 20% were imputed using grouped plurality while missing rates of 20% or more were imputed with the new phenotype "MISS".

Subsequently, we initially screened categorical and continuous variables using the chi-square test and random forest, respectively, to eliminate features with minimal or no impact on grouping. The remaining features' importance was ranked using the logistic regression (LR), random forest (RF), and least absolute shrinkage and selection operator (LASSO) methods. This step was repeated 10 times to mitigate random bias in data splitting. We took the intersection of the features selected by different models and weighted the importance of each feature, summing them to obtain the importance of weighted features for manual screening.

2.4 Machine learning modeling and validation

We employed five machine learning methods, namely LR, RF, eXtreme Gradient Boosting (XGBoost), KNN, and support vector machine (SVM), for modeling within the caret framework in R. The data were randomly divided into 10 repetitive groupings based on an 8:2 ratio (training group: validation group) to generate 10 sets of training and validation datasets. We modeled the training sets using the aforementioned five methods.

For all methods except LR, we predefined a wide range of parameters and evaluated them using the Grid Searching method using 3 independent 10-fold cross-validations to obtain the most appropriate modeling parameter within the current parameter space, which was then used for model construction.

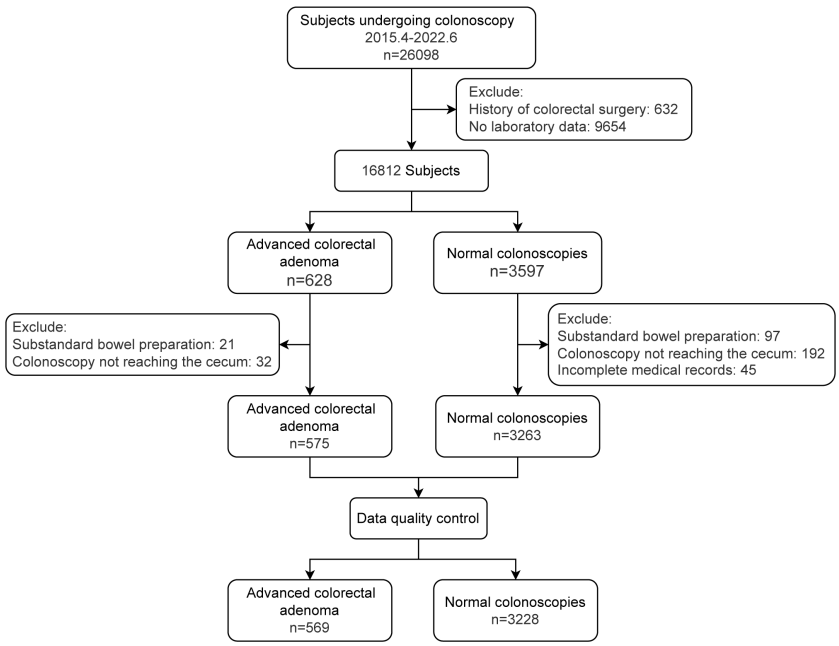

FIGURE 1
Study population flowchart.

We predicted scores on the training set data using the models obtained from the five methods. Based on the prediction results of the training set, we plotted receiver operating characteristic (ROC) curves, and the point closest to the top-left corner was selected as the classification threshold (closest.topleft). We applied the model and threshold to the validation set data and calculated the area under the curve (AUC), sensitivity, and specificity to evaluate the model performance and determine the final resultant model.

2.5 Evaluating model performance based on the latest WEO guidelines

We assessed the diagnostic performance of the outcome model in patients with NAA, AA, and CRC in the adenoma-carcinoma sequence using true positive rate (TPR) and false positive rate (FPR). Qualitative FOBT was selected as a validated non-invasive screening test, and we compared the diagnostic performance of the outcome model and the FOBT in patients with FOBT results. We also employed an adjustable positivity threshold to assess disease risk based on an arbitrary risk scale from 0 to 100, calculating the true positives (TP), false negatives (FN), true negatives (TN), false positives (FP), sensitivity (%), specificity (%), positive predictive value (PPV, %), and negative predictive value (NPV, %) (18).

2.6 Statistical analysis

To compare the differences among groups, we adopted the Wilcoxon test, t-test, or chi-square test, depending on the type and distribution of the data. We performed ROC curve analysis using the pROC package in R, and the Delong method was used to calculate the confidence intervals. The bootstrap method was applied to calculate the 95% confidence intervals for sensitivity and specificity. The Hanley-McNeil test was used to analyze the statistical significance of the difference in AUC between the outcome model and FOBT (19).

3 Results

3.1 Study participants

We initially included a total of 575 AAs and 3263 controls. After QC, 569 AAs and 3228 controls were eligible for machine learning modeling and validation. The demographic and clinical characteristics of the study participants are shown in Table 1. Supplementary Table 2 provides more descriptive information on features.

TABLE 1 Demographic and clinical characteristics of the study participants.

Variables	Case n = 569	Control n = 3228	*P*-value
Age, yr, Mean ± SD	61.4 ± 10.2	50.5 ± 13.0	< 0.001
Sex, male, n (%)	369 (64.9)	1208 (37.4)	< 0.001
Weight, kg, Mean ± SD	70.1 ± 11.9	66.2 ± 12.6	< 0.001
Comorbidities, n (%)			
Ischemic cerebrovascular disease	73 (12.8)	301 (9.3)	0.01
Coronary heart disease	90 (15.8)	339 (10.5)	< 0.001
Diabetes mellitus	158 (27.8)	481 (14.9)	< 0.001
Hypertension	235 (41.3)	700 (21.7)	< 0.001

Data are presented as the mean ± SD, median (quartile 1–quartile 3), or N (%).

3.2 Feature screening

We collected 167 features, and after data QC and feature screening, 60 features were retained for machine learning modeling (see Supplementary Table 3 for details). In ROC analyses using separate variable to differentiate between the AA and control groups (Figure 2, Table 2), none of these indicators demonstrated strong discriminatory power (AUC<0.8), with age exhibiting the highest discriminatory power (AUC=0.77).

3.3 Modelling and validation using different models

We successfully built five models using different machine learning methods (KNN, XGBoost, LR, RF, and SVM). We calculated the AUC, sensitivity, and specificity for both the training and validation sets to characterize the diagnostic performance of these models (Figure 3A, Table 2). Overall, the XGBoost model showed the most promising diagnostic performance for identifying patients with AA while maintaining a validation set specificity of at least 0.8. The XGBoost model demonstrated good diagnostic performance in both the training and validation sets, with a sensitivity of 87.5% (95% CI, 84.4–90.4%) (AA=456, Control=2583) and a specificity of 88.4% (95% CI, 87.2–89.6%) in the training set. And the validation set performance resulted in 70.8% (95% CI, 62.0–78.8%) sensitivity and 83.4% (95% CI, 80.5–86.1%) specificity (AA=113, Control=645). Conversely, the RF model, which performed well in the training set, exhibited 97.2% specificity but only 23.9% sensitivity in the validation set, suggesting potential overfitting. The combined diagnostic performance of KNN, LR, and SVM in the validation set did not match that of XGBoost. Thus, based on these results, we concluded that the XGBoost method provided the best performance on the dataset and selected it as the final model.

3.4 Evaluating the diagnostic performance of models based on the latest WEO guidelines

3.4.1 Diagnostic performance in the adenoma-carcinoma sequence

We validated the diagnostic performance of the XGBoost model in the validation set for AA (n=113), NAA (n=3047), and CRC

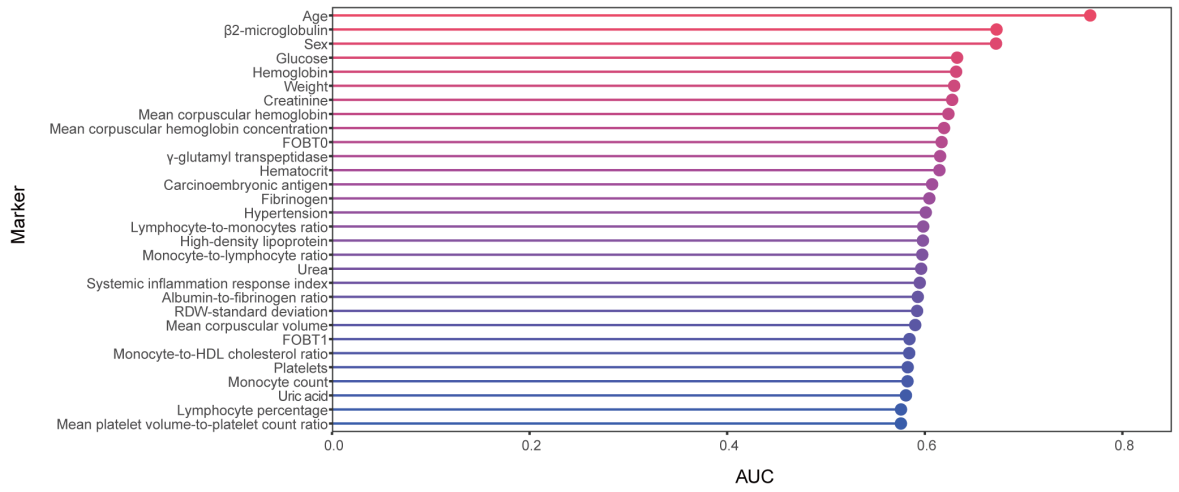

FIGURE 2
Cleveland dot plots show AUCs for Top 30 parameters identifying AAs and controls. AA, advanced adenoma.

TABLE 2 Diagnostic performance of various models in training and validation sets.

Methods	AUC	Sensitivity, % (95% CI)	Specificity, % (95% CI)
KNN			
Train	0.938 (0.929-0.946)	90.4 (87.7-93.0)	83.4 (81.9-84.8)
Valid	0.754 (0.708-0.801)	56.6 (47.8-65.5)	78.8 (75.7-81.9)
LR			
Train	0.844 (0.826-0.863)	79.2 (75.2-82.7)	74.8 (73.1-76.4)
Valid	0.833 (0.790-0.875)	77.0 (69.0-84.1)	75.5 (72.1-78.9)
RF			
Train	1	100	100
Valid	0.820 (0.778-0.861)	23.9 (15.9-31.9)	97.2 (95.8-98.5)
SVM			
Train	0.920 (0.904-0.936)	84.7 (81.1-87.9)	91.6 (90.4-92.6)
Valid	0.773 (0.724-0.823)	69.0 (60.2-77.9)	74.6 (71.2-77.8)
XGBoost			
Train	0.955 (0.947-0.963)	87.5 (84.4-90.4)	88.4 (87.2-89.6)
Valid	0.850 (0.813-0.887)	70.8 (62.0-78.8)	83.4 (80.5-86.1)

AUC, area under the curve; CI, confidence interval; LR, logistic regression; RF, random forest; SVM, support vector machine; KNN, k-nearest neighbors; XGBoost, eXtreme Gradient Boosting.

(n=488) (Table 3). In these three groups, the FPR was 16.6% and the TPR was 70.8% (AA), 42.7% (NAA), and 80.1% (CRC), respectively.

3.4.2 Comparison of diagnostic performance of XGBoost model and FOBT

In this study, we screened three subsets with FOBT results: CRC (n=343), NAA (n=1996), and AA (n=65). This was done to compare the diagnostic performance of the XGBoost model with that of the FOBT, as shown in Table 4. The FPR of the XGBoost model (15.5%) was superior to that of the FOBT (16.5%). The TPR of the XGBoost model for NAA and AA was 40.03% and 70.8%, respectively, which were better than FOBT (25.2% and 47.7%). However, in CRC, the TPR of the XGBoost model (84.8%) was lower than that of FOBT (91.6%). The ROC curves of the XGBoost model and FOBT for these three subsets are depicted in Figures 3B–D, respectively. Moreover, we analyzed the difference in AUC between the XGBoost model and FOBT. As shown in Table 4, we found that in all three validation sets, the AUC of the XGBoost model was significantly higher than that of FOBT (all $P<0.05$). This indicates that from the perspective of AUC, the XGBoost model outperforms FOBT.

3.4.3 Adjustable positivity thresholds for the XGBoost model

We transformed the calculation results of the XGBoost model into risk scores with a score range of 0 to 100, allowing visualization of sensitivity, specificity, and other indicators at different thresholds (Table 5). For example, choosing a score of 10 as the positive threshold resulted in a sensitivity of 87.6% and specificity of 64.34%, while a score of 20 yielded a sensitivity of 74.3% and specificity of 82.5.

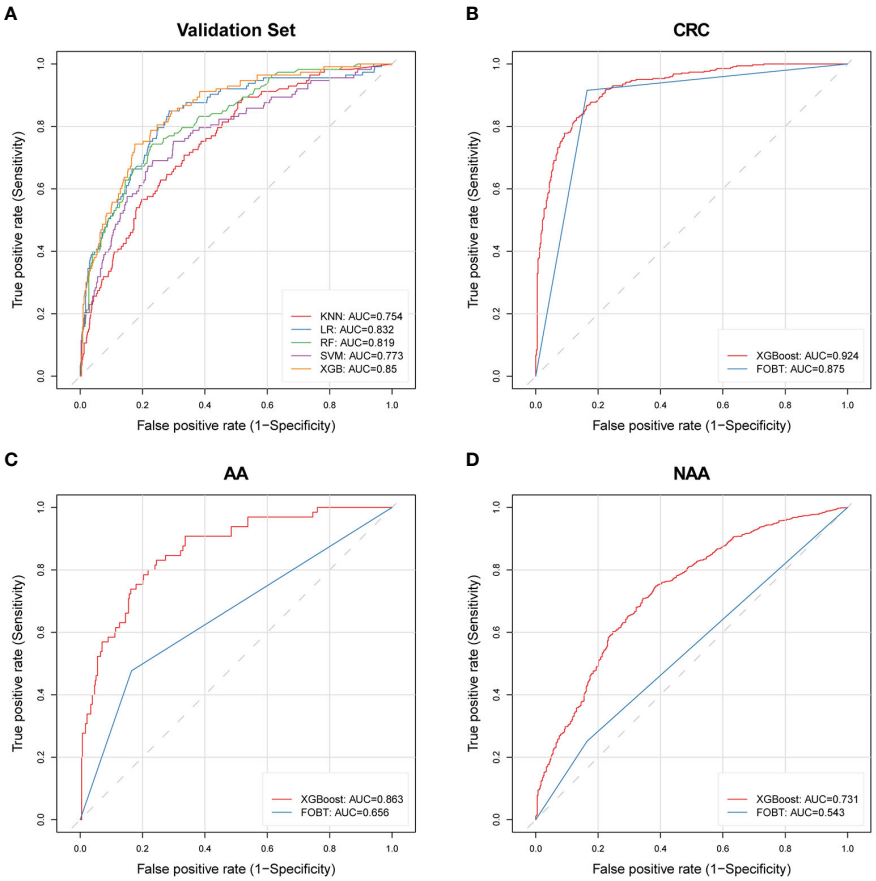

FIGURE 3
ROC curves of machine learning models and FOBT in different validation cohorts. **(A)** Five constructed machine learning models in the validation set; **(B)** XGBoost model and FOBT in the CRC validation set with FOBT results; **(C)** XGBoost model and FOBT in the AA validation set with FOBT results; **(D)** XGBoost model and FOBT in the NAA validation set that includes FOBT results. AA, advanced adenoma; NAA, non-advanced adenoma; CRC, colorectal cancer; ROC, receiver operating characteristic; XGBoost, eXtreme Gradient Boosting; FOBT, fecal occult blood test; LR, logistic regression; RF, random forest; SVM, support vector machine; KNN, k-nearest neighbors; AUC, area under the curve.

4 Discussion

The recent guidelines from the WEO for endoscopic CRC screening have incorporated principles such as treating screening as a multistep process, recognizing precursor lesions for CRC as legitimate targets, using FIT as a current comparator, and providing the ability to adjust thresholds for new test positivity. In light of this, we conducted a phase I exploratory study using 60 clinical and laboratory data points to develop and validate an XGBoost model for identifying patients with AA. The model exhibited a sensitivity

TABLE 3 Diagnostic performance of the XGBoost model and FOBT in the validation set of advanced adenoma, non-advanced adenoma, and colorectal cancer.

Subgroups	Case, n	Control, n	XGBoost				FOBT			
			TP, n	TPR, %	FP, n	FPR, %	TP, n	TPR, %	FP, n	FPR, %
AA	113	645	80	70.8	107	16.6				
With FOBT	65	413	46	70.8	64	15.5	31	47.7	68	16.5
NAA	3047	645	1300	42.7	107	16.6				
With FOBT	1996	413	799	40.0	64	15.5	502	25.2	68	16.5
CRC	488	645	391	80.1	107	16.6				
With FOBT	343	413	291	84.8	64	15.5	314	91.6	68	16.5

AA, advanced adenoma; NAA, non-advanced adenoma; CRC, colorectal cancer; XGBoost, eXtreme Gradient Boosting; FOBT, Fecal occult blood test; TP, true positives; TPR, true positive rate; FP, false positives; FPR, false positive rate.

TABLE 4 Comparison of AUC between XGBoost and FOBT in different validation sets.

Validation sets	AUC (95% CI)		Estimate Difference	Z	*P*-value
	XGBoost	FOBT			
AA	0.863 (0.805-0.921)	0.656 (0.580-0.732)	0.207	4.231	< 0.001
NAA	0.731 (0.708-0.755)	0.543 (0.514-0.573)	0.188	9.708	< 0.001
CRC	0.924 (0.903-0.945)	0.875 (0.849-0.902)	0.049	2.865	0.004

of 70.8% and specificity of 83.4% in the validation set, successfully detecting NAA with a sensitivity of 42.7% and CRC with a sensitivity of 80.1%. The risk assessment scale, transformed by the XGBoost model, showcased varying levels of disease risk at different positivity thresholds, and notably, the XGBoost model outperformed FOBT in identifying more patients with AA.

Detecting and endoscopically resecting colorectal precancerous lesions, such as AA, has been recognized as an effective method for preventing the occurrence of CRC and reducing CRC-induced mortality (20). Ensuring the identification of AA is a crucial objective in CRC screening programs (21). Despite colonoscopy being the most frequently recommended and performed screening method, its adoption remains low among the Chinese population, with some individuals preferring less invasive alternatives such as FOBT or FIT (22). Additionally, a significant number of subjects show a preference for blood-based screening tests over stool-based tests (23), which poses challenges to the widespread implementation of stool tests. Developing AA identification tools based on easily accessible data without imposing additional burdens on patients or healthcare providers increases the likelihood of enabling patients to benefit from screening. Pan et al. (24) constructed a diagnostic model based on serum N-glycan levels with machine learning involving a population comprising cases of AA and CRC. In this model, the sensitivity and specificity for diagnosing AA were reported as 58% and 85%, respectively. However, it's important to note that, like many existing CRC diagnostic models, Pan et al. did not create a dedicated model exclusively for AA (25–28). This approach could explain the poor performance of the model in identifying AA. Xiang et al. (20) developed a serum metabolite-based diagnostic model for AA (255 AAs and 178 controls) with a sensitivity of 44.7% and a specificity of 88.9%. The study highlighted that the sensitivity of all current AA diagnostic models remains below 45% at a similar level of specificity. While our model achieves a sensitivity above 50% for detecting AA at this level of specificity, it does not meet the requirements set by certain agencies, such as the United States Preventive Services Task Force, which mandates an acceptable sensitivity of at least 70% for CRC and a specificity of at least 90% for both cancer and advanced precursor lesion (29).

In China, certain large-scale CRC screening programs and hospitals typically employ the qualitative immunogold method for FOBT (30–32). However, there remain individuals who either cannot or choose not to provide stool samples. Importantly, the diagnostic model utilized in this study does not necessarily rely on FOBT results; it is designed to apply to subjects without FOBT. In the current exploratory study of the adenoma-carcinoma sequence, the XGBoost model demonstrated superiority over FOBT in diagnosing NAA and AA but was found to be less effective than FOBT in diagnosing CRC. The simplicity and rapidity of the FOBT, and notably high sensitivity for CRC screening render it irreplaceable in the context of the adenoma-carcinoma sequence. Additionally, the XGBoost model offers potential benefits to patients who do not undergo FOBT for various reasons.

The test positivity threshold plays a crucial role in determining various important parameters. Specifically, it influences the test positivity rate, which subsequently impacts the workload of colonoscopy, the quantity of CRC or AA that warrant detection through colonoscopy (a potentially cost-effective alternative measure), the detection rate of the target lesion, and the positive predictive value (33). Non-invasive screening tests with adjustable positivity thresholds or algorithms enable the selection of test accuracy parameters, including diagnostic sensitivity and specificity, as well as test positivity rates that optimally align with the intended goals of the screening program (5). We present test accuracy parameters at different positivity thresholds in the risk assessment table. The capacity to modify detection thresholds can effectively manage the expenses related to colonoscopy, workforce availability, treatment costs, and the public expectations that are integral to equity-focused programs (5). By offering diverse risk stratification data, it can enhance physicians' clinical decision-making process for individual patients.

This study has several limitations. Firstly, the study population originates from a single center, warranting further validation in diverse countries or regions to achieve widespread applicability. Secondly, it's noteworthy that a significant portion of the AA cases were recruited from clinical settings with relatively high prevalence rates, which might limit the full representativeness of our results in the general population. Lastly, certain non-routine laboratory indicators included in this study, such as tumor markers and coagulation function, may contribute to an increase in the cost for the patient.

In conclusion, we adhered to WEO guidelines, constructing the XGBoost model of the AA patients using clinical and laboratory data in a phase I exploratory study. We established adjustable positivity thresholds to accommodate diverse screening program objectives. This model significantly outperforms FOBT in identifying patients with NAA and AA in the adenoma-carcinoma sequence; however, it cannot replace FOBT for CRC patients. Despite the XGBoost model's substantially improved accuracy in AA identification compared to existing screening

TABLE 5 Relative risk scores for predicting a diagnosis of AA within the next 30 days at different thresholds in the test set.

Cut off	Negative		Positive		TP, n	FN, n	TN, n	FP, n	Sensitivity, %	Specificity, %	PPV, %	NPV, %
	Total, n (%)	AA, n (%)	Total, n (%)	AA, n (%)								
1	0 (0)	0 (0)	758 (100)	113 (14.91)	113	0	0	645	100	0	14.91	NA
2	52 (6.86)	0 (0)	706 (93.14)	113 (16.01)	113	0	52	593	100	8.06	16.01	100
3	147 (19.39)	2 (1.36)	611 (80.61)	111 (18.17)	111	2	145	500	98.23	22.48	18.17	98.64
4	210 (27.7)	4 (1.9)	548 (72.3)	109 (19.89)	109	4	206	439	96.46	31.94	19.89	98.1
5	258 (34.04)	4 (1.55)	500 (65.96)	109 (21.8)	109	4	254	391	96.46	39.38	21.8	98.45
6	294 (38.79)	6 (2.04)	464 (61.21)	107 (23.06)	107	6	288	357	94.69	44.65	23.06	97.96
7	329 (43.4)	8 (2.43)	429 (56.6)	105 (24.48)	105	8	321	324	92.92	49.77	24.48	97.57
8	378 (49.87)	10 (2.65)	380 (50.13)	103 (27.11)	103	10	368	277	91.15	57.05	27.11	97.35
9	402 (53.03)	10 (2.49)	356 (46.97)	103 (28.93)	103	10	392	253	91.15	60.78	28.93	97.51
10	429 (56.6)	14 (3.26)	329 (43.4)	99 (30.09)	99	14	415	230	87.61	64.34	30.09	96.74
11	451 (59.5)	16 (3.55)	307 (40.5)	97 (31.6)	97	16	435	210	85.84	67.44	31.6	96.45
12	475 (62.66)	18 (3.79)	283 (37.34)	95 (33.57)	95	18	457	188	84.07	70.85	33.57	96.21
13	491 (64.78)	21 (4.28)	267 (35.22)	92 (34.46)	92	21	470	175	81.42	72.87	34.46	95.72
14	502 (66.23)	22 (4.38)	256 (33.77)	91 (35.55)	91	22	480	165	80.53	74.42	35.55	95.62
15	516 (68.07)	24 (4.65)	242 (31.93)	89 (36.78)	89	24	492	153	78.76	76.28	36.78	95.35
16	528 (69.66)	27 (5.11)	230 (30.34)	86 (37.39)	86	27	501	144	76.11	77.67	37.39	94.89
17	533 (70.32)	28 (5.25)	225 (29.68)	85 (37.78)	85	28	505	140	75.22	78.29	37.78	94.75
18	545 (71.9)	29 (5.32)	213 (28.1)	84 (39.44)	84	29	516	129	74.34	80	39.44	94.68
19	552 (72.82)	29 (5.25)	206 (27.18)	84 (40.78)	84	29	523	122	74.34	81.09	40.78	94.75
20	561 (74.01)	29 (5.17)	197 (25.99)	84 (42.64)	84	29	532	113	74.34	82.48	42.64	94.83
25	604 (79.68)	45 (7.45)	154 (20.32)	68 (44.16)	68	45	559	86	60.18	86.67	44.16	92.55
50	718 (94.72)	83 (11.56)	40 (5.28)	30 (75)	30	83	635	10	26.55	98.45	75	88.44
75	758 (100)	113 (14.91)	0 (0)	0 (0)	0	113	645	0	0	100	NA	85.09

AA, advanced adenoma; TP, true positives; FP, false positives; PPV, positive predictive value; NPV, negative predictive value; NA, not records.

methods (e.g., FOBT), it has not yet met the recommendations of certain organizations. Nevertheless, it holds the potential to provide valuable benefits for individuals who are unable to undergo the FOBT test due to various reasons.

Data availability statement

The raw data supporting the conclusions of this article will be made available by the authors, without undue reservation.

Ethics statement

The studies involving humans were approved by Medical Ethics Committee of Shijiazhuang Traditional Chinese Medicine Hospital. The studies were conducted in accordance with the local legislation and institutional requirements. The ethics committee/institutional review board waived the requirement of written informed consent for participation from the participants or the participants' legal guardians/next of kin because the requirements for informed consent were waived due to the retrospective nature.

Author contributions

HW: Conceptualization, Investigation, Writing – original draft, Writing – review & editing. XC: Conceptualization, Project administration, Writing – original draft. PM: Data curation, Investigation, Writing – original draft. CZ: Data curation, Investigation, Writing – original draft. JL: Data curation, Investigation, Writing – original draft. TPZ: Data curation,

Investigation, Writing – original draft. YL: Data curation, Investigation, Writing – original draft. XL: Data curation, Investigation, Writing – original draft. XYS: Data curation, Investigation, Writing – original draft. XXS: Data curation, Investigation, Writing – original draft. TZ: Data curation, Investigation, Writing – original draft. HYZ: Data curation, Investigation, Writing – original draft. ZW: Data curation, Investigation, Writing – original draft. XF: Formal analysis, Methodology, Writing – review & editing. HL: Formal analysis, Methodology, Writing – review & editing. HWZ: Conceptualization, Funding acquisition, Writing – review & editing, Supervision.

Funding

The author(s) declare financial support was received for the research, authorship, and/or publication of this article. This work was supported by the Hebei Administration of Traditional Chinese Medicine (grant number 2023145), the Hebei Provincial Health Commission (Grant Number 20171005), and the National Famous Old Traditional Chinese Medicine Experts Inheritance Studio Construction Program of National Administration of TCM (grant number: [2022] No. 75).

Conflict of interest

XF and HL were employed by Wuhan Metware Biotechnology Co., Ltd.

The remaining authors declare that the research was conducted in the absence of any commercial or financial relationships that could be construed as a potential conflict of interest.

Publisher's note

Supplementary material

The Supplementary Material for this article can be found online at: https://www.frontiersin.org/articles/10.3389/fonc.2024.1325514/full#supplementary-material

References

1. Maomao C, He L, Dianqin S, Siyi H, Xinxin Y, Fan Y, et al. Current cancer burden in China: Epidemiology, etiology, and prevention. *Cancer Biol Med* (2022) 19:1121–38. doi: 10.20892/j.issn.2095-3941.2022.0231

2. Dong C, Ding Y, Weng S, Li G, Huang Y, Hu H, et al. Update in version 2021 of csco guidelines for colorectal cancer from version 2020. *Chin J Cancer Res* (2021) 33:302–7. doi: 10.21147/j.issn.1000-9604.2021.03.02

3. Rabeneck L, Chiu H-M, Senore C. International perspective on the burden of colorectal cancer and public health effects. *Gastroenterology* (2020) 158:447–52. doi: 10.1053/j.gastro.2019.10.007

4. Rex DK, Boland CR, Dominitz JA, Giardiello FM, Johnson DA, Kaltenbach T, et al. Colorectal cancer screening: Recommendations for physicians and patients from the u.S. Multi-society task force on colorectal cancer. *Gastroenterology* (2017) 153:307–23. doi: 10.1053/j.gastro.2017.05.013

5. Robert SB, Carlo S, Graeme PY, James A, Robert B, Sally B, et al. An efficient strategy for evaluating new non-invasive screening tests for colorectal cancer: The guiding principles. *Gut* (2023) 72:1904–18. doi: 10.1136/gutjnl-2023-329701

6. Bosch LJW, Melotte V, Mongera S, Daenen KLJ, Coupé VMH, van Turenhout ST, et al. Multitarget stool DNA test performance in an average-risk colorectal cancer screening population. *Am J Gastroenterol* (2019) 114:1909–18. doi: 10.14309/ajg.0000000000000445

7. Jin P, You P, Fang J, Kang Q, Gu F, Cai Y, et al. Comparison of performance of two stool DNA tests and a fecal immunochemical test in detecting colorectal neoplasm: A multicenter diagnostic study. *Cancer Epidemiol Biomarkers Prev* (2022) 31:654–61. doi: 10.1158/1055-9965.EPI-21-0991

8. Francis KLC, Martin CSW, Andrew TC, James EE, Han-Mo C, Govind KM, et al. Joint asian pacific association of gastroenterology (apage)–asian pacific society of digestive endoscopy (apsde) clinical practice guidelines on the use of non-invasive biomarkers for diagnosis of colorectal neoplasia. *Gut* (2023) 72:1240. doi: 10.1136/gutjnl-2023-329429

9. Saberi-Karimian M, Khorasanchi Z, Ghazizadeh H, Tayefi M, Saffar S, Ferns GA, et al. Potential value and impact of data mining and machine learning in clinical diagnostics. *Crit Rev Clin Lab Sci* (2021) 58:275–96. doi: 10.1080/10408363.2020.1857681

10. Li X, Lu J, Hu S, Cheng KK, De Maeseneer J, Meng Q, et al. The primary health-care system in China. *Lancet* (2017) 390:2584–94. doi: 10.1016/S0140-6736(17)33109-4

11. Ngiam KY, Khor IW. Big data and machine learning algorithms for health-care delivery. *Lancet Oncol* (2019) 20:e262–73. doi: 10.1016/S1470-2045(19)30149-4

12. Gould MK, Huang BZ, Tammemagi MC, Kinar Y, Shiff R. Machine learning for early lung cancer identification using routine clinical and laboratory data. *Am J Respir Crit Care Med* (2021) 204:445–53. doi: 10.1164/rccm.202007-2791OC

13. Li H, Lin J, Xiao Y, Zheng W, Zhao L, Yang X, et al. Colorectal cancer detected by machine learning models using conventional laboratory test data. *Technol Cancer Res Treat* (2021) 20:15330338211058352. doi: 10.1177/15330338211058352

14. Yan W, Shi H, He T, Chen J, Wang C, Liao A, et al. Employment of artificial intelligence based on routine laboratory results for the early diagnosis of multiple myeloma. *Front Oncol* (2021) 11:608191. doi: 10.3389/fonc.2021.608191

15. Tsai IJ, Shen W-C, Lee C-L, Wang H-D, Lin C-Y. Machine learning in prediction of bladder cancer on clinical laboratory data. *Diagnostics* (2022) 12:203. doi: 10.3390/diagnostics12010203

16. Stegeman I, de Wijkerslooth TR, Stoop EM, van Leerdam ME, Dekker E, van Ballegooijen M, et al. Colorectal cancer risk factors in the detection of advanced adenoma and colorectal cancer. *Cancer Epidemiol* (2013) 37:278–83. doi: 10.1016/j.canep.2013.02.004

17. Baron JA, Cole BF, Sandler RS, Haile RW, Ahnen D, Bresalier R, et al. A randomized trial of aspirin to prevent colorectal adenomas. *N Engl J Med* (2003) 348:891–9. doi: 10.1056/NEJMoa021735

18. Soerensen PD, Christensen H, Laursen SGW, Hardahl C, Brandslund I, Madsen JS. Using artificial intelligence in a primary care setting to identify patients at risk for cancer: A risk prediction model based on routine laboratory tests. *Clin Chem Lab Med* (2022) 60:2005–16. doi: 10.1515/cclm-2021-1015

19. Hanley JA, McNeil BJ. A method of comparing the areas under receiver operating characteristic curves derived from the same cases. *Radiology* (1983) 148:839–43. doi: 10.1148/radiology.148.3.6878708

20. Xiang J, Li L, Guo X, Li X, Lin K, Yang L, et al. Abstract 3346: Evaluation of a serum-based test integrating tumor tissue and gut microbiome derived metabolites for diagnosis of advanced colorectal adenoma. *Cancer Res* (2023) 83:3346. doi: 10.1158/1538-7445.AM2023-3346

21. Lidgard GP, Domanico MJ, Bruinsma JJ, Light J, Gagrat ZD, Oldham–Haltom RL, et al. Clinical performance of an automated stool DNA assay for detection of colorectal neoplasia. *Clin Gastroenterol Hepatol* (2013) 11:1313–8. doi: 10.1016/j.cgh.2013.04.023

22. Hongda C, Ni L, Jiansong R, Xiaoshuang F, Zhangyan L, Luopei W, et al. Participation and yield of a population-based colorectal cancer screening programme in China. *Gut* (2019) 68:1450. doi: 10.1136/gutjnl-2018-317124

23. Osborne JM, Flight I, Wilson CJ, Chen G, Ratcliffe J, Young GP. The impact of sample type and procedural attributes on relative acceptability of different colorectal cancer screening regimens. *Patient Prefer Adher* (2018) 12:1825–36. doi: 10.2147/ppa.S172143

24. Pan Y, Zhang L, Zhang R, Han J, Qin W, Gu Y, et al. Screening and diagnosis of colorectal cancer and advanced adenoma by bionic glycome method and machine learning. *Am J Cancer Res* (2021) 11:3002–20.

25. de Meij TG, Larbi IB, van der Schee MP, Lentferink YE, Paff T, Terhaar sive Droste JS, et al. Electronic nose can discriminate colorectal carcinoma and advanced adenomas by fecal volatile biomarker analysis: Proof of principle study. *Int J Cancer* (2014) 134:1132–8. doi: 10.1002/ijc.28446

26. van Keulen KE, Jansen ME, Schrauwen RWM, Kolkman JJ, Siersema PD. Volatile organic compounds in breath can serve as a non-invasive diagnostic biomarker for the detection of advanced adenomas and colorectal cancer. *Aliment Pharmacol Ther* (2020) 51:334–46. doi: 10.1111/apt.15622

27. Telleria O, Alboniga OE, Clos-Garcia M, Nafría-Jimenez B, Cubiella J, Bujanda L, et al. A comprehensive metabolomics analysis of fecal samples from advanced adenoma and colorectal cancer patients. *Metabolites* (2022) 12:550. doi: 10.3390/metabo12060550

28. Xu J, Zheng Z, Yang L, Li R, Ma X, Zhang J, et al. A novel promising diagnosis model for colorectal advanced adenoma and carcinoma based on the progressive gut microbiota gene biomarkers. *Cell Biosci* (2022) 12:208. doi: 10.1186/s13578-022-00940-1

29. Force, U. P. S. T. Screening for colorectal cancer: Us preventive services task force recommendation statement. *JAMA* (2016) 315:2564–75. doi: 10.1001/jama.2016.5989%JJAMA

30. Huang Y, Li Q, Ge W, Cai S, Zhang S, Zheng S. Predictive power of quantitative and qualitative fecal immunochemical tests for hemoglobin in population screening for colorectal neoplasm. *Eur J Cancer Prev* (2014) 23:27–34. doi: 10.1097/CEJ.0b013e328364f229

31. Huang Y, Cai S, Li Q, Song Y, Yuan Y, Zhang S, et al. Six years of colorectal cancer mortality surveillance in the screening population for a risk stratified screening program. *Cancer Epidemiol* (2021) 73:101937. doi: 10.1016/j.canep.2021.101937

32. Zhang M, Zhao L, Zhang Y, Jing H, Wei L, Li Z, et al. Colorectal cancer screening with high risk-factor questionnaire and fecal immunochemical tests among 5, 947, 986 asymptomatic population: A population-based study. *Front Oncol* (2022) 12:893183. doi: 10.3389/fonc.2022.893183

33. Young GP, Symonds EL, Allison JE, Cole SR, Fraser CG, Halloran SP, et al. Advances in fecal occult blood tests: The fit revolution. *Dig Dis Sci* (2015) 60:609–22. doi: 10.1007/s10620-014-3445-3

Frontiers in Immunology

Explores novel approaches and diagnoses to treat immune disorders.

The official journal of the International Union of Immunological Societies (IUIS) and the most cited in its field, leading the way for research across basic, translational and clinical immunology.

Discover the latest Research Topics

See more →

Frontiers

Avenue du Tribunal-Fédéral 34
1005 Lausanne, Switzerland
frontiersin.org

Contact us

+41 (0)21 510 17 00
frontiersin.org/about/contact